

BERICHTE

aus dem Fachbereich Geowissenschaften
der Universität Bremen

No. 229

Fabian, M.

NEAR SURFACE TILT AND PORE PRESSURE CHANGES
INDUCED BY PUMPING IN
MULTI-LAYERED POROELASTIC HALF-SPACES

Berichte, Fachbereich Geowissenschaften, Universität Bremen, No. 229,
121 pages, Bremen 2004



ISSN 0931-0800

The "Berichte aus dem Fachbereich Geowissenschaften" are produced at irregular intervals by the Department of Geosciences, Bremen University.

They serve for the publication of experimental works, Ph.D.-theses and scientific contributions made by members of the department.

Reports can be ordered from:

Monika Bachur

Forschungszentrum Ozeanränder, RCOM

Universität Bremen

Postfach 330 440

D 28334 BREMEN

Phone: (49) 421 218-8960

Fax: (49) 421 218-3116

e-mail: MBachur@uni-bremen.de

Citation:

Fabian, M.

Near Surface Tilt and Pore Pressure Changes Induced by Pumping in Multi-Layered Poroelastic Half-Spaces.

Berichte, Fachbereich Geowissenschaften, Universität Bremen, No. 229, 121 pages, Bremen, 2004.

ISSN 0931-0800

Near Surface Tilt and Pore Pressure Changes Induced by Pumping in Multi-Layered Poroelastic Half-Spaces

Dissertation

zur
Erlangung des Doktorgrades (Dr. rer. nat.)
der
Mathematisch–Naturwissenschaftlichen Fakultät
der
Rheinischen Friedrich–Wilhelms–Universität Bonn

vorgelegt von

Dipl.-Phys. Marcus Karl Fabian

aus Siegburg

Bonn 2004

First electronically published and online accessible as 'Bonner Dissertationen und Habilitationen online der
Mathematisch-Naturwissenschaftlichen Fakultät':

http://hss.ulb.uni-bonn.de/diss_online/math_nat_fak/2004/fabian_marcus/index.htm

Diese Arbeit wurde angefertigt mit der Genehmigung der Mathematisch–Naturwissenschaftlichen Fakultät der Rheinischen Friedrich–Wilhelms–Universität Bonn.

1. Referent: Prof. Dr. H.-J. Kümpel
2. Referent: Priv. Doz. Dr. A. Hördt

Tag der Promotion: 16.03.2004

Abstract

Title: Near Surface Tilt and Pore Pressure Changes Induced by Pumping in Multi-Layered Poroelastic Half-Spaces.

Keywords: Tilt Measurements, Surface Deformation Fields, Pump Tests, Tilt Reversals, Noordbergum Effect, Poroelastic Modelling.

At three sites in Germany, called OE, BV and WD, pump test experiments were conducted. The aim was the observation and ensuing modelling of near surface tilt and pore pressure changes induced by pumping in nearby wells. The observations were carried out with ‘bubble tiltmeters’ as borehole and platform instruments. The nominal resolution of the instruments was $0.1 \mu rad$. Pore pressure changes in the subsoil were recorded through water level fluctuations in wells by means of pressure transducers with a resolution better than $1 mm H_2O$. The model calculations were carried out with the program POEL. With an assumption of a subsoil model, the program allows an accurate and rapid signal simulation. The models are time resolved and account for multi-layered fully saturated poroelastic half-spaces.

At site OE, 12 tiltmeters were used for measurements. They were installed at 16 shallow observation positions. A waterworks was operated at the site and caused pump induced effects. The tilt data was used for imaging the surface deformation fields. This new method of deformation imaging turned out to be promising for further investigations. Heterogeneities in the subsoil might cause disturbances in the symmetry of a surface deformation image. Subsoil consolidation could be monitored and an exhaustion of the lower-lying reservoir might become predictable.

The most striking discoveries are transient pump induced reversals of the tilt signal, which were observed at the locations OE and BV. At BV, the ‘Noordbergum effect’ was recorded in well level data parallel to the tilt reversals. At this site, two tiltmeters were used. The tilt reversals document in the matrix strain the strong coupling between the soil matrix and the pore fluid. This type of signals could be reproduced by poroelastic modelling.

The modelling reveals that the transient signals are sensitive to parameter adjustments in deeper layers of the model. Accordingly, the transient signal part seems generally well suited for a fast experimental determination of effective poroelastic subsoil parameters. Additionally, modelling showed a direct connection between the type of tilt reversal and the arrangement of the layers in the subsoil.

Further aspects of the investigations were: At the site WD tilt observations were conducted with two tiltmeters above a buried quaternary channel from which the groundwater was extracted. Steady state models were calculated for predicting the position and strength of the pump induced tilt maximum at the surface. Refinements of experiments are discussed.

Kurzfassung

Deutscher Titel: Oberflächennahe Neigungssignale und Porendruckvariationen induziert durch Pumpen in mehrfach geschichteten poroelastischen Halbräumen.

Schlüsselwörter: Neigungsmessungen, Oberflächendeformationsfelder, Pumptestes, Neigungsumkehrungen, Noordbergum Effekt, Poroelastische Modellierung.

An drei Lokationen in Deutschland, bezeichnet mit OE, BV und WD, wurden Pumptestexperimente durchgeführt. Ziel war die Erfassung und die anschließende Modellierung von pumpinduzierten oberflächennahen Neigungssignalen und Porendruckvariationen. Die Neigungsmessungen erfolgten mit „Bubble-Tiltmetern“, und zwar sowohl mit Bohrloch- als auch Plattforminstrumenten. Die nominelle Auflösung der Geräte betrug $0,1 \mu rad$. Die Porendruckschwankungen im Untergrund wurden anhand von Pegelveränderungen in Brunnen erfasst. Hierzu wurden Drucksensoren mit Auflösungen besser als $1 mm H_2O$ in die Brunnen eingebracht. Die Modellrechnungen wurden mit dem Programm POEL ausgeführt. Für ein angenommenes Untergrundmodell erlaubt das Programm eine genaue und schnelle Signalberechnung. Die Modelle sind zeitaufgelöst und berücksichtigen geschichtete vollständig gesättigte poroelastische Halbräume.

An der Lokation OE wurde mit 12 Tiltmetern gemessen. Diese wurden an 16 verschiedenen Positionen oberflächennah installiert. Ein an der Lokation gelegenes Wasserwerk verursachte pumpbedingte Effekte. Die Neigungsdaten wurden zur Darstellung von Oberflächendeformationsfeldern genutzt. Es zeigte sich, daß diese neue Methode für weitere Untersuchungen vielversprechend ist. Heterogenitäten im Untergrund können sich als Abweichungen von der Symmetrie im Oberflächendeformationsfeld abzeichnen. Die Konsolidierung des Untergrundes könnte fortlaufend kontrolliert und eine Erschöpfung des tieferliegenden Reservoirs frühzeitig erkannt werden.

Die herausragendsten Entdeckungen sind transiente pumpinduzierte Umkehrungen des Neigungssignals, die an den Lokationen OE und BV beobachtet wurden. An BV wurde der „Noordbergum Effekt“ parallel zu diesen Neigungsumkehrungen im Brunnenpegelsignal nachgewiesen. Hier wurde mit zwei Tiltmetern gemessen. Die Neigungsumkehrungen dokumentieren in der Bewegung des Korngerüsts die starke Kopplung zwischen Untergrundformation und Porenflüssigkeit. Diese Art von Signalen konnte in den poroelastischen Modellen nachvollzogen werden.

Die Modellrechnungen zeigen, dass die transienten Signalanteile sensitiv auf Parametervariationen in tieferen Schichten des Modells reagieren. Danach scheint für eine schnelle experimentelle Bestimmung von effektiven poroelastischen Untergrundparametern der transiente Signalanteil gut geeignet. Die Rechnungen zeigen zudem einen direkten Zusammenhang zwischen der Art der Neigungssignalumkehr und der konkreten Schichtenfolge im Untergrund.

Weitere Aspekte der Untersuchungen waren: An der Lokation WD fanden Neigungsmessungen mit zwei Tiltmetern oberhalb einer quartären Rinne statt, aus der gepumpt wurde. Stationäre Modelle zur Bestimmung von Lage und Stärke des pumpinduzierten Neigungsmaximums an der Oberfläche wurden gerechnet. Verbesserungen der Experimente werden diskutiert.

Contents

1	Introduction	1
2	Theoretical Sketch	3
2.1	Experimental Concept	3
2.2	Tiltmeters and Tilt Measurements	4
2.3	Formal Definition of Tilt	5
2.4	Pore Pressure Measurement and Well Head Changes	6
2.5	Poroelastic Equations	7
2.6	Poroelastic Parameters	7
2.7	Solutions of Poroelastic Equations	11
3	Experiments	16
3.1	Oberelvenich, OE	17
3.1.1	Tilt and Well Level Response, November 2001	20
3.1.2	Surface Deformation Imaging, March 2002	22
a.	Experimental Set-up	22
b.	Data Basis from Borehole Tiltmeters	23
c.	Surface Deformation Images from Borehole Tilt	27
d.	Platform Tiltmeters	33
e.	Transient Borehole Tiltmeter Signals – Positive Tilt Reversals	35
3.2	Bürvenich, BV	39
3.2.1	Pump Test from GW1 _{BV} – Elliptical Hodographs	41
3.2.2	Pump Test from GW2 _{BV} – Negative Tilt Reversals and Noordbergum Effect	44
3.3	Wulsdorf, WD	48
4	Poroelastic Forward Modelling	53
4.1	Preconditions of Modelling	54
4.2	Steady State Models	55

4.2.1	3(5)-Layer Model, One and Two Buried Slabs	56
4.2.2	4-Layer Model	59
4.2.3	6-Layer Model	60
4.3	Dynamic Models	65
4.3.1	Homogeneous Half-Space	66
4.3.2	3-Layer Model	68
4.3.3	4-Layer Model	70
4.3.4	Adjusted 6-Layer Model	71
4.3.5	Long-Term Signal Evolution, Adjusted 6-Layer Model	76
4.3.6	Sensitivity of Transient Signals to Variations of Parameters and Layering	78
5	Discussion	81
5.1	Surface Deformation Imaging	81
5.2	Tiltmeter Operation	82
5.3	Modelling Approach	83
6	Summary	84
A	Appendix	86
A.1	Assembling of an Observation Position	86
A.1.1	Tiltmeters	86
A.1.2	Pressure Transducers	88
A.2	Transformations of Tilt Angles	89
A.3	Auxiliary Data to Site OE	90
A.3.1	Configuration Data of Wells and Tiltmeters	90
A.3.2	Second Regional Geological Cross Section, OE	92
A.3.3	Correction of Tilt Data	92
A.3.4	Error Plots of Deformation Image Data, OE	95
A.4	Auxiliary Data to Site BV	96
A.5	Auxiliary Data to Site WD	96
A.6	POEL	96
A.6.1	A Comparison with the Analytic Solution	97
A.6.2	Difference between Point- and Line-Sink	97
A.7	Time Slices – Half-Space, 3, 4, 6 Layers	98
	Bibliography	103
	Acknowledgements – Danksagung	111

List of Figures

2.1	Experiment with observables tilt $\Delta\gamma$, pore pressure Δp	3
2.2	Tiltmeter, tilt components and hodograph	4
2.3	Bubble tilt sensor	5
2.4	Installation scheme of tiltmeters	5
2.5	Formal definition of vertical tilt	6
2.6	Tilt in a horizontal t-r plane	6
2.7	Analytical poroelastic steady state full-space solutions	12
2.8	Pump induced tilt in a homogeneous half-space	13
2.9	Analytical poroelastic steady state solutions in half-space	14
3.1	Location of test sites OE, BV, WD in Germany	16
3.2	Location of OE, BV in the Lower Rhine Embayment	17
3.3	Map of site OE	18
3.4	Photo from site OE	19
3.5	Local geological cross section, OE	19
3.6	First regional geological cross section, OE	20
3.7	Data from the first pump test, November 2001, OE	21
3.8	Depths of tiltmeters and topsoil layer, OE	23
3.9	Tilt data from the deformation near field, OE	24
3.10	Tilt data from the deformation far field, OE	26
3.11	Example snap-shot of tilt data from position T4 _{OE}	27
3.12	Determination of tilt response to a pump cycle	28
3.13	Tilt fields by B1 _{OE} , B3 _{OE} and B2 _{OE} , B3 _{OE}	29
3.14	Tilt fields by B1 _{OE} , B2 _{OE} and sum of B1 _{OE} , B3 _{OE} and B2 _{OE} , B3 _{OE}	31
3.15	Tilt difference fields, OE	32
3.16	Platform tiltmeter data, OE	34
3.17	Tilt response during four pump cycles of B1 _{OE}	36
3.18	Positive tilt reversals, pumping from B1 _{OE}	37

3.19	Tilt response during four pump cycles of B2 _{OE}	38
3.20	Map of site BV	40
3.21	Lithology log, BV	40
3.22	Photo from pump test at BV	41
3.23	Tilt and pore pressure changes, GW1 _{BV}	42
3.24	Hodographs, pump test in GW1 _{BV}	44
3.25	Two processes causing hodographs	44
3.26	Negative tilt reversals and Noordbergum effect, GW2 _{BV}	46
3.27	Hodographs, pump test in GW2 _{BV}	48
3.28	Map of site WD	49
3.29	Photo from site WD	49
3.30	Simplified geological cross section, WD	50
3.31	Time series from a six day one-cycle pump test, WD	51
3.32	Hodographs from pump test, WD	52
4.1	Grid of the calculation points for poroelastic response	54
4.2	Steady state POEL solution, 3-layer model	56
4.3	Steady state POEL solution, 2 symmetric slabs, 5 layers	58
4.4	Steady state POEL solution, 4-layer model	59
4.5	Steady state POEL solutions, first 6-layer model	61
4.6	6-layers, variations i, ii of the model in Fig.4.5	63
4.7	6-layers, variations iii, iv of the model in Fig.4.5	64
4.8	6-layers, influence of change in Poisson ratio ν	65
4.9	Signal evolution in homogeneous half-space	67
4.10	Tilt response and relaxation	67
4.11	Double reversal of the pore pressure signal	68
4.12	Long-term pore pressure signal in homogeneous half-space	68
4.13	Signal evolution in 3-layer model	69
4.14	Signal evolution in 4-layer model	71
4.15	Tilt signal evolution in adjusted 6-layer model	74
4.16	Sketch, possible vertical motions and tilt, 6-layers	75
4.17	Pore pressure signal evolution in adjusted 6-layer model	76
4.18	Tilt, steady state and long-term evolution, 6-layers	77
4.19	Pore pressure, steady state and long-term evolution, 6-layers	78
4.20	A long-term pore pressure signal, adjusted 6-layer model	78
4.21	Parameter sensitivity of transient signals	79

A.1	Borehole drilling with a spiral drill, $T4_{OE}$	86
A.2	Installation, lowering of the casing, $T1_{OE}$	87
A.3	Borehole tiltmeter, AGI 722a	87
A.4	Installation of a borehole tiltmeter by tampering, $T4_{OE}$	88
A.5	Platform tiltmeter, AGI 701-2	88
A.6	Data retrieval and maintenance tools, $T2_{OE}$	89
A.7	Pressure transducer In-Situ Inc. TROLL-4000	89
A.8	Transformation of tilt between coordinate systems	89
A.9	Tilt $\Delta\gamma$ and its strike Γ in a x-y system	90
A.10	Radial distances between tiltmeters and $B1_{OE}$	91
A.11	Radial distances between tiltmeters and $B2_{OE}$	91
A.12	Radial distances between tiltmeters and $B3_{OE}$	92
A.13	Second regional geological cross section, OE	92
A.14	Data correction, borehole and platform tiltmeter, OE	93
A.15	Error plots of surface deformation image data, OE	95
A.16	Difference – steady state analytic and POEL solutions	97
A.17	Difference – well as a point and a line sink	97
A.18	Time slices, tilt, homogeneous half-space	99
A.19	Time slices, pore pressure, homogeneous half-space	99
A.20	Time slices, tilt, 3-layer model	100
A.21	Time slices, pore pressure, 3-layer model	100
A.22	Time slices, tilt, 4-layer model	101
A.23	Time slices, pore pressure, 4-layer model	101
A.24	Time slices, tilt, adjusted 6-layer model	102
A.25	Time slices, pore pressure, adjusted 6-layer model	102

List of Tables

2.1	Bibliographical values of parameters G, ν	8
2.2	K_f -values	10
2.3	Poroelastic (start) parameters for modelling, G, ν, ν_u, B, D	11
4.1	Grid geometry for POEL models	55
4.2	Parameters and geometry, 3-layer model	56
4.3	Radial distances of tilt maximum at surface, 3-layer model	57
4.4	Parameters and geometry, 2 symmetric slabs, 5 layers	58
4.5	Parameters and geometry, 4-layer model	59
4.6	Parameters and geometry, first 6-layer model	60
4.7	Parameter variations of the first 6-layer model	62
4.8	Parameters and geometry, homogeneous half-space	66
4.9	Parameters and geometry, adjusted 6-layer model	72
4.10	Transient tilt signals and layer structure	80
A.1	Configuration and hydrological data of wells, OE	91
A.2	Configuration data of tiltmeters and wells, BV	96
A.3	Configuration data of tiltmeters and wells, WD	96

Chapter 1

Introduction

Tiltmeters installed at shallow depth are apt to record signals which are related to subsidence. The subsidence can be caused for instance by pump activities in nearby wells. Tilt measurements are a high resolution method for the detection of subsoil motions, i. e. allow recordings of motions related to soil displacements in the range of sub-micrometers. The measurements have the capability to record quasi continuous data over a broad range of signal periods, from seconds to years (Kümpel et al., 2001). Observations of induced soil motions in the vicinity of pumped wells can be a new method for monitoring of subsoil dynamics and reservoir consolidation. These observations can be combined with well level recordings to gain additional information about the related pump induced pore pressure changes. The observations of tilt and pore pressure changes could be described by poroelastic models, i. e. on the basis of the rheology of poroelasticity, which is also called the theory of consolidation (Terzaghi, 1925, 1943, Biot, 1941). The poroelastic parameters and geological structure used in these models might be applicable for a characterization of the subsoil (Kümpel, 1996, Kümpel et al., 1999, Vasco et al., 1998, 2001).

The concept of this combined experimental and modelling approach is that tilt and pore pressure signals are generated by fluid withdrawal in the close surrounding of the production well's screen. The signals spread throughout the subsoil and were 'seen' by the tiltmeters installed near the surface, and recorded as well level changes in observation wells. These signals carry information about the response behaviour and the structure of that part of the subsurface where the signals passed through. The pump induced tilt field spreading out near the surface can be depicted as a contour diagram drawn from the tilt data that were obtained at different observation points. This contour diagram provides an image corresponding to the pump induced surface deformations. This experimental method is called 'surface deformation imaging'. Inhomogeneities in the subsoil can disturb the signal dispersion which is expected from a regular subsoil structure like a homogeneous or a horizontally layered half-space. The inhomogeneities can be recognized as a deviation from the expected, regular signal course at individual observation points and thus as a perturbation in the tilt field near surface, i. e. in the contour diagrams. Poroelasticity appears to be a suitable theory for a comprehensive description of pump induced tilt and pore pressure changes (Kümpel, 1989, 1991, 1997, Lehmann, 2001, Wang & Kümpel, 2003). Construction of a poroelastic subsoil model is possible on the basis of the geological interpretation of the drilling log of the used wells, or by means of geophysical surveying. The poroelastic parameters and the structure of the model can be adjusted using an iterative approach. The model, which fits the observations best, can be used to describe the recorded response of tilt and pore pressure to the water withdrawal from the well.

An application of the method is the reduction of the ambiguity of classical hydrological methods in which well level fluctuations were analysed (Krauss, 1974, Krauss-Kalweit & Kalweit, 1984, Krusemann & de Ridder, 1994, Hölting, 1996). Since a single well, especially if it is deep, is costly, the number of observation points is limited. Moreover, measurement of well heads mostly accounts for the related pore pressure dynamics in the tapped aquifer. Therefore, determination of subsoil parameters in classical methods is focused to this aquifer, but not to the complete subsurface (Hölting, 1996, Krusemann &

de Ridder, 1994). With the new method, the number of observation points can be increased. Tiltmeters can be installed in shallow boreholes, in depths of a few meters at positions between observation wells. These tilt recordings account for the pump induced response of the whole subsoil between the depth of the well screen and the surface, and they account for the dynamics of soil-matrix and fluids. In a further state of development, near surface tilt measurements could be used as an additional method for geophysical surveying, too (Karasaki et al., 2000). Surface displacements and consolidation processes caused by water, gas or oil production (Lewis et al., 2003) and also related to flooding of old tunnels from coal mining could be assessed. The optimal injection rate for e. g. geothermal exploitation (Walters et al., 2002) could be controlled and estimated. Tilt monitoring in ground water extraction areas close to cities can be used to indicate serious subsidence of special purpose buildings, or to monitor induced geodynamic processes. However, this method using tilt observations during pump tests is still in its development. This study will add a further step.

The study bases on investigations which apply the theory of poroelasticity for the interpretation of tilt and pore pressure data from pump test experiments: The works of Kümpel (1989) and Lehmann (2001) mostly deal with the time dependency of pump induced tilt and pore pressure changes in the homogeneous full-space and the steady state situation in the homogeneous half-space, respectively. Wang & Kümpel (2003) presented the program POEL to model the time dependent tilt and pore pressure response to pumping from a homogeneous and a layered poroelastic half-space. They used POEL to compute the tilt data from a test site in Hungary (Kümpel et al., 1996). Fabian & Kümpel (2003) showed a new type of transient pump induced tilt signals, jumps and reversals, which were observed contemporaneously with the hydrological phenomenon of the ‘Noordbergum effect’.

The aim of this study is to clarify some questions arising from these previous works. The questions are: (1) Which capabilities has the method of surface deformation imaging by means of tiltmeter clusters and which improvements can be recommended? (2) Which types of transient pump induced tilt signals and pore pressure changes can be observed here? (3) How do pump induced tilt and pore pressure distributions look in layered half-spaces – in the steady state and during the transient phase of withdrawal – and how do the field distributions in subsoil depend on poroelastic parameters and arrangement of layers? (4) Is it possible to model the transient jumps and reversals observed in tiltmeter data, and are these signals useful for the derivation of subsoil parameters?

To provide an answer to question (1), at the site called OE, two experimental case studies were conducted. A first experiment with two borehole tiltmeters and a second one with a cluster of tiltmeters and different types of instruments (borehole and platform tiltmeters) and installations was carried out. The experiment with two tiltmeters served as a preliminary test for the second experiment. In the second experiment the method of surface deformation imaging was applied and tested in detail. Question (2) was assessed by the experiments at site OE too, as well as by two further experiments at the sites called BV and WD with two borehole tiltmeters each. The transient part of selected pump induced signals was inspected. Question (3) was answered by the computation of several models for multi-layered poroelastic half-spaces by means of the program POEL. The models are generalized. They were constructed to account for different kinds of layering in subsoil, for the steady state and the transient phase. An answer to question (4) was given by adjusting a multi-layer model with respect to the gross geological settings at the experimental sites OE and BV.

In the following chapter 2, the most important aspects of the experimental techniques used in the study and the necessary terms for poroelastic modelling are stated. In chapter 3, the experiments to provide an answer to questions (1) and (2) will be explained and the data presented and discussed. Chapter 4 shows and explains the model calculations. Questions (3) and (4) will be answered. In chapter 5 is a discussion of some important aspects of the investigations. The appendix provides additional data and information about the set-up of tiltmeter experiments, transformations of tilt data, the experimental sites and the corrections of data.

Chapter 2

Theoretical Sketch

This chapter briefly states the most important aspects of the applied experimental methods and of the theory of poroelasticity used for interpretations and modelling. Many other researchers deal with a consequent methodical and theoretical treatment of the use of tiltmeters and of poroelasticity, e.g. [Biot \(1941, 1973\)](#), [Rice & Cleary \(1976\)](#), [Wyatt & Berger \(1980\)](#), [Kümpel \(1982, 1989, 1991\)](#), [Agnew \(1986\)](#), [Wyatt et al. \(1988\)](#), [Wang \(1993, 2000\)](#), [Lehmann \(2001\)](#), [Wang & Kümpel \(2003\)](#), [Neuzil \(2003\)](#).

The experimental concept, tilt measurements, tiltmeters, a formal definition of tilt, pore pressure measurements by means of pressure transducers, the poroelastic equations, the parameters used for modelling and the analytical steady state solutions in the homogeneous full-space and the half-space as well as methods for solving more complex situations will be itemized in that sequence in the following.

2.1 Experimental Concept

Experiments as sketched in [Fig.2.1](#) show that pumping through a production well leads to deformations of the subsoil, related tilt signals nearby the well and well head changes in observation wells ([Kümpel et al., 1996](#), [Fabian et al., 2000](#), [Lehmann, 2001](#), [Fabian & Kümpel, 2003](#)). The observables, which have to be measured and modelled, are pump induced tilt, $\Delta\gamma$ with $[\Delta\gamma] = 1\mu rad$, and pore pressure changes, Δp with $[\Delta p] = Pa$. The latter are assumed to be related to well head changes. Measurements of the well head can be obtained through pressure transducers in the production and observation wells. (Sub-) surface tilting can be monitored by tiltmeters.

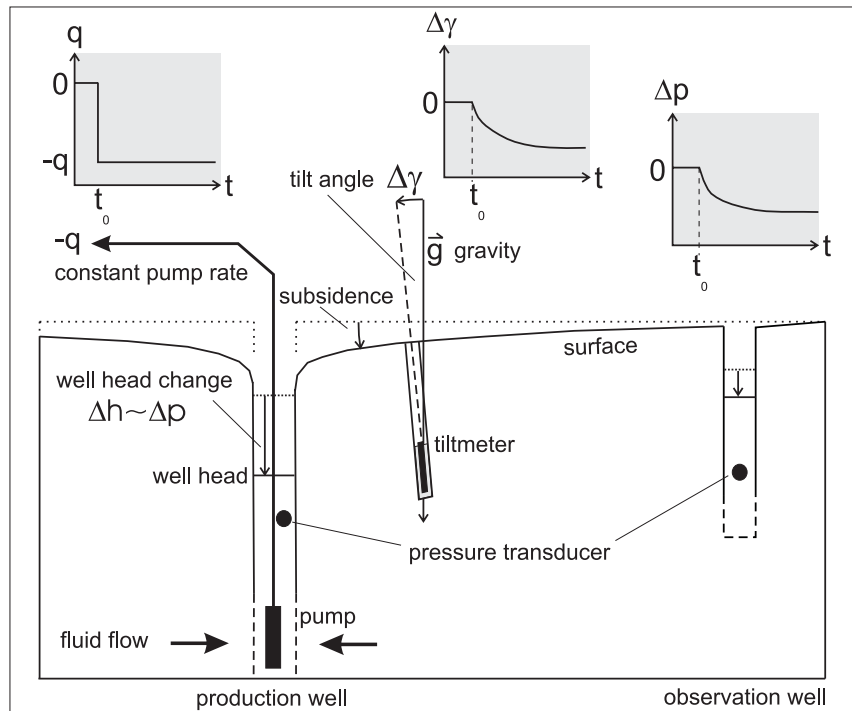


Figure 2.1: Experiment with observables $\Delta\gamma$ (tilt) and Δp (pore pressure change). q denotes the pump rate, t is time and t_0 time of onset of the pump, Δh is the well head change to which pore pressure change is related. Pumping leads to well head changes, induced subsidence of the surface and tilt. The figure is not true to scale.

Only pump induced tilt and pore pressure changes were investigated, namely the relative signals with respect to the equilibrium levels before the pump test has been started. In the experimental situation, there are additional signal parts of tilt and pore pressure changes. They can be e.g. a long term drift and fluctuating signals like noise. These additional signal parts are not respected by the theory used for interpretations. The theory only accounts for the relative, pump induced signals. The relationship between soil deformation (including tilt) and pore pressure change, their coupling and their time dependency can be described by the theory of linear poroelasticity (Biot, 1941, Rudnicki, 1986, Kümpel, 1989, Wang, 2000). The subsoil is seen as a so called poroelastic medium. The medium consists of two components. First, a poroelastic matrix – herein called grain matrix or matrix. Second, a pore fluid in the pores of the matrix. Since pore fluid and matrix are coupled, a change in pore pressure, i.e. a pore pressure gradient established for instance by pumping water from a well, leads to deformations, and vice versa deformations can generally cause pore pressure changes.

2.2 Tiltmeters and Tilt Measurements

A tiltmeter detects the angle between the tiltmeter itself and the local gravity vector, Fig.2.2. Connected to a data logger, tilt measurements are time resolved and therefore also report angular motions. The measured angle can be divided in two perpendicular angles. The values of these perpendicular angles can be plotted in a horizontal plane against each other. The resulting trace, called hodograph, shows the course of the tiltmeters top with respect to its bottom, Figs.2.1, 2.2.

Tilt measurements can not distinguish between angular motions of the instrument body and changes in the direction of the plumb line (i.e. the gravity vector). It is assumed that only angular motions of the tiltmeter with respect to gravity occur and that the local plumb line is stable. Moreover, a tiltmeter is not able to detect any translations, i.e. parallel displacements of the instrument. Tilt itself is associated with a rotation and/or a shearing in subsoil (Kümpel, 1989, Lehmann, 2001). Due to cohesion, as it is assumed, any linear motion of a part of the subsoil will be accompanied by an angular motion nearby this linear displacement. A movement of a part of the subsoil with respect to another not moving one ends up in a local shearing between the moving and the resting part, or a rotation of the moving one around the fixed. The range of the spatial signal wave length that can be accessed in the measurements depends on the tiltmeter body's extension, i.e. the (effective) base length (Kümpel, 2003a).

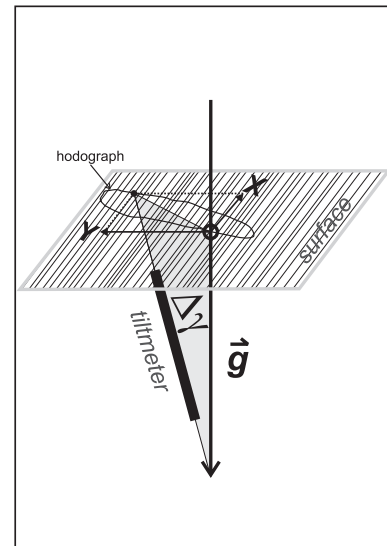


Figure 2.2: Tiltmeter, tilt angle $\Delta\gamma$ with respect to gravity \vec{g} , perpendicular tilt components X and Y and hodograph.

In this study two types of tiltmeters were used, first borehole tiltmeters (AGI, 1991, 1999a), second platform tiltmeters (AGI, 1997). The borehole tiltmeters were the main instruments, since there is some experience with their application (Fabian et al., 2000, Kümpel et al., 2001, Mentis & Fabian, 2001a,b, Campbell et al., 2002, Fabian & Kümpel, 2003, Kümpel & Fabian, 2003). The platform tiltmeters were used to test their applicability.

Borehole tiltmeters can only detect angles in horizontal direction, called vertical tilt (as in Fig.2.2). Platform tiltmeters measure tilt angles in vertical direction, called horizontal tilt (Agnew, 1986). The strike direction of pump induced near surface tilt is obtained from measurements of the tilt angle in two perpendicular horizontal directions, X and Y in Fig.2.2. Hence, all instruments used utilize two build-in (electrolytical bubble tilt) sensors. The sensors have a nominal angular resolution of $0.1 \mu rad$. This almost equals a sideways deflection of $0.1 \cdot 10^{-6} m$ of a $1 m$ long line. Connected to a high resolution data logger at least a two to five times better resolution could be achieved in all, i.e. $0.05 \mu rad$ to $0.02 \mu rad$. Fig.2.3 shows a sketch of a bubble tilt sensor. The gas bubble's position in the quartz tube depends on the orientation of the sensor with respect to the plumb line. If an alternating-current is applied to the outer electrodes, a varying electrical potential field is established in the electrolyte.

That potential field, i. e. the complex resistivity between the electrodes, depends on the position of the bubble. A movement of the bubble will change the electrical potential between the upper and lower electrode. This allows a calibration of the output voltage between these two electrodes in dependency of the tilting of the sensor (Agnew, 1986, Mentis et al., 1996). Both sensors of a tiltmeter are operated independent of each other. An integrated low-pass Butterworth filter with $40dB/dec$ roll-off in the range below the cut-off period of $7.5s$ can be applied simultaneously to both. The instruments have an additional thermistor element that enables temperature control (AGI, 1997, Holzhausen, 1997, AGI, 1999a,b, 2000). Other types of tiltmeters utilize vertical or horizontal pendulums as sensors (Gouly, 1976, Peters & Beaumont, 1985, Rogers et al., 1986, Valliant & Burris, 1987, Bilham, 1993, Bonatz, 2000).

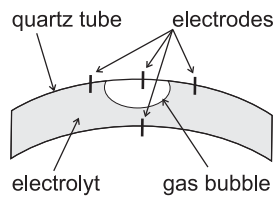


Figure 2.3: Bubble tilt sensor.

In the experiments borehole tiltmeters were installed in quartz-sand beds in shallow boreholes at depths between $1.5m$ and $4m$. The tiltmeters were adjusted with respect to the plumb line by tampering the sandy fill in the ring space between the tiltmeter body and the casing of the borehole, Fig.2.4.

Body length, i. e. base length of a tiltmeter is $0.85m$; its diameter measures $0.065m$ (AGI, 1991, 1999a). Some of the borehole tiltmeters used were self made. Their body is of somewhat larger dimensions, i. e. has a diameter of $0.080m$ and a length of $0.90m$, but hosts the same type of sensors and electronics like the other instruments (AGI, 1999b, 2000, Grüneberg, 2002). Platform tiltmeters were placed on concrete plates lying in a sand bed in $0.4m$ deep hollows (Tofani & Horath, 1990, AGI, 1997). A shelter box placed beside the tiltmeters or in the borehole above the borehole tiltmeter held rechargeable batteries and a data logger.

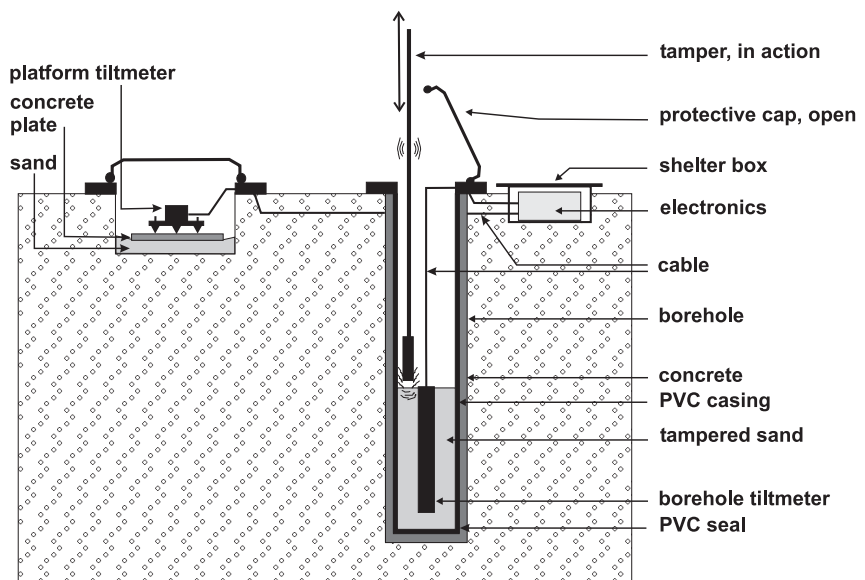


Figure 2.4: Installation of platform and borehole tiltmeters. For short-term installations with borehole tiltmeters PVC casing and concrete were not used.

A continuous record of the voltage output of the tiltmeter sensors was obtained. The tiltmeters come with a calibration sheet to convert voltages in tilt values. The appendix, section A.1.1, has an additional description of the necessary field work for the installation of tiltmeters. A well suited explanation of the borehole tiltmeter installation is also in AGI (1999a) and for platform tiltmeters in AGI (1997) and d'Orey de Lantremange (1998).

2.3 Formal Definition of Tilt

Vertical tilt in radial direction towards a well, $\Delta\gamma_r$ is defined as the change Δu_r in position along the horizontal axis per change in depth Δz , Fig.2.5. Infinitesimally the definition is:

$$\Delta\gamma_r := -\frac{\partial u_r}{\partial z}, \quad [\Delta\gamma_r] = 1\mu rad, \quad \text{e. g. } \frac{1\mu m_{horizontal}}{1m_{vertical}}, \quad (2.1)$$

where the sign¹ accounts for negative tilt, if the tiltmeter, i. e. its body's top, strikes towards a pumped well like outlined in Figs.2.1 and 2.5. Horizontal tilt can be defined similarly as $\Delta\gamma_z := -\partial u_z / \partial r$. Later, for modelling and interpretations, only vertical tilt (in the radial direction towards a well) is used, if nothing else is explicitly mentioned.

This definition of tilt is in a plane containing the well, i. e. for a 2-D case. In the three dimensional case, additional tilt in a perpendicular direction to the plane in Fig.2.5 can appear. This additional tilt can be defined separately as:

$$\Delta\gamma_t := \frac{\partial u_t}{\partial z}, \quad (2.2)$$

where t denotes a third axis. Fig.2.6 shows the two tilt angles, $\Delta\gamma_r$ for the tilt component in radial direction with negative sign towards a well, and $\Delta\gamma_t$, which strikes tangentially, or more exactly, in a perpendicular direction to $\Delta\gamma_r$.

The total tilt angle, i. e. the sum of $\Delta\gamma_r$ and $\Delta\gamma_t$ can be obtained by vector addition:

$$\Delta\gamma = \sqrt{\Delta\gamma_r^2 + \Delta\gamma_t^2}. \quad (2.3)$$

$\Delta\gamma_r$ and $\Delta\gamma_t$ or any dependent linear combination of these two tilt angles are the values measured by the two perpendicular sensors of the tiltmeters used. For practical purposes it is sometimes useful to transform tilt angles measured with respect to an arbitrary orientation of the tilt sensors to tilt angles with a special orientation, e. g. towards a well. Section A.2 in the appendix outlines such transformations.

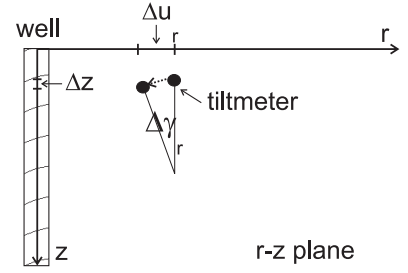


Figure 2.5: Definition of vertical tilt in a r-z plane: the change in position at the horizontal axis Δu_r per drop in depth Δz , Eq.2.1.

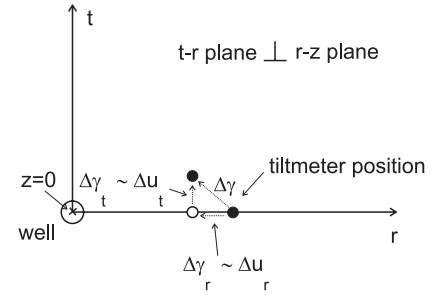


Figure 2.6: Tilt in a horizontal t-r plane in three dimensions: Besides the radial tilt $\Delta\gamma_r$ tangential tilt $\Delta\gamma_t$ can occur as an additional tilt component.

2.4 Pore Pressure Measurement and Well Head Changes

In a well connected to a fluid reservoir the fluid will rise up until the weight of the fluid balances the pore pressure in the reservoir, i. e. the pore pressure at the open section of the well. A change in reservoir pore pressure will lead to a fluctuation of the well level. Consequently, a pressure transducer installed below the well level can record the well level fluctuation as a pressure change at its sensor element, and this pressure change is taken as the measure for the pore pressure change in the reservoir. For the data analysis it is assumed that the fluids in the well and the pore fluids in subsoil consist of clean water with a temperature of $T_{H_2O} = 11^\circ C$ and a constant density of $\rho_{H_2O} = 999.6 \text{ kg/m}^3$ (Kuchling, 1988). The value of gravity, $|\vec{g}|$, is assumed to be 9.81 m/s^2 . The water column above the pressure transducer is related to the recorded pressure value by:

$$1m_{H_2O} \hat{=} \underbrace{999.6 \frac{\text{kg}}{\text{m}^3}}_{\rho_{H_2O}} \cdot \underbrace{1\text{m}}_{\text{water column}} \cdot \underbrace{9.81 \frac{\text{m}}{\text{s}^2}}_g = 9806.13 \text{ Pa} \hat{\approx} \quad (2.4)$$

$$\hat{\approx} 10 \text{ kPa} = 0.1 \text{ bar}.$$

A description of the pressure transducers (with build-in air pressure compensation) used in this study is in the appendix, in section A.1.2.

¹The sign convention is as in Wang & Kümpel (2003) and opposite to Lehmann (2001)!

2.5 Poroelastic Equations

The poroelastic equations are the equations of motion for the soil matrix and the pore pressure of the pore fluid in a poroelastic medium that shows intrinsic fluid-matrix coupling. The medium is assumed to be isotropic, homogeneous and fluid saturated. The poroelastic equations are (Biot, 1941, Wang, 2000):

$$\begin{aligned} G\nabla^2 u_i + \frac{G}{1-2\nu} \frac{\partial}{\partial x_i} \left(\sum_j \frac{\partial u_j}{\partial x_j} \right) - \alpha \frac{\partial p}{\partial x_i} &= f_i \\ Q^{-1} \frac{\partial p}{\partial t} + \alpha \frac{\partial}{\partial t} \left(\sum_j \frac{\partial u_j}{\partial x_j} \right) - \varkappa \nabla^2 p &= q. \end{aligned} \quad (2.5)$$

u_i for $i \in \{1, 2, 3\}$ are the components of the displacement vector with $[u_i] = m$, $p = p(x_1, x_2, x_3, t)$ is (excess) pore pressure, here pore pressure induced by pumping, with $[p] = Pa$, $f_i = f_i(x_1, x_2, x_3, t)$ for $i \in \{1, 2, 3\}$ are the three components of a body force per unit volume acting on the matrix with $[f_i] = N/m^3$, and $q = q(x_1, x_2, x_3, t)$ is a fluid volume extraction rate with $[q] = m^3/s$. x_i for $i \in \{1, 2, 3\}$ are the space coordinates with $[x_i] = m$ and t is time with $[t] = s$. Five independent parameters, $G, \nu, Q^{-1}, \alpha, \varkappa$ which characterize the poroelastic medium enter in the equations. These parameters will be discussed in the next section 2.6. The term $\sum_j \partial u_j / \partial x_j$ describes the change in medium volume. The term $\partial p / \partial x_i = (\nabla p)_i$ is the i -th component of the pore pressure gradient. As these terms enter in both equations, $\nabla^2 p = \nabla(\nabla p)$, coupling between matrix and fluid is taken into account.

Gravity is not explicitly respected in the equations and the solutions. Chemical reactions, temperature influence as well as inertial forces are neglected, too. All motions are assumed to be quasi static. Anisotropy, nonlinearity and semi-linear cases were discussed by e.g. Biot (1955, 1973) whereas fast, not quasi static motions, i.e. wave propagation in porous media, is treated by e.g. Biot (1956b,c), Jianfeng (1999) and Diallo & Appel (2000). Dynamic patterns in poroelasticity are, for instance, treated by Dvorkin & Nur (1993) and Sahay (2001). A study investigating of the similarity between thermoelasticity and poroelasticity is outlined by e.g. Zimmerman (2000). Neuzil (2003) discussed thermo-poroelasticity where coupling between matrix, fluid and temperature is considered.

Eqs.2.5 are coupled linear partial differential equations. Solutions of two or more vector fields $\vec{u}_1, \vec{u}_2, \dots$ and two or more scalar fields p_1, p_2, \dots superimpose independently. The solution fields are symmetrically with respect to the symmetry of acting stresses and pressures and with respect to the symmetries of the poroelastic medium and the boundary conditions. The parameters are constants. For a description of an inhomogeneous, but not a time dependent medium, i.e. spatially dependent parameters, the medium can possibly be divided into homogeneous parts, where parameters do not change. In this case, Eqs.2.5 can be used in each homogeneous part of the medium. Solutions can be found separately and connected to each other by linking the boundary conditions between the different parts of the medium (Sommerfeld, 1978).

For the experimental purposes $\partial u_i / \partial x_3$, where $i \in \{1, 2\}$ account for the horizontal directions, can be measured by (borehole) tiltmeters and p is detectable with pressure transducers recording well head fluctuations. q can be obtained from a flow meter attached to the outlet tube of a pump. $\forall i, f_i$ are assumed to be zero.

2.6 Poroelastic Parameters

Poroelastic parameters characterize the behaviour of a poroelastic medium. The parameters themselves are defined by means of selected physical processes under special conditions. An example is a compression of a medium under ‘drained’ conditions. Drained means that the pressure of the pore fluid remains constant. This equals the case, where the fluid does not interact with the matrix or is simply absent.

Undrained conditions can also be applied during the determination process of poroelastic material parameters. The parameter which is determined in a special process is then called the drained or the undrained parameter. Undrained conditions mean that the fluid interacts with the matrix and remains in the pores in spite of any matrix movement. The fluid can move in the pores, but is unable to escape from the volume taken into consideration. The matrix volume is ‘jacketed’ as [Biot & Willis \(1957\)](#) stated. The undrained case can be marked with the condition $M = const$ in contrast to $p = const$ for drained conditions. This should indicate that the fluid mass M is preserved due to inhibited fluid escape. A constant volume or a fixed volume strain, i. e. $\sum_i \epsilon_{ii} = const$ and $\epsilon_{ij} := (1/2)(\partial u_j/\partial x_i + \partial u_i/\partial x_j)$ is the strain tensor, are other possible conditions under which a poroelastic parameter can be determined. Generally, for a description of a poroelastic medium both, drained and undrained parameters, as well as a mixture of them, or even parameters determined under further different conditions can be used. It is only important that, however, the parameters form a complete and independent set ([Wang, 2000](#)).

Parameters $G, \nu, Q^{-1}, \alpha, \varkappa$ from [Eqs.2.5](#) form a complete and independent set ([Wang, 2000](#)). Other parameters can be deduced from these five ones to obtain a different parameter set ([Kümpel, 1991, 2003b](#)). The set of parameters that will be used here is G, ν, ν_u, B, D . G is the shear modulus, ν_u is the undrained Poisson ratio, B Skempton’s coefficient and D the hydraulic diffusivity, all described here below.

The *shear modulus* G accounts for the matrix reaction especially to shear stresses, i. e. forces acting tangentially on a surface of the medium. This is well known from elasticity ([Sommerfeld, 1979, Feynman et al., 1991](#)). Since fluids (in a poroelastic medium) are unable to hold these stresses, [Biot \(1941\)](#) stated that

$$G = G_u, \quad [G] = [G_u] = Pa \quad (2.6)$$

where G_u is the undrained shear modulus.

The *Poisson ratios* ν and ν_u account for the drained and undrained case, respectively. The definition of both is the same, but for ν_u in a saturated undrained porous medium, i. e. with intrinsic fluid-matrix interaction. Using the strain tensor ϵ_{ij} the Poisson ratios can be written after [Kümpel \(1991\)](#) and [Wang \(2000\)](#) as

$$\nu = -\left. \frac{\epsilon_{ii}}{\epsilon_{kk}} \right|_{p=const}, \quad \nu_u = -\left. \frac{\epsilon_{ii}}{\epsilon_{kk}} \right|_{M=const}, \quad i \neq k, \quad [\nu] = [\nu_u] = 1. \quad (2.7)$$

A compressed jacketed (undrained) medium will stronger extend sideways while stress acts in a particular direction than if the medium is drained. Therefore, in a poroelastic medium $\nu \leq \nu_u$. The reason is, because pores are saturated and will be less compressible than drained (unsaturated) pores. [Tab.2.1](#) lists some bibliographical values for G and ν . For ν_u values for sedimentary subsoil taken from [Grecksch \(1999\)](#) and [Lehmann \(2001\)](#) range between 0.40 and 0.49.

material	$G/[GPa]$	$\nu/[1]$
ice*** ($-4^\circ C$)	9.6	0.33
basalt***	27	0.3
Ruhr sandstone*	12 ... 13	0.12 ... 0.15
sand/gravel****	1 ... 5	0.2 ... 0.4
small-grained sand**	0.1 ... 0.3	0.1 ... 0.15
sandy clay****	0.1 ... 1	0.4 ... 0.48
clay****	0.1 ... 5	0.4 ... 0.48
water***	$E = 2 GPa$	0.5

Table 2.1: Bibliographical values of parameters, shear modulus, G and Poisson ratio, ν after [*Rice & Cleary \(1976\)](#), [**Domenico \(1977\)](#) (for Ottawa sand with gas fill), [***Kuchling \(1988\)](#), [****Maruyama \(1994\)](#). The modulus of elasticity, E depends on G and ν by $E = 2G(1 + \nu)$ ([Sommerfeld, 1979, Feynman et al., 1991](#)). The values for water are deduced from the compressibility ([Kuchling, 1988](#)).

The parameter Q^{-1} is called *Biot compressibility*. It expresses ‘the amount of water which can be forced into the soil under pressure while the volume of the soil is kept constant’ (Biot, 1941). If Θ describes the increment of fluid content in soil (Biot, 1941) the Biot compressibility can be defined after Wang (2000) as

$$Q^{-1} := \left. \frac{\partial \Theta}{\partial p} \right|_{\Delta V=0}, \quad [Q^{-1}] = \frac{kg}{ms^2}, \quad (2.8)$$

where p is the pore pressure and ΔV is the change in medium volume. The shape of the volume can change. Even if the definition of Q^{-1} in Eq.2.8 is more or less easy to imagine, it is neither under drained nor under undrained conditions. It is difficult to keep the volume constant in experimental set-ups and Q^{-1} can hardly be measured. This is the reason why Q^{-1} is often expressed by other parameters for experimental purposes. After Rice & Cleary (1976) the Biot compressibility can be expressed as

$$Q^{-1} = \frac{9}{2} \frac{(1 - 2\nu_u)(\nu_u - \nu)}{(1 - 2\nu)(1 + \nu_u)^2 GB^2}, \quad (2.9)$$

where B is Skempton’s coefficient as outlined below.

The next parameter to be named is α , the *coefficient of effective stress* (Biot & Willis, 1957). It is the change of the pore volume in a poroelastic medium, if the gross volume of the medium (matrix and pores) is changed under drained conditions. After Kümpel (1991) this can be expressed as

$$\alpha = \left. \frac{\partial V_n}{\partial V} \right|_{p=const}, \quad [\alpha] = 1, \quad (2.10)$$

where V_n is the volume of the pores and V is the gross volume. With the porosity $n := V_n/V$ of a poroelastic medium Schiffmann (1970) showed that

$$0 \leq n \leq \alpha < 1. \quad (2.11)$$

Because of the necessity to distinguish between the pore volume and the gross volume, α is difficult to determine in simple experiments, too. Hence, it was not used for calculations adapting experimental data and was expressed by other parameters. On the other hand, α is an important control value for the choice of poroelastic parameters related to α . Rice & Cleary (1976) showed that after Biot (1941)

$$\alpha = \frac{3(\nu_u - \nu)}{(1 - 2\nu)(1 + \nu_u)B}. \quad (2.12)$$

With Eq.2.12 and Eq.2.11 the range of values for the set of the parameters ν , ν_u and B is restricted. The concept of effective stress is discussed in comprehension e. g. in Skempton (1960a,b), Nur & Byerlee (1971) and Zimmerman et al. (1986).

The parameter \varkappa is the *Darcy conductivity* known from Darcy’s law (Hölting, 1996). \varkappa can be related after Kümpel (1991) and Hölting (1996) to the so called *K_f -value*, which is used in hydrology, by

$$K_f = \underbrace{\rho_{fluid}}_{density} \underbrace{g}_{gravity} \varkappa, \quad [K_f] = \frac{m}{s}, \quad [\varkappa] = \frac{m^3 s}{kg}. \quad (2.13)$$

The K_f value can be measured in laboratory tests. For laboratory measurements Hölting (1996) mentions a range of K_f -values typically for sediments. He characterized the ranges of the K_f -values by the perviousness of the material. Tab.2.2 summarizes these ranges for the most important sediments occurring here. The K_f -value can also be determined in field experiments. For instance, slug and bail tests, forced well head oscillations and quasi static step-rate pump tests (Krauss, 1974, Krauss-Kalweit & Kalweit, 1984, Hölting, 1996).

Skempton’s coefficient B can be defined under undrained conditions as

$$B := \left. \frac{\partial p}{\partial p_c} \right|_{M=const}, \quad [B] = 1 \quad (2.14)$$


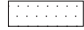
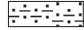
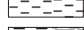

material	K_f -value/ $\frac{m}{s}$	perviousness	signature
gravel	$10^{-1} \dots 10^{-2}$	very high	
coarse-grained sand	$\approx 10^{-3}$	high ... very high	”
mid-grained sand	$10^{-3} \dots 10^{-4}$	high	
small-grained sand	$10^{-4} \dots 10^{-5}$	normal	”
silty sand	$10^{-5} \dots 10^{-7}$	normal ... low	
silt/(clay)	$10^{-6} \dots 10^{-9}$	low ... very low	
clay	$< 10^{-9}$	very low	

Table 2.2: K_f -values after Hölting (1996) for the most important sediments in this study, printed together with a characterization by the perviousness and their signature hereafter. Mixtures of sediments will be denoted by a mixed signature.

where p_c is a confining pressure acting equally on all sides of a saturated and jacketed medium volume (Skempton, 1954). For instance, imagine a rubber bag filled with water saturated sand and placed in a pressure chamber. If the pressure (confining pressure) in the chamber is increased, the rubber bag is compressed, but the water in the sand in it can not escape. One part of the chamber's pressure acting on the bag is hold by the sand, the other part is hold by the fluid saturating the sand. In Eq.2.14 p denotes the pore pressure, i. e. the pressure of the water in the sand. Hence, in the example, B accounts for the part of the chamber pressure acting on the fluid in the bag, and $1 - B$ accounts for the part acting on the sand grains (the matrix) in the bag. The coefficient B was introduced by Skempton (1954). An experimental determination of B for Berea sandstone was done by Green & Wang (1986) and yields values close to unity. Assuming a homogeneous half-space of water saturated sediments, Fabian (1998) calculated after Rojstaczer & Agnew (1989) values for B from fluid level variations in a 100 m deep well located in the Lower Rhine Embayment. The level variations were caused by static loading effects of precipitation. From this calculation values of B with respect to equal horizontal and vertical elastic properties of the subsoil, as Rojstaczer & Agnew (1989) stated with their parameter $H = 1$, are in the range $0.7 \leq B \leq 0.8$ assuming $\nu_u = 0.4$. If only the elastic properties of the subsoil in vertical direction were taken into account, i. e. $H = 0$, $0.9 \leq B \leq 1.0$ with $\nu_u = 0.4$. B is physically restricted to $0 \leq B \leq 1$. $B = 0$ would account for a (solid) medium without fluids ($\partial p = 0$) and $B = 1$ for a pure fluid ($\partial p = \partial p_c$).

The *hydraulic diffusivity* D can be defined through a diffusion equation for $p_\delta := (p/B - p_c)$ (Rice & Cleary, 1976). p_δ is the pressure difference between an increment in the confining pressure p_c and the resulting change in pore pressure. A diffusivity law for p_δ can be written formally as

$$\frac{\partial}{\partial t} p_\delta = \vec{\nabla} D (\vec{\nabla} p_\delta), \quad [D] = \frac{m^2}{s}. \quad (2.15)$$

Rice & Cleary (1976) derived Eq.2.15 from the poroelastic equations. They showed that

$$D = \frac{2(1-\nu)(1+\nu_u)^2}{9(1-\nu_u)(\nu_u-\nu)} \varkappa G B^2. \quad (2.16)$$

Eq.2.16 shows the complex dependency of D from other parameters described before. Through B , in the formula for p_δ fluid and matrix are respected. D characterizes diffusion with fluid-matrix coupling in a poroelastic medium. With Eq.2.13 D can be related to the possibly more familiar K_f -value from hydrology than to \varkappa . In principle, G can vary over some and K_f over many orders of magnitude and the difference between ν and ν_u can become small. Thus, the variation of D can be quite large. Bibliographical values of D vary between 10^{-5} and $10^3 m^2/s$ (Maruyama, 1994, Grecksch, 1999, Lehmann, 2001, Wang & Kümpel, 2003).

Tab.2.3 shows some examples of sets of poroelastic parameter values used for unconsolidated sediments during the modelling in chapter 4. The values of G, ν, ν_u, B and K_f (not D) are guesses for a general poroelastic start model not accounting for a certain subsoil situation. D and α in Tab.2.3 were always calculated from the other parameters through Eqs.2.16, 2.13 and Eq.2.12, respectively. Like stated above, K_f is used to derive D , since the K_f -value may be more familiar. The growing values of α from top to bottom in Tab.2.3 are caused by a constant, averaged ν_u , Eq.2.12, 2.11. During model

material	$G[GPa]$	ν	ν_u	B	$D[m^2/s]$	α	$K_f[m/s]$
coarse-grained sand	0.30	0.20	0.40	0.85	64	0.84	$1 \cdot 10^{-3}$
mid-grained sand	0.20	0.15	0.40	0.85	18	0.90	$5 \cdot 10^{-4}$
small-grained sand	0.20	0.15	0.40	0.85	3.6	0.90	$1 \cdot 10^{-4}$
silty sand	0.25	0.20	0.40	0.75	0.42	0.95	$1 \cdot 10^{-5}$
silt	0.35	0.20	0.40	0.75	0.29	0.95	$5 \cdot 10^{-6}$
mix of loam, silt	0.50	0.20	0.40	0.75	0.042	0.95	$5 \cdot 10^{-7}$
loam	0.50	0.20	0.40	0.75	0.0083	0.95	$1 \cdot 10^{-7}$
clay	0.50	0.20	0.40	0.75	0.00042	0.95	$5 \cdot 10^{-9}$
Ruhr sandstone	13.0	0.12	0.31	0.88	0.0053	0.65	$2 \cdot 10^{-9}$

Table 2.3: Example of poroelastic (start model) parameters for unconsolidated sediments. The values for (consolidated) Ruhr sandstone, which are from [Rice & Cleary \(1976\)](#), excepted. The K_f -value of the Ruhr sandstone seems somewhat low. However, since this material serves only for a comparison with a consolidated formation, the distinctive assignment between the parameter values and the material is minor important here. Values with two significant digits.

refinements, this behaviour usually changes. The values should become, in their general trend, smaller for less porous material like loam and bigger for a sandy formations ([Schiffmann, 1970](#)). The values in Tab.2.3 were chosen with respect to bibliographical values ([Domenico, 1977](#), [Maruyama, 1994](#), [Grecksch, 1999](#), [Lehmann, 2001](#), [Wang & Kümpel, 2003](#)) and to the results of some test modelling using the models of chapter 4. In these tests the synthetic signals were fitted grossly to the overall range of the signal rise times and amplitudes of observed tilt and pore pressure changes.

2.7 Solutions of Poroelastic Equations

Solutions of the poroelastic equations, especially obtained from adapting a model to field data, provide a description of the deformations of the medium and of pore pressure changes – here in response to pumping. The solutions depend on the choice of the parameters and the model geometry, i. e. on a description (interpretation) of the soil composition. Thus, in principle, the modelling of tilt and pore pressure measurements in a subsoil that can be described by poroelasticity allows a comprehensive understanding of subsoil properties and dynamics.

Analytical solutions of poroelastic equations in media with simple geometry were developed early by e. g. [Biot \(1941, 1956a\)](#), [Rice & Cleary \(1976\)](#) and others. [Cleary \(1977\)](#) and [Rudnicki \(1986\)](#) found analytical solutions for the stress and pore pressure field in a saturated homogeneous infinitely extended poroelastic medium (homogeneous full-space) with a single point sink for fluid withdrawal. Analytical solutions in a homogeneous half-space were found by [Rajapakse & Senjuntichai \(1993\)](#), but neglecting the second term of the second equation in Eqs.2.5, i. e. neglecting one part of coupling between fluid and matrix. An investigation of the influence of that second term on the numerical solutions obtained with finite element calculations was done by [Lewis \(1991\)](#) and [Gambolati et al. \(2000\)](#).

[Kümpel \(1989\)](#) adopted the solutions of [Rudnicki \(1986\)](#) to describe tilt and pore pressure in a homogeneous full-space. He also proofed the theory with data obtained in pump tests at larger depths beside deep production wells, first. The poroelastic parameters were used as integral values for the full-space. [Kümpel \(1989\)](#) has given solutions where the center of the well screen was taken as a point sink at a position $\vec{x}_0 \in \mathbb{R}^3$ with an extraction rate of

$$q(\vec{x}, t) = q_0 \delta(\vec{x} - \vec{x}_0) H(t - t_0) \quad (2.17)$$

where q_0 is a constant rate, $\delta(\vec{x} - \vec{x}_0)$ is *Dirac's* function and $H(t - t_0)$ is the *Heaviside* function to express the onset of the pump at time $t = t_0$. The cessation of pumping at a time $t = t_1$, $t_1 > t_0$ can be

simulated by adding a second Heaviside function $(-1) \cdot H(t - t_1)$. The steady state solutions of Kümpel (1989) for pump induced vertical radial tilt and pore pressure in a full-space are

$$\begin{aligned} \Delta\gamma_r &= \frac{q_0(1 + \nu_u)B}{24\pi(1 - \nu_u)D} \frac{r(z - d)}{\sqrt{(z - d)^2 + r^2}^3}, \\ p &= \frac{q_0}{4\pi\kappa} \frac{1}{\sqrt{(z - d)^2 + r^2}}. \end{aligned} \quad (2.18)$$

The full-space solutions for tilt and pore pressure are plotted in Fig.2.7. d is the depth of the well screen's center. z is the depth below a fixed horizontal plane (with respect to gravity acting in vertical direction) in full-space. r is the radial distance from the well's (vertical) axis. q_0 is in m^3/h , and the other expressions are as used before.

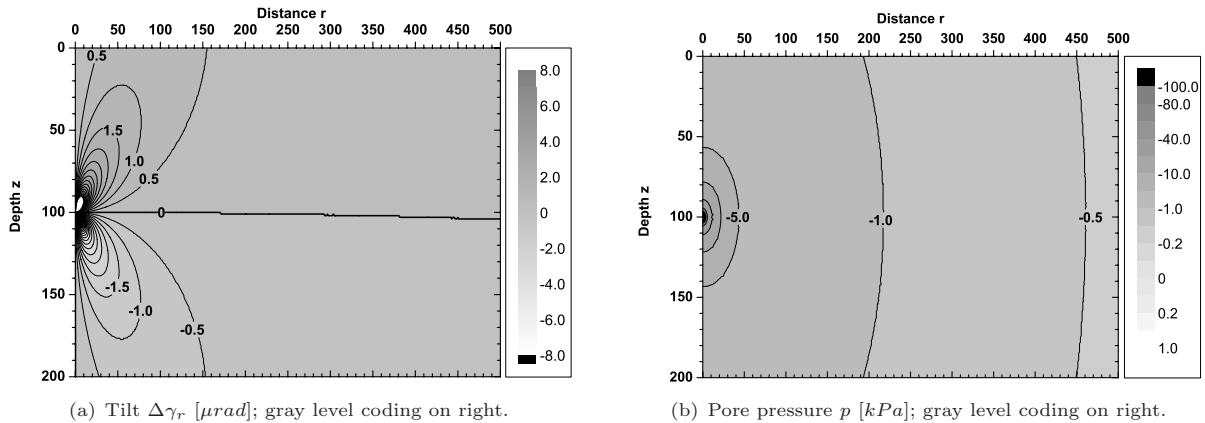


Figure 2.7: Example for an analytical poroelastic steady state solution, Eqs.2.18, for pumping in a full-space after Kümpel (1989), for a sedimentary subsoil of small-grained sand, Tab.2.3. Geometry in m . Depth z of the well screen's center is $100 m$, extraction rate is $100 m^3/h$. Parameters are $G = 0.2 GPa$, $\nu = 0.15$, $\nu_u = 0.4$, $B = 0.85$, $D = 3.6 m^2/s$ ($K_f = 10^{-4} m/s$). Numerical values are chosen to match the absolute range of data of this study. The vertical deflection of the zero-line of tilt is an artifact of the plotting program.

In the full-space the tilt field has a rotational symmetry with respect to the vertical axis of the well and inverse mirror symmetry with respect to the horizontal plane running through the well screen's center. The pore pressure field is spherically symmetric around the well screen center and amplitudes depend reciprocally from the radial distance. These symmetries are valid for all times t with $t_0 \leq t \leq \infty$ after onset of pumping (Rudnicki, 1986, Kümpel, 1989). The tilt and pore pressure fields hold their shape as in Fig.2.7 for all times. Only the amplitudes will change monotonously until the steady state is reached. Moreover, the shape of the isolines does not depend on any of the poroelastic parameters.

The interpretation of experiments using tiltmeters at shallow depth (near a free surface), requires at least solutions of Eqs.2.5 in the homogeneous half-space. The influence of the free surface must be taken into account. Tilt values near the surface will be different to the situation in the full-space. This is schematically illustrated for the steady state situation in an experiment of thoughts as sketched not true to scale in Fig.2.8. As the surface can move free, it will be the subject of a subsidence right above the well. The subsidence is caused by a decrease in pore pressure due to withdrawal of water. The subsidence leads – in a homogeneous half-space – to a funnel with its center at the well axis. Tiltmeters installed exactly at zero or at very shallow depth move like the surface. The tilt values will be negative, see Eq.2.1. After Lehmann (2001) and Wang & Kümpel (2003), the reason for this movement is dominance of rotational over shear motions close to the surface. Only at larger depths and in the close surrounding of the well screen, tiltmeters react to pumping like in the full-space situation. The change of the sign of the tilt values between a position at the surface and a position close to the well screen, at depths more shallow than the well screen center, indicates that a zero-line for tilt values must be running along a certain path from the well screens center through the half-space to the surface. This is a consequence of steadiness of the solution functions. Thus, in a half-space, the shape of the tilt field's pattern differs substantially

from the full-space situation. At the surface, the pore pressure has to be zero since immediately above the surface fluids are absent. In a real situation the fluid level is usually somewhat below the half-space's surface.

For the homogeneous half-space, i. e. a space with one boundary where pore pressure and stresses vanish, [Lehmann \(2001\)](#) and [Wang & Kümpel \(2003\)](#) found the analytical steady state solutions for a single well (point sink). To take the free surface into account, [Lehmann \(2001\)](#) and [Wang & Kümpel \(2003\)](#) first applied (for the point sink) the method of mirror loading from electrostatics ([Greiner, 1991](#)) to the solution fields for tilt and pore pressure in the full-space. Second, they applied a correction term to the mirror loading solution to take care for movements of the free surface. The steady state solutions of the poroelastic equations in a homogeneous half-space after [Wang & Kümpel \(2003\)](#) are

$$\Delta\gamma_r = \frac{q_0(1 + \nu_u)B}{24\pi(1 - \nu_u)D} \cdot r \cdot \left(\frac{z - d}{\sqrt{(z - d)^2 + r^2}^3} - \frac{z + (4\nu - 5)d}{\sqrt{(z + d)^2 + r^2}^3} - \frac{6dz(z + d)}{\sqrt{(z + d)^2 + r^2}^5} \right), \quad (2.19)$$

$$p = \frac{q_0}{4\pi\kappa} \left(\frac{1}{\sqrt{(z - d)^2 + r^2}} - \frac{1}{\sqrt{(z + d)^2 + r^2}} \right),$$

where $z \geq 0$ points downwards and the other symbols are as before.

Important properties of Eqs.2.19 after [Lehmann \(2001\)](#) are: (a) the possibility to calculate tilt and pore pressure values at or very close to a free surface, (b) the special course of the zero-line of tilt and its dependency on the parameter ν (Poisson ratio), and (c) the position of maximum tilt excursion, which is at the surface in a radial distance from the well at $1/\sqrt{2}$ times the depth of the well screen's center and is independently from the poroelastic parameters. The main aspect for practical purposes is that interpretations of measurements at shallow depth become possible. [Lehmann \(2001\)](#) developed a method for the determination of integral poroelastic parameters from pump induced tilt data recorded near the surface. For instance, Fig.2.9 shows plots of Eqs.2.19 for a half-space with the same poroelastic parameters like previously used for the full-space solutions in Fig.2.7.

Even if the homogeneous half-space does not fit a real subsoil, the solutions are an important reference for experimental data. The poroelastic equations are linear partial differential equations and superposition principle is valid. In a situation where withdrawal of water is done from two or more wells, or the well's screen can not be simplified by a point sink, the solution can be found by a superposition of solutions from single point sinks. Generally, a real subsoil will be more or less heterogeneous. A heterogeneous situation might be seen as a superposition of a homogeneous 'background' half-space and embedded structures. The tilt and pore pressure fields that laterally extend at or near the surface can be seen to contain an axially symmetric part (with respect to the well) after Eqs.2.19 superimposed by an additional tilt and pore pressure field caused by the inhomogeneities. A recognition of heterogeneities in subsoil and their modelling is desirable not only for identifying, but also for a time resolved description of their influence on the soil and reservoir properties. Therefore, solutions of poroelastic equations in more complex half-spaces and with time resolution are necessary. [Kümpel \(1989\)](#) used the early pump induced signal part for a determination of poroelastic properties in full-space. [Fabian & Kümpel \(2003\)](#) observed (transient) anomalous signals with respect to the above out-

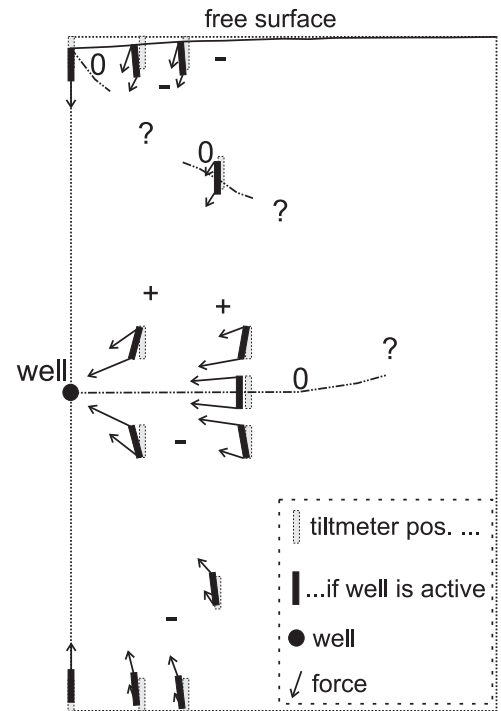


Figure 2.8: Pump induced tilt in a homogeneous half-space. +, - denote the sign of tilt, opposite to the convention of [Lehmann \(2001\)](#). Possible course of the zero-line (0, ---), where no tilt occurs is drawn.

lined solutions in the homogeneous full and half-space. These anomalous signals seem to bear additional information about the subsoil composition.

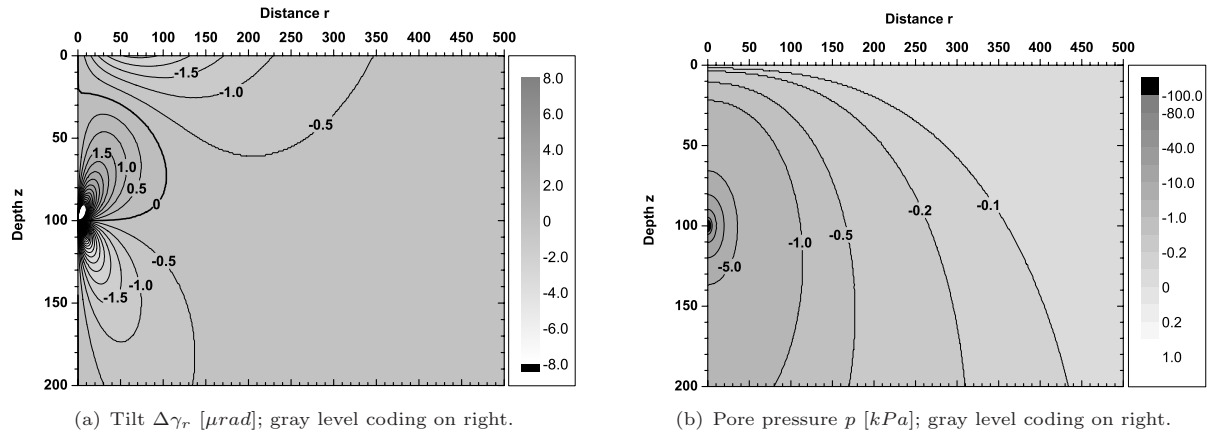


Figure 2.9: Example of pump induced analytical poroelastic steady state solutions, Eqs.2.19, in a half-space after Wang & Kümpel (2003), for a sedimentary subsoil of small-grained sand after Tab.2.3. Geometry scaling in m . Set-up and parameters are the same like in Fig.2.7, but now the solutions grossly match range and sign of the observed data.

The analytical solutions for more complex situations than the homogeneous half-space are hard to obtain. Generally, these solutions have to be found with the aid of semi-analytical or numerical methods. Different methods are available. One possibility is the usage of finite element or finite difference methods, often implemented in software packages. When a high time resolution of the solution is required or sharp material boundaries with high contrasts in parameter values, like between a layer of sand and clay, are present, this purely numerical approach may need large computational power even for simple poroelastic models. Grecksch (1999) used finite elements to solve poroelastic problems for pore pressure disturbances in homogeneous half-spaces with simple block structures included. Lehmann (2001) used the same algorithms to solve for pump induced pore pressure changes and tilt in the homogeneous half-space. Burbey & Helm (1999) used finite elements to calculate simple three-dimensional consolidation problems, whereas Kim & Parizek (1999) compared the method of finite elements with analytical approaches to find solutions in an-isotropically disturbed poroelastic half-spaces. Gambolati et al. (1999) showed finite element calculations of the poroelastic behaviour of a finite embedded fluid reservoir in a homogeneous half-space for strain and pore pressure. Gambolati et al. (2000) calculated 2-D and 3-D strain – pore pressure models with the aid of finite elements. In more heterogeneous situations with lenses, slopes, wedges and faults buried in subsoil, this will possibly be the only way to a solution. A study using finite elements and accounting for single pores, i. e. a microscopic approach, is that of Zeng et al. (1999).

A semi-analytical method to solve the poroelastic problem can be the field inversion of measured data. The solution is (partly) known from measurements and can be inverted with special restrictions to account for the geological composition of subsurface. Vasco et al. (2000) showed such calculations for tilt and Vasco et al. (2001) for tilt and pore pressure. However, comprehensive investigations, especially of the time dependency of the solutions, are still rare. Just for interpretations of data from new experimental techniques there is the need for fast and accurate solution methods.

Another method is propagating the solution, initially only known at the place of the well screen and at the boundaries of the model, with the aid of numerical transformations through a poroelastic model of the subsoil. Parameters and geometry in the model are adjusted in an iterative approach until the propagated solution at a certain position and time fits the observation. This method is applied here with use of the program POEL developed by R. Wang. A short description of POEL is in section A.6 in the appendix. A similar approach, solving for the Green's function in a layered poroelastic half-space was done by Pan (1999), but accounts not for tilt and is not applied to an experiment. Another presentation of solutions, also not for tilt and in a full-space using semi-analytic propagator methods is the one of Taguchi & Kurashige (2002).

A common disadvantage of all solving methods (and experiments) is the large number of unknown parameters. In contrast to laboratory experiments a strongly underestimated and open system has to be described. The structure of the subsoil must be simulated by highly abstracted models. For easier interpretations, experimental set-ups for tilt and pore pressure observations should be made as controllable as possible. Sensors could be arranged in symmetrical patterns with respect to each other and to known geological structures in the surrounding. Well defined forcing functions could be applied to the fluid and to the matrix.

Chapter 3

Experiments

Experiments were conducted at three different test sites. The sites were near the cities of Cologne and Bonn in western Germany and near the city of Bremen in northern Germany. The selected locations were close to villages called Oberelvenich (OE), Bürvenich (BV) and Wulsdorf (WD), Fig.3.1.

The test sites were all situated in sedimentary areas with large ground water deposits and aquifers at shallow depth. The subsoil conditions were suited for pump tests. Experimental set-up at all sites was very similar, as outlined in sections 2.1, 2.2. During the pump test experiments, induced near surface tilt and pore pressure changes in nearby observation wells were recorded.

Local geology was different from site to site: At OE the subsoil could be described by a mostly horizontal stack of sedimentary strata. The stack was interrupted at some distance from the central part of the location by a distinct fault passing the test site. BV was characterized by a similar horizontal layer structure like at OE, but with a different geometrical scaling. At both sites the uppermost part of the subsoil was disturbed and compacted, stronger at BV. Site WD was in an area with buried quaternary channels. One channel crossed the test site and held the main aquifer used for the pump test.

Number and density of observation points, area covered by the experiments and ground water extraction rate was different between the sites, too: OE was equipped with 16 borehole tiltmeter and three platform tiltmeter positions, three production wells with extraction rates of several hundred cubic meters per hour and two observation wells with different casings that tapped the upper aquifers. At site OE an area of approximately $500 \times 600 m^2$ was covered by observation points. At BV two borehole tiltmeters and two wells for observation and production, rate $2.5 m^3/h$, were used. The area here was very local, with a spatial extension of nearly $10 \times 20 m^2$. At WD the covered area was about $300 \times 450 m^2$. Besides of two tiltmeters and two production wells operated with rates of some hundred cubic meters per hour, three observation wells in contact with the two upper aquifers were available.

At OE two experiments were conducted: First, the response of the well heads from the four upper aquifers as well as induced tilt at two positions, one close to the wells and one somewhat apart, were assessed. Second, tilt measurements were used to image surface deformations caused by withdrawal of ground water. The second experiment was a pilot study to show the potential and the limitations of the method of surface deformation imaging. In this experiment several transient tilt signals were recorded and investigated. The experiment at BV was a separate investigation of transient reversals of tilt, elliptically shaped hodographs and the ‘Noordbergum effect’. Measurements at WD were a case study under highly heterogeneous geological conditions.

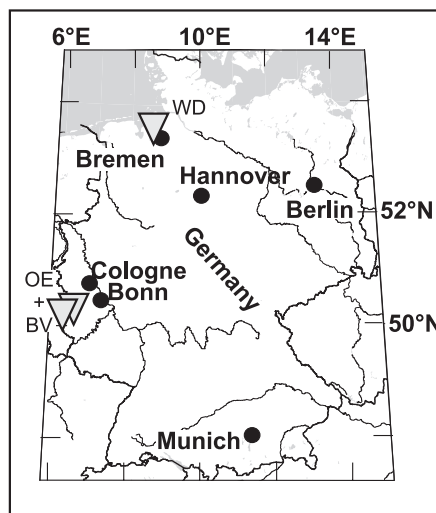


Figure 3.1: Location of the three test sites OE, BV (close to Cologne/Bonn) and WD (close to Bremen).

Together with the presentation of the experiments first proposals and discussions about possible interpretations will be provided. Poroelastic multi-layered half-space models will be used later in chapter 4 to qualitatively, and in their range quantitatively describe some of the observations.

3.1 Oberelvenich, OE

Site OE was situated in the south western part of the Lower Rhine Embayment, Fig.3.2. The embayment is a tectonically active tertiary basin with overlying quaternary sediments. It is surrounded by pre-tertiary rock formations. In the subsoil mostly horizontal strata of sand and gravel are hydraulically insulated by layers of silt, clay or lignite beds. At faults crossing the Lower Rhine Embayment, the whole stack of layers is often nearly vertically displaced and slightly inclined. Here, tectonic processes can establish a boundary at which aquifers face impermeable strata. Hence, the horizontal extension of layers conducting ground water can be strongly limited. Thickness of the whole sedimentary stack above the tertiary ranges in the Lower Rhine Embayment between some 10 m and more than 1000 m (GLA-NW, 1988, Erftverband, 1996, Henningsen & Katzung, 1998, Klostermann et al., 1998).

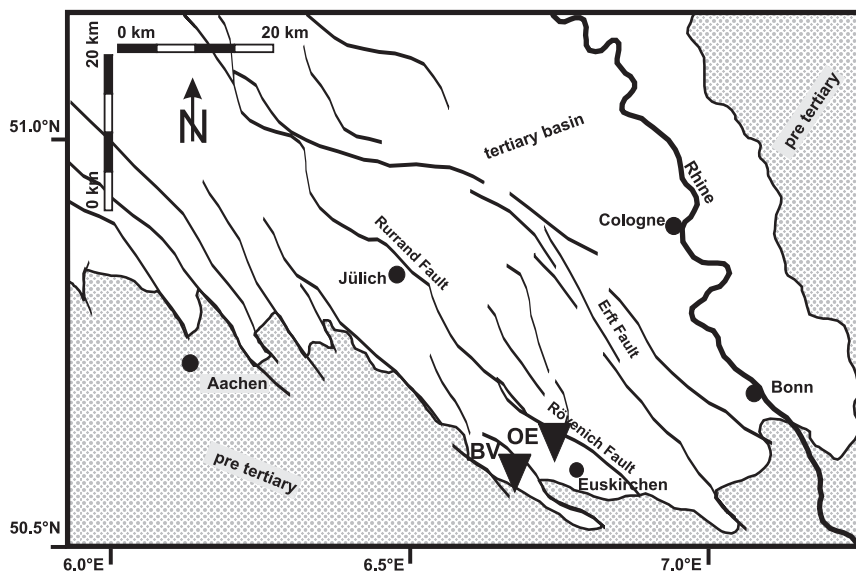


Figure 3.2: Locations of test sites OE, BV in the Lower Rhine Embayment.

The tertiary sediments at site OE have an overall thickness of more than 200 m and include four aquifers, GW1_{OE} to GW4_{OE}. Three production wells, B1_{OE}, B2_{OE}, B3_{OE}, were regularly operated by a waterworks company, Fig.3.3. Nearly 700 m north east of the site, the sub horizontal layering is intersected by the extensional Rövenich fault. There is a smooth ramp of about 4.5 m descent over a distance of 100 m to the opposite site of the fault in south west direction, from 158.2 m above sea

level at position T4_{OE} to 153.7 m. The remaining area is flat at a mean height at position of B1_{OE} of 155.5 m above sea level. Height variation across the whole site is not larger than ± 3 m with respect to the sites' boundaries. In Fig.3.4 is a photo from site OE.

The geological cross section in Fig.3.5 shows the simplified subsoil structure in north west to south east direction below the central part of the test site, compare the dotted line A—B in Fig.3.3. The four aquifers can easily be identified. The upper aquifer, GW1_{OE} consists of a layer of gravel and coarse-grained sand and has a very high perviousness. At the piece of land between B1_{OE} and B2_{OE} it is overlaid by a layer of topsoil. However, due to construction of the waterworks, and possibly agricultural field work, the uppermost part of the subsoil is assumed to be compacted (Kau, 2000). The main production aquifer, GW2_{OE}, consists of mid-grained sand and is bounded at its top and its bottom by a 10 m to 20 m thick layer of clay and silt, respectively. B1_{OE} and B2_{OE} are in contact to GW2_{OE}. Aquifer GW3 that is composed of a mixture of sand and silt, is less pervious than GW1_{OE} and GW2_{OE} and was therefore not used for ground water production (Hoffmann, 2002). The deepest aquifer, GW4_{OE}, lies below a bed of lignite, is highly pervious and was used for production through B3_{OE}. The hydrological K_f -values are, in m/s, $1 \dots 3 \cdot 10^{-3}$ (GW1_{OE}), $10^{-4} \dots 10^{-3}$ (GW2_{OE}), $\approx 10^{-5}$ (GW3_{OE}), $10^{-4} \dots 10^{-3}$ (GW4_{OE}), (Rheinbraun, 1997, Hoffmann, 2002).

A regional geological cross section along the line C—D in the inset of Fig.3.3 is given in Fig.3.6. The cross section extends over the boundaries of the site and shows the active fault and two additional wells. These wells were not used for measurements, but for the geological interpretation. The appendix, section A.3.2, Fig.A.13, shows another regional geological cross section with the subsoil interpretation below the line E—F in the inset of Fig.3.3. These regional cross sections support the assumption of a mostly horizontally layered subsoil at site OE.

Wells B1_{OE} and B2_{OE} have a 60 m deep casing, are of similar construction and extracted ground water through well screens extending from 30 m to 55 m depth; B3_{OE} is 170 m deep and has open sections from 149 m to 159 m and from 162 m to 165 m. Depending on the demand for water, an automatic control of the waterworks operated the pumps in the three wells in different combinations, namely (1) B3_{OE} and either B1_{OE} or B2_{OE}; (2) B1_{OE} and B2_{OE}; (3) either B1_{OE} or B2_{OE}; or (4) all wells off. Production rates were 250 m³/h for each of B1_{OE} and B2_{OE}, and 85 m³/h for B3_{OE}. When wells B1_{OE} and B2_{OE} were operated simultaneously, the rates were trifling lower caused by backwater in the outlet tubes. Extracted water was guided through pipelines to consumers in the surrounding cities (Verbandswasserwerk, 1998).

Hydraulic heads in the production wells were continuously monitored by pressure transducers. The heights of the heads varied by about 3 m due to the pumping. Mean hydraulic heads were 17 m below surface for B1_{OE} and B2_{OE}, and 21 m below surface for B3_{OE}. The two observation wells, P1_{OE} and P2_{OE}, allowed a monitoring of hydraulic heads in individual aquifers through separate casings. In the first pump test experiment, four level recorders were used to monitor the heads of the confined aquifers GW2_{OE}, GW3_{OE}, GW4_{OE} through P1_{OE} (open sections are from 33 m to 35 m and from 38 m to 40 m for GW2_{OE}, from 92 m to 95 m for GW3_{OE}, and from 155 m to 158 m for GW4_{OE}), and the head of aquifer GW2_{OE} through P2_{OE} (open section from 30 m to 31.5 m and from 37 m to 38.5 m). Mean hydraulic heads were 7.5 m (GW1_{OE}), 13 m (GW2_{OE}), 15 m (GW3_{OE}), and 19 m (GW4_{OE}) below surface at location P1_{OE}; 6.5 m (GW1_{OE}) and 15 m (GW2_{OE}) at location P2_{OE}. The water table of the unconfined aquifer GW1_{OE} was observed manually at the

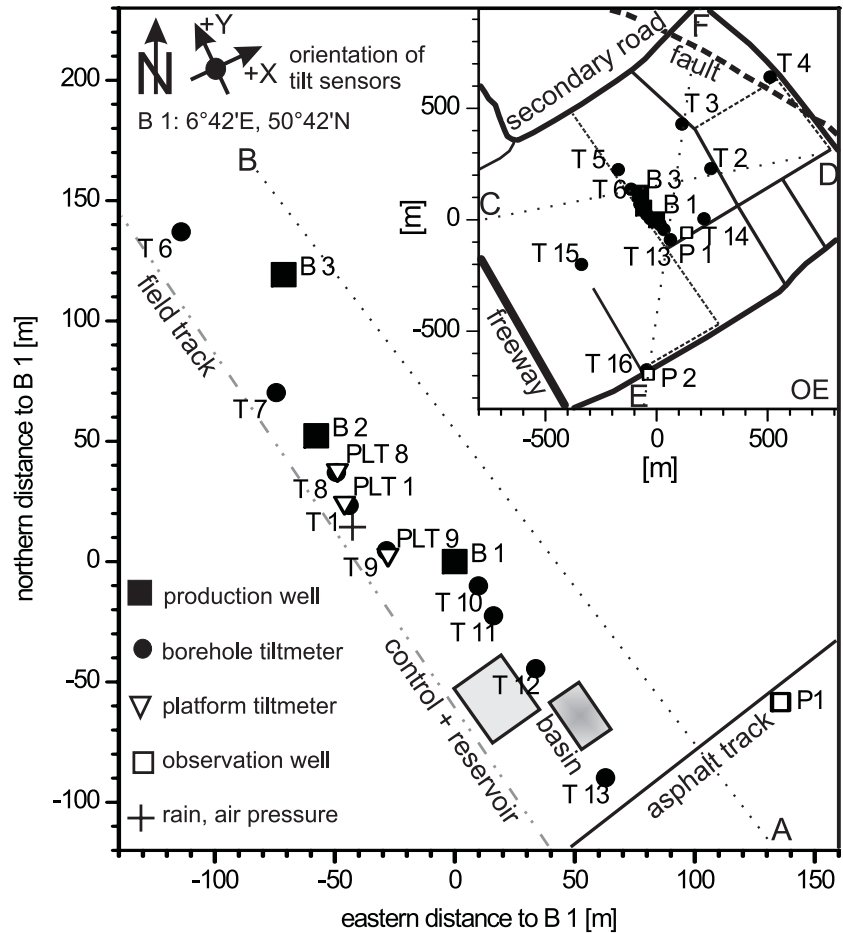


Figure 3.3: Map of site OE with locations of borehole tiltmeters T1_{OE} to T16_{OE}, platform tiltmeters PLT1_{OE}, PLT8_{OE}, PLT9_{OE}, production wells B1_{OE}, B2_{OE}, B3_{OE}, observation wells P1_{OE} and P2_{OE} and a meteorological station for monitoring rain fall and air pressure. The heights of the heads varied by about 3 m due to the pumping. Mean hydraulic heads were 17 m below surface for B1_{OE} and B2_{OE}, and 21 m below surface for B3_{OE}. The two observation wells, P1_{OE} and P2_{OE}, allowed a monitoring of hydraulic heads in individual aquifers through separate casings. In the first pump test experiment, four level recorders were used to monitor the heads of the confined aquifers GW2_{OE}, GW3_{OE}, GW4_{OE} through P1_{OE} (open sections are from 33 m to 35 m and from 38 m to 40 m for GW2_{OE}, from 92 m to 95 m for GW3_{OE}, and from 155 m to 158 m for GW4_{OE}), and the head of aquifer GW2_{OE} through P2_{OE} (open section from 30 m to 31.5 m and from 37 m to 38.5 m). Mean hydraulic heads were 7.5 m (GW1_{OE}), 13 m (GW2_{OE}), 15 m (GW3_{OE}), and 19 m (GW4_{OE}) below surface at location P1_{OE}; 6.5 m (GW1_{OE}) and 15 m (GW2_{OE}) at location P2_{OE}. The water table of the unconfined aquifer GW1_{OE} was observed manually at the

beginning and at the end of the experiments. Differences in well heads between $GW1_{OE}$ and $GW2_{OE}$, and $GW2_{OE}$ and $GW4_{OE}$ indicate a hydrological separation of these pairs of aquifers, whereas a separation between $GW2_{OE}$ and $GW3_{OE}$ is less obvious. Tab.A.1 in the appendix summarizes the well data. The mean well heads of $GW2_{OE}$ showed a difference of nearly 3 m between production wells $B1_{OE}$ and $B2_{OE}$ on the one and observation well $P1_{OE}$ on the other hand. This indicates a mean pump funnel that did not vanish in between two pump-cycles of both the production wells. Subsoil was not fully saturated since the head of $GW1_{OE}$ was not at surface.



Figure 3.4: Photo from site OE taken during experiments in March 2002 in south east direction parallel to the field track at the right side which passes the waterworks. At the left side in foreground is position $T5_{OE}$, see inset in Fig.3.3. The control building is in the background in the upper right part.

At site OE, the first pump test experiment was conducted in November 2001, the second in March 2002. The tiltmeters $T1_{OE}$, $T2_{OE}$ and $T4_{OE}$, see Fig.3.3, have previously been installed at the site, since the end of 1999 for other experimental purposes like described by Kümpel et al. (2001). $T1_{OE}$, $T2_{OE}$ could be used for both the tests here. The measurements at $T4_{OE}$ were completed earlier. This older data was used with the second experiment. The other tiltmeters, which positions are shown in Fig.3.3, were installed for the second experiment only.

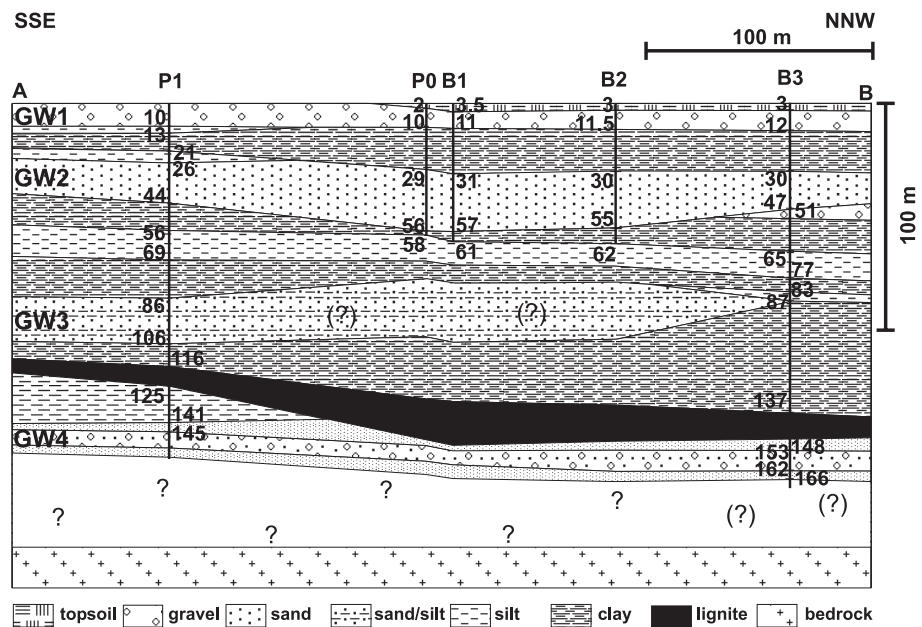


Figure 3.5: Local simplified geological cross section along the line A—B in Fig.3.3. Deep boreholes at site OE are sketched with numbers indicating the depth of the layer boundaries in m. $P0_{OE}$ is not accessible for measurements and left out in Fig.3.3. Aquifers $GW1_{OE}$ to $GW4_{OE}$ are marked. The geological interpretation was mostly done by Martau (2001) on the basis of GLA-NW (1988), Wallbraun (1992), Erftverband (1999), Verbandswasserwerk (1999), Rheinbraun (2000), Hoffmann (2002).

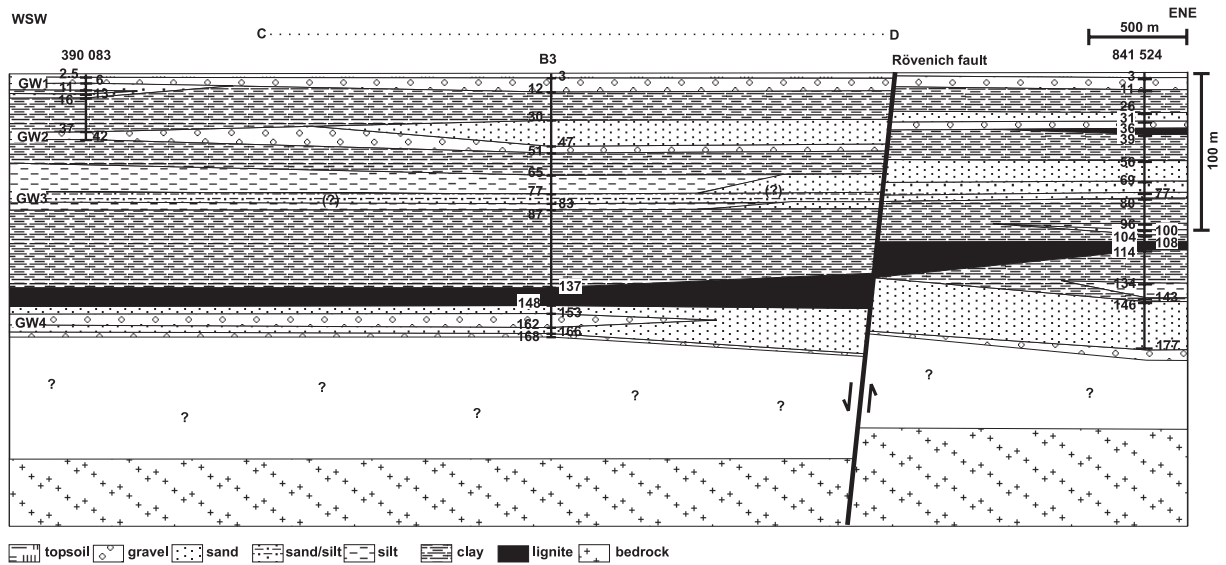


Figure 3.6: One of two regional simplified geological cross sections, OE, C—D in Fig.3.3. 4 times vertically exaggerated. The cross section extends over the borders of Fig.3.3. Additional wells, 390 083, 841 524 are sketched. Numbers at the wells indicate depth in m of the boundaries between adjacent layers. Aquifers GW1_{OE} to GW4_{OE} are marked. Geological interpretation was mostly done by Martau (2001) on the basis of GLA-NW (1988), Wallbraun (1992), Erftverband (1999), Verbandswasserwerk (1999), Rheinbraun (2000), Hoffmann (2002).

3.1.1 Tilt and Well Level Response, November 2001

Purpose of the first pump test experiment in November 2001 at OE was getting insights into pump induced tilt and well level fluctuations caused by the pump activity of the waterworks.

Observation was done with pressure transducers in both observation wells, P1_{OE} and P2_{OE}, and in the production wells B1_{OE}, B2_{OE}, B3_{OE}. The casings of well P1_{OE}, which are in contact to the aquifers GW2_{OE} to GW4_{OE}, and the casing of well P2_{OE} with contact to GW2_{OE} were equipped with instruments. Near surface tilt was recorded with the borehole tiltmeters T1_{OE}, T2_{OE}. Due to the long time span since installation (since 1999), these tiltmeters were assumed to be completely settled. T1_{OE} was asymmetrically placed between the production wells B1_{OE} and B2_{OE}. The bottom end of the instrument was at 3.7 m depth. The position of this tiltmeter was chosen to obtain maximum pump induced tilt signals in response to pumping in wells B2_{OE} and B3_{OE}, assuming ground water is produced from a homogeneous half-space through the wells' open sections (open section are assumed to be point sinks), and using the formulas of Lehmann (2001). Tiltmeter T2_{OE} rested at 3.95 m depth (bottom end), approximately 300 m north east of T1_{OE}, see Fig.3.3. Both tiltmeters were installed within the unsaturated zone above the water table. Their boreholes had a cemented and sealed casing, see Fig.2.4.

Data presented here is from two observation days, November 6th and 7th, 2001. At the 6th of November between 6:00 and 16:00 the automatic pump control was switched off. The pumps were controlled manually with pump cycles lasting from about 30 min to 4.5 h . Before and after that time the waterworks was in regular operation. Sampling of tilt data and of pressure transducers was 1 min , and of the other observables, air pressure and precipitation, 5 min . As the waterworks operated the pumps in quasi continuous mode since several years, see Tab.A.1, a steady state situation of consolidation might have been achieved for the productive aquifers.

Fig.3.7 presents the tilt and well level data. Pump activities in wells B1_{OE}, B2_{OE}, and B3_{OE} are highlighted. The pumping is reflected in the hydraulic heads of aquifers GW2_{OE}, GW3_{OE} and GW4_{OE} in wells P1_{OE} and P2_{OE} and in the not active production wells. Fluctuations in the heads of GW2_{OE} and GW3_{OE} correlate best with pumping in the wells B1_{OE} and B2_{OE}. The response in P2_{OE}, which is roughly 700 m away from B1_{OE}, was delayed by about 25 min . The head of GW4_{OE} responds best to pumping in B3_{OE} (see the cycle where only B3_{OE} was active, lasting from approximately 12:00 to 13:00

at November 6th). This confirms the effective hydrological separation between GW2_{OE} , GW3_{OE} on one hand, and GW4_{OE} on the other, as already concluded from the difference in mean static well head. A comparison of data from GW2-B2_{OE} with GW2-P1_{OE} on the one and GW3-P1_{OE} on the other hand shows a decrease in amplitude and a slight signal delay of about 5 min , respectively. The latter fact also indicates a separation between GW2_{OE} and GW3_{OE} . Thus, the dynamic well level data is in agreement with the gross geological interpretation of Fig.3.5 showing a good separation of the aquifers.

There was no precipitation during this pump test and only negligible changes in atmospheric pressure. A trend that seems to be in the tilt signals was not removed and was most likely caused by seasonal effects, i. e. cooling and moistening of subsoil (Berger, 1975, Bonaccorso et al., 1999, Braitenberg, 1999, Kümpel et al., 2001). The comb-like spikes that are sporadically visible in tilt T2||T1T_{OE} and T2||T1R_{OE} were caused by loading from a farmer's harvest machine. The machine was regularly passing the tiltmeter position (at November 6th from around 10:30 till 11:45 and from 15:00 till 19:00 and at November 7th from 10:15 till 17:15). The lack of data in tilt at position T1_{OE} at 10:15, November 7th, and the faint spike in the signal from GW2-P2_{OE} is an artifact caused by data retrieval from the data logger.

Pumping in B3_{OE} seems to have no influence, nor on T2_{OE} , neither on T1_{OE} . There was no response in T2||T1T_{OE} and T2||T1R_{OE} , see 12:00 to 13:00 at November 6th. Also, no clear tilt signals of T1_{OE} were in response to pumping in B3_{OE} . For instance, see the signal of T1_{OE} between 8:00 to 10:00 at November 6th. This might be explained, because the screen of B3_{OE} is at a depth of about three times larger than the depth of the screens of B1_{OE} and B2_{OE} , and the yield in B3_{OE} was less than half of that in B1_{OE} , B2_{OE} .

Strike direction of T2_{OE} caused by pumping was in direction towards the waterworks (when in Fig.3.7 the tilt signal amplitudes get smaller). Due to the orientation of the tilt sensors, response in T2||T1T_{OE} was five times larger than the amplitude of T2||T1R_{OE} . Both tilt signals from the components of T2_{OE} do not report any activity of the individual wells B1_{OE} , B2_{OE} .

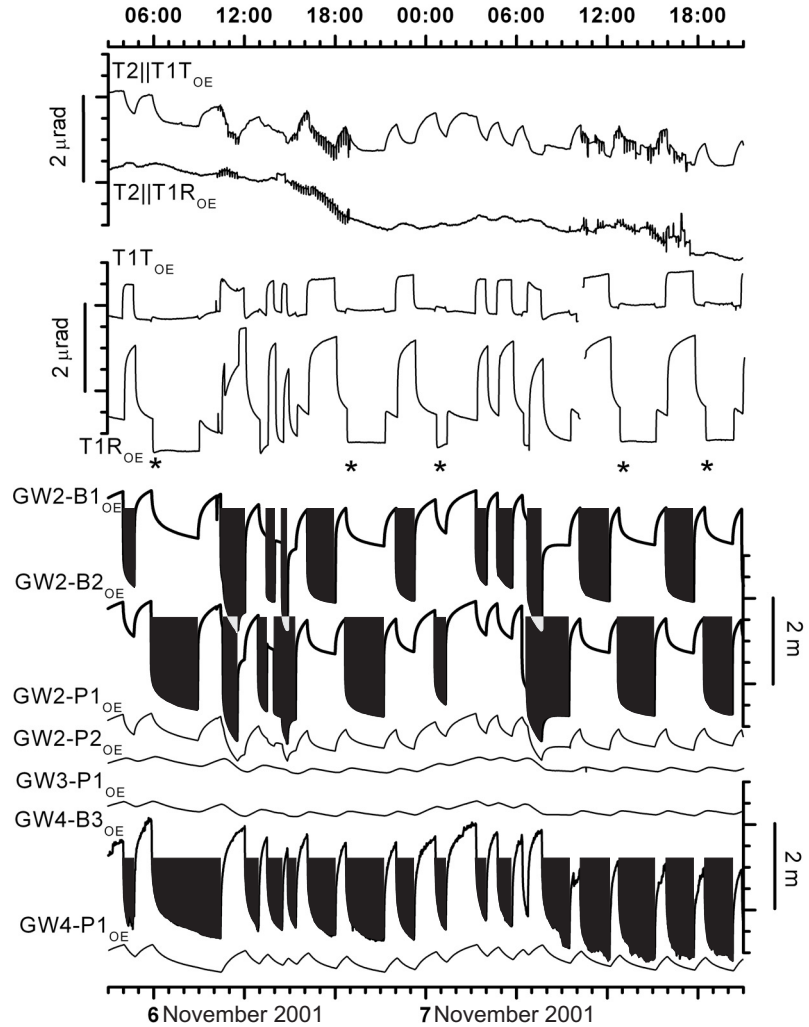


Figure 3.7: Data from the first pump test, November 2001, OE, over a period of 42 h. Upper four curves display tilt data T2||T1T_{OE} and T2||T1R_{OE} , T1T_{OE} , T1R_{OE} from positions T2_{OE} and T1_{OE} . The first component of T2_{OE} is parallel to T1T_{OE} and the second to T1R_{OE} . Due to the orientation of tilt sensors, see Fig.3.3, the latter both components show the tilt values in tangential and radial directions to B2_{OE} , respectively (defined in Eqs.2.1, 2.2). The lower part of the figure depicts signals from well level observations (GWn-M_{OE} denotes the hydraulic head in the n-th aquifer in the well at position M). Times of pump activity in the three production wells B1_{OE} , B2_{OE} , B3_{OE} are marked by filled black parts; e.g. at the times indicated by the asterisks, pumps in B2_{OE} and B3_{OE} started simultaneously.

If $B2_{OE}$ (and $B3_{OE}$) was active, striking of the tilt response of $T1_{OE}$ was oriented in direction to $B2_{OE}$. The radial component $T1R_{OE}$ with respect to $B2_{OE}$ showed an amplitude of $-1\mu rad$ (tilt in radial direction is taken negative if the top of the tiltmeter body strikes with respect to its bottom in direction towards the well, see Eq.2.1), whereas $T1T_{OE}$ had a signal slightly fluctuating below an amplitude of $0.1\mu rad$ (e.g. at November 6th around 6:00 and 19:00 in Fig.3.7). In contrast to this behavior, both components $T1R_{OE}$ and $T1T_{OE}$ responded with amplitudes of $-2\mu rad$ and $1\mu rad$, respectively, when water was extracted from $B1_{OE}$ (and $B3_{OE}$). At position $T1_{OE}$ influence of pumping from wells $B1_{OE}$ and $B2_{OE}$ was individually resolved.

The field of pump induced surface deformations at site OE might be divided in a ‘far field’ and a ‘near field’. A tiltmeter is in the far field when the activity of individual wells can not be separated by the corresponding tilt response. Thus, $T2_{OE}$ was in the far field. On the other hand, a tiltmeter is in the near field, when the activity of individual wells can be distinguished by the corresponding pump induced tilt signals. Hence, $T1_{OE}$ was in the near field.

A closer look to $T1R_{OE}$ shows small reversals of the tilt amplitude after simultaneous onset of pumping in $B2_{OE}$ and $B3_{OE}$ (e.g. around 6:00 at November 6th and marked by the asterisks in Fig.3.7). The course of the tilt signal $T1R_{OE}$ induced during these pump cycles shows a sharp response followed by a small transient reversal and ends up in a plateau. This behavior is well reproduced in the data from position $T1_{OE}$. It appeared with opposite strike direction when pumping in $B2_{OE}$ and $B3_{OE}$ stopped. Such a signal type was first observed at the site BV (discussed later). A reversal of tilt is also in Fig.3.7 in $T1T_{OE}$ at November 6th, 10:30, November 7th, 7:00. However, these latter signals are nothing special since these reversals resulted from switching the pump activity between the roughly opposite located wells $B1_{OE}$ and $B2_{OE}$ with respect to $T1_{OE}$. In contrast to this configuration of $B1_{OE}$ and $B2_{OE}$, $B2_{OE}$ and $B3_{OE}$ are located in nearly the same direction with respect to $T1R_{OE}$.

If behavior of the subsoil is described by poroelasticity, due to fluid-matrix coupling, a transient interaction process between fluid and matrix might appear and explain the observed reversals. This process should be called a balancing process. However, a pure diffusion without fluid-matrix coupling, as used for process description in classical hydrology (i.e. Darcy’s law), can not result in any signal reversal if the pore pressure disturbance caused by pumping is applied monotonously as here. Also, a pure quasi static elastic response of the subsoil does not revert, if the applied forces act monotonously.

Summarizing the first experiment, highly significant pump induced tilt signals and pore pressure changes, also at distances of several hundred meters from the production wells, could be observed. The observations from the two tiltmeter positions $T1_{OE}$ and $T2_{OE}$ reflect the build-up of a rather widespread surface deformation field. This situation is favorable for a more thorough and systematical investigation of the near surface deformation signal, which was done in a second experiment.

3.1.2 Surface Deformation Imaging, March 2002

Like mentioned before, the aim of the second experiment was applying a new method, i.e. some special field and analysis techniques, for imaging the surface deformation field in the surrounding area of active wells. There was no special intention to observe the influence of buried local structures onto the shape of the deformation field, nor to derive any further conclusions about the subsoil, even if these aspects were not explicitly excluded. Instead, practical suitability of this method of surface deformation imaging was tested by carrying out the hereafter presented tasks. The experiment was conducted between the 11th and 23rd March 2002. In the following subsections the type of tiltmeter installation, progression of borehole drilling and set-up, as well as data correction, data presentation (plotting), interpretations and data processing, and a comparison between platform and borehole tiltmeters will be taken into consideration. In the last subsection transient signals observed at individual positions will be discussed.

a. Experimental Set-up

Ten borehole tiltmeters were used to measure pump induced near surface tilt at 16 different positions, marked in Fig.3.3 ($T4_{OE}$ included). Two platform tiltmeters were mutually installed close to $T1_{OE}$,

T8_{OE} and T9_{OE}. Their data will be discussed separately. During the experiment the waterworks were in continuous automatic operation and generated ongoing pump cycles, see section 3.1.

Except at positions T1_{OE}, T2_{OE} and T4_{OE} the borehole tiltmeters were installed at different depths between 1.5 m and 2.8 m bottom end of the instrument below surface in freshly drilled boreholes without a casing. Drilling of the boreholes had to be stopped when subsoil gets to tough, i. e. the drilling tool was blocked. As a consequence the depth of the various boreholes was not equal. The platform tiltmeters were installed in hollows of 0.4 m depth. Fig.3.8 shows the installation depths of the various tiltmeters. The topsoil layer above the underlying layer of gravel and coarse-grained sand is depicted, too. Additionally, the days of March 2002 (dates between 11th and 23rd) during which the tiltmeters were operated at the positions are listed in Fig.3.8. The instruments were operated only for some days at one place and then moved to a new position. The instruments at T1_{OE} and T2_{OE} were operated continuously during the experiment. They

were useful as reference stations for tilt signals in the near- and the far field of surface deformations. The signal character at these positions is already known from the first experiment, section 3.1.1. Positions of boreholes were chosen so that at least two tiltmeters were operated at about the same radial distance to a production well, and at two different horizontal azimuths preferably in opposite directions of each of the wells. The radial distances between different tiltmeter positions and wells grow nearly logarithmically to provide a better spatial resolution of shorter deformation wavelengths in the near field and also be able to detect widespread signals of the deformational far field. This selection is very similar to the geometrical set-up of observation wells for classical hydrological investigations (McCarthy & Yeh, 1990, Hölting, 1996).

The appendix lists the configuration data for site OE, section A.3.1. Pressure transducers were installed in the three production wells only. Heads of observation wells were not recorded. Besides tilt and well level observations, air pressure and precipitation were logged at a position close to T1_{OE}, see Fig.3.3. At T1_{OE} and T2_{OE} the subsoil temperature was recorded in 0.5 m and 1 m depth, respectively. Sampling of tilt data was between 10 s and 1 min depending on the type of the used data logger, 2 min of pressure transducers and 5 min of the other observables.

b. Data Basis from Borehole Tiltmeters

Fig.3.9 shows the data from borehole tiltmeter positions in the near field, obtained during three days from 14th to the end of 16th March 2002. The data from tiltmeters that were installed without a casing are corrected with respect to influences from settling after installation and from precipitation. The correction is outlined in detail in the appendix in section A.3.3. Data of the tiltmeters at T1_{OE} and T2_{OE} was not corrected for any influences, except artificial disturbances that occurred during maintenance and

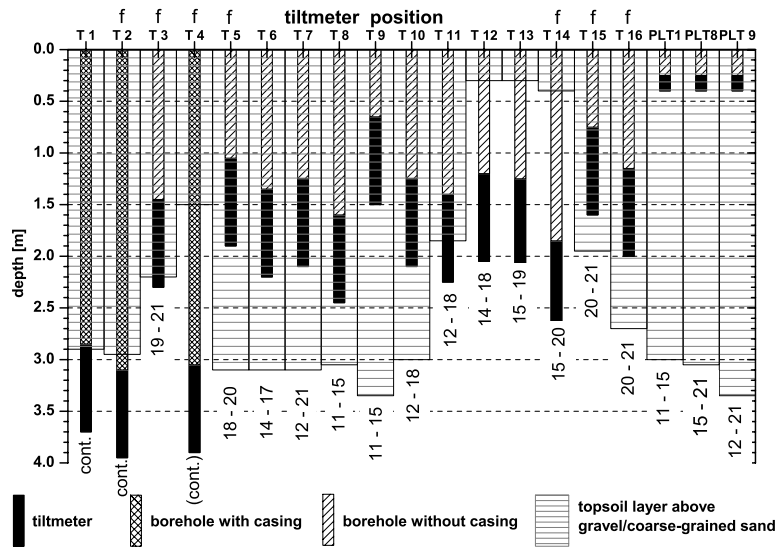


Figure 3.8: Depths of tiltmeters, thickness of topsoil layer and installation date at site OE. The three positions for T1_{OE}, T2_{OE} and T4_{OE} were erected for long term monitoring. The corresponding boreholes are therefore deeper and with a cemented casing. These tiltmeters were operated continuously. T4_{OE} was removed earlier in 2001. The other boreholes are without a casing, more shallow and of various depths. At these positions, the tiltmeters were installed only for a short duration. Numbers below the columns indicate the dates of the days in March 2002 of installation and removal. 'f' marks positions in the far field of induced surface deformations, compare section 3.1.1.

data retrieval. From top to bottom, the single time series in Fig.3.9 are: $ST_{05_{OE}}$, soil temperature measured in 0.5 m depth (close to $T1_{OE}$) and $ST_{1_{OE}}$, soil temperature in 1 m depth below surface (close to $T2_{OE}$) and RF_{OE} , rain fall. The next part of the figure shows the tilt data, from $T13_{OE}$ with components $T13N_{OE}$, $T13E_{OE}$, and with decreasing position numbers down to location $T6_{OE}$, i. e. $T6N_{OE}$, $T6E_{OE}$ as well as tilt from the two reference positions, $T2_{OE}$ in the far field and $T1_{OE}$ in the near field. Tilt was

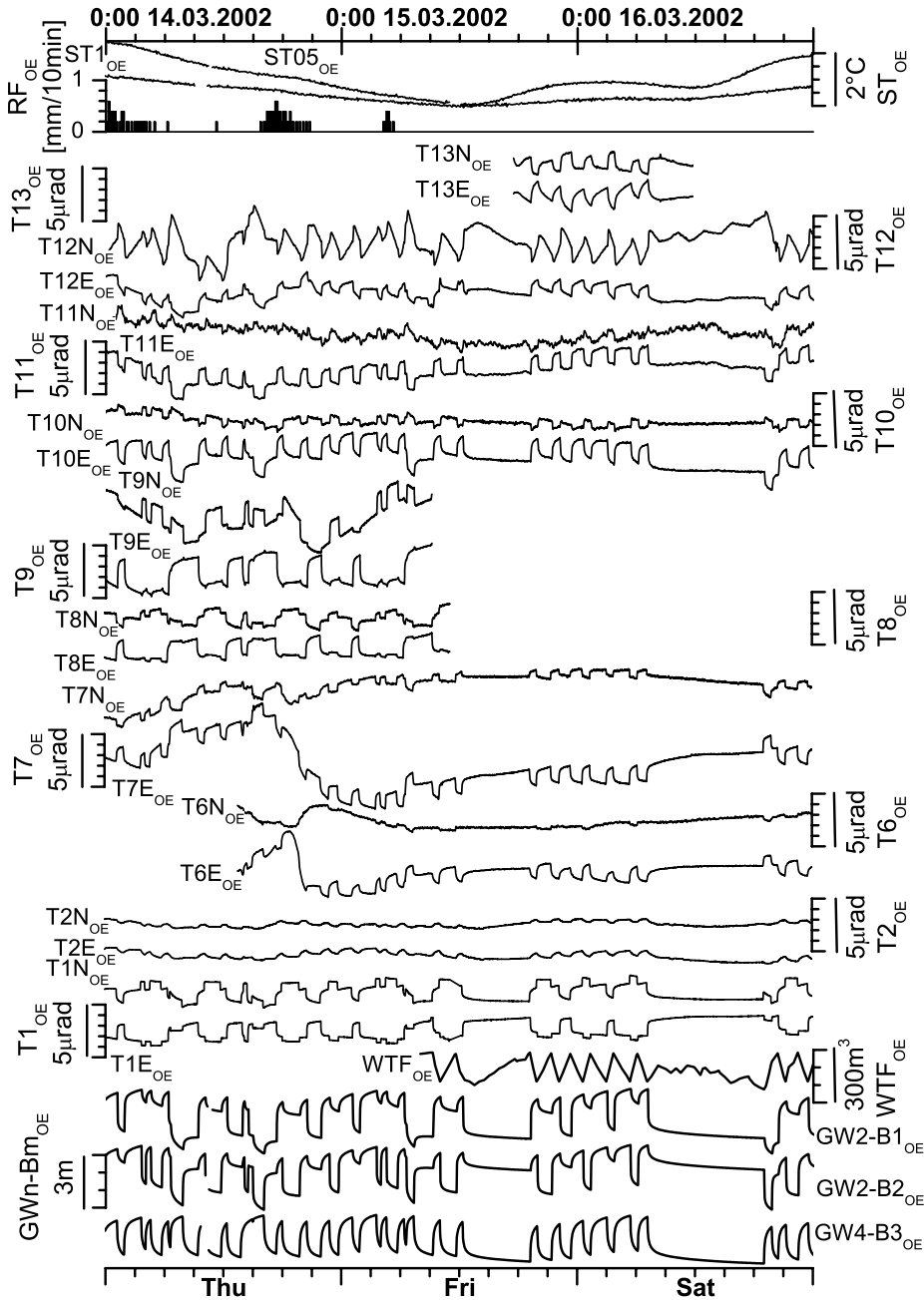


Figure 3.9: Data from near field of near surface tilt, i. e. at positions in the map of Fig.3.3 except positions only included in the inset there. From top to bottom: soil temperatures STn_{OE} , rain fall, RF_{OE} , tilt, Tn_{OE} , the water tank fill, WTF_{OE} and well heads $GWn-Bm_{OE}$. Original data of tilt components X, Y was transformed into a north east (N-E) reference system.

transformed and oriented into a positive north east (N-E) system. Tilt has a positive sign if the top end of the tiltmeter strikes to northern (or eastern) direction with respect to the bottom end. The transformation is a left handed rotation of the original data, similar to Eq.A.4 in the appendix, of the tilt components X and Y, see Fig.3.3. The lower part of the figure shows WTF_{OE} , the water tank fill of the fresh water reservoir, and the well heads of the three production wells. Amplitude scaling of tilt data is equal for all time series, as it is for the well heads. Some of the time series did not cover the full time span. This was caused by moving the individual instruments between the different positions.

All tilt records in Fig.3.9 show significant pump induced signals that are easy to correlate with the activity of individual wells $B1_{OE}$ and $B2_{OE}$. The different patterns of the course of the well heads, their variations in the amplitudes and the durations of pump cycles, e.g. around 21:00 at 14/03 till 4:00 at 15/03 or between 18:00 at 15/03 and 9:00 at 16/03/2002, can be identified in the corresponding time series of

tilt. Pumping from B3_{OE} again does not seem to have significant influence. A significant influence of soil temperature variations on the tilt measurements, and of variations of the air pressure (not drawn) on the well head observations is not obvious. The three rain fall events around 0:00 at 14/03, 17:00 at 14/03 and 4:30 at 15/03/2002 caused a disturbance in some of the tilt signals. The data was already corrected for influences from precipitation and settling, see section A.3.3. Still, correction is not complete and some irregularities remain. The largest residuals from those disturbances are in T9_{OE}, T7_{OE} and T6_{OE}. T9_{OE} was installed at 11th March in 1.5 m depth (bottom end), whereas T7_{OE} and T6_{OE} were deeper, but freshly installed at 13th and 14th March. It may be possible that influence of precipitation to T9_{OE} was strongest due to the shallow installation depth, and settling of T7_{OE} and T6_{OE} is still the dominant effect in the corresponding data sets. However, in the depth range between ≈ 1 m and ≈ 3 m, for installations without a casing, there seems to be no exact correlation between disturbances of tilt measurements and near surface influences. The very local geological settings and disturbances of subsoil, for instance from drilling, seem to have been biased the effects more by chance. Therefore, correction of data was focused on the removal of disturbances without any consideration of the precise physical causes of the influences.

With the correction applied, all tiltmeters yielded signal parts of pump induced response useful for trying a quantitative analysis. Except T13E, T12N and T12E look somewhat strange. These three records show some triangularly shaped signal excursions. These signals suggest a linear tilting progress in contradiction to the exponentially-shaped curved signals from most of the other positions. The reason is most probably the loading effect of the nearby fresh water reservoir in the cellar of the waterworks control building, see Fig.3.3. This fresh water reservoir is a heterogeneity in subsoil that may disturb spreading of the pump induced signals. The record of the reservoirs fill, WTF_{OE}, is well correlated to these tilt signals. This water tank is used as a buffer for the waterworks. If there is a demand on fresh water, first the water from that reservoir is pumped into the pipes to the consumers. When the level of the tank drops below a certain value, the automatic control switches the production wells on to refill the reservoir. This can be seen between 21:00 at 15/03 and 7:30 at 16/03. In that time the water tank was refilled five times in succession by pumping from B1_{OE} and B3_{OE} or B2_{OE} and B3_{OE}. After 7:30 at 16/03 there was a longer lasting peak demand on fresh water. Both wells, B1_{OE} and B3_{OE} had to run without interruption till 19:00 in the evening of 16/03, but the water tank's fill continuously dropped. At 19:00 the automatic control stopped the pump in B3_{OE} and started B2_{OE} to achieve the maximum production rate of nearly 500 m³/h. In the following one and a half hours the reservoirs fill was recovered. The water level in the basin beside the waterworks control building, see Fig.3.3, did not change worth mentioning during the experiments.

Data from the tilt measurements in the far field of surface deformations are shown in Fig.3.10 together with meteorological data, soil temperatures and the well level data, similar to Fig.3.9. The data is from noon 18th till noon 21st March 2002 and has been oriented in a positive north east system. A data correction was applied like in the previous case. Besides the data from T1_{OE}, T2_{OE} and T13_{OE}, tilt data from the more distant positions T16_{OE}, T15_{OE}, T14_{OE} and T5_{OE}, see the inset in Fig.3.3, is included. The scaling of the tilt amplitudes is enhanced in comparison with Fig.3.9. Measurements at positions T14_{OE}, T13_{OE}, T5_{OE}, T3_{OE}, T2_{OE}, and T1_{OE} yielded useful data. Somewhat larger disturbances are in the records from T5_{OE} due to settling and moistening effects, from the beginning of the data till 6:00 at 19/03/2002. Unfortunately, two longer lasting rain fall events from midnight at 20/03 and 19:00 at 21/03 have disturbed the measurements at positions T16_{OE} and T15_{OE}. Since the time for the experiment was limited, it was not possible to get longer data sets from these two positions. Nevertheless, the data from T15E shows pump induced tilt response, as the excursions of that signal are correlated with pump activity. At T16_{OE} tilt response to the pump activity is not significant, i. e. it has an error equal to the strength of the response amplitude. In that case, tilt response can be estimated, if the data is rotated, compare section A.2, until one of the tilt components matches the strike orientation of pump induced total tilt. Then, the largest signals are only in one of both components and some guesses about the induced tilt become possible. After this was made, strongest tilt response of about $0.1 \mu rad \pm 0.05 \mu rad$ results, but is at the tiltmeters' nominal resolution.

For a comparison, at position T4_{OE} that was at a similar radial distance to the waterworks like T16_{OE}, long term measurements were made over more than a year. From an inspection of all data of these mea-

measurements total tilt response was obtained to be about $0.15 \mu\text{rad} \pm 0.03 \mu\text{rad}$ to pumping from B1_{OE} and B3_{OE} or B2_{OE} and B3_{OE} and around $0.25 \mu\text{rad} \pm 0.03 \mu\text{rad}$ to pumping from B1_{OE} and B2_{OE}. Fig.3.11 shows example data from T4_{OE} for three days in July 2000. The instrumental set-up at T4_{OE} was different to T16_{OE}. T4_{OE} had a 4 m deep casing that was built into concrete. However, the data from T4_{OE} was also disturbed. Therefore, number of significant pump cycles is small, compared with the observation time. Hence, the determination of the pump induced tilt response signals at T4_{OE} was only possible, because the best signals could be selected from a large data basis. The sensitivity of T4_{OE} to rain fall events turned out to be much smaller than that of T16_{OE}. This is most likely a consequence of the more tough construction at position T4_{OE}, and also at T1_{OE} and T2_{OE}, which had all a cased borehole. However, with a longer observation time, i.e. with data not disturbed by precipitation, a more significant pump induced tilt response might also be recognized at T16_{OE}.

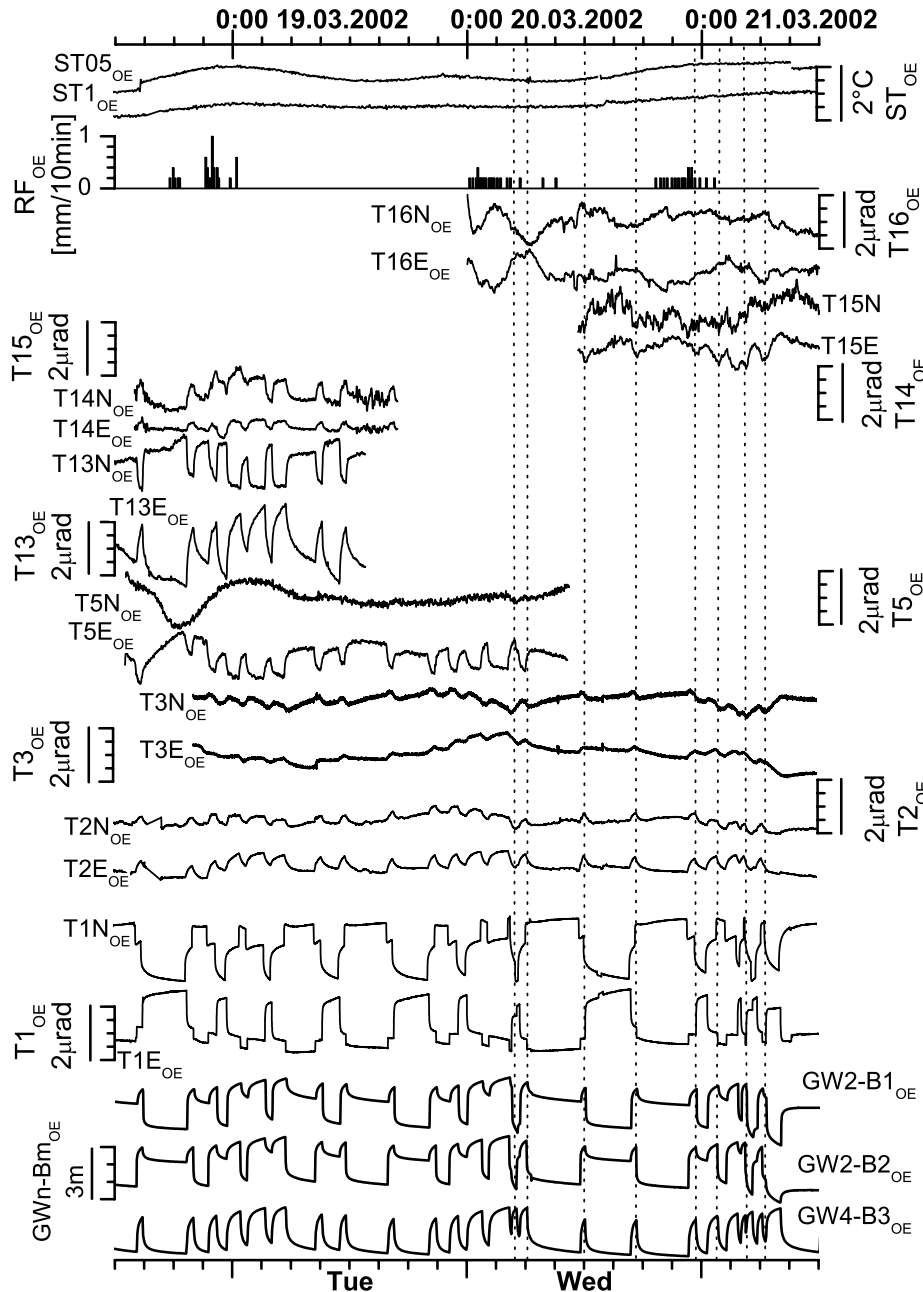


Figure 3.10: Data from far field of near surface tilt, i.e. at positions in the outer area in the inset of Fig.3.3. From top to bottom: soil temperature ST_{OE}, rain fall, RF_{OE}, tilt, T_{nOE}, well heads GW_n-B_{mOE}. Original data of tilt components X, Y was transformed into a north east (N-E) reference system. Some of the instances where significant signals were induced are indicated by the dashed vertical lines.

the data logger and data retrieval) and by temperature disturbances in the internal sensor/electronics system caused by an interruption of the power supply (e.g. if batteries were changed). In general, such artificially evoked signals (e.g. harsh spikes) in any of the data sets were removed, but some annoying parts, especially long lasting offsets in temperature logs remained.

c. Surface Deformation Images from Borehole Tilt

Both the data, from the borehole tiltmeters in the near- and in the far field, were used to image the pump induced surface deformation fields. The images were drawn from derived values of induced total tilt amplitudes, $\Delta\gamma$ and strike directions, Γ at the individual tiltmeter positions. The values of the total tilt amplitudes and of the strike directions were derived from the amplitude differences in each of the two single tilt components, i. e. between tilt values at the start and immediately before the end of pumping. Total tilt $\Delta\gamma$ can be calculated from the data with Eq.2.3 or Eq.A.1. The strike orientation Γ , see Eq.A.6 in the appendix, can be derived with respect to e. g. a north east reference system like used in Figs.3.9, 3.10. In detail, three steps to produce a surface deformation image were carried out:

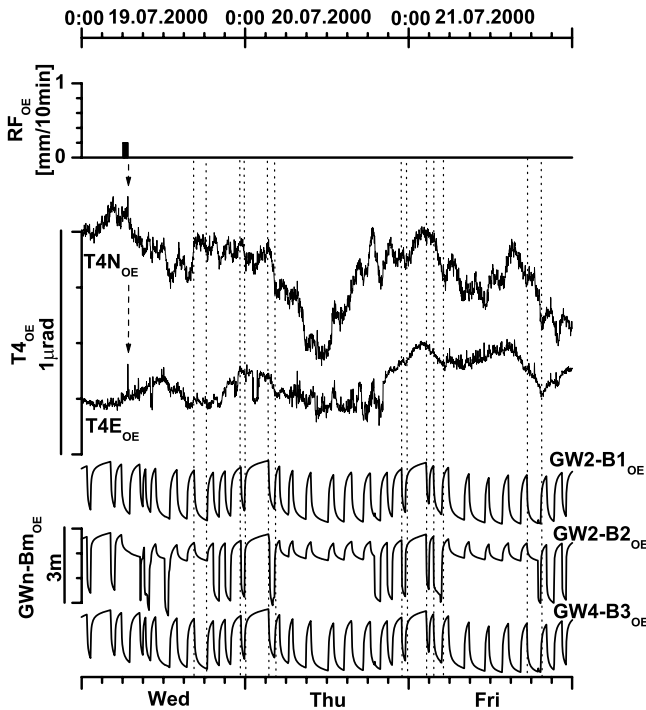


Figure 3.11: Example snap-shot of tilt data from position $T4_{OE}$, compare Fig.3.3. From top to bottom: rain fall, RF_{OE} , tilt, $T4N_{OE}$, $T4E_{OE}$ and well heads $GWn-Bm_{OE}$. Original data of tilt components X, Y was transformed into a north east (N-E) reference system. Some pump cycles are indicated by the dotted lines. However, the data from times where all three wells were operated simultaneously, were not used. A lot of small disturbances with strengths in the range of the pump induced signals can be seen. The rain fall event caused only a faint tilt signal, denoted by the dashed arrows.

ble to use only data from pump cycles that were of equal length in time. The data basis would have been too small. In fact, data corresponding to times of pumping far less than one hour and longer than six hours was left out. Due to these conditions, the derived tilt responses $\Delta\gamma_x$ and $\Delta\gamma_y$ are not necessarily the steady state values, nor valid for a certain time after onset of pumping.

Second, for every tilt component at any of the positions, the arithmetic mean and its standard deviation were calculated from the previously determined values of tilt response for all three well combinations. After that, these averaged values of the tilt components and their standard deviations were transformed to the north east reference system. Then, the required value of mean total tilt amplitude $\Delta\gamma$ at every tiltmeter position and its mean strike Γ were calculated. At some tiltmeter positions only a small number of induced pump cycles was recorded. Thus, the errors of the values for these positions became considerably high. The only way to reduce these errors is improving the statistics through longer data sets. The error plots for the mean tilt values at the 16 positions of borehole tiltmeters are in the appendix, section A.3.4.

First, the responses $\Delta\gamma_x$ and $\Delta\gamma_y$ of the tilt sensors/components of each tiltmeter at every position, together with the corresponding errors, had to be determined for all pump cycles of the wells. As three combinations of well activity had to be taken into account, activity of $B1_{OE}$ and $B3_{OE}$, $B2_{OE}$ and $B3_{OE}$, and $B1_{OE}$ and $B2_{OE}$, three deformation images were finally obtained. The excursion values in both components of tilt were taken only from that corrected data in which disturbances from settling and rain fall were significantly reduced. For positions $T15_{OE}$ and $T16_{OE}$ all available data was used, for $T4_{OE}$ selected data. The obtained tilt response of e. g. $\Delta\gamma_x$, Fig.3.12, is the difference between the tilt value in the X-component taken at the time t_1 , exactly when the pump starts, and the value of the same tilt component, taken immediately before cessation of the pump, at time t_2 . Derived difference values varied among the single pump cycles that were produced by activity of a certain well configuration. This variation was caused by residual disturbances in the tilt signals and different durations of pumping. A signal delay between the production wells' level change and induced tilt can influence this determination of induced tilt response, too. However, the observed delays led only to a negligible error, much smaller than the errors caused by disturbances and different durations of pumping. It was not possi-

Third, the surface deformation images were plotted in the map of site OE. The images contain two parts: (1) Arrows of a length proportional to the mean total tilt amplitude and pointing in the mean strike direction. The arrows are attached at the installation points of the instruments. (2) A contour plot. A correlation gridding process (Microcal Software, Inc., 1999) was applied to the mean total tilt amplitudes for the spatially irregular distributed 16 tiltmeter positions. Initially, the corresponding tilt values on a synthetical regular 100×100 grid of fictitious positions at the experimental site were calculated. Then, a contour image from the gridded values was drawn in the site map. The isoline values in the contour plot were depicted with a negative sign to indicate subsidence. Due to the heterogeneous and still sparse number of tiltmeter positions, the shape of the isoline pattern should not necessarily reflect the real situation. Rather, these contour diagrams are very suggestive.

Figs.3.13(a), (b) show the images for pumping from wells B1_{OE}, B3_{OE} and B2_{OE}, B3_{OE}, for the near field, and for the far field in the inset, compare also Fig.3.3. Despite the sparse number of tiltmeter positions and the various data sets with larger statistical errors, the surface deformation images of Fig.3.13 (and hereafter the following images) show four noticeable aspects:

(1) The tiltmeters responded to pumping in a grossly coherent manner and seem to reflect tilting of the shallow subsoil nearby the production wells. Differences between the pumping effects of different wells are best seen in the near field. In the far field, tilt signals seem more coherent, even when they are associated with larger statistical errors. The observed surface deformation field is quite extended like already deduced from the first pump test.

(2) Pumping from B1_{OE}, B3_{OE} seems to cause larger overall mean tilt than pumping from B2_{OE}, B3_{OE} although the wells B1_{OE} and B2_{OE} were built in a very similar way. The tiltmeters at positions T1_{OE}, T8_{OE} and T9_{OE} responded with larger amplitudes to pumping in B1_{OE} than to pumping in B2_{OE}¹. Especially T10_{OE}, T11_{OE}, T9_{OE}, T1_{OE} and T7_{OE} were at about the same radial distance to B1_{OE}, see Fig.3.13(a), like T8_{OE}, T7_{OE}, T1_{OE}, T9_{OE} and T10_{OE} to B2_{OE}, respectively, in that order. The responses of these tiltmeters can be compared one by one:

Response signal of T10_{OE} to pumping in B1_{OE} is larger than the signal of T8_{OE} to pumping from B2_{OE}. Contradictory to the assumption of a bigger effect of pumping from B1_{OE} than from B2_{OE} is the difference between response of T10_{OE} and T11_{OE} to B1_{OE} and T7_{OE} to B2_{OE}. Here, T7_{OE} shows a larger amplitude than T11_{OE}. The amplitude of T10_{OE} seems to be the same for B1_{OE} or B2_{OE}. Strike directions of the tilt responses at both the positions, T7_{OE} (in response to B2_{OE}) and T11_{OE} (in response to B1_{OE}) are very similar, if the symmetrical configuration of these wells and these tiltmeters are considered. Response at T9_{OE} to activity in B1_{OE} can be compared with that at T1_{OE} to pumping in B2_{OE} and vice versa. The induced tilt amplitudes at the prevailing closer positions to the active wells, i.e. response at T9_{OE} to B1_{OE} and at T1_{OE} to B2_{OE}, turn out to be different. However, tilt amplitudes at the prevailing farther position are very similar, if the prevailing other well is active, i.e. response at T9_{OE} to B2_{OE} and at T1_{OE} to B1_{OE}. Hence, strike direction with respect to the wells is different, and not radial, for the prevailing farther positions, i.e. response at T1_{OE} to B1_{OE} and at T9_{OE} to B2_{OE}. For the prevailing closer positions, i.e. response at T9_{OE} to B1_{OE} and at T1_{OE} to B2_{OE}, strike is very well oriented towards the active well. However, with the assumption of a homogeneous half-space, the largest amplitudes, with strike direction towards the active well, should be at position T1_{OE} for pumping from B2_{OE} and at T9_{OE} and T11_{OE} for activity in B1_{OE}. This is confirmed for T9_{OE}, but not for T1_{OE} and T11_{OE}.

With respect to the well locations of B1_{OE} and B2_{OE}, T1_{OE} and T9_{OE} as well as T8_{OE} and T10_{OE} were at nearly the same radial distances (but at different azimuths towards the line connecting both wells), respectively. Three possible explanations for the difference in the tilt response at mostly symmetrically placed positions can be hypothesized.

¹ If obvious from the context, hereafter, pump activity of B1_{OE}, B3_{OE} or B2_{OE}, B3_{OE} is simply denoted by B1_{OE} or B2_{OE}, respectively. In this experiment B1_{OE} or B2_{OE} were always operated in parallel to B3_{OE}, or together and without B3_{OE}.

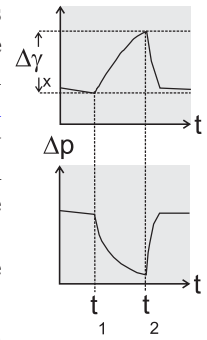


Figure 3.12: Determination of tilt response, $\Delta\gamma_x(t_2 - t_1)$, to a pump cycle recorded by a pressure transducer, $\Delta p(t)$.

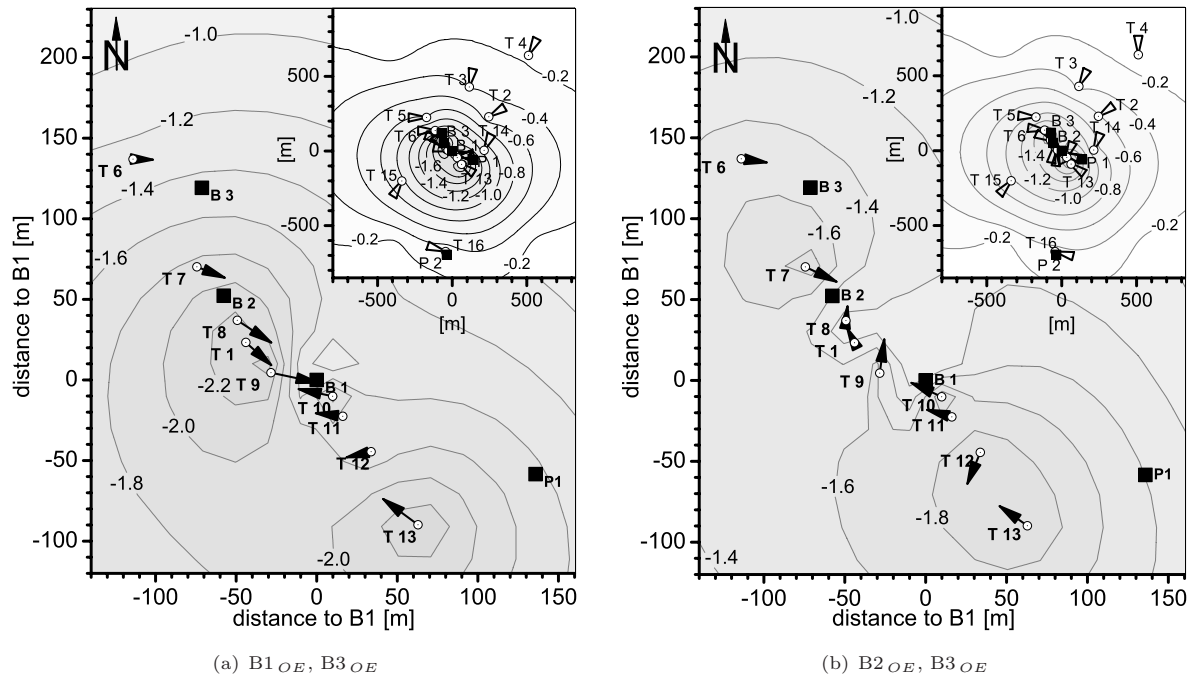


Figure 3.13: Surface deformation fields from tilt data caused by pumping from $B1_{OE}$, $B3_{OE}$ (a) and $B2_{OE}$, $B3_{OE}$ (b). Arrows show mean strike directions and their length mean total tilt amplitudes. The contour reflects a correlation gridding process from the mean total tilt values at the 16 tiltmeter positions (regular 100×100 grid). Negative contour values indicate subsidence in μrad . Pumping in $B1_{OE}$ seems to cause overall larger signals than pumping in $B2_{OE}$.

In a first explanation, subsoil in the depth range of the second aquifer can be assumed to be heterogeneously. Close to $B1_{OE}$ subsoil is not strictly horizontally layered. Aquifer $GW2_{OE}$ may become somewhat thinner, see Fig.3.5. The aquifer here can also have a lower hydraulic diffusivity than nearby $B2_{OE}$. This might have caused an overall larger induced tilt, if $B1_{OE}$ was active. However, it contradicts the observations of similar tilt amplitudes at positions $T7_{OE}$ and $T10_{OE}$.

Second, the more shallow installation of $T9_{OE}$, especially with respect to the depth of $T1_{OE}$, can possibly explain the larger tilt amplitudes at $T9_{OE}$. Both tiltmeters, $T1_{OE}$ and $T9_{OE}$, were installed at a radial distance to the respective well, where the maximum tilt amplitude should occur in a homogeneous half-space in steady state. Around this radial distance, near surface tilt strongly decreases with depth in a homogeneous half-space, see Fig.2.9.

A third explanation refers to the topsoil layer, see Fig.3.5. That layer laterally dies out into the underlying gravel layer south south east of $B1_{OE}$. Indeed, drilling of the boreholes at the positions $T10_{OE}$ to $T14_{OE}$ confirmed the topsoil layer to become slimmer with growing position number, compare Fig.3.8. Thus, a thicker layer of topsoil, which is possibly somewhat compacted from agricultural traffic and the construction of the waterworks, may prevent tiltmeters to respond with larger amplitudes, if the installation depth is more shallow than the layer thickness. On the other hand, tiltmeters installed at positions, where the topsoil is thin, may respond stronger to pumping. This would explain the tilt amplitude observed at $T7_{OE}$ and at $T10_{OE}$ to pumping from $B2_{OE}$. However, amplitudes of $T11_{OE}$, $T12_{OE}$ and $T13_{OE}$ can not be explained by that aspect. A geophysical campaign with seismic and electrical sounding and radar measurements in the most shallow subsoil would be useful to verify these speculations.

(3) Loading and subsoil disturbance, both caused by the waterworks control building and its fresh water reservoir, are a further aspect for interpretations of some of the tilt signals shown in Fig.3.13. The large tilt signals and their strike directions at positions $T12_{OE}$ and $T13_{OE}$ confirm the influence of the control building and the tank fill as already seen in the corresponding time series in Fig.3.9. $T12_{OE}$ was close to the building, compare Fig.3.3, that clearly disturbed the surface deformation field. Loading of the reservoirs fill influenced the tiltmeters by adding a tilt component directed towards the building. Since the

well pairs B1_{OE}, B3_{OE} and B2_{OE}, B3_{OE} were operated with the same extraction rate, the corresponding loading effect of the fresh water reservoir must have been the same. However, B1_{OE} is closer to the building. Therefore, the direct effect from pumping in B1_{OE} was more strongly superimposed by the effect of the reservoir. Thus, depending on the geometrical configuration, tilt amplitudes at positions closer to B1_{OE} and the building could become stronger, especially in response to pumping from B1_{OE}. On the other hand, for positions close to the building, the direct effect of B2_{OE} did not superimpose to the effect of the building with the same strength as the direct effect of B1_{OE} did. B2_{OE} is at a larger distance from the building than B1_{OE}. This will explain the amplitude of T12_{OE} in Fig.3.13(b) in response to pumping from B2_{OE}. The data of T12_{OE} seems to be influenced stronger by the buildings loading than by the well's pumping effect.

(4) The principle of superposition is valid for linear poroelasticity. This should also be reflected in the tilt data. To show some possible tasks which seem to be useful for data analysis, exemplary calculations with the complete deformation field data were done. Fig.3.14(a) shows the observed surface deformation field that was caused by simultaneous pumping from the wells B1_{OE}, B2_{OE}. For a comparison, Fig.3.14(b) shows (as arrows) the surface deformation field calculated as the vector sum of both the vector fields of Fig.3.13(a) and Fig.3.13(b), and (as contour plot) the scalar sum of the total tilt response. Hereafter, the type of field in Fig.3.14(b) is called 'sum field'.

Some of the differences between Figs.3.14(a) and (b) should result from measurement and calculation errors. Possible influences of twice the pump induced surface deformation effect of B3_{OE} may cause differences, too. The strongest difference may be the result of a (non linear) loading effect from the fresh water reservoir. The loading effect depends on the varying actual fill of the tank during each pump cycle and the current demand for fresh water. In the worst case, the difference caused by loading of the reservoir will be a factor two. Namely if the tank is completely filled up at the end of the pump cycles used for the calculation of the averaged data shown in Figs.3.13(a), (b). If both the fields of Figs.3.13(a), (b) are added, the result, drawn in Fig.3.14(b), will show two times the loading effect of the reservoir. In contrast to this, in Fig.3.14(a), the loading of the completely filled tank after a pump cycle of B1_{OE} and B2_{OE} can enter only once. Unfortunately, a full record of the water tank fill could not be obtained.

In Fig.3.14 overall amplitudes of induced tilt are larger in the sum field (b) than in (a), indicated by the contour. This is also valid for the far field. Despite artificial effects of contour plotting, that difference was most possibly caused by the different loading effect of the fresh water reservoir, as in Fig.3.14(b) the total tilt responses at positions T12_{OE} and T13_{OE} are significantly larger than in (a). The loading and disturbance by the waterworks control building and its tank is indicated by larger values in the contour plot in Fig.3.14(b), in particular close to T12_{OE} and T13_{OE}. Nevertheless, the surface deformation fields of Fig.3.14(a),(b), especially the vector fields, look similar.

In the far field, strike directions of T2_{OE}, T3_{OE}, T4_{OE}, T5_{OE} and T14_{OE} are similar between Figs.3.14(a) and (b). Those of T15_{OE} and T16_{OE} are not significant due to the statistical errors. Moreover, strike orientations in the near field were nearly equal for positions T6_{OE}, T7_{OE}, T8_{OE}, T11_{OE} and T12_{OE} and T13_{OE}. At position T6_{OE} the amplitudes in Figs.3.14(a) and (b) are different. A reason could have been influence of withdrawal from B3_{OE}. Or it might have been due to error propagation during the calculation of the sum field. The amplitude difference is within the error ranges. T10_{OE} showed a resemblance to T6_{OE}, but possibly an additional influence of the statistical errors on the strike direction. The larger amplitude at T6_{OE} causes the contour plot, to show overall larger values in north west direction. The similarity in both figures (a) and (b) may actually reflect a resemblance between the real pump induced field patterns. It could also be an artifact of the gridding process as the real tiltmeter positions were the same for both diagrams. However, a gridding with an other density of artificial positions, 50×50 and 200×200, results in nearly the same contour plots.

At positions T1_{OE} and T9_{OE} strike and amplitude values showed larger differences between Figs.3.14(a) and (b). At position T1_{OE} the vector sum in Fig.3.14(b) mostly cancels out. From the geometrical configuration of T1_{OE} with respect to B1_{OE}, B2_{OE} and error propagation follows that the tilt value at T1_{OE} is very sensitive to the summation of error-prone values. Signal parts of nearly opposite strike orientation (due to pumping in the different wells), but similar in amplitude range, were added. Hence, the reason for the difference in tilt response can be statistical errors. Alternatively, the difference could be

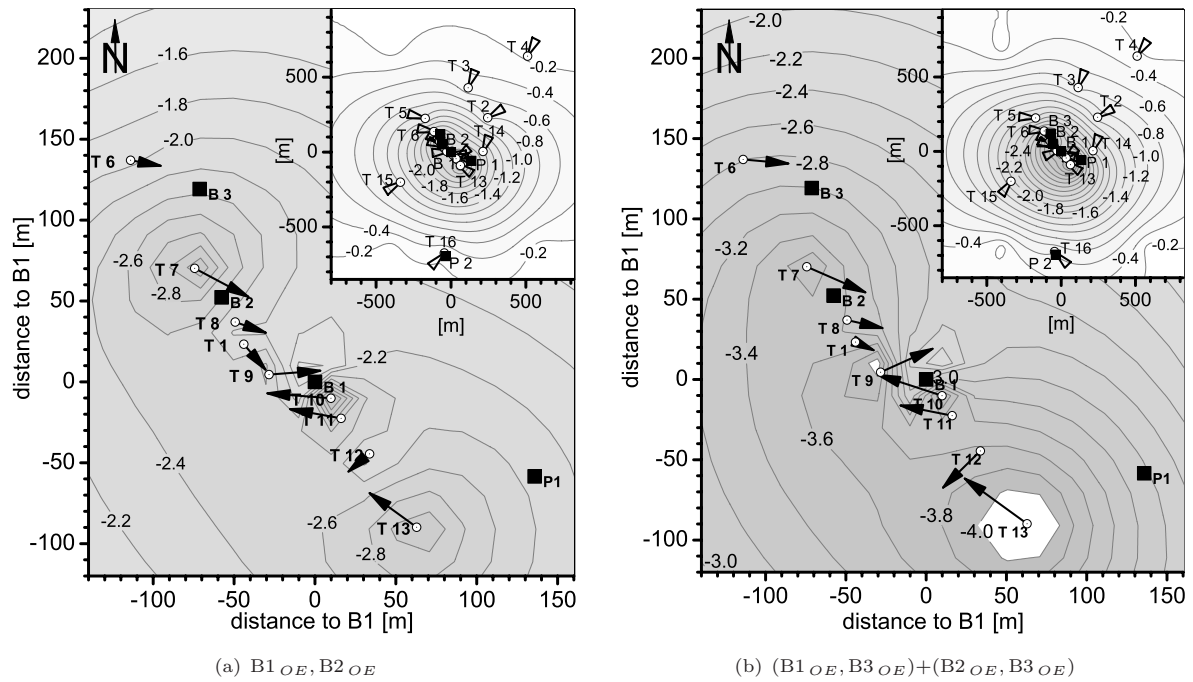


Figure 3.14: Surface deformation fields from tilt data caused by (a) pumping from $B1_{OE}$, $B2_{OE}$, and (b) the sum of the fields from Fig.3.13. Scaling and symbols are like in Fig.3.13. Both the figures, (a) and (b) depict a somewhat similar image, despite the influence of twice the loading of the fresh water tank and possibly the pumping from $B3_{OE}$ in (b). Significant is a larger subsidence south west of $T12_{OE}$, $T13_{OE}$ where the control building of the waterworks is, and larger amplitudes at $T1_{OE}$ in (a) and at $T6_{OE}$ in (b).

caused by withdrawal from $B3_{OE}$, but in that case, the signals at $T7_{OE}$ and $T8_{OE}$ should be influenced, too. A likewise sensitivity to summation of error-prone values can be assumed for positions $T8_{OE}$ and $T9_{OE}$.

After a calculation of difference fields, a somewhat closer inspection of the superposition of pump induced surface deformations is allowed. However, this calculation may lead to larger disturbances by error propagation, but possibly uncovers some useful signal parts. Fig.3.15(a) shows the difference (vector and total tilt response) of the deformation field caused by $B1_{OE}$, $B3_{OE}$ and $B2_{OE}$, $B3_{OE}$, i.e. of the fields in Figs.3.13(a), (b). Fig.3.15(b) depicts the difference of the fields in Fig.3.14(a) and (b), i.e. the difference of the measured field caused by pumping from $B1_{OE}$, $B2_{OE}$ and the sum field that was calculated through addition of the fields corresponding to activity of $B1_{OE}$, $B3_{OE}$ and $B2_{OE}$, $B3_{OE}$.

Accordingly, Fig.3.15(a) should show the difference between the induced effects of wells $B1_{OE}$ and $B2_{OE}$. Influence of loading of the fresh water reservoir and of $B3_{OE}$ should mostly be removed. Since the fill rate of the water tank was fairly equal for pumping from $B1_{OE}$, $B3_{OE}$ and $B2_{OE}$, $B3_{OE}$ loading should have been vanished completely in the error boundaries. Indeed, this seems to be the case as tilt response in Fig.3.15(a) at the positions from $T10_{OE}$ to $T13_{OE}$ is very small. Moreover, in the surrounding of $B3_{OE}$ tilt amplitudes were minor and negligibly in the far field – see the zero line that worms through the site map (inset) from south to north. Only at the positions of $T8_{OE}$, $T9_{OE}$ and $T1_{OE}$ occurred a significant residual tilt response. It might have been an artificial effect of the calculation, too. However, the sign of total tilt at these positions was negative. The field caused by pumping from $B2_{OE}$, $B3_{OE}$ was subtracted from that by $B1_{OE}$, $B3_{OE}$. Due to the sign convention here, a negative sign indicates the residual subsidence effect of $B1_{OE}$, and a positive sign the subsidence caused by $B2_{OE}$. Thus, it seems that pumping from $B1_{OE}$ caused a larger effect on the tiltmeters installed at $T8_{OE}$, $T9_{OE}$ and $T1_{OE}$ than pumping from $B2_{OE}$. This may point to an inhomogeneity in the subsoil between the two wells as already argued above. The two candidates for the inhomogeneity can be first the topsoil layer that dies out in south south east direction from $B1_{OE}$. Second, the aquifer $GW2_{OE}$ which might become thinner or has a lower hydraulic diffusivity close to $B1_{OE}$. Though, the heterogeneous distribution of the tiltmeter positions can lead to an additional artifact in the data. Spatial resolution of tilt measurements

(due to the distribution of observation points) was generally higher in the direction of extension of the piece of land of the waterworks, i. e. from south east to north west. Therefore, a residual effect of pumping from $B1_{OE}$ must not have been localized to the small area of positions of $T8_{OE}$, $T9_{OE}$ and $T1_{OE}$, but might have been somewhat more extended in south west to north east direction.

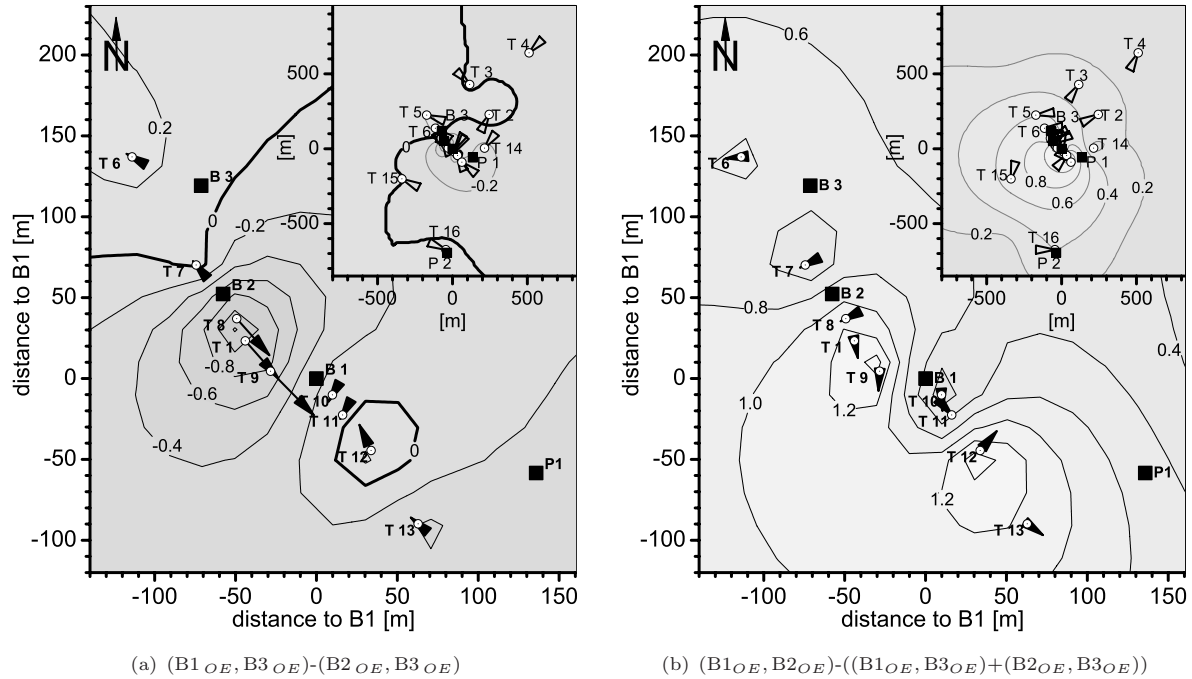


Figure 3.15: Surface deformation fields from tilt data calculated from (a) the difference between the fields in Fig.3.13, and (b) from the difference between the observed field caused by pumping from $B1_{OE}$, $B2_{OE}$ in Fig.3.14(a) and the sum field of Fig.3.14(b). Scaling and symbols are as in the foregoing cases, but the range for amplitudes of the contour plots were lowered to include both signs (and no longer indicate only subsidence). The total range in the contour is kept unchanged. Missing arrows indicate values too small to show up.

Still, the difference field in Fig.3.15(b) should show at first, twice the surface deformations caused by pumping from $B3_{OE}$. At second, it should indicate the discrepancy between the loading of the reservoir, if it was filled during activity of $B1_{OE}$ and $B2_{OE}$ on one hand, and if the mathematical sum of the load through filling by $B1_{OE}$, $B3_{OE}$ plus $B2_{OE}$, $B3_{OE}$ was calculated on the other hand. Both the effects, from pumping through $B3_{OE}$ and the discrepancy in the reservoir load, should be indicated by a positive sign in the total tilt response. For an induced effect of the $B3_{OE}$ -activity, above all, a positive sign in the contour plots should appear at distances to $B3_{OE}$ where the tilt maximum for a homogeneous half-space is expected, e. g. close to $T1_{OE}$. For an artificially calculated excess loading by the reservoir a positive total tilt value should appear close to the location of the reservoir. The corresponding strike orientation of tilt should be away from $B3_{OE}$ and away from the location of the reservoir, respectively.

In the surrounding of $B3_{OE}$, i. e. at positions $T5_{OE}$, $T6_{OE}$ and also at $T8_{OE}$, tilt amplitude was really positive, but not strong enough to be actually significant. Strike of tilt at $T6_{OE}$, $T7_{OE}$ and $T8_{OE}$ was, at best, only very grossly away from $B3_{OE}$. Around $T1_{OE}$ amplitudes were somewhat stronger, i. e. about $1.3 \mu rad$. Strike at $T1_{OE}$ was away from $B3_{OE}$. However, it is hard to decide, if an influence of pumping from $B3_{OE}$ on the tilt field exists.

In the contour plot of Fig.3.15(b) a disturbance of the deformation field caused by the discrepancy in the reservoir load can be seen. The absolute total tilt response shows significant positive values nearby the water tank. Moreover, strike directions of tilt at positions $T12_{OE}$ and $T13_{OE}$ are away from the reservoir. This reflects an artificially calculated excess loading with respect to the loading effect that occurs during withdrawal through $B1_{OE}$, $B2_{OE}$ only. The excess loading effect is a result of adding the fields from $B1_{OE}$, $B3_{OE}$ and $B2_{OE}$, $B3_{OE}$. In mean, the fill of the water reservoir caused by pumping

from $B1_{OE}$, $B3_{OE}$ or $B2_{OE}$, $B3_{OE}$ was larger than half the fill that was reached on average by pumping through $B1_{OE}$, $B2_{OE}$. Finally, excess loading might be a consequence of the water amount pumped from $B3_{OE}$, and possibly from a slightly reduced extraction rate in $B1_{OE}$ and $B2_{OE}$ due to backwater in the outlet tubes, if both the latter wells are contemporaneously active.

In conclusion, the surface deformation images of Figs.3.13, 3.14 and 3.15 together with the outlined analyses showed that in principle, surface deformation imaging with the aid of tilt measurements at shallow depths looks to be a promising new technique for subsoil exploration and monitoring in ground water extraction areas. At site OE, the observations in the far field confirmed the foregoing assumption from measurements in the first pump test, section 3.1.1, of a rather widespread catchment area of the waterworks' wells. Influence of the waterworks' control building with the fresh water reservoir was identified by the type of tilt response at $T13_{OE}$ and the strong discrepancy of strike in $T12_{OE}$ with respect to the coherent pattern of the overall surface tilt field. Tilt signals from positions $T12_{OE}$ and $T13_{OE}$ correlated best with the water tanks fill record, Fig.3.9. A comparison of the surface deformation image with the map of site OE, Fig.3.3, showed that the strikes of $T12_{OE}$ and $T13_{OE}$ were in direction towards the control building. Calculations with the averaged tilt vector fields on the basis of the superposition principle seem to be applicable for data inspection. Some less prominent and more speculative aspects are the possible influence of pumping from $B3_{OE}$, of a topsoil layer, and the second aquifer, $GW2_{OE}$ which might become thinner or gets a lower hydraulic diffusivity in its section nearby $B1_{OE}$.

In further investigations, the technique should be improved. It may be expanded to areas used for oil and gas production or for injecting fluids like at geothermal works. This is also supported by other investigations (Vasco et al., 1998, 2000, 2002a). For a more precise interpretation, additional tiltmeter observations are necessary. At site OE preferably in south west to north east direction close to the wells, and at outer positions in perpendicular direction, from south east to north west. At the opposite site of the Rösenich fault, at least one additional tiltmeter position seems to be useful. Hence, grossly estimating the number of additional fictitious positions, together with the used places, a feasible number of observation points at OE might be at least 25. Due to the disturbances from precipitation a longer observation interval at each position, where tiltmeters are installed without a casing, is desirable. Data should be taken from response signals caused by single pump cycles of nearly equal duration. The duration of measurement at each position should be, with respect to the observation here, at least 10 days, but strongly depends on the actual signal to noise ratio. To be efficient, outer positions at a site should be installed first, to get longer data sets where generally signal to noise ratio is less favorable. (Here, the inner positions in the near field of surface deformations were installed first, to be sure to get useful data. Moreover, instruments had to be moved between most of the positions since the number of instruments was limited.)

d. Platform Tiltmeters

Platform tiltmeters have, compared with borehole instruments, several advantages. First, platform instruments are cheaper. A larger number can be purchased to densely cover an area around a well. Second, the installation can be done by one person without use of any drilling tool in 30 min to 60 min. Third, removal of a platform instrument is simple. The instrument can easily be replaced to a different position. The positions could be already prepared some time before the pump test to minimize settling effects. Hence, applicability of platform tiltmeters for the purpose of the observation of pump induced near surface tilt was tested with two instruments.

Fig.3.16 shows the complete corrected data sets (drawn with grey background) from the three platform tiltmeter positions, $PLT1_{OE}$, $PLT8_{OE}$, and $PLT9_{OE}$. The corresponding borehole tiltmeter data from positions, $T1_{OE}$, $T8_{OE}$ and $T9_{OE}$, compare Fig.3.3, are depicted, too. Measurements at position $PLT9_{OE}$ were carried out during the whole experiment. The other platform instrument was moved at March 15th from position $PLT1_{OE}$ to $PLT8_{OE}$. Also included in the figure is soil temperature data from surface, $ST0_{OE}$, measured directly under the cap of the field box accommodating the electronics, and from 0.5 m depth, $ST05_{OE}$, measured in subsoil next to position $T1_{OE}$. RF_{OE} denotes precipitation data. The well level records from $B1_{OE}$ and $B2_{OE}$ are shown at the bottom of the figure. Scaling for

all tilt data is equal. Due to the very strong excursions of platform tilt signals during the rain fall events at the 14/3, 18/3, 20/3 and 21/3/2002, the time series are cut if they leave the grey background area.

At a first view, the disturbances caused by the rain fall events are obvious, even if the data was already corrected for these influences. Compare also the data correction that is outlined for the platform tiltmeter at position $PLT8_{OE}$ in the appendix, section A.3.3. Pump signals can also be identified, especially if platform tilt data is compared with the well level records and the borehole tilt data. In Fig. 3.16 two pump cycles in $B1_{OE}$ and $B2_{OE}$ are marked by dashed vertical lines. All platform tiltmeters responded to the pumping. Compared with the borehole data the signal curves are significantly disturbed. For instance, there is a sharp spike in the records of $PLT1_{OE}$ before the first two vertical lines. At the fourth vertical line the end of the pump cycle is not clear in the records of $PLT8_{OE}$.

Due to the shallow installation in hollows of about 0.4 m depth, influences of precipitation were strong. Generally, that type of installation is sensitive to other, not clearly identified disturbances, like nearby traffic or wind. Influence of temperature variations in the platform tiltmeters surroundings is not obvious from Fig. 3.16. Possibly, temperature decrease from 14/3 to 15/3 in $ST05_{OE}$ is reflected in the tilt data, but was also overlaid by the influences from precipitation. The diurnal cycles in the temperature can not be identified in the tilt data.

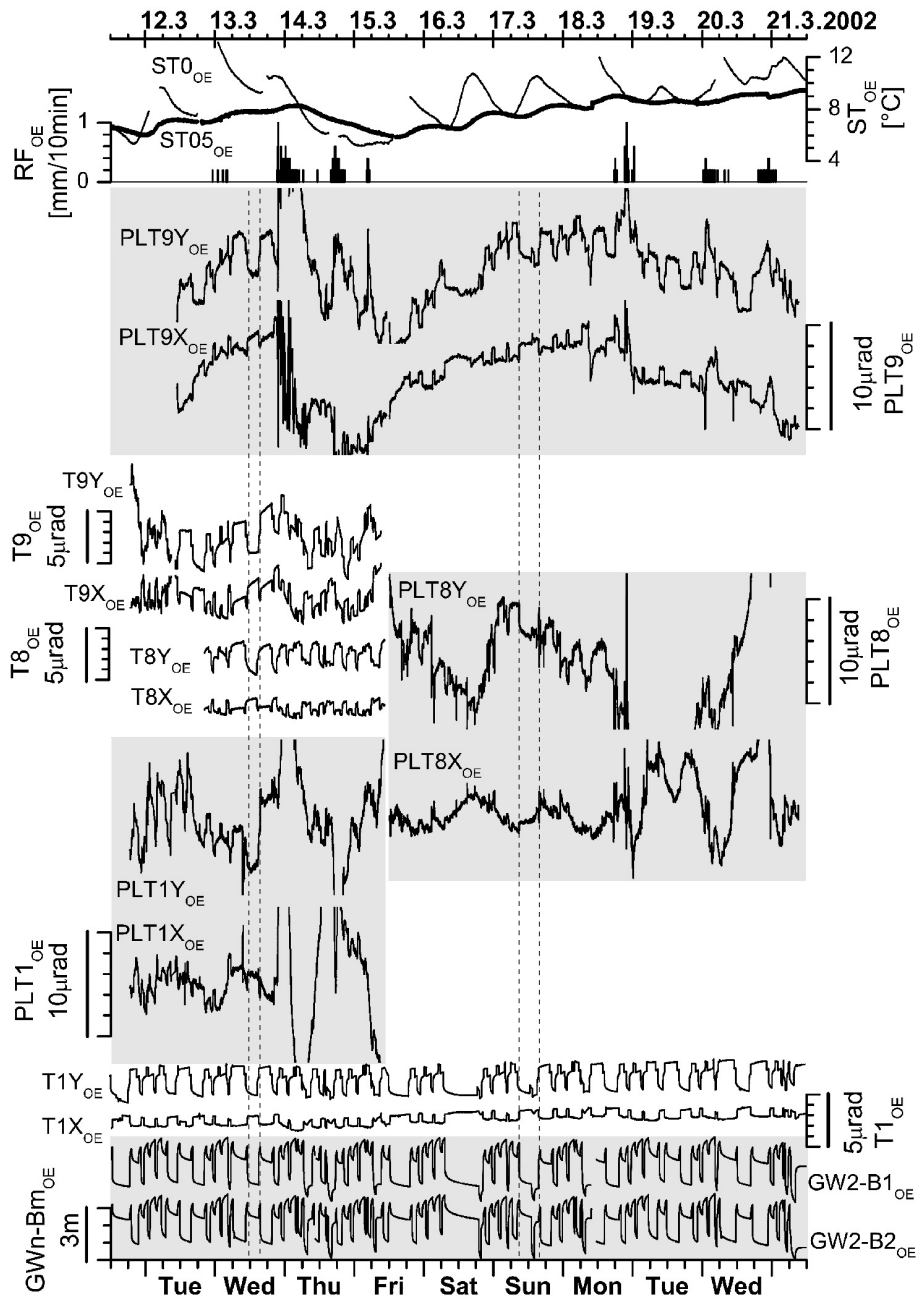


Figure 3.16: Platform tiltmeter data. Records from positions $PLT1_{OE}$, $PLT8_{OE}$, $PLT9_{OE}$ (highlighted) together with the borehole data from positions $T1_{OE}$, $T8_{OE}$ and $T9_{OE}$ and well levels from $B1_{OE}$ and $B2_{OE}$. Data of soil temperature at surface, $ST0_{OE}$, at 0.5 m depth, $ST05_{OE}$, and precipitation, RF_{OE} is at top.

The platform tiltmeters were installed at positions where nearly the largest pump induced tilt signals occurred. It is questionable, whether the instruments will record significant data, even for a longer duration of the measurements, when installed at a larger distance to the wells, e.g. besides of T4_{OE}. A problem with longer observation intervals is also the fact that the platform tiltmeters were not well protected against vandalism.

Platform tiltmeter observations turned out to be less suited for a detailed quantitative investigation like borehole data. However, the platform tiltmeters recorded data that is in principle well correlated with the pump activity and with the data of the borehole instruments, even if strongly disturbed. Generally the data seems useful, particularly after a data correction. Hence, the use of platform tiltmeters can be an alternative to borehole instruments if: (1) pump induced tilt is stronger, i.e. generally of larger amplitude than at site OE, and faint signals should not be resolved, (2) measurements last over a time span with a lot of pump cycles for better statistics, (3) the area around a well should be densely covered by tiltmeter positions, e.g. in between borehole tiltmeter locations, (4) to get a rapid estimation if pump induced tilt to a certain threshold occurs or not.

e. Transient Borehole Tiltmeter Signals – Positive Tilt Reversals

To assess the transient signal part, selected pump cycles from the borehole tiltmeter data were inspected. The radially symmetric and the tangential parts of tilt signals, see section 2.3, allow a closer view to the tilt responses caused by single pump cycles in the wells B1_{OE} or B2_{OE}. Therefore, the data was transformed into a system (t-r system), where one axis points to the well, the radial component TnR_{OE}, and the other one points in perpendicular direction right hand side, the tangential component TnT_{OE}. The ‘n’ holds for the tiltmeter position number. See Eq.A.5 in the appendix for the transformation of tilt data. A negative amplitude in the TnR_{OE} components indicates strike towards the well, compare also Figs.2.8, 2.9. In this coordinate system, the radial signal part can be inspected independently. This data presentation allows a direct comparison of the measured radial component with the radial tilt response calculated from the analytical solution in a homogeneous half-space. Radial tilt response becomes comparable with model generated solutions computed in a horizontally layered half-space. All measured signal parts in the tangential components of tilt, TnT_{OE}, were attributed to disturbances of the subsurface model’s radial symmetry with respect to the well’s vertical axis.

Four selected pump cycles with corresponding tilt responses to pump activity in B1_{OE} are drawn in Fig.3.17. The duration of pumping was about 50 min in (a) and 90 min in (b),(c),(d). The examples are from different day times. From top to bottom the four figures show tilt response in both components of T7_{OE} (not in (a)), T8_{OE}, T1_{OE}, T9_{OE}, T11_{OE} and T10_{OE}. The radial distances between the tiltmeter positions and B1_{OE} decrease in that sequence, as indicated at the right side in the plots. At the bottom of the diagrams are the well level records of B1_{OE} and B2_{OE}. With the assumption that the influence of pumping from B3_{OE} was negligible the fluid level record of this well is not shown. The radial components of tilt and the fluid level record of the active well are highlighted by a somewhat thicker line graph. Vertical axis scaling is the same for the tilt signals as well as for the well heads. The graphs show four main aspects:

(1) Tilt response to pumping appears in all tilt records and in the head of B2_{OE} (that serves as observation well). A drift in some of the signals of T7_{OE}, T9_{OE}, T11_{OE} and T10_{OE} was most likely caused by influences from settling and precipitation. The somewhat fluctuating signal parts in T7_{OE}, T11_{OE} and T10_{OE} are artifacts from the data loggers that were installed at these positions.

(2) The largest total tilt response, among the depicted observations, was at a distance not smaller than 28.8 m (distance between B1_{OE} and T9_{OE}). Due to the shallow installation depth of T9_{OE} with respect to the other tiltmeters, enhanced tilt amplitudes at this position can be assumed. If this aspect is taken into account, the strongest tilt response could be assumed to occur at a larger distance than 28.8 m. Responses at the farther positions T1_{OE} and T8_{OE} are significantly larger than at the more closer position T10_{OE}. At T11_{OE}, at 27.8 m distance, response is significantly smaller in the radial component than in T9_{OE}. Here, a slight influence of the loading of the fresh water reservoir and of the topsoil layer

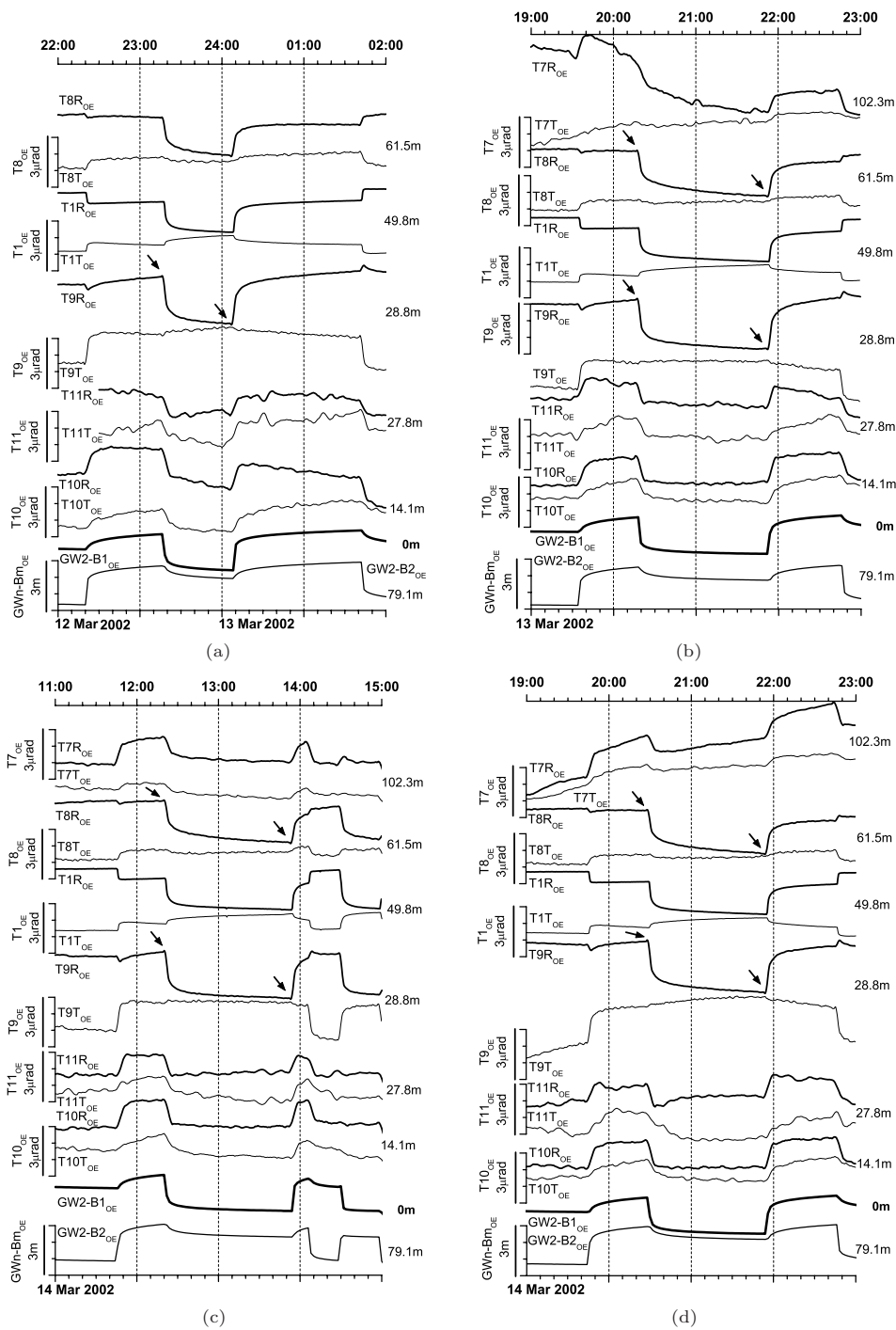


Figure 3.17: Tilt response during four pump cycles of $B1_{OE}$ (and $B3_{OE}$). The data is rotated into a t - r system, where TnR_{OE} is oriented towards the well and TnT_{OE} perpendicular to TnR_{OE} (right hand side). At the right side of the plots the radial distances to $B1_{OE}$ are printed. Arrows mark the so called ‘positive’ tilt reversals.

must be respected, too. In a homogeneous half-space with the same geometrical arrangement of wells and tiltmeters like here, the maximum of radial tilt response in steady state should occur close to the subsoil’s surface at 30.1 m radial distance to the wells $B1_{OE}$ or $B2_{OE}$. However, it is hard to decide from the data, where the maximum exactly would be. Moreover, the calculation of its position in a homogeneous half-space assumes steady state in tilt response. Here, most of the tilt signals look like steady state was not achieved. The slope of most of the signal curves is not nearly zero when pumps/wells were switched. Furthermore, subsoil at OE can most likely not be described by a homogeneous half-space.

(3) The tangential components of tilt at the selected positions had different strengths in relation to the radial components. At position $T7_{OE}$, $T8_{OE}$, $T1_{OE}$ and $T9_{OE}$ the tangential components had small or negligible amplitudes. This indicates a rather radially symmetric subsoil reaction in the area between tiltmeters and well. However, the tangential components at positions $T11_{OE}$ and $T10_{OE}$ show a response with nearly the same strength as the radial components. Here, the subsoil, i.e. radially symmetric response, was disturbed, possibly by an influence of the topsoil layer that dies out in the region around these two positions. Or, besides of further unknown reasons, the significant response in the tangential components might be attributed to the influence of the loading of the fresh water reservoir.

(4) Reversals of tilt have repeatedly been observed in the radial components of $T8_{OE}$ and $T9_{OE}$. The initial strike direction at $T8R_{OE}$ and $T9R_{OE}$ in response to pumping had an opposite sign with respect to the initial strike already seen at position $T1_{OE}$ in Fig.3.7. As these faint reversals are not easily seen, in Fig.3.17, the reversals marked by the arrows in Fig.3.17(c),(d), are printed with a four times enlarged amplitude scaling in Fig.3.18(a),(b), respectively. Although small, the signals in question are clearly reproduced and resolved. These tilt reversals are characterized by a transient strike of the tiltmeters top with respect to its bottom end in radial direction away from the active production well (temporarily growing amplitudes), followed by a strike in opposite direction, i.e. towards the well (decreasing amplitudes). Such type of reversals were previously predicted from calculations by Wang & Kümpel (2003) in a homogeneous poroelastic half-space. Transient tilt reversals may also occur in the radial component of $T11_{OE}$, but are not significant due to the somewhat noisy signal.

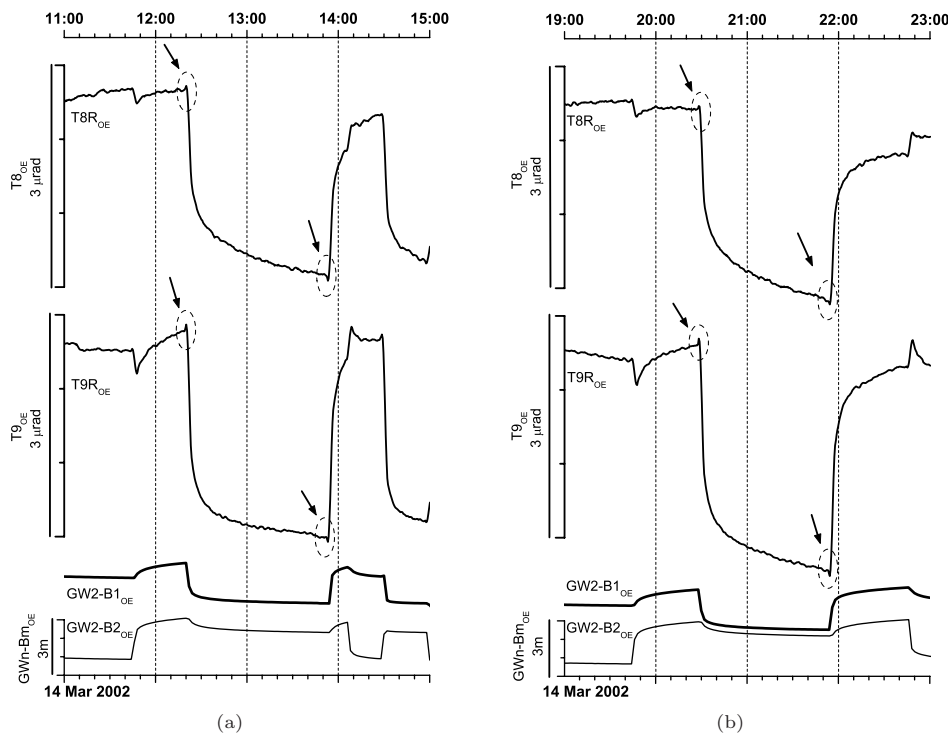


Figure 3.18: Positive tilt reversals caused by pumping from $B1_{OE}$ (and $B3_{OE}$). Four times vertically enlarged view of the radial components from tilt positions $T8_{OE}$ and $T9_{OE}$ of Fig.3.17(c),(d), respectively. The transient tilt reversals in the dashed circles and marked by the arrows have an opposite sign of initial strike than the previously described negative reversals, see Fig.3.7. Sampling rate of tilt data was 10 sec.

Because of the first response direction of the reversals in Fig.3.18, and to make a distinction from the reversals seen in Fig.3.7 (first pump test), the reversals in Fig.3.18 will be called ‘positive reversals’, whereas the type of reversals seen in Fig.3.7 will be called ‘negative reversals’.

Fig.3.19 shows data of five pump cycles in $B2_{OE}$ with the corresponding tilt responses. Tilt signals caused by simultaneous pumping from $B1_{OE}$ and $B2_{OE}$ are depicted, too. Scaling is like in Fig.3.17. The tilt signals are from positions $T11_{OE}$, $T6_{OE}$ (both only in (c),(d)), $T9_{OE}$, $T1_{OE}$, $T7_{OE}$ and $T8_{OE}$,

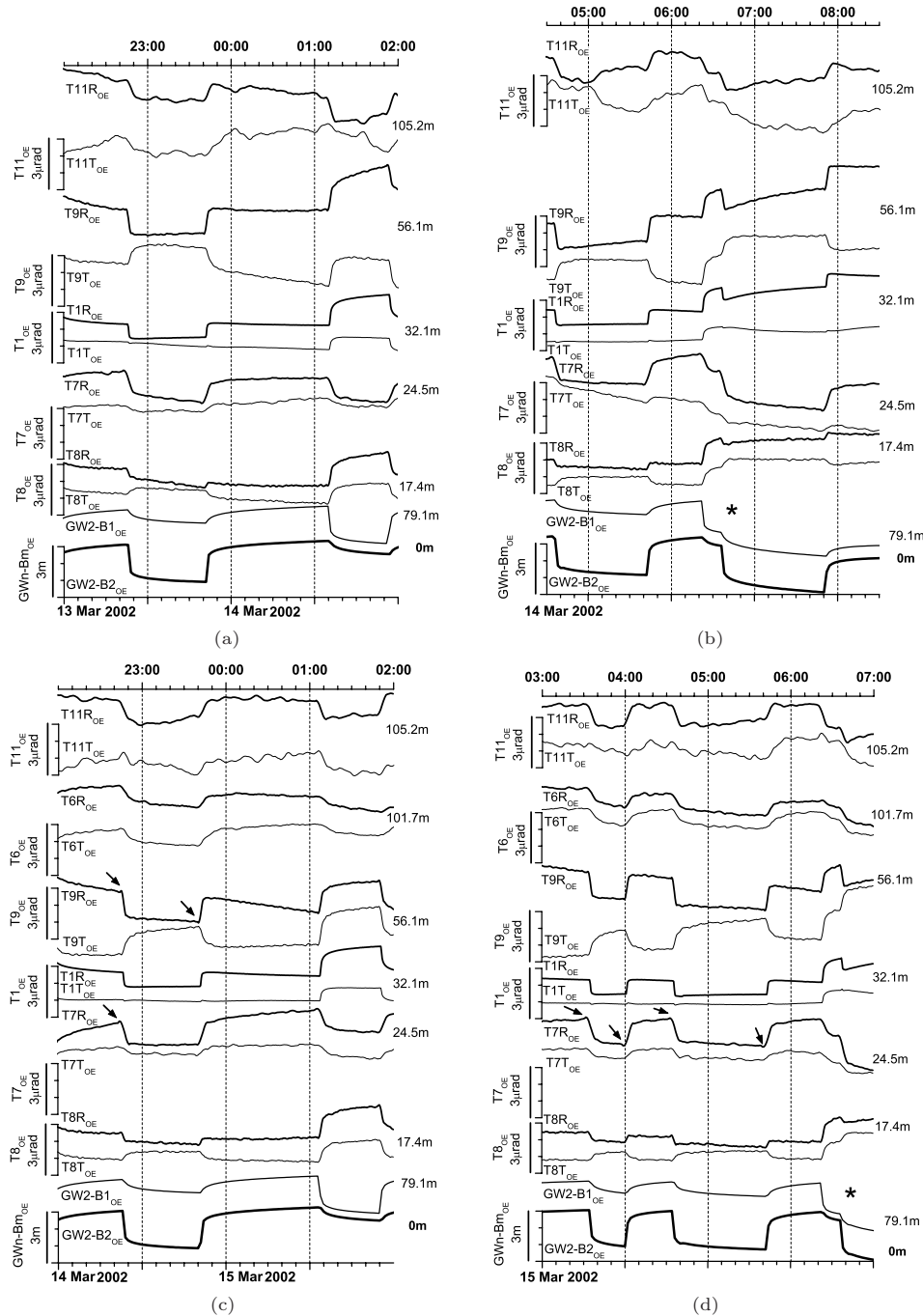


Figure 3.19: Tilt response during four pump cycles of $B2_{OE}$ (and $B3_{OE}$). The data is depicted in a t - r system, where TnR_{OE} is oriented towards the well and TnT_{OE} perpendicular to TnR_{OE} (right hand side). At the right side of the plots the radial distances to $B2_{OE}$ are printed. The asterisks mark onset of pumping from both wells $B1_{OE}$ and $B2_{OE}$ (without $B3_{OE}$), (b), (d). The arrows mark positive tilt reversals like in Fig.3.17, (c), (d).

all listed according to the decreasing distance from the active well. Well level in $B1_{OE}$ (and its distance to $B2_{OE}$) is also printed in Fig.3.19. The four aspects of Fig.3.17, outlined previously, are also valid in Fig.3.19, even if some deviations occur:

- (1) The tiltmeters respond to pumping in a coherent manner.
- (2) Largest tilt responses in the radial tilt components occur at radial distances to $B2_{OE}$ that are between 24.5 m and 56.1 m, i. e. between the distance of $T7_{OE}$ and $T9_{OE}$. However, it is difficult to specify a more accurate value. At $T1_{OE}$, in a distance of 32.1 m, the amplitudes were smaller than at $T7_{OE}$ and $T9_{OE}$,

even if at T1_{OE} the maximum tilt in steady state should occur for a homogeneous half-space. Reasons might be the larger installation depth of T1_{OE}, layering in subsoil, the different type of installation (in a cemented casing at T1_{OE} and without a casing at T7_{OE} and T9_{OE}), and the fact that steady state was not achieved.

(3) Tangential components show small or negligible response signals at positions T1_{OE} and T7_{OE}. At the other tiltmeter locations, significant tangential tilt was recorded. The amplitudes at the latter positions were in the range of the corresponding signals in the radial components. At position T9_{OE}, where in the previous case the tangential response nearly vanished, a large response was observed. The reason is not yet clear, but again may be attributed to some heterogeneities in the subsoil between both wells. Some possible inhomogeneities were already indicated by the surface deformation images.

(4) Positive tilt reversals are seen in Fig.3.19, in the radial components of T7_{OE} and T9_{OE}.

Another aspect here add the transient signal parts in Fig.3.19(b) which show overlying processes acting in an opposite manner. There was a pump cycle with simultaneous extraction from B1_{OE} and B2_{OE}: Around 6:20 of March 14th, 2002, pumps in B1_{OE} (and B3_{OE}) were started. The tiltmeters at the positions T9_{OE}, T1_{OE} and T8_{OE}, situated between B1_{OE} and B2_{OE}, responded with a strike directed towards B1_{OE}. Due to the orientation of the data in a t-r system with respect to B2_{OE}, tilt response at these three positions was temporarily positive in the radial component. Around 6:40 the pump in B2_{OE} was switched on (and B3_{OE} off) to enlarge the total production rate of the waterworks. The three tiltmeters shortly responded in their radial component with a strike in direction towards B2_{OE}, i.e. with negative amplitudes. Later, around 7:50, the temporarily negative response towards B2_{OE} in the radial components was mostly compensated by the stronger subsoil deformation effect caused by ongoing pumping in B1_{OE}. Responses in the tangential components of the tiltmeters remains nearly constant.

3.2 Bürvenich, BV

The pump test experiments at BV were aimed at the recording of special transient pump induced signals. These were the hydrological ‘Noordbergum effect’ and its counterparts in ground movements resulting from strong poroelastic coupling (Fabian & Kümpel, 2003). Additionally, elliptically shaped hodographs in tilt were observed. Former investigations of the Noordbergum effect showed that it preferably occurs in a two-aquifer system when both aquifers are confined and hydraulically separated (Verruijt, 1969, Rodriguez, 1983, Langguth & Treskatis, 1987, 1989, Maruyama, 1994, Kim & Parizek, 1997). Ground water is extracted from one of them and the well head, i.e. pore pressure, shows a transient reverse response in the other aquifer. After an inspection of the geological setting at the site BV, the hydrological condition for an observation of the Noordbergum effect seemed promising. At site BV experiments were conducted in 1999. The pump tests were much smaller in yield and spatial extension of observation points was minor than at OE, compare section 3.1. Two borehole tiltmeters at shallow depth as well as pore pressure transducers were brought in contemporaneously.

Site BV was about 10 km south west of site OE, in the Lower Rhine Embayment, Fig.3.2. It was located at the triangle road junction of the secondary roads connecting the small villages Bürvenich, Schwerfen and Sinzenich. The area is flat except for a shallow ditch of 0.7 m depth and some vegetation, i.e. bushes and a tree, Fig.3.20. Earth’s surface is slightly dipping in east north east direction (LVerma-NW, 1995). On the grass verge at site BV, three wells, B1_{BV}, B2_{BV}, B3_{BV}, tapping aquifers at different depths were accessible. The site was used since 1996 with one tiltmeter, T1_{BV}, for long term monitoring of geodetic point stability (Kümpel et al., 2001, Campbell et al., 2002). Measurements at tiltmeter position T2_{BV} were started in 1998, for long term monitoring and for the experiments here.

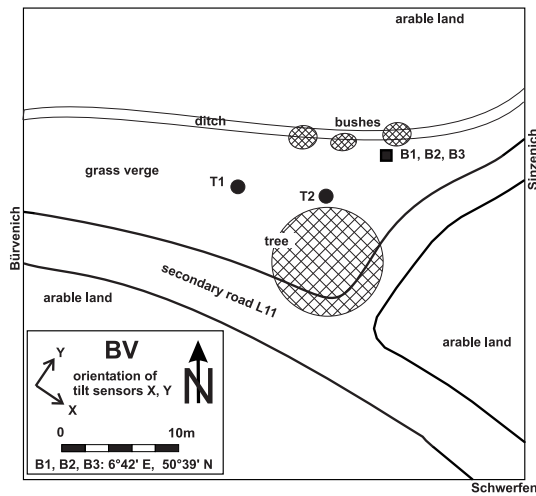


Figure 3.20: Map of test site BV drawn after LVerma-NW (1995).

Geology is of similar structure to site OE, but total thickness of quaternary sediments is only about 90 m. The deeper sequence of strata is known from drilling of the three observation wells (Erftverband, 1995), see Fig. 3.21. The topsoil layer was partially replaced down to 0.3 m from road construction many years ago, and thus is highly compacted. A comparison between the recent map, LVerma-NW (1995) and the 100 year older one, Landes-Aufn. (1895) showed that formerly, a road crossed the grass verge where the tiltmeter positions and wells were located. The upper compacted layer of a mixture of clay and gravel confined the upper aquifer, GW1_{BV}. The deeper aquifers, GW2_{BV} and GW3_{BV} were confined, too.

Well B1_{BV} was 11 m deep and in contact with aquifer GW1_{BV} at depths 5 m to 6 m and 8 m to 9 m. Well B2_{BV} was 29 m deep and in contact with GW2_{BV} through its open sections from 24 m to 25 m and from 26 m to 27 m. Open sections are highlighted by the black parts of the boreholes drawn in Fig. 3.21. At the surface, all wells were less than 1 m apart from each other. The mean hydraulic head of GW1_{BV} was at 1.6 m below surface, that of GW2_{BV} was at 2.1 m depth. GW3_{BV} had its level at 6.5 m. The levels confirm a confinement of the aquifers and shows that they were not hydraulically connected. The hydrological K_f -values in m/s, were $1 \dots 2 \cdot 10^{-4}$ (GW1_{OE}), $< 10^{-5}$ (GW2_{OE}), $< 10^{-4}$ (GW3_{OE}) (Rheinbraun, 1997, Lehmann, 2001, Hoffmann, 2002). The borehole tiltmeters were installed at 13.1 m (T1_{BV}) and at 6.1 m radial distance (T2_{BV}) from the wells. PVC-casings were erected in boreholes. The casings were coupled to the ground by filling the space between casing and borehole with cement. The tiltmeters were installed in the PVC-casings. Bottom ends of instruments were at depths 2.65 m and 3.1 m, respectively. Both tiltmeters resided within aquifer GW1_{BV}. Tab. A.2 in the appendix has an overview of the configuration data. Meteorological data, precipitation and air pressure were logged roughly 800 m apart from the site BV in western direction. Soil temperature was recorded in 0.5 m depth close to position T1_{BV}, and at surface, i. e. below the cover of the electronics box that accommodated the data logger. The electronic box was placed close to T1_{BV}.

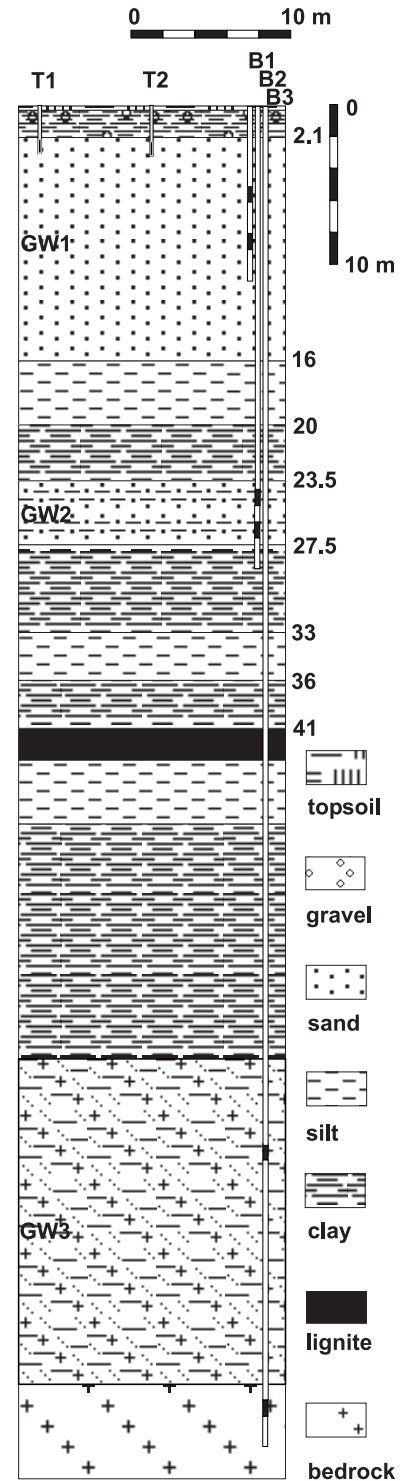


Figure 3.21: Simplified lithology, BV.

The pump tests were conducted in the upper two aquifers through wells B1_{BV} and B2_{BV}. A rate of $2.5\text{ m}^3/\text{h}$ lasting over 2 hours in each test could be achieved by a submersible pump of type Grundfos MP-1 (Grundfos, 2002). Fig.3.22 shows a photo from site BV taken during the pump tests. Another pump test was carried out in B3_{BV}, but resulted in no significant response in any of the observables. The extracted water was pumped off through a 50 m long tube in north east direction, away from the experimental site into the nearby ditch. This was to avoid artificially loading of the ground and to prevent a hydrological short-circuit. No regular pumping was done from the wells prior or after the experiments. There was no precipitation during the tests, and atmospheric pressure was mostly stable. The change of the surface temperature during the single pump cycles was minor. Over a whole day the temperature signal was cyclic. To minimize aliasing in the data, sampling of tilt and well heads was done every 2 seconds and the low-pass filter of the tiltmeters was applied. All raw data was digitally smoothed by a moving window average with a width of 40 seconds, i.e. 20 data points. Some data sets in the following show a slightly noisy signal during pumping. This was caused by the power generator used for the pump.



Figure 3.22: View at site BV in western direction over the grass verge. In foreground is the control box of the pump and the generator. In background is the outlet tube for extracted ground water.

3.2.1 Pump Test from GW1_{BV} – Elliptical Hodographs

Fig.3.23 shows four examples of near surface tilt and induced pore pressure changes recorded during the pump tests from B1_{BV}. The data is from both tiltmeters and from well B1_{BV}. The tilt data was numerically rotated from the original x-y system of the tilt sensors in a t-r system with a radial component in direction towards the respective well, compare section A.2. Each subfigure of Fig.3.23 shows from top to bottom: radial tilt, TnR_{BV}, tangential tilt, TnT_{BV}, ('n' holds for the position number) and GW1-B1_{BV}, the well head in B1_{BV}. Decreasing tilt values in TnR_{BV} account for a strike of the tiltmeter towards the well, decreasing values in TnT_{BV} for a strike perpendicular to TnR_{BV} in direction to the left hand side, i.e. towards north west.

The tilt signals from T1_{BV} and T2_{BV} were clearly correlated to the pump event and its recovery phase. Response in the radial direction towards the well was of equal amplitude as in the tangential direction. This indicates an anisotropy in the subsoil's structure. After cessation of pumping, the radial components did not fully return to their initial values. A similar behaviour has been observed in the well head of GW1_{BV}. The tangential components, especially at T1_{BV}, look like they merged in a somewhat longer lasting recovery drift. Total response at T1_{BV}, which is the more distant position, was significantly higher than at T2_{BV}. Moreover, the radial signal of T1_{BV} responded with a rapid drop at the beginning of the pumping, in opposite direction to that of T2_{BV}, what is somewhat surprising. The sharp rise in the amplitude T2R_{BV}, immediately after onset of the pumping, points to a fast transfer of the induced signal from the well screen through the subsoil to the tiltmeter. Such a sharp response can (most likely) only occur due to (poro)elastic deformation rather than through pure diffusion.

With the assumption of a homogeneous half-space, the steady state maximum at the surface for radial tilt response to pumping from B1_{BV} should occur at a radial distance of 4.95 m. In this assumption the well screens and tiltmeters are described as mathematical points and the center depth of the well screen is at 7 m. From the geometrical configuration at the surface it looks like T2_{BV} was closer to that maximum position than T1_{BV}. The larger signal excursions should have been at T2_{BV}, but the reverse was the case. The reason is probably the installation depth of T2_{BV}: Observations were made at a depth of the same order as the well's open section.

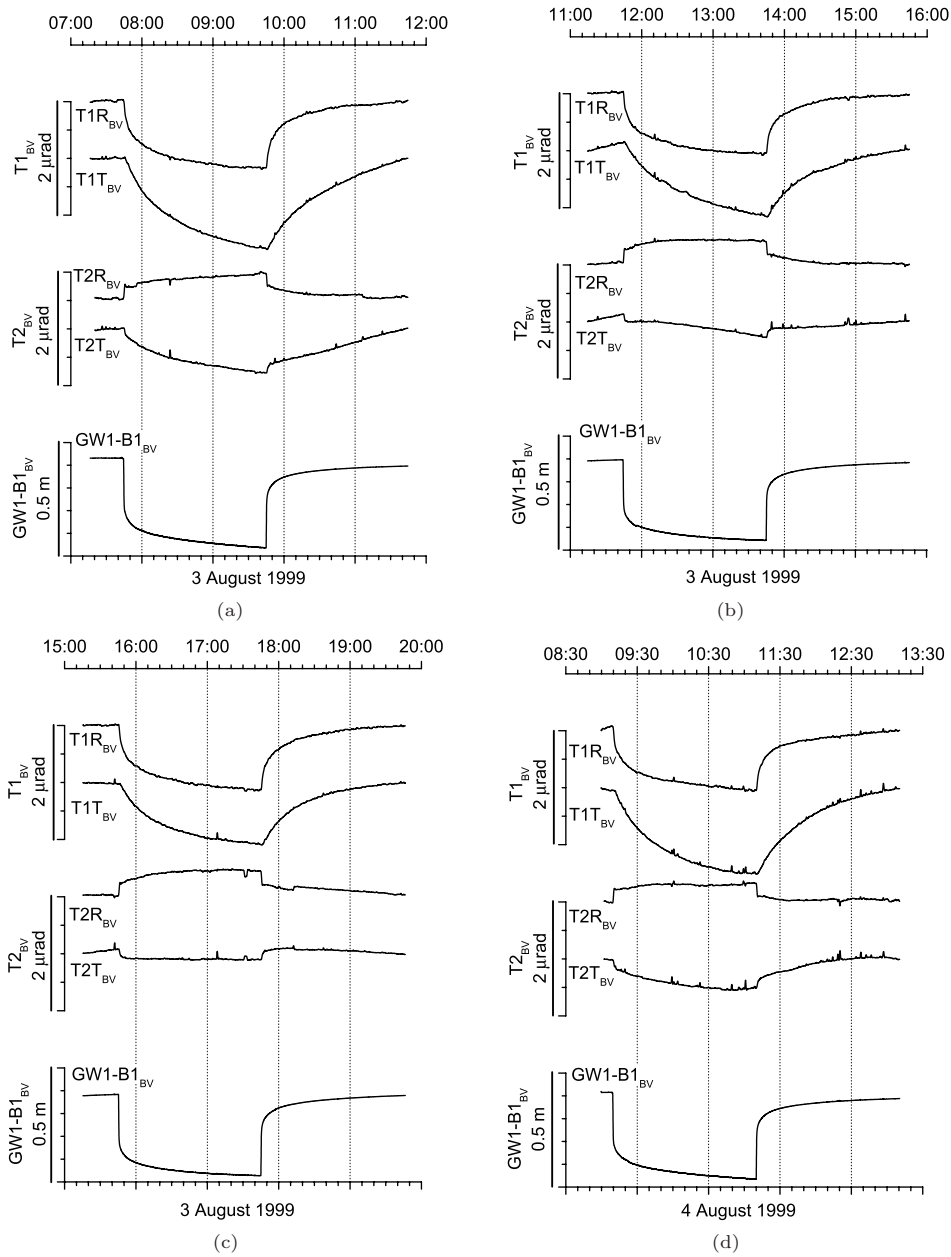


Figure 3.23: Four examples of tilt and pore pressure changes induced by pumping from $GW1_{BV}$ through $B1_{BV}$. Tilt response in the radial components TnR_{BV} was in different directions between both tiltmeters and amplitudes were larger at the more distant position $T1_{BV}$.

For an estimation, the geometry of site BV can be scaled to the half-space solution plot in Fig.2.9(a). The scaling factor is $100m/(well\ screen\ center\ depth)$, i.e. 14.29. $T2_{BV}$'s installation depth of 3.1m bottom end of instrument below surface and its radial distance of 6.1m from the well corresponds in Fig.2.9(a) with a radial distance $r = 87.1m$ and a depth of $z = 38.3m$. In Fig.2.9(a) tiltmeter $T2_{BV}$ would be in the zone of negative tilt and close to the zero-line, i.e. where tilting is of minor strength and strikes with the instruments top end towards the well. This strike direction is in contradiction to the observation. Position of $T1_{BV}$, if scaled to Fig.2.9(a), is at $r = 187m$ and $z = 32m$, where amplitudes were indeed larger than at the equivalent of position $T2_{BV}$, and with a radial strike like observed.

With respect to the above scaling to Fig.2.9(a), the different sign of tilt response between T1R_{BV} and T2R_{BV} can be explained by a more spatially extended zero-line of tilt than depicted in Fig.2.9(a). Then, T2_{BV} was not installed ‘near-surface’, but in the zone of positive tilt, compare also Fig.2.8. In the case of a homogeneous half-space, the course of the zero-line (i. e. the geometry of the solution field) depends only on the parameter ν , the drained Poisson ratio, see Eq.2.19. A value of $\nu \geq 0.35$ would be necessary to calculate a zero-line of tilt that crosses the position of the center depth of T2_{BV}, or passing it at a more shallow depth to describe (positive) radial tilt as observed at T2_{BV}. Typical values of ν for a more sandy subsoil like at site BV are smaller, see Tab.2.1.

It is obvious from the lithology log in Fig.3.21 that subsoil at site BV is not a homogeneous half-space. The subsoil can hardly be described by a single set of poroelastic parameters. It is more a stack of sedimentary layers with different properties each. The properties change more or less rapidly at the layer boundaries. Installation of T2_{BV} was in the sandy layer of GW1_{BV}, immediately below the shallow, strongly compacted mixed layer of clay and gravel. The installation was in a casing that was build in cement and thus had a good coupling even to this shallow, compacted stratum. Hence, tilt response at T2_{BV} may be described by a value of ν that is about the value of this highly compacted layer. As a result, to understand the radial part of the observed signal at T2_{BV} layering should be taken into account.

T1_{BV} is more distant from the well than T2_{BV}. The signals at T1_{BV} may be described somewhat effortlessly through a model of a homogeneous half-space. Such a model might be seen as an integral description of the subsoil. At T1_{BV} the longer spatial signal wave lengths, in a range of about several meters, may dominate. This might be a reason why influences of small scale structures in subsoil, with a spatial extension of a few meters, would be minor for the signals at T1_{BV}. The uppermost layering at site BV changes in vertical direction within a few meters. At T1_{BV} this layering might not have been influenced tilt response significantly. Lehmann (2001) discussed earlier pump tests from this site with tilt observations at the position of T1_{BV} only and a pump test in B1_{BV}. He estimated a Poisson ratio of about 0.1 varying in the range between 0.08 and 0.12. His analyses based on steady state solutions for a homogeneous poroelastic half-space and his value of ν accounts for a mainly sandy subsoil, in mean. His ν -value may reflect the subsoil properties of the tapped first aquifer at site BV, which takes up most of the soil volume between the well screen of B1_{BV} and T1_{BV}.

Moreover, the strong tangential parts in the tilt responses point to an inhomogeneous subsoil. Hence, only a 3-D description will fit the complete observation. This becomes more apparent from the hodographs in Fig.3.24, plotted from the data in Fig.3.23. In the first moment after onset of the pumping, the overall strike of both tiltmeters was aligned roughly parallel, but with an opposite sign, i. e. T1_{BV} struck towards north east and T2_{BV} towards south west. Thus, strike orientation was in a line running from south west to north east, grossly in the direction from the tiltmeters towards the well. The time series in Fig.3.23 also showed a somewhat stronger initial response in the radial components. A few moments later the courses of the individual hodographs turned in different directions: the course of T1_{BV} towards north north east, that of T2_{BV} to north west. Only in Fig.3.24(c) the course of T2_{BV} is somewhat different caused most likely by a disturbance in the initial signal part. Generally, in a poroelastic description, tilt, e. g. presented by hodographs, is aligned with the strain and parallel to the pore pressure gradient. The latter points in the direction of fluid flow. Therefore, the hodographs seem to suggest the direction of ground water current. From Fig.3.24, it could be assumed that in overall, ground water streamed more in northern direction than straight towards the well. Similar tilt observations were reported by K umpel (1989) from a site in northern Germany. From a DC ground-resistivity study he found evidence for a channel like fluid flow to the pumped well. However, the truth is not yet known.

Furthermore, the hodographs in Fig.3.24 show that the tilt response to the pumping and the recovery phase followed some elliptical path. Irrespective of the orientation of the ellipse, such a course of the signal is not expected from a homogeneous poroelastic medium. The hodographs may be the result of at least two processes following each other and causing tilt in different spatial directions. Fig.3.25

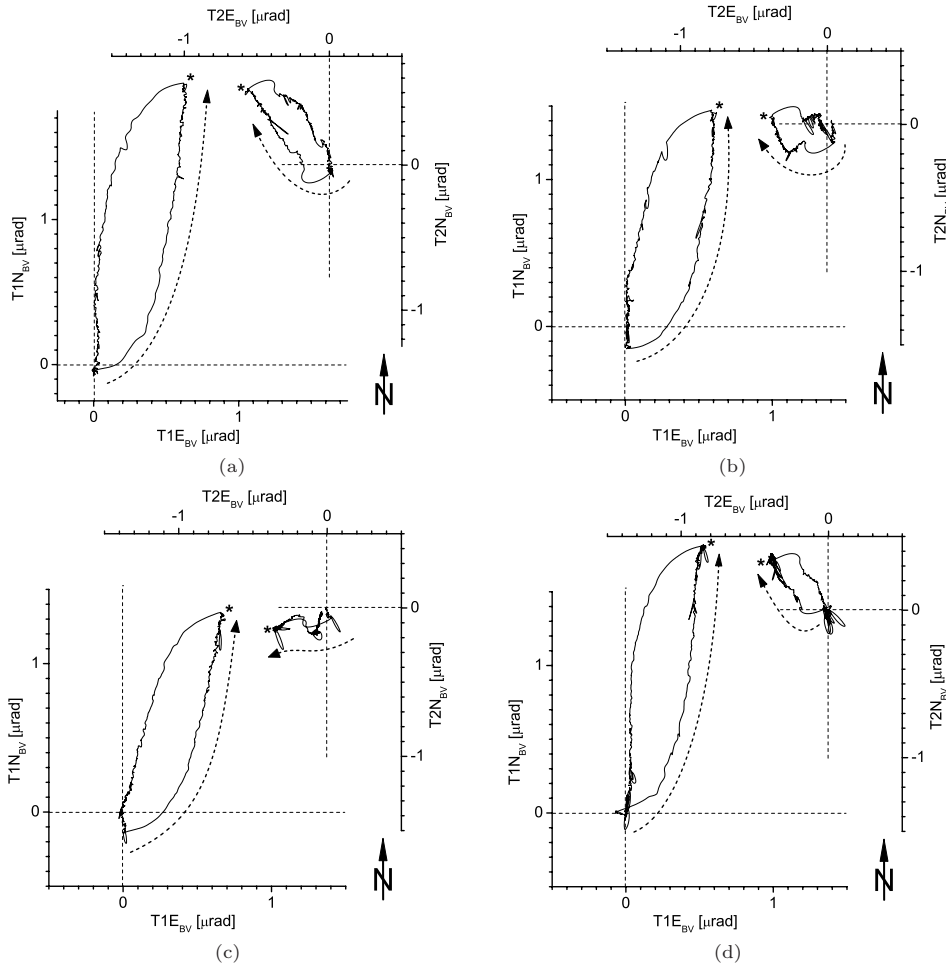


Figure 3.24: Hodographs drawn from the data of Fig.3.23. Starting point is the point of intersection of the straight dashed lines. The dashed arrows depict the overall excursion and the asterisks cessation time of pumping.

presents a sketch. The first process could be a fast (poro)elastic response to the rapid withdrawal of ground water right after onset of the pumping. The second process is induced tilt by a slowly changing pore pressure gradient. The latter process is a result of the fluid diffusion due to ongoing withdrawal. If the pump stops, again a fast (poro)elastic response occurs first, but in its opposite manner. Thereafter, a slow diffusion process, also opposite, occurs due to the regeneration of the pore pressure disturbance. A similar observation of elliptic like hodographs have reported [Weise et al. \(1999\)](#).

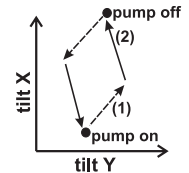


Figure 3.25: Sketch: processes (1), (2) cause tilt in different directions.

3.2.2 Pump Test from GW2_{BV} – Negative Tilt Reversals and Noordbergum Effect

Fig.3.26 shows data from four one-cycle pump tests conducted in B2_{BV}. The tilt data was transformed into a t-r system like in the foregoing case. The rate of withdrawal and the duration were the same as with the test in B1_{BV}. Here, the well level disturbance caused through the pumping was about 19 m in aquifer GW2_{BV}. During the previous test in B1_{BV} it was only 0.35 m in GW1_{BV}. Both tiltmeters responded to the pumping with nearly equal strength. The ratio between the radial and the tangential response was more in favour of the radial ones. The strong well level reduction (pore pressure disturbance) may explain why the tilt response was larger than in the previous case. Particularly for T2_{BV}, response was stronger, although the locations of the open sections of B2_{BV} are considerably deeper than in B1_{BV}.

The overall tilt amplitudes are clearly smaller in Fig.3.26(a),(b) than in (c),(d) for equal withdrawal from B2_{BV}. This possibly indicates some (non-linear) alterations in the subsoil from cycle to cycle, caused by the large pore pressure disturbance.

Like in the previous case, the geometry of the pump test can be translated to the general Fig.2.9(a), with the assumption of a homogeneous half-space in steady state. The scaling factor for the distances is 3.92, $100\text{ m}/(\text{well screen center depth})$. Scaled to Fig.2.9(a), T1_{BV} would be at $r = 51.4\text{ m}$ and $z = 8.74\text{ m}$ and T2_{BV} at $r = 23.9\text{ m}$ and $z = 10.5\text{ m}$. Hence, from this point of view, tiltmeters were actually installed ‘near surface’. This is due to the much deeper well screen of B2_{BV}. Both tiltmeter positions were above the zero-line of tilt. In fact, both instruments recorded negative tilt in response to pumping. However, in a homogeneous half-space like in Fig.2.9(a), the steady state amplitude in T1R_{BV} should be by two thirds larger than in T2R_{BV}. This was not the case. Possibly, steady state was not achieved in Fig.3.26, or the special amplitude ratio between T1R_{BV} and T2R_{BV} was caused by an influence of the layering.

In the amplitudes of both components of both tiltmeters was a jump at the start and the stop of the pumping. This is somewhat similar to the response of the tiltmeter at T2_{BV} in the foregoing pump test. Here at T1_{BV}, the signals rapidly approached about 40% to 80% of their final value. Then they grew slowly until the pump stopped. During the recovery phase the signals took a similar course with opposite sign.

Furthermore, the radial component of the signal T2R_{BV} attained a maximum excursion towards the well (a minimum value) shortly after initiation of pumping. Thereafter, a reversal in its course appeared. This is in Figs.3.26(a), (b), (c). This type of signal, a negative tilt reversal, was already reported from site OE, even without such a rapid response at the beginning of the pumping like here. There, the signal type was repeatedly observed several times at the position T1_{OE}, see Fig.3.7.

In all sub-figures of Fig.3.26 the recovery process can be seen after the cessation of the pump. The signal of T2R_{BV} did not return on the direct route to its neutral position (like the signal of T1_{BV}). It almost jumped to its maximum excursion away from the well, in opposite direction, from where it slowly approached the initial tilt value.

Simultaneously to the tilt jumps and reversals in Figs.3.26(b), (c), (d) a faint, but clearly significant reaction to the strong and rapid level disturbance in GW2_{BV} is seen in the recordings of the hydraulic head of GW1_{BV}. For these measurements, a pressure transducer with a level resolution of better than 0.1 mm was used (Fabian, 1998). The observations show an initial rise of the hydraulic head in GW1_{BV} in response to pumping in B2_{BV} before the level starts falling. The reverse effect, a drop in the hydraulic head followed by a rise occurs after the pump stopped. In hydrogeology, this reverse well level phenomenon is usually called ‘Noordbergum effect’. The effect was first reported from a site close to the small town Noordbergum in the Netherlands (Verruijt, 1969). It has repeatedly been reported as an initial rise of pore pressure in an aquifer that is different from the one that is being pumped (Rodriguez, 1983, Langguth & Treskatis, 1989, Maruyama, 1994, Karasaki et al., 2000, Wang, 2000, Vasco et al., 2001). Adopting linear poroelasticity, Gambolati (1974), Maruyama (1994), Kim & Parizek (1997) and Wang & Kümpel (2003) have presented computational schemes to simulate this phenomenon. In Fig.3.26(a), (b) a similar signal excursion like the Noordbergum effect is in GW2_{BV} at the end of the pumping. This is an artifact that occurred by chance (caused by some backwater in the vertical part of the outlet tube of the pump).

The jumps and reversals of the tilt signals in response to pumping in B2_{BV} look like a matrix reaction that is the counterpart to the Noordbergum effect in pore pressure. This view is supported by the observation of the reverse well level change in aquifer GW1_{BV}. Except in Fig.3.26(a) where the Noordbergum effect did not appear, even if the jumps and reversals in tilt occur. However, the Noordbergum effect in the well level in B1_{BV} is assumed to be related to a transient volumetric compaction in the aquifer GW1_{BV}. This compaction was caused by the rapid withdrawal from the deeper aquifer GW2_{BV} through B2_{BV}. Rapid onset of pumping led, due to strong poroelastic coupling, to a matrix deformation close to the open section of well B2_{BV}. This induced matrix deformation signal propagated rapidly, with a velocity in the speed range of elastic waves. It spread out much faster than the likewise generated signal of diffusion that is related to the fluid deficit and flow. Because of different velocities of deformation and diffusion

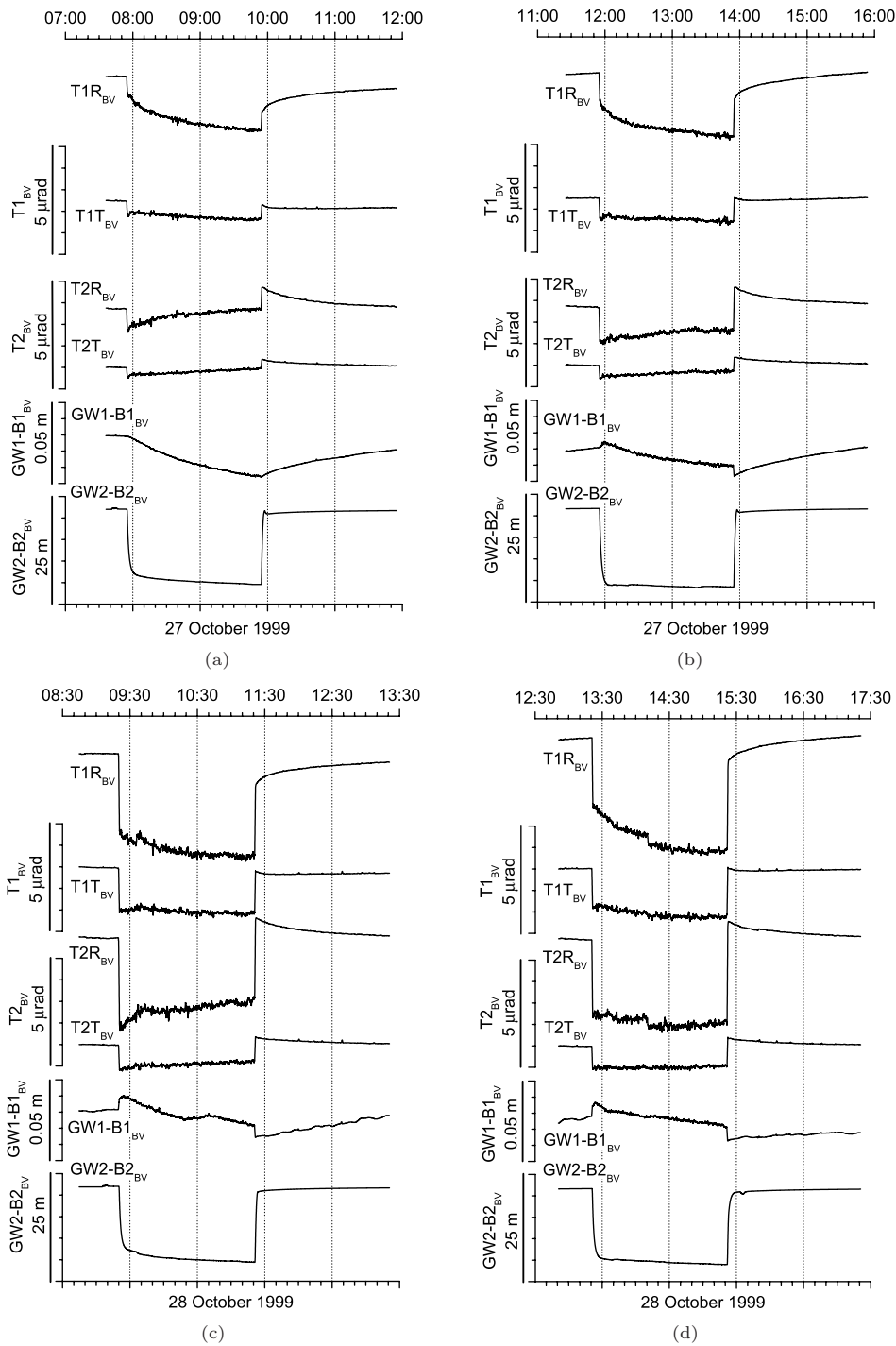


Figure 3.26: Four examples of tilt and pore pressure changes induced by pumping from GW2_{BV} through B2_{BV}. Especially the radial components T2R_{BV} show jumps and transient negative tilt reversals in their course. The Noordbergum effect occurred in GW1-B1_{BV},(b),(c),(d) contemporaneously to the tilt jumps and reversals.

signals, together with the poroelastic coupling of both, travel-time-effects and thereafter a balancing in fluid-matrix interaction appeared. At some distance from the well screen, especially close to the surface, after onset of pumping the pore fluid was still not streaming while the matrix started to move. This deformation led to a subsidence at surface, too. Somewhat deeper it caused a compaction of the subsoil, as reflected in the jumps of the tilt signals in Fig.3.26.

Appearance of the Noordbergum effect depends at least on two factors: first on the strength and the speed of the transient volumetric compaction and second on the perviousness of subsoil. If the perviousness is too high and the compaction too small, the local diffusion rapidly equals pore pressure differences. A significant rise in pore pressure can not appear. However, even a somewhat weaker volumetric compaction should be observable as a matrix movement without occurrence of a reverse well level response. The tiltmeters are able to detect ground matrix displacements in the sub-micrometer range. Therefore, it is assumed that they can measure a tilt component of the transient volumetric compaction movement. In Fig.3.26 this tilt component caused the sharp jump in the tilt signals towards the well. These jumps appeared in all tilt components, whereas in Fig.3.26(a) the Noordbergum effect did not occur. In this sub-figure, tilt response and the jump was at least two times weaker than in the other sub-figures. It might be speculated, why the response was so small. As stated above, it can be the reason of some remanent changes in aquifer GW2_{BV} caused by the large pore pressure disturbance. The fact that the tilt responses grow from cycle to cycle also points to this assumption. The pump tests depicted in Fig.3.26(a), (b) and (c), (d) follow each other at two consecutive days. If the signals would be pasted together one after another, a mean negative tilt response extending over all diagrams with growing strength results. This averaged behaviour looks somewhat similar to a single longer lasting pump test. However, in the pump cycle of Fig.3.26(a), the transient volumetric compaction seemed to be not sufficient to significantly generate the Noordbergum effect. The effect was possibly canceled out by diffusion.

At T2_{BV} the initial volumetric compaction of GW1_{BV}, indicated by the tilt jump, partly (in Fig.3.26(a) completely) recedes after the negative reversal, i. e. during ongoing withdrawal. This receding at T2_{BV} could correspond to a volumetric extension of GW1_{BV}. At T1_{BV}, indicated by the not reverting tilt signal, processes might have been different, because the compaction seems to go on after the initial jump. However, tilt consists of two parts, shearing and rotation. Therefore, the equivalence between tilt and volume strain is not exact even at observation points slightly apart the surface. Only if tilt is measured immediately at surface, a subsidence observed as a tilt response can be related to a volumetric compaction. Nevertheless, the observed signal behaviour at T2_{BV} can point to a volumetric extension of GW1_{BV} that followed the Noordbergum effect.

The positive tilt reversals recorded at site OE, remember e. g. the observations at position T8_{OE} and T9_{OE} in Fig.3.18, can be compared with the negative ones observed here. The positive reversals show first a faint and fast transient excursion to the opposite direction than the negative ones. Then, the typical smooth strike towards the well follows. The positive reversals may suggest a slight uplift of the surface, which precedes the common response, or, as tiltmeters are not exactly at the surface, a transient exchanging process between shearing and rotation movement. More generally, again, a balancing process between local deformation and local diffusion close to the surface can be responsible, too. A local induced rise in pore pressure in somewhat less shallow parts below surface could lead to a feedback reaction, i. e. to a volumetric expansion in response to the Noordbergum effect. However, at site OE the upper part of the subsoil was not saturated. An induced pore pressure rise with a succeeding feedback of the soil matrix seems hardly possible under this condition. The detailed physical motion process of the matrix remains indistinct, but some of the assumptions here will be supported by the model calculations in chapter 4.

The tilt hodographs of the data sets from Fig.3.26 were plotted in Fig.3.27. The ones of tiltmeter T2_{BV} confirm that these signals have an inversion point. The signals of T1_{BV} did not show that behaviour. As mentioned before, the amplitudes in the first two pump cycles were smaller than in the other. Despite these differences between the hodographs, they also show similar features, especially in Fig.3.27(c),(d). Again, elliptical patterns were observed.

A comparison with the hodographs from the first pump test in Fig.3.24 shows that here, overall response in both tiltmeters was better aligned in one direction, to north east, but likewise not directly towards the well. Again, the mostly parallel strike in tilt suggests a preferred orientation of induced pore pressure gradients and therefore of fluid flow in the second aquifer.

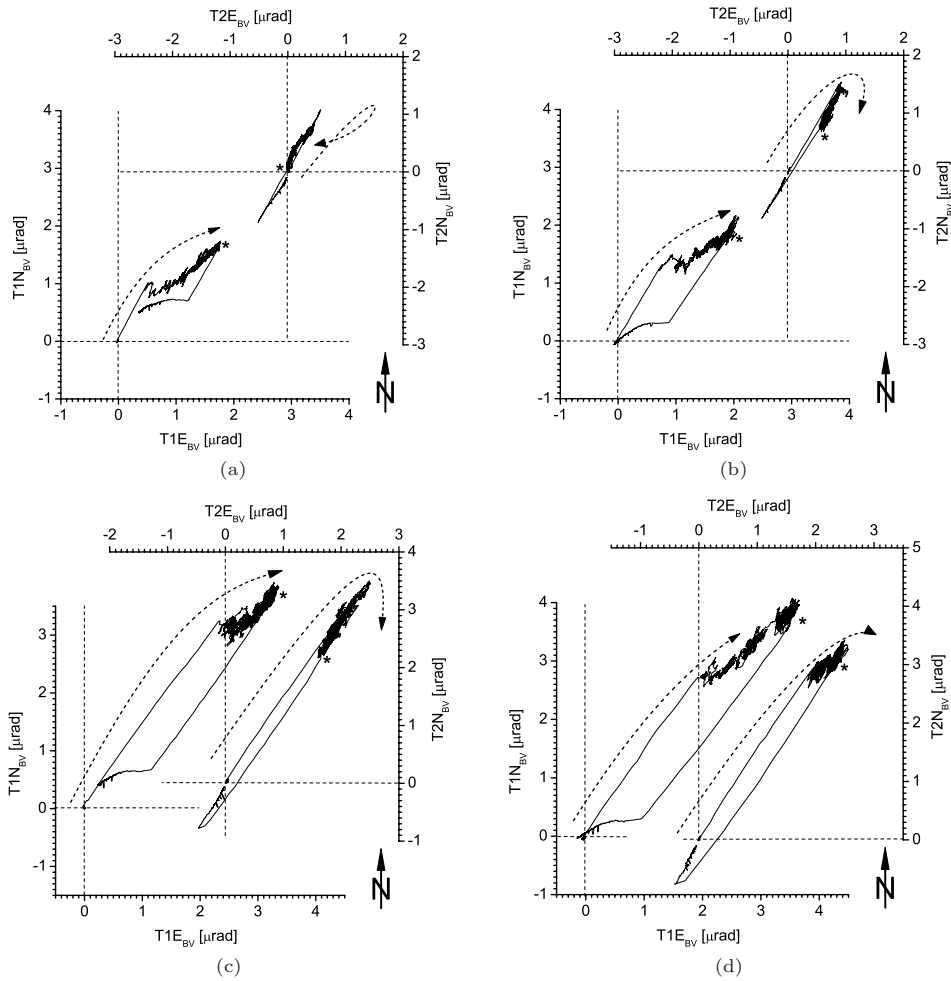


Figure 3.27: Hodographs drawn from the data of Fig.3.26. Starting point is the point of intersection of the straight dashed lines. The dashed arrows depict the overall excursion and the asterisks cessation of pumping.

3.3 Wulsdorf, WD

Site WD was in a district of the city of Bremerhaven, north of Bremen in northern Germany, see Fig.3.1. The experiments were conducted in spring 1999. They were different from the previous ones. At this site the subsoil is not layered. It is highly heterogeneous on a larger spatial scale of some tens of meters. The subsoil structure is dominated by a buried quaternary channel embedded in tertiary sediments. The channel crosses the site and is more than 150 m deep. Like in the foregoing cases the area is flat. Fig.3.28 presents an overview of the site with the locations of tiltmeters $T1_{WD}$, $T2_{WD}$, production wells $B1_{WD}$ and $B2_{WD}$, deep observation wells $P1D_{WD}$, $P2D_{WD}$ and shallow observation well $P2S_{WD}$. The dashed-dotted contour lines in Fig.3.28 mark the depth to the basement of the buried quaternary channel. At the western border of the site passes a freeway built on an embankment straight in south north direction. The observation points were close to the boundary of a deciduous forest growing at the site. The forest covers the central part of the location. In Fig.3.29 is a photo with a view in western direction along the asphalt track of Fig.3.28. The site is bordered by grass land with single bushes and is situated in marsh land. Shallow ditches drain the area. The produced water from the pump test was guided through an outlet tube in the creek at the southern part of the site.

The geological profile extending from A to B is depicted in Fig.3.30. At a depth grossly between 10 m to 30 m is a low permeable layer of Lauenburger silt with a thickness of up to 20 m. The Lauenburger silt

dies out in north north west and south south east direction. A layer of clay with a thickness of roughly 8 m partly overlays this stratum. Both the layers separate the sandy fill of the channel bed in two aquifers, $GW1_{WD}$ and $GW2_{WD}$.

Both borehole tiltmeters $T1_{WD}$ and $T2_{WD}$ were installed on a profile extending radially with respect to $B1_{WD}$, at distances 70 m and 140 m from this well. The bottom ends of the instruments were 2 m below surface. The water table of the upper, free aquifer, $GW1_{WD}$, was at roughly 1 m depth and the mean hydraulic head of $GW2_{WD}$ was at 1.3 m below surface. Pressure transducers were installed in the two deep observation wells with contact to $GW2_{WD}$, $P1D_{WD}$ and $P2D_{WD}$; likewise in the shallow observation well, probably in contact to $GW1_{WD}$, $P2S_{WD}$. Depths of the open sections of these three wells were 34 m to 39 m for $P1D_{WD}$, 48.6 m to 50.6 m for $P2D_{WD}$, and 22.6 m to 24.6 m for $P2S_{WD}$.

The two production wells, $B1_{WD}$ and $B2_{WD}$, were used simultaneously. The depths of the wells' open sections were 81.5 m to 107.5 m for $B1_{WD}$ and 92.5 m to 106.5 m for $B2_{WD}$. Both wells were in contact with the lower aquifer, $GW2_{WD}$. Ground water was pumped off at rates of $200\text{ m}^3/\text{h}$ in $B1_{WD}$ and $150\text{ m}^3/\text{h}$ in $B2_{WD}$. The pump test was conducted in a single run with a duration of 6 days. The well level was recorded in $B1_{WD}$, too, but it dropped out of the range of the pressure transducer during the first day. The maximum decrease in the well head of $B1_{WD}$ has been estimated to be roughly 8 m.

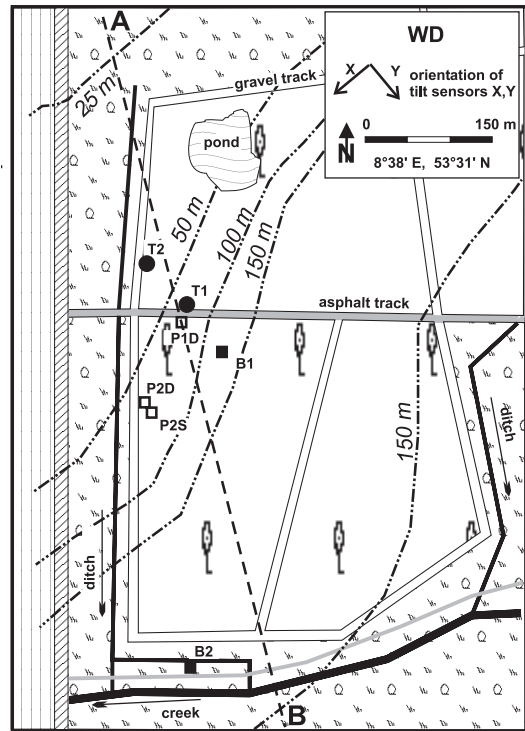


Figure 3.28: Map of test site WD with observation points, course of the quaternary channel and geological profile line.



Figure 3.29: Photo from site WD with a view in western direction along the asphalt track. At the left is the outlet tube of the pump in $B1_{WD}$. $T1_{WD}$ is right beside the car that was later used for a loading test. In background is a bridge of the freeway.

Except for one hour of pumping in the week before the experiment, no pump activity was in the two preceding nor in the three successive weeks of the main pump test. Tab.A.3 in the appendix summarizes the geometrical configuration and production rates of the main pump test. The car shown in Fig.3.29 (weight 2.7 tons) was used for a loading test prior to the main test. It was slowly driven along the asphalt track next to $T1_{WD}$ and produced a distinct tilt anomaly at this tilt-meter position. The test confirmed coupling of $T1_{WD}$ to the ground.

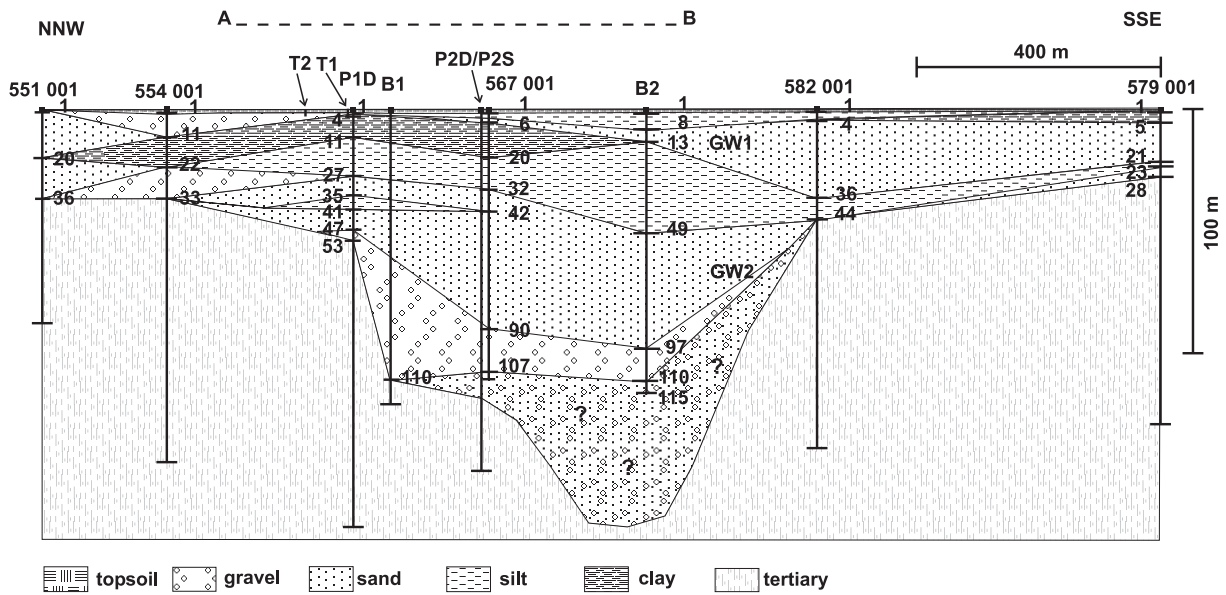


Figure 3.30: Simplified geological section crossing the quaternary channel along the line A–B in Fig.3.28. The profile is drawn by a linear interpolation between the lithology logs of the depicted boreholes. Data from further boreholes indicated by the six-figured numbers and not shown in Fig.3.28 were used. P2D and P2S are at close positions, so that they are depicted by the same log line. Vertical exaggeration is fourfold. Numbers beside the borehole lines indicate known depths of layer boundaries in *m*. The logs were kindly offered by Fritz (1998, 2001).

Data from both tiltmeters, their temperatures, soil temperatures at the position of tiltmeter $T2_{WD}$, well level data from the observation wells and changes in atmospheric pressure are plotted in Fig.3.31. From top to bottom Fig.3.31 shows: Tilt data from the X- and Y-components of tiltmeters $T2_{WD}$ and $T1_{WD}$, respectively, instrument temperatures $T-T1_{WD}$, $T-T2_{WD}$, soil temperatures $ST05_{WD}$ at 0.5 *m* depth and SUT_{WD} at surface, and well level changes in the upper part of the subsoil ($GW1_{WD}$) from shallow observation well $P2S_{WD}$, the changes in the hydraulic head of aquifer $GW2_{WD}$ in the deep wells $P1D_{WD}$, $P2D_{WD}$ and $B1_{WD}$, and the variation in local atmospheric pressure, AP_{WD} . There was no rainfall during the pump test and only minor precipitation in the succeeding weeks.

The strong tilt excursion of $T1_{WD}$ correlating with the well level drop that was caused by pumping in $B1_{WD}$ (and $B2_{WD}$) is the most obvious feature in the data. After termination of withdrawal, the hydraulic heads in the aquifers $GW1_{WD}$ and $GW2_{WD}$ recovered, but the tilt signal did not return to its original value. Its recovery was about 40 % of its pump induced total tilt response. A response of tiltmeter $T2_{WD}$ to the pump test is not evident from the data. Other tilt fluctuations were diurnal variations measured by both instruments $T1_{WD}$ and $T2_{WD}$. These fluctuations correlated with surface temperature SUT_{WD} and could be caused by thermo-elastic deformation from surface heating during day time (Berger, 1975), or may result from indirect effects such as ground deformation caused by water-consumption of nearby trees (Rebscher, 1996).

The hodographs in Fig.3.32 offer a better overview of the general direction of strike. Integrated in Fig.3.32 is a map of the locations of the tiltmeter positions, of well $B1_{WD}$, direction to well $B2_{WD}$ and three contour lines that indicate bottom depth of the buried quaternary channel. The open circles mark initial positions of tilt sensors as well as geometrical positions of $T1_{WD}$ and $T2_{WD}$. The dashed arrows indicate the overall course of the hodographs. The end of the pumping is noted by asterisks. The spatial scale is depicted at lower right.

From Fig.3.32 is obvious that the pump induced tilt of $T1_{WD}$ stroke mostly in parallel orientation to the course of the channel. Surprisingly, the strike was with the top of the tiltmeter away from the locations of the wells. At $T2_{WD}$, the main direction of the tilt signal appears to be slightly perpendicular to the course of the channel. Here, the signal reverses during the pumping and some doubts remain of its significance with respect to the pump test. More likely $T2_{WD}$ was not influenced by the pumping.

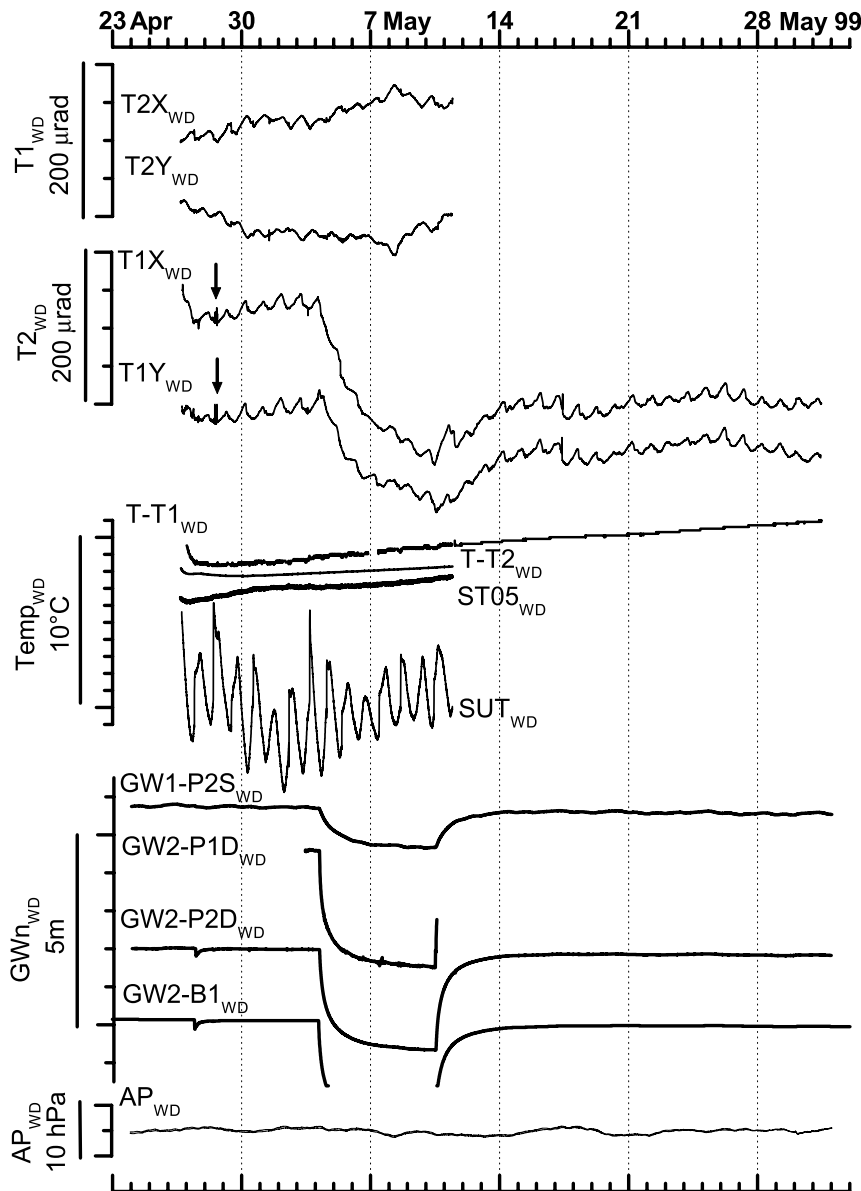


Figure 3.31: Time series from the one-cycle pump test at site WD. The pump test started at 4:15 a.m. on May 4th 1999, in wells B1_{WD} and B2_{WD} and lasted till 4:10 a.m. on May 10th 1999. The drop in hydraulic head during pumping in well GW2-B1_{WD} was probably around 8 m and exceeded the range of the pressure transducer. The arrows above signals T1X_{WD} and T1Y_{WD} mark the time of a loading test through a car next to the tiltmeter. The load resulted in clear tilt steps in both components. The tilt steps in T1_{WD} that occurred on May 17th, 1999, could be from a similar loading of agricultural traffic. Diurnal fluctuations in the tilt signals probably reflect surface temperature changes.

fluid flow could be assumed to be minor. Thus, pore pressure gradients near T2_{WD} might have been weak and not caused any significant movements of subsoil here, explaining the lack of a clear pump induced tilt signal at T2_{WD}. The sign of strike, especially at T1_{WD}, is hard to explain. It might be due to local heterogeneities (Fabian et al., 2000). Or it is due to stronger shear components in tilt than rotational ones, possibly caused by the more shallow heterogeneous fill of the channel.

If a homogeneous half-space is used as a reference for the observed tilt data, the hodographs may indicate presence of a major heterogeneity in the subsurface. Strike direction and amplitude of tilt at both tiltmeter positions is not in agreement with the signals that were expected in a homogeneous half-space. The heterogeneity which causes the tilt signals to deviate from the homogeneous half-space situation could be the quaternary channel and its uppermost massive and heterogeneous fill of clay and sand.

Most of the channel's deeper fill can be assumed to be more permeable than its tertiary surroundings. Pump induced pore pressure gradients will spread out with different strength in north east direction, i.e. parallel to the course of the quaternary channel, than in north west direction. These gradients cause a local strain field that depends on the poroelastic soil parameters in the channel and its surroundings. T1_{WD} was right above the channels steep north west flank and therefore should respond strongly to the pumping. Somewhat beside the channels boundaries, near T2_{WD},

The catchment volume for ground water extraction, i. e. the effective reservoir volume tapped by the wells, is assumed to be constrained by the channel's geometrical extension. In contrast to a homogeneous and even a layered half-space, the available volume in the subsoil that can be used for production, is limited to one spatial dimension. With the same production rate, compared to a homogeneous or layered half space, the loss in fluid per unit volume is much higher. This 'channeling' should lead to larger pore pressure gradients. Therefore, stronger pump induced tilt amplitudes may occur in the channel or close to its boundary. If the tilt response at site OE is compared with the one here, tilt signals induced at OE are about hundred times smaller than those at WD, although the total yield rates are comparable. The catchment volume of the production wells at OE may be much more widespread than at WD. Moreover, the short durations of the pump cycles of one or a few hours at OE are in contrast to the nearly 144 hours of pumping at WD. The induced pore pressure gradients thus could be stronger at site WD and the produced fluid volume much larger. Absence of the full recovery of the pump induced tilt in $T1_{WD}$ could indicate that pumping has caused some persistent consolidation of the matrix. Therefore, the net-deformation in the inner part of the channel may be much larger, i. e. non-linear, than the mean deformation nearby the wells at OE. At the latter site, the pump induced tilt signals seem to fully recover after cessation of each of the pumps.

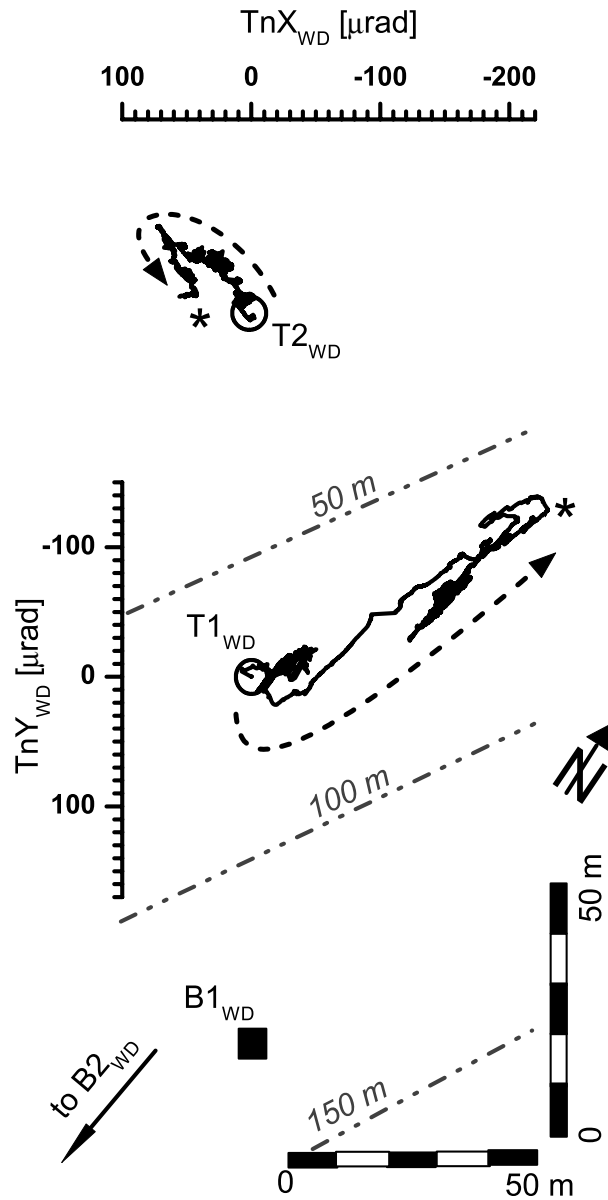


Figure 3.32: Tilt hodographs, pump test WD.

Chapter 4

Poroelectric Forward Modelling

This chapter deals with 1-D poroelectric forward modelling in multi-layered half-spaces. It provides the interpretation bases for the most important features of the observed (radial) tilt and pore pressure signals. The signal features, which are addressed by the modelling are: absolute range of tilt and pore pressure changes in response to pumping, the strike direction of tilt, towards or away from the production well, the transient signal part, and dependency from the radial and vertical distance from the well screen, i. e. the shape of the isoline pattern.

The solutions for tilt and pore pressure changes were calculated for a vertical cross section that is axially symmetric with respect to the production well. Thus, the models account for the radial part of vertical tilt and pore pressure changes that are induced by pumping. The subsoil is described by a stack of sedimentary layers with individual values of poroelectric parameters for each stratum. The model calculations were carried out with the semi-analytic program POEL for the steady state situation and for the evolution over time.

In reality, most parts of a subsoil are unknown. Variation of poroelectric parameters can be quite large. Depth, thickness and number of layers are only grossly known, if at all. This leads to a nearly incalculable amount of possible model scenarios. The broad range of model variations was reduced to simplified geological subsoil models that were constructed on the basis of the lithology of the production and observation wells. Selected examples of models will be presented. The choice of the models was tried to be representative especially for a sedimentary subsoil like at the two experimental sites, OE and BV. However, since depths and layer thicknesses are quite different between both sites, a quantitative scaling of the models could not be achieved. Direct applicability to observations remains qualitative and is concentrated on the description of the type of observations. The models will usually not fit the measurements. They serve as a first approach to a more detailed understanding of the underlying processes.

At first the preconditions of modelling are discussed. In the following, different steady state cases are taken into account. These models deal with three, four, five and six layers of sediments. It is tried to give an insight into stationary tilt and pore pressure distribution, if the number of layers grows. An analogy to the channeling effect in spatially restricted aquifers, see geology of site WD in Fig.3.30, will be shown. For the 6-layer case, different poroelectric parameter combinations, i. e. sets of different types of sediment layers, are considered. Further dynamic models deal with the time development of tilt and pore pressure. These investigations treat transient signals, i. e. signals occurring in a time span from shortly after onset of pumping until the steady state. The transient signals showing reversals are attributed to here called ‘balancing processes’ in subsoil occurring due to coupled diffusion and deformation in the poroelectric medium. Dynamic modelling will be done for the homogeneous half-space, a three-, a four- and an adjusted 6-layer model. Tilt reversals and their occurrences in homogeneous and layered half-spaces will be addressed as well as the Noordbergum effect.

4.1 Preconditions of Modelling

It is assumed that the subsoil can be described by a multi-layered fully saturated half-space with strata of unconsolidated sediments. The sediments are characterized by their name, which corresponds directly to a set of poroelastic parameters after Tab.2.3. Additionally, a short name for each layer material that will be obvious from the context, is used to describe the strata. Boundary conditions are a stress free surface, where pore pressure vanishes, a central axis at the position of the well (rotational symmetry), and infinitely extended boundaries in radial direction and downwards. The input or source signal at the well screen is described by a Heaviside function that accounts for activity (on, off) of the pump, Eq.2.17. The well's screen is described by a line sink. For all models the well's screen is assumed to extend vertically from depth $z = 90\text{ m}$ to $z = 110\text{ m}$ below surface and has a radius of 0.2 m . The extraction rate is $100\text{ m}^3/h$. The spatial dimensions of all models are given in meters. With these conditions the program POEL computes the steady state and time dependent response/output signal (the time series). Fig.4.1 shows the positions at which POEL calculated the poroelastic response. The output signal of radial vertical tilt $\Delta\gamma_r$ corresponds directly to the radial component of observed tilt values $\Delta\gamma$, the output signal of pore pressure, p , corresponds to the observable Δp , compare Fig.2.1. Tab.4.1 has the coordinates and geometry of the grid of calculation points, of the layers and the well screen. For a comparison of the solutions from POEL and the analytical solutions in a homogeneous half-space see section A.6.1 in the appendix.

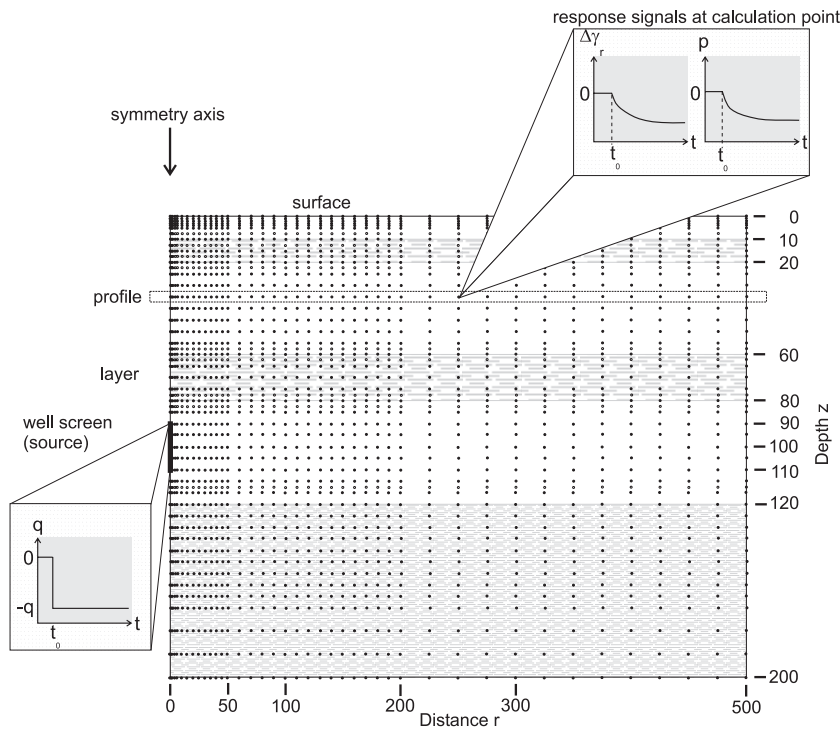


Figure 4.1: Grid of the calculation points for poroelastic response determined with POEL. Since the signal distribution of tilt strongly varies near surface, and that of pore pressure near the well, grid density is enhanced there. Also, grid density at layer boundaries (if present) is somewhat higher. At each grid point, POEL calculates a complete time series for tilt $\Delta\gamma_r$ and pore pressure response p with its beginning at onset of the pump. q_0 is a constant extraction rate with which the well is operated since time t_0 . By arranging all values for a selected time during build-up of the response signal a snapshot of the field development can be obtained. It is also possible, to directly calculate steady state values for infinite pumping. Distances are in m .

The data from modelling are arranged in a matrix representing a collection of time series, one time series at each of the calculation points of Fig.4.1. The results at a special time contemporaneously at all calculation points, are presented in a contour diagram that is a time slice of the build-up of the tilt and pore pressure distribution. Additionally, the complete time series of tilt and pore pressure calculated at any special position is zoomed out from the contour diagram to directly compare it with measured data.

The gridding process that is necessary to obtain contour plots will be taken into somewhat closer consideration. Gridding interpolates between the known values, calculates contour lines (isolines) and provides a grey scale value for every point. The interpolation was done with 2-D splines. These splines were attenuated by a factor depending on their

own, direction dependent correlation length over adjacent data points (Press et al., 1988, Microcal Software, Inc., 1999). In principle, the problem is the same as for printing a time series, where the single data points are interconnected by straight lines or by distinct curves. A smooth course and controlled

behaviour of the signal between known values is suggested, but is not necessarily real. The type of interpolation determines the signal character between data points. It is possible that, e.g. in a cubic interpolation, a local maximum occurs, where actually no data was measured and no maximum is present. In contour plots, such an interpolation can lead to small loops, bends and fluctuations of the contour pattern with a spatial wavelength in the range of the displacement of data points. Such artificial data will appear frequently in the following sections. Due to a limited density of calculation points and limited settings in the drawing software Origin (Microcal Software, Inc., 1999), a complete reduction of these effects was not possible. If the data shows strong gradients between adjacent calculation points, the errors of that contour gridding are smaller and are determined mostly by the distance between data points. This will be the case for the steady state diagrams for tilt. However, if gradients in data are small, the gridding procedure experiences more problems and errors are larger. Amplitudes ranging in some region in the diagram over several orders also cause inaccurate contour lines in other regions of the plot, where amplitudes get small and remain small. This will occur in the steady state pore pressure contour plots in the region close to surface. Furthermore, these problems will occur preferably in the very first time-slice plots showing solutions straight after onset of pumping while signal build-up is still small. To solve this plotting problem the complete time series will be extracted, ‘zoomed-out’, for selected calculation points, if necessary.

distance, radial profile (42 pts.)	0, 1, 2, <u>4</u> , <u>5</u> , <u>6</u> , <u>8</u> , 10, 15, 20, 25, 30, 35, 40, 45, 50, 60, 70, 80, 90, 100, 110, <i>115</i> , 120, 130, <i>135</i> , 140, 150, <i>155</i> , <u>160</u> , 170, 180, 190, 200, 225, 250, 275, 300, 325, 350, 375, 400, 425, 450, 475, 500
profile depth, 40(to 49) steps	0, 1, 2, 3, 4, 5, <i>7.5</i> , 10, <i>12.5</i> , 15, <i>17.5</i> , 20, <i>22.5</i> , 25, 30, 35, 40, 45, 50, 55, <i>57.5</i> , 60, <i>62.5</i> , 65, 70, 75, <i>77.5</i> , 80, <i>82.5</i> , 85, 90, 95, 100, 105, 110, 115, <i>117.5</i> , 120, 125, 130, 135, 140, 145, 150, 155, 160, 170, 180, 190
less-pervious layers, extensions	layer-1: 10...20, layer-2: 60...80, layer-3: 120...∞, layer-4(not in Fig.(4.1)): 120...140
well geometry	start depth: 90, end depth: 110, diameter: 0.4

Table 4.1: Grid of calculation points, layer extensions and well geometry. All values in m . Italic values for the radial distances indicate different positions that were used in the dynamic 6-layer model. These replace the underlined values, which are used in all other models. Italic values for the profile depth are only included, if close to these depths a layer is present in the model.

In all contour diagrams of the tilt distributions presented in the following sections, the contour lines indicate steps of $0.5 \mu rad$ in tilt amplitude. Hence, the field gradient is indicated by the contour line density in the plots. If the lines are not too close to each other, the amplitude value is also printed. In pore pressure contour diagrams, it was tried to print the amplitude values for all contour lines. Here, amplitude separation between the lines is not equal in a single plot, but equal between different plots.

Poroelastic parameter values of deeper layers will generally depend somewhat on the loading of the overlying strata. At a depths below $z = 80 m$, similarly to Wang & Kümpel (2003), $0.1 GPa$ was added to the shear modulus to account for loading and compaction. If calculation is done for much larger depths, like for super deep boreholes (Schulze, 2002), tuning of the shear modulus and possibly of other parameters may be more important than here. At a depth of $100 m$, confining pressure caused by loading of the overlying (sedimentary) subsoil (density of $2000 kg/m^3$) is nearly $2 MPa$. At depths between $1 km$ and $10 km$ this value would be close to or in the range of the used shear modules. However, at larger depths the layer material will be different, too, i.e. not (un)consolidated sediments. A study dealing with the depth dependent change of porosity, although not in sediments, is the one of Gouly (1998).

4.2 Steady State Models

This section presents steady state solutions for tilt and pore pressure. The solutions were calculated for multi-layered half-spaces and models with a successively growing number of layers.

4.2.1 3(5)-Layer Model, One and Two Buried Slabs

The first model illustrates the influence of one buried horizontal slab which is less pervious than its surrounding. It is placed at a depth between the well screen and the surface and consists of a mixture of loam with parts of silt. Parameters and geometry are listed in Tab.4.2. Fig.4.2 shows the steady state solutions for tilt and pore pressure.

depth	sediment	G	ν	ν_u	B	D	α	K_f
0 ... 60	mid grained sand	0.20	0.15	0.40	0.85	18.2	0.90	$5 \cdot 10^{-4}$
60 ... 80	mix of loam, silt	0.50	0.20	0.40	0.75	0.0416	0.95	$5 \cdot 10^{-7}$
80 ... ∞	small grained sand	0.30	0.15	0.40	0.85	3.64	0.90	$1 \cdot 10^{-4}$

Table 4.2: Parameters and geometry for the 3-layer model, ‘mid sand–loam mix–small sand’. [G] = GPa , [D] = m^2/s , [K_f] = m/s . Geometry in m . The values are as in Tab.2.3 and not adjusted to match any specific situation.

There are several changes in the tilt and pore pressure pattern with respect to the analytical solution for the homogeneous half-space in Fig.2.9:

(1) In Fig.4.2 the slab constricts the course of the zero-line of tilt. At the depth of 65 m the line is completely cut at all radial distances. At the top surface of the slab, tilt shows in general a similar behaviour as at the free surface of the whole half-space. Tilt is negative due to the changed course of the zero-line. The slab causes a sharp pore pressure gradient. At depths below 100 m , the tilt distribution looks more similar to the homogeneous half-space and the full-space case. Here, pore pressure is somewhat increased.

(2) Tilt at and near the surface has slightly bigger amplitudes, with the same sign, i. e. strike direction, as in the homogeneous case. The parameters in the bottom layer, where the well screen is located, are the same as in Fig.2.9 except an increased shear modulus G due to loading. In the homogeneous case, an increased shear modulus would lead (due to a higher rigidity) to overall smaller tilt amplitudes, also at the surface. The different parameters in the top layer with respect to the homogeneous half-space case show a larger hydraulic diffusivity D that would also lead to a smaller tilt response at the surface. (Compare Eqs.2.15 and 2.19 for the dependency of tilt from G and D .) Thus, the larger amplitudes are due to the influence of the additional layer (the slab).

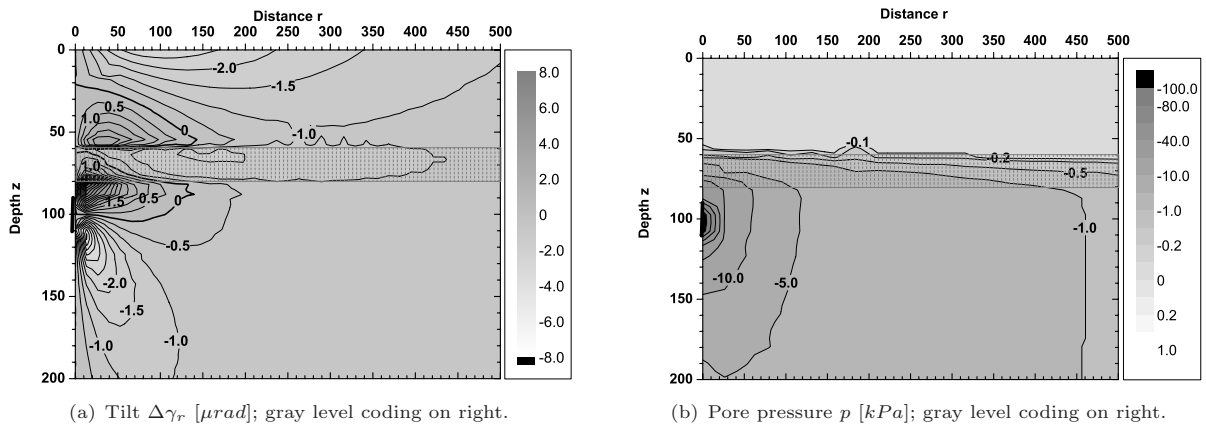


Figure 4.2: Steady state POEL solution, 3-layer model, ‘mid sand–loam mix–small sand’. Parameters and geometry are listed in Tab.4.2. Tilt maximum at surface is in a radial distance of nearly 92 m and has an amplitude of $-2.9 \mu rad$.

(3) For the homogeneous half-space, the position of the maximum of tilt at the surface is independent from the parameter values and occurs at a radial distance of $(1/\sqrt{2}) \cdot \text{depth of well screen's center}$, i. e. at 70 m , see section 2.7. Here, maximum surface tilt is at nearly 92 m . If the slab would be in the depth range from 120 m to 140 m with the same parameters as in Tab.4.2, i. e. with the well screen in the

more pervious midgrained sandy top-layer, the maximum at the surface would be at a radial distance of nearly 70 m (not depicted), like in a homogeneous half-space. Tab.4.3 shows the radial distance of the tilt maximum and its strength at surface for a clay and a sandstone slab, which are embedded in different depths above and below the well screen in a half-space consisting exclusively of small grained sand. Tab.4.3 has also the values for the slab of Fig.4.2 and the homogeneous half-space situation from Fig.2.9.

depth z of slab [m]	material of the slab buried in small grained sand	$r_{\Delta\gamma_{r_{MAX}}}$ [m]	$\Delta\gamma_{r_{MAX}}$ [μ rad]
0 ... 20	clay	89	-3.8
60 ... 80	clay	92	-2.9
120 ... 140	clay	70	-3.7
0 ... 20	Ruhr sandstone	120	-2.2
60 ... 80	Ruhr sandstone	110	-2.4
120 ... 140	Ruhr sandstone	70	-4.0
60 ... 80	<i>loam mix-slab of Fig.4.2</i>	92	-2.9
120 ... 140	<i>loam mix-slab of Fig.4.2</i>	70	-0.7
	<i>homogeneous of Fig.2.9</i>	70	-2.6

Table 4.3: Radial distance $r_{\Delta\gamma_{r_{MAX}}}$ of the tilt maximum $\Delta\gamma_{r_{MAX}}$ at surface in a 3-layer model with an embedded clay or a Ruhr sandstone slab above or below the well's screen. The layers above and below the slab are both of small grained sand with parameters as in Tab.4.2; the parameters for Ruhr sandstone are assumed to be like in Tab.2.3. The distance $r_{\Delta\gamma_{r_{MAX}}}$ is as accurate as the grid in Fig.4.1 allows identification of its position from the series of radial calculation points.

Tab.4.3 reveals that a less pervious and more rigid slab between the well screen and the surface leads to a larger radial distance of the tilt maximum at surface than in the homogeneous case. If the slab is deeper than the well screen, it looks like it has no influence of the maximums' position. In that case, only the amplitude of the maximum tilt is increased. An increase of the maximums' amplitude is also caused if the slab is more shallow than the well screen, except for the sandstone slab. If the situation with the buried clay layer in Tab.4.3 is compared with the 3-layer case of Fig.4.2, where the upper layer is more pervious than the lower one, no difference between position and amplitude of the maximum is seen for a depth of the slab between 60 m and 80 m. A larger difference in amplitude occurs, if the slab is between 120 m and 140 m. This may be explained by a reduced reservoir volume (a smaller catchment volume) that is tapped by the well. At the same extraction rate, in mean, fluid loss per unit volume is larger, i. e. the pore pressure gradient gets stronger. Thus, tilt response to pumping is generally increased. This is also valid for the shallow and the deep sandstone slab in the 3-layer case. However, the shallow sandstone slab prevents tilt to be large since the slab is more rigid, i. e. less deformable. If the sandstone slab is deep, the high pervious upper midgrained sand layer is tapped, and, caused by the large hydraulic diffusivity, see Tab.4.2, tilt response is minor.

It would be interesting to know whether a second deep zero-line builds-up downwards, below the wells screen's depth, and is constricted in the case when an additional slab is placed between depths of 120 m to 140 m. The parameters for a layered half-space with two buried slabs, one above and one below the well screen, are shown in Tab.4.4. Steady state solutions for tilt and pore pressure are in Fig.4.3.

At the surface, and also in the middle part (depths between 50 m and 150 m) in the diagram of Fig.4.3, tilt amplitudes are further increased with respect to the 3-layer case. The tilt maximum at the surface is still nearly at a radial distance of 92 m. The largest difference to the previous case occurs in the shape of the patterns of tilt and pore pressure distribution.

Again, strike of tilt is negative at the upper surface of the more shallow slab, i. e. sign is as at the free surface at zero depth. The zero-line of tilt is intersected by that slab. At the deeper slab, no additional zero-line appears as one may expect from symmetry. However, that situation is not vertically symmetric as the model region extends to infinity below and terminates at the free surface at its top. At the deeper slab, isolines of tilt are intersected by the slab without any change in strike direction. The patterns of the deeper tilt signal distribution, and also of the pore pressure field, are significantly influenced by the additional slab. Due to the low hydraulic diffusivity of the slabs, strong pore pressure gradients occur

depth	sediment	G	ν	ν_u	B	D	α	K_f
0 ... 60	mid grained sand	0.20	0.15	0.40	0.85	18.2	0.90	$5 \cdot 10^{-4}$
60 ... 80	mix of loam, silt	0.50	0.20	0.40	0.75	0.0416	0.95	$5 \cdot 10^{-7}$
80 ... 120	small grained sand	0.30	0.15	0.40	0.85	3.64	0.90	$1 \cdot 10^{-4}$
120 ... 140	mix of loam, silt	0.50	0.20	0.40	0.75	0.0416	0.95	$5 \cdot 10^{-7}$
140 ... ∞	mid grained sand	0.30	0.15	0.40	0.85	18.2	0.90	$5 \cdot 10^{-4}$

Table 4.4: Poroelastic parameters and geometry for two symmetrically placed impervious layers, 5 layers, called ‘mid sand–loam mix–small sand–loam mix–mid sand’. $[G] = GPa$, $[D] = m^2/s$, $[K_f] = m/s$. Geometry in m . The values are as in Tab.2.3 and not adjusted to match any specific situation.

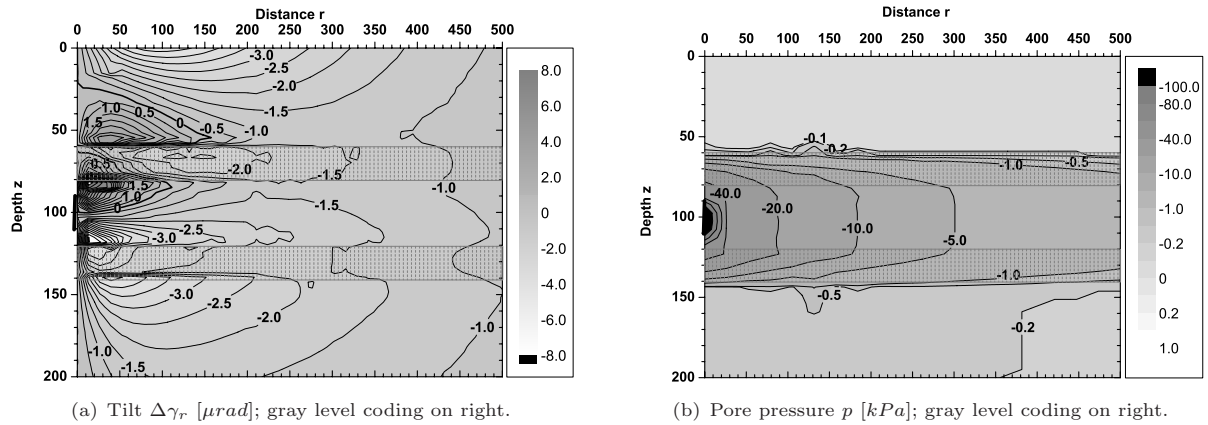


Figure 4.3: Steady state POEL solution, two symmetrically buried impervious slabs, ‘mid sand–loam mix–small sand–loam mix–mid sand’. Parameters and geometry are listed in Tab.4.4. Tilt maximum at surface is in a radial distance of nearly $92 m$ and has an amplitude of $-4.9 \mu rad$.

along the boundaries of both slabs and induce tilt. The deeper tilt field below about $120 m$ is stretched in direction of the slabs extension. Spatial extension of the zero-line is also altered. It is more laterally extended above the shallow slab, whereas its vertical extension is minor than with one slab. Between the slabs, both, lateral and vertical extension of the zero-line is reduced.

The pore pressure field in Fig.4.3(b) shows a restriction of fluid flow. The stream of ground water is perpendicular to the contour lines of pore pressure by definition, and therefore concentrated in the 2-D horizontal layer between the slabs. It seems obvious that this restriction leads to enhanced tilt amplitudes. Here too, the catchment volume, i. e. the effective volume of the reservoir that is tapped by the well, is reduced and a much higher pore pressure change is induced. Pore pressure change in the homogeneous half-space, Fig.2.9(b), was found to be around $-5 kPa$ close to the well ($r \approx 40 m$, $z \approx 100 m$). With one slab this value is nearly doubled, Fig.4.2(b), and increases up to $-30 kPa$ with two slabs.

It is possible that this geometrical ‘channeling’, i. e. the restriction of fluid flow to the layer between the slabs, was a reason for the strong total tilt amplitude measured at position T1_{WD}, see section 3.3. It can be assumed that in the model, total tilt response near surface will further increase, if an additional vertical slab is placed somewhat closer to the well between the two slabs in Fig.4.3. In that case the catchment volume for pumping is drastically reduced to a narrow 1-D channel. However, to simulate a 1-D channel, 2-D modelling is necessary, which can not be carried out with POEL and is thus omitted.

4.2.2 4-Layer Model

Considering the geological sections of site OE, see Figs.3.5, 3.6, A.13 and the lithology log of site BV, Fig.3.21, the previous half-space models seem not to be really applicable. The geological models show a stack of alternating aquifers and aquicludes. At both sites, OE and BV, below the upper two aquifers, a massive section of less pervious layers resides. A 4-layer model was constructed to simulate such a situation. It describes a two-aquifer system with a free and a confined aquifer. Both are situated over a thicker, mostly impervious subsoil. Tab.4.5 lists the geometry and parameters.

depth	sediment	G	ν	ν_u	B	D	α	K_f
0 ... 60	mid grained sand	0.20	0.15	0.40	0.85	18.2	0.90	$5 \cdot 10^{-4}$
60 ... 80	mix of loam, silt	0.50	0.20	0.40	0.75	0.0416	0.95	$5 \cdot 10^{-7}$
80 ... 120	small grained sand	0.30	0.15	0.40	0.85	3.64	0.90	$1 \cdot 10^{-4}$
120 ... ∞	clay	0.60	0.20	0.40	0.75	0.00042	0.95	$5 \cdot 10^{-9}$

Table 4.5: Poroelastic parameters and geometry of a 4-layer model, called ‘mid sand–loam mix–small sand–clay’. [G] = GPa , [D] = m^2/s , [K_f] = m/s . Geometry in m . The values are as in Tab.2.3 and not further adjusted.

The steady state POEL solution for the 4-layer model for tilt and pore pressure is shown in Fig.4.4. The pattern of the tilt distribution in the upper 100 m is somewhat similar to the previous case with two buried slabs. However, amplitudes are enhanced, vertical extension of the upper part of the zero-line is only up to a depth of 30 m , laterally it extends to a distance of 130 m . Spatial extension of the zero-line below the intermediate layer of loam mix is minor. The tilt maximum at the surface has an amplitude of $-7.7 \mu rad$ occurring at a radial distance of 110 m . Different to the previous case are the tilt and pore pressure patterns at depths below 100 m . The overall tilt amplitudes are similar, but the strongest gradients are closer to the well and moderate at somewhat larger depth. For instance, at a depth of 150 m and radial distance of 50 m , tilt has an amplitude of $-3.0 \mu rad$ but does not show a stronger spatial variation around that position. At the same place, induced pore pressure has an amplitude of about $-30 kPa$. In steady state, pumping lasted for an infinite time. The induced pore pressure distribution is build up completely and does no longer change in all parts of the model, even if the hydraulic diffusivity is rather low in the deeper model sections.

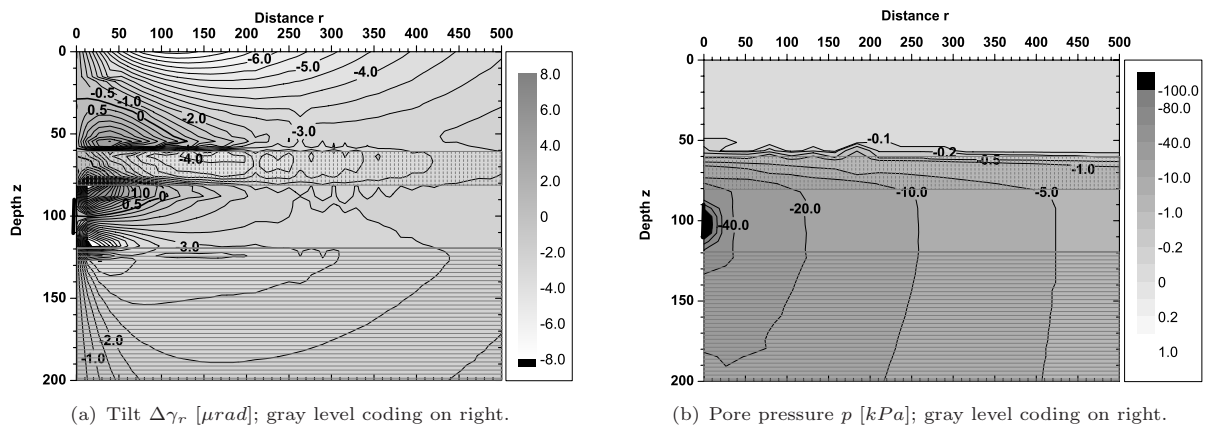


Figure 4.4: Steady state POEL solution for the 4-layer model, ‘mid sand–loam mix–small sand–clay’. Parameters and geometry are listed in Tab.4.5. Tilt maximum at surface is in a radial distance of nearly 110 m and has an amplitude of $-7.7 \mu rad$.

Below the deeper of the two slabs in Fig.4.3, at the same position, $z = 150 m$, $r = 50 m$, tilt amplitude is $-3.5 \mu rad$ and the gradient is stronger. Amplitude of pore pressure in this previous model is only $-0.45 kPa$. These differences are due to the infinitely extended clay layer here at bottom, in contrast

to the slab of Fig.4.3. In the previous case, strong pore pressure gradients occur at both boundaries of the deeper slab whereas here, the bottom layer has only one boundary at its top, where gradients of pore pressure are strong. Since tilt depends on the pore pressure gradient this will explain the general appearance of the tilt distribution. However, it is questionable if the here depicted values of tilt and pore pressure will be nearly achieved in a real pump test. The very low value of the hydraulic diffusivity in the bottom clay layer will lead to a corresponding long duration for pumping (i. e. the transient time span) until the steady state. This aspect will be clarified in the time dependent, dynamic models.

4.2.3 6-Layer Model

A comparison between the previous model and the geological subsoil interpretations of sites OE and BV shows that the topsoil layer is still not respected by the 4-layer model. A topsoil layer would lead to a 5-layer model with an extra stratum near the surface. Now, the topsoil is taken into account by a slightly deeper, less pervious layer. For this purpose, a 6-layer subsoil model with two confined and one upper free aquifer was constructed. The question, whether a zero-line of tilt will build up above the additional shallow layer in the free upmost aquifer will be answered. Furthermore, the layer material in that more complex situation will be varied. The resulting variations of tilt and pore pressure distributions will be discussed. The first of the following models is based on the previous 4-layer situation with an additional shallow less pervious layer. The further 6-layer models will result from changing the material parameters of the strata for the same geometry. Tab.4.6 lists the geometry and parameters of the first 6-layer model.

depth	sediment	G	ν	ν_u	B	D	α	K_f
0 ... 10	mid grained sand	0.20	0.15	0.40	0.85	18.2	0.90	$5 \cdot 10^{-4}$
10 ... 20	mix of loam, silt	0.50	0.20	0.40	0.75	0.0416	0.95	$5 \cdot 10^{-7}$
20 ... 60	mid grained sand	0.20	0.15	0.40	0.85	18.2	0.90	$5 \cdot 10^{-4}$
60 ... 80	mix of loam, silt	0.50	0.20	0.40	0.75	0.0416	0.95	$5 \cdot 10^{-7}$
80 ... 120	small grained sand	0.30	0.15	0.40	0.85	3.64	0.90	$1 \cdot 10^{-4}$
120 ... ∞	clay	0.60	0.20	0.40	0.75	0.00042	0.95	$5 \cdot 10^{-9}$

Table 4.6: Poroelastic parameters and geometry for the first 6-layer model, called ‘mid sand–loam mix–mid sand–loam mix–small sand–clay’. $[G] = GPa$, $[D] = m^2/s$, $[K_f] = m/s$. Geometry in m . The values are as in Tab.2.3 and not further adjusted.

The corresponding results from the POEL calculation are depicted in Fig.4.5. With respect to the 4-layer model the largest alterations of the solutions are in the depth range between $0m$ and $60m$, especially where the new layer has been introduced. At the surface, the tilt maximum is shifted to a larger radial distance, and tilt response at distances beyond the surface maximum is stronger. A steep pore pressure gradient and therefore a changed tilt distribution is established at the boundaries of the top layer between $10m$ and $20m$ depth. The zero-line of tilt vertically extends up to the additional layer, its lateral extension is larger, too. The layer of ‘loam mix’ between $60m$ and $80m$ depth is the same in both models (4-layer and 6-layer). The zero-line is still completely cut at a depth around $65m$. The pore pressure gradient at the top boundary of this deep loam mix layer is not as strong as in the 4-layer model and tilt response in this depth range is somewhat smaller (e. g. compare the tilt contour line of $-3.0 \mu rad$ in Figs.4.5 and 4.4). In the deeper part of the models differences are minor.

It is obvious from Fig.4.5 that in a subsoil with shallow layers tilt response near the surface can sensitively depend on the installation point of the tiltmeter. This will mostly be valid for positions within the distance of the maximum at surface and at depths close to layer boundaries. If the contrasts between the layers’

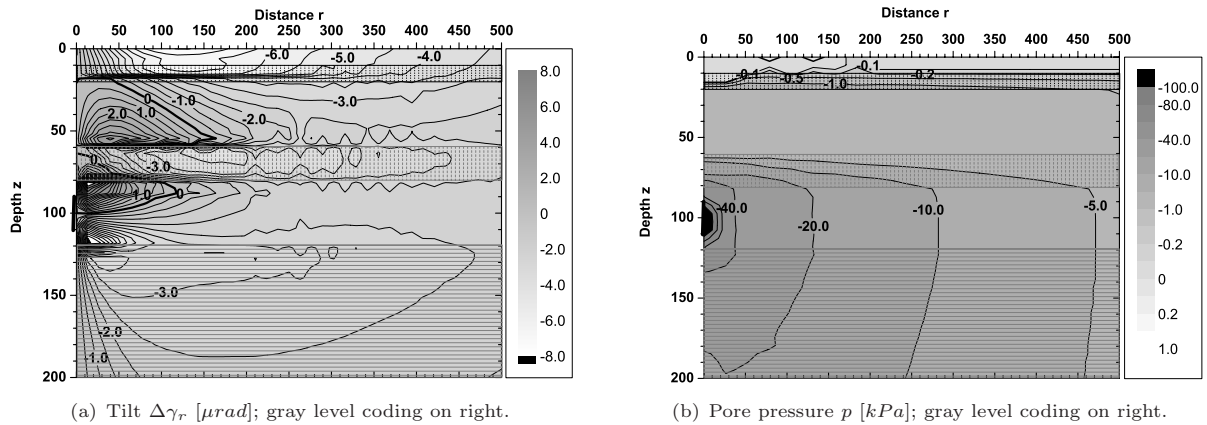


Figure 4.5: Steady state POEL solutions for the first 6-layer model, ‘mid sand–loam mix–mid sand–loam mix–small sand–clay’. Parameters and geometry are listed in Tab.4.6. Tilt maximum at surface is at radial distance of about 116 m and has an amplitude of $-7.6 \mu\text{rad}$. The course of the zero-line of tilt is ‘pulled up’ by the additional layer with respect to the 4-layer model.

parameters are not so strong like here, the gradients and therefore spatial variance in the solution fields will be minor. At larger distances, the gradients of the tilt field are generally minor, also at boundaries of strata.

In the next step modelling will deal with parameter variations in the strata. Instead of the ‘loam mix’ layers ‘silt sand’ layers are used. Moreover, the material of the productive aquifer, small grained sand, will be replaced with a more pervious stratum, mid grained sand. This will lead to four extra models, i – iv. Tab.4.7 lists the parameters of these variations together with the layer geometry for the two less pervious layers and the main aquifer. The other layers are kept unchanged.

The first variation, i in Tab.4.7, is characterized by two less pervious layers of silty sand. Fig.4.6(a), (b) present the POEL solutions. The hydraulic diffusivity D (and the K_f -value) in these layers is one order of magnitude less than in the main aquifer (between 80 m and 120 m) and one and a half order of magnitude smaller than in the other aquifers. D mostly accounts for the perviousness of the material. Hence, pore pressure gradients at the boundaries of these two layers are minor than in the first 6-layer model. Moreover, due to the increased overall perviousness of the whole model, the effective reservoir volume for groundwater extraction is (in mean) larger than before. This might explain the overall smaller tilt response. On the other hand rigidity, characterized mostly by the shear modulus G , is halved for the intermediate layers. The material is more deformable. Thus, larger tilt amplitudes could also be explained. The fact that overall tilt is smaller than in the first 6-layer model points to a stronger influence of the applied changes in D than in G .

Fig.4.6 (c), (d) show POEL solutions for variation ii. In this model only the deeper, less pervious ‘loam mix’ layer is replaced by ‘silt sand’. As the very low pervious loam mix layer is close to surface, here too, the effective reservoir volume is larger than in the first 6-layer model. Overall tilt amplitudes are smaller. In the depth range between 0 m and 30 m tilt is increased with respect to case i. This latter effect is due to the stronger pore pressure gradients at the upper loam mix layer.

In both model variations i and ii the course of the zero-line of tilt is influenced by the deeper silt sand layer, but is not completely cut. In i, the zero-line does not vertically extend up to the upper intermediate layer, but it does so in ii, similarly to the first 6-layer model. However, the line in ii is steeper in the depth range between 20 m and 60 m than in the first 6-layer case. At larger depths and distances tilt distributions of both variation i and ii look similar, but in ii the field has overall stronger amplitudes. This is also confirmed by the pore pressure contour, where larger gradients appear in ii. Another aspect is that the steady state response of tilt and pore pressure in the underlying clay stratum is significantly influenced by the properties of the overlying sediment stack. Tilt maximum at the surface is located at a radial distance of 82 m for case i and 87 m for ii. The amplitudes are $-5.1 \mu\text{rad}$ and $-5.3 \mu\text{rad}$, respectively.

no.	depth	sediment	G	ν	ν_u	B	D	α	K_f
i	10 ... 20	silty sand	0.25	0.20	0.40	0.75	0.416	0.95	$1 \cdot 10^{-5}$
	60 ... 80	silty sand	0.25	0.20	0.40	0.75	0.416	0.95	$1 \cdot 10^{-5}$
	80 ... 120	small grained sand	0.30	0.15	0.40	0.85	3.64	0.90	$1 \cdot 10^{-4}$
ii	10 ... 20	mix of loam, silt	0.50	0.20	0.40	0.75	0.0416	0.95	$5 \cdot 10^{-7}$
	60 ... 80	silty sand	0.25	0.20	0.40	0.75	0.416	0.95	$1 \cdot 10^{-5}$
	80 ... 120	small grained sand	0.30	0.15	0.40	0.85	3.64	0.90	$1 \cdot 10^{-4}$
iii	10 ... 20	silty sand	0.25	0.20	0.40	0.75	0.416	0.95	$1 \cdot 10^{-5}$
	60 ... 80	mix of loam, silt	0.50	0.20	0.40	0.75	0.0416	0.95	$5 \cdot 10^{-7}$
	80 ... 120	small grained sand	0.30	0.15	0.40	0.85	3.64	0.90	$1 \cdot 10^{-4}$
iv	10 ... 20	silty sand	0.25	0.20	0.40	0.75	0.416	0.95	$1 \cdot 10^{-5}$
	60 ... 80	mix of loam, silt	0.50	0.20	0.40	0.75	0.0416	0.95	$5 \cdot 10^{-7}$
	80 ... 120	mid grained sand	0.30	0.15	0.40	0.85	18.2	0.90	$5 \cdot 10^{-4}$

Table 4.7: Parameters of the variations of the first 6-layer model of Tab.4.6 for the two separating less pervious intermediate strata and the main aquifer that hosts the well screen. Changes are emphasized. Other values from Tab.4.6 remain unaltered. $[G] = GPa$, $[D] = m^2/s$, $[K_f] = m/s$. Geometry in m . The values are due to Tab.2.3 and not further adjusted.

The following two model variations, iii and iv, see Tab.4.7, are characterized by the upper intermediate layer composed of silty sand and replacing the layer of the mix of loam and silt. In the latter of these variations the material of the main aquifer is replaced by much more pervious mid grained sand. The hydraulic diffusivity D of mid grained sand is five times larger than for small grained sand. D directly influences the amplitude of overall tilt response, e.g. the surface maximum might be assumed to be roughly five times smaller in iv than in iii. Fig.4.7 shows the solution fields for the model variations iii and iv. For model iii the tilt maximum at surface is at $113m$ and for model iv at $137m$ radial distance from the well's axis. The amplitudes are $-7.7 \mu rad$, case iii, and $-1.4 \mu rad$, case iv. This confirms a factor of grossly five (indeed a factor of 5.5) between the maximum amplitudes. With respect to model iii in model iv tilt amplitudes are drastically decreased. Also, a different pattern of the tilt and pore pressure solutions appears between model variation iii and iv. The course of the zero-line is changed, i.e. the line is laterally less extended and gradients in tilt and pore pressure are comparatively small.

The solutions for variation iii, Figs.4.7(a), (b) look similar to the first 6-layer model in Figs.4.5(a), (b). This is due to the strong influence of the deep intermediate loam mix layer that dominates the pattern of the fields. The most important deviations between the first 6-layer model and the variation model iii are the course of the zero-line between the less pervious layers (depth $20m$ to $60m$) and the tilt gradient at the upper intermediate layer. In the first 6-layer model the zero-line runs through the lower part of the upper layer and the gradient in tilt amplitudes is large. Accordingly, the zero-line in model iii has vertically collapsed and is laterally less extended. The pore pressure gradient at the deeper layer is stronger in model iii. There, nearly the complete signal amplitude drops down. In the first 6-layer model, Fig.4.5, the drop in pore pressure amplitude at the upper less pervious layer is larger, i.e. by a factor of ten, but decrease at the lower loam mix layer is not so strong than in iii.

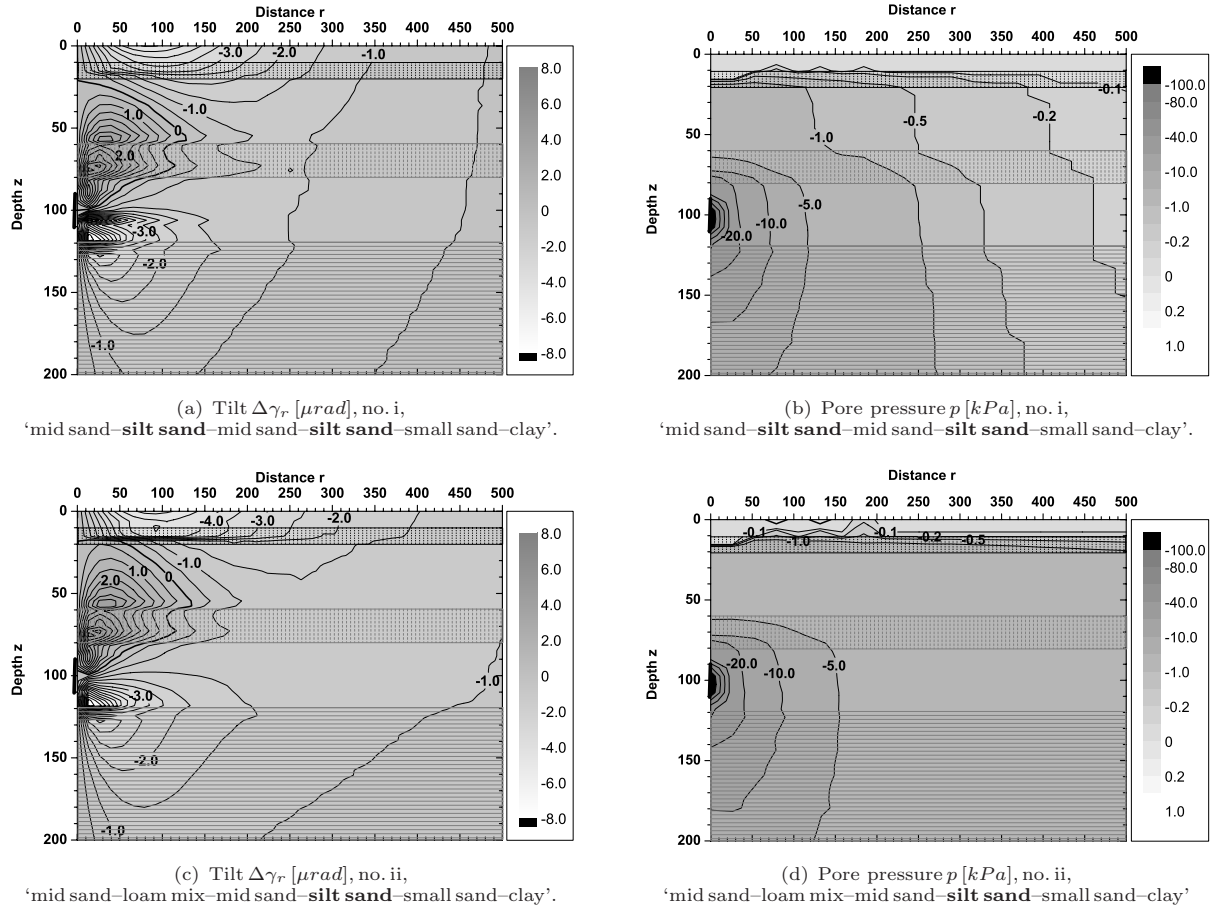


Figure 4.6: 6-layers, variations of the model in Fig.4.5 after Tab.4.7, i, (a), (b) and ii, (c), (d).

For the adjustments of a poroelastic model, when fitting measured data, the hydraulic diffusivity D turned out to be the first 'tuning button'. It looks like D influences the poroelastic response strongest. Moreover, the contrast in D between adjacent layers seems to be important. At a boundary, where strata with a large difference in D are in contact, a strong pore pressure gradient and thereafter a strong tilt response is induced. In the case of the homogeneous half-space, except for the next vicinity of the well screen, the largest tilt amplitudes occur at the free surface. There, the contrast in D (and also in the other parameters) is large. G turned out to be the second parameter that can be used for model refinements. Generally, if G is high, the tilt amplitude is decreased due to higher rigidity of the material.

The last parameter that will be varied is the Poisson ratio ν . From Eq.2.19 follows that ν is the only parameter which influences the pattern of the tilt distribution and the course of the zero-line in the homogeneous half-space. To look for a similar influence in the multi-layer case, two further steady state models were calculated. One model where ν is increased by the same amount for all layers is named model variation v. In a second model, named vi, ν is decreased by the same amount in each of the model strata. The variation of ν was done with reference to the model iii. The range of variation for ν is restricted by the parameter α , which can only diverge in its physical boundaries through Eqs.2.11 and 2.12. The other corresponding parameters of the model layers, ν_u and B , were not changed. Thus, the largest possible increase for ν is +0.15 (model v) and the largest decrease is -0.03 (model vi).

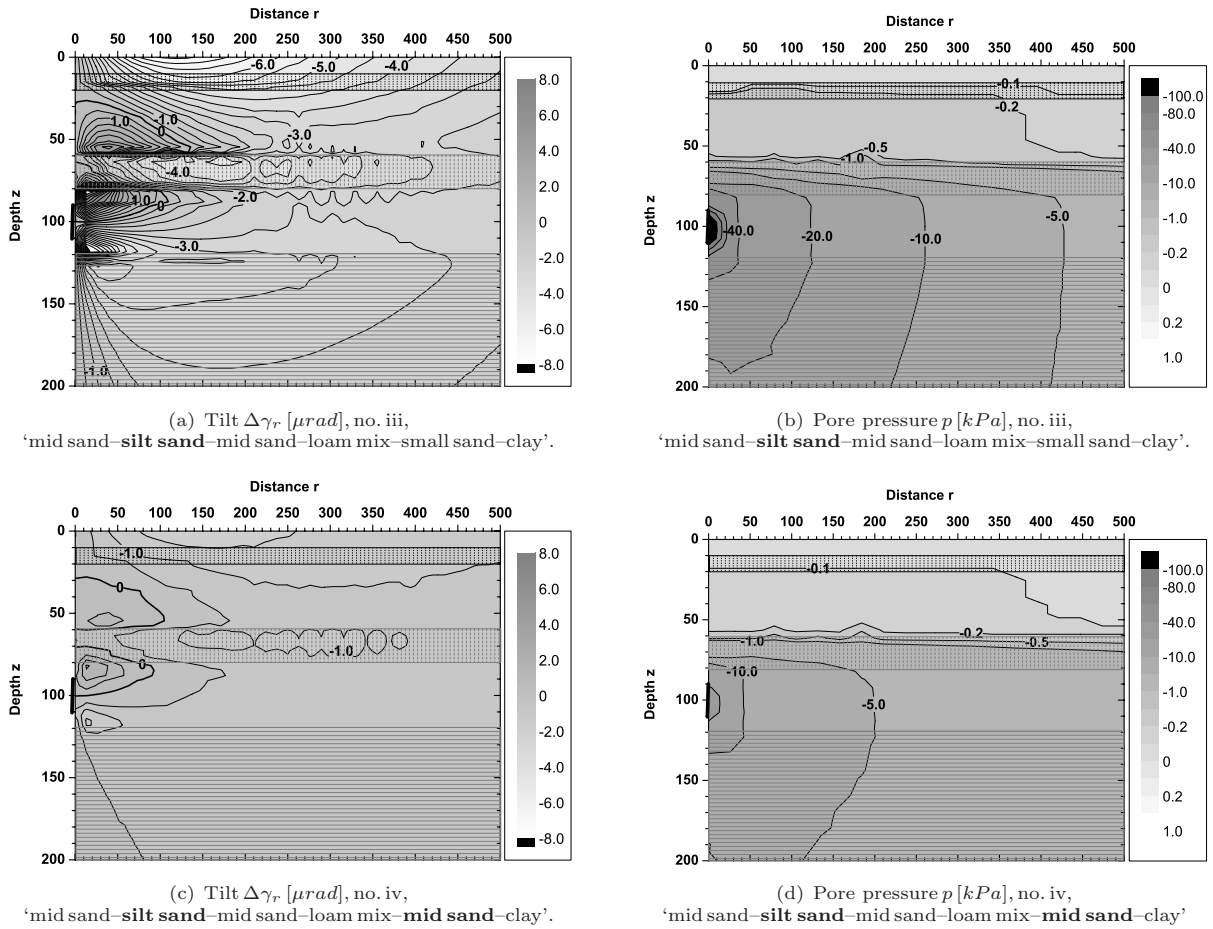


Figure 4.7: 6-layers, variations of the model in Fig.4.5 after Tab.4.7, iii, (a), (b) and iv, (c), (d).

Fig.4.8(a), (b) show the solutions for model variation v, and Fig.4.8(c), (d) for model variation vi. The diagrams can be directly compared with the solutions depicted in Fig.4.7(a), (b). The increased Poisson ratio in Fig.4.8(a), (b) leads to overall reduced tilt amplitudes. The gradients in tilt are also decreased. The position of the tilt maximum at the surface is at a radial distance of 105 m with an amplitude of $-2.6 \mu\text{rad}$. If compared with model iii, the maximum is closer to the well. Moreover, the course of the zero-line is altered. It is laterally more extended. The line runs through the deeper, less pervious layer (between 60 m and 80 m) and meets the well axis at a depth around 65 m. Likewise, the course of the zero-line is different to model iii if ν is decreased, Fig.4.8(c), (d). The zero-line is completely cut by the less pervious layer between 60 m and 80 m and laterally more contracted. For a decreased ν with respect to model iii, the overall tilt response is increased and tilt gradients are stronger. At the surface the maximum is slightly more distant from the well (115 m) and has a larger amplitude ($-8.7 \mu\text{rad}$).

The pattern of the pore pressure solution is not significantly biased by a change in the Poisson ratio. Differences between Fig.4.7(b), Fig.4.8(b) and Fig.4.8(d) are minor. Obviously, the course of the zero-line of tilt, of the contour lines and the tilt amplitudes can be manipulated with the aid of ν , without changing the pore pressure response. Together with a tuning of the hydraulic diffusivity and shear modulus in adjacent layers, a comparatively good control over the course of isolines for tilt can be achieved. This might be helpful if the tilt amplitude at a certain position (radial distance and depth) has to be calculated.

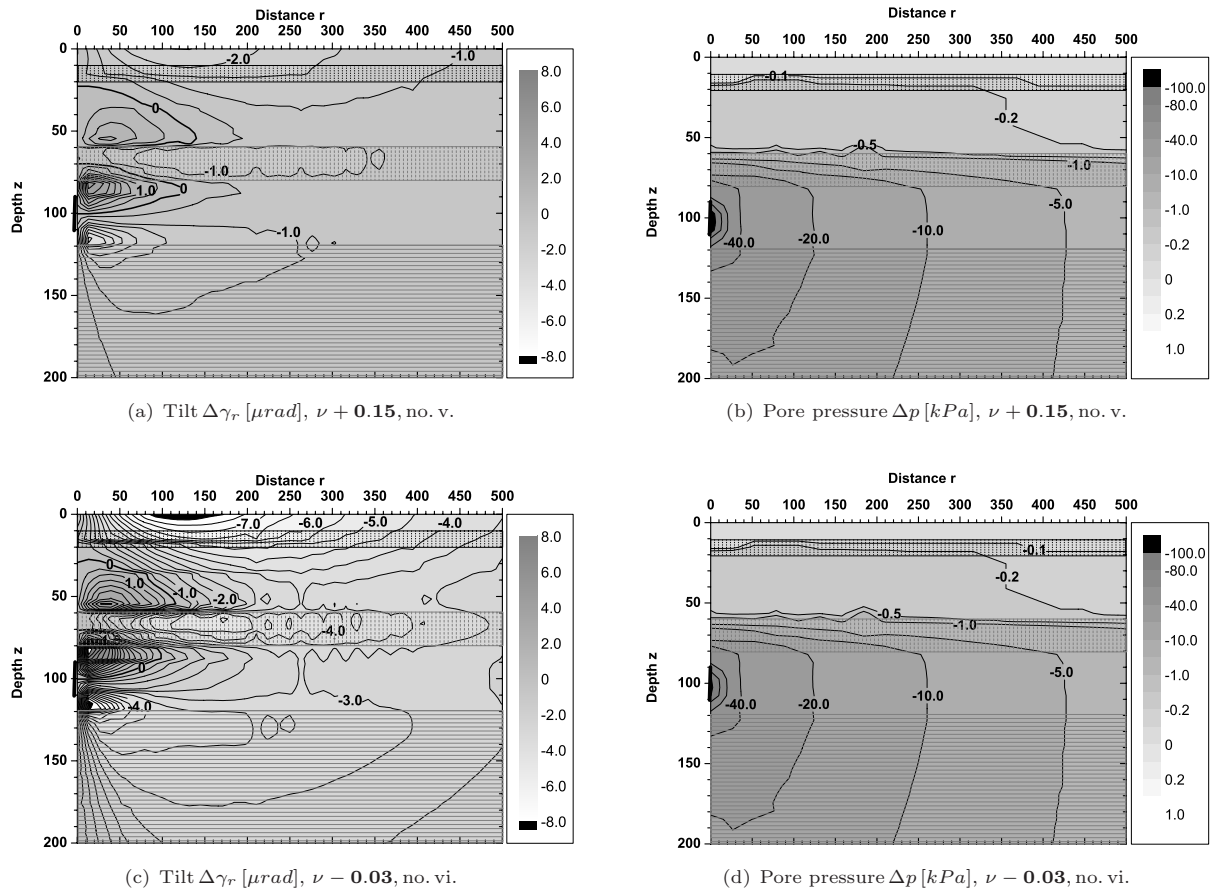


Figure 4.8: 6-layer models, v, (a), (b) and vi, (c), (d) from variation of ν for all strata of the model iii; compare with Tab.4.7 and Fig.4.7. The model is called ‘mid sand-silt sand-mid sand-loam mix-small sand-clay’.

Variations of the undrained Poisson ratio ν_u and the Skempton coefficient B will not be shown in further models. Both bias the tilt response, but influence on the steady state solutions seemed to be not as strong as influence of the previous three parameters. Variation of ν_u is assumed to be not very large in practice, see the definition and values in section 2.6. ν_u influences the tilt solution through the formula of D , Eq.2.16. B is a factor in the solution for tilt and is related to D by a power of two, see Eqs.2.19 and 2.16, respectively. Generally this would indicate a strong influence, but the real range of values of B is restricted by physical properties of the sediment material. Therefore, the tuning of B with values in a realistic range for fully saturated sediments has a reduced influence on the solution. A much larger variation of B , especially to smaller values like here, can be applied in the formulas. B gets smaller in partly saturated or unsaturated media. Here, such a situation is not considered. However, an estimation of the influence of ν_u and B might be outlined in a further investigation.

4.3 Dynamic Models

Like in the previous section, models of poroelastic multi-layered half-spaces with a growing number of strata will be taken into consideration. The aim is, to show subsoil/model conditions that will lead to the types of observed transient tilt and pore pressure response to pumping. Tilt reversals of both signs and the Noordbergum effect will be assessed with respect to the observations at the sites OE and BV. A long-term calculation of transient signals occurring after several hours to days of withdrawal will be done.

It was intended to see the possible further evolution of signals after the early transient phase of pumping. The dependence of modelled tilt reversals from layering as well as the sensitivity of the calculated signal to parameter variations in a layer at a larger depth are considered.

Inspection of the modelled time development of the tilt and pore pressure distribution will be done in a sector of the half-space section which is close to the well ($r = 0\text{ m}$ to 200 m and $z = 0\text{ m}$ to 150 m). In this section the transient processes are strongest and tilt reversals as well as the Noordbergum effect occur. In the contour diagrams, only the zero-line of tilt will be plotted as an isoline. The line is depicted for different times that are indicated by the line signature. Some computed time series of tilt, pore pressure and also matrix displacement are plotted as ‘zoom-outs’ from selected calculation points (compare also Fig.4.1 and Tab.4.1 for the model geometry). A small collection of time-slices showing the field evolution of tilt and pore pressure at selected time steps in the first hour after onset of pumping is in section A.7, in the appendix.

4.3.1 Homogeneous Half-Space

The first scenario is the homogeneous half-space of smallgrained sand as it is frequently referenced. Tab.4.8 summarizes parameter values and geometry.

depth	sediment	G	ν	ν_u	B	D	α	K_f
0	small grained	0.20	0.15	0.40	0.85	3.64	0.90	$1 \cdot 10^{-4}$
$\dots \infty$	sand							

Table 4.8: Parameters and geometry for the homogeneous half-space model of ‘smallsand’. [G] = GPa , [D] = m^2/s , [K_f] = m/s . Geometry in m .

Fig.4.9 shows the signal evolution in the homogeneous half-space. The contour plot of the tilt zero-line is drawn in the center for seven different times in the first hour after onset of pumping (see the legend at the right side of the figure) and for the steady state (thickest line). The steady state line is the asymptote for the other lines. During the build-up of the tilt field, the zero-line (and the whole pattern) changes its position, i. e. ‘moves’. The overall motion of the zero-line is indicated by the two thin black arrows. The line first clasps a larger area and then contracts during further withdrawal. The somewhat strange excursion of the zero-line around position $z = 110\text{ m}$, $r = 90\text{ m}$ is an artifact of the gridding process, see also section 4.1. It vanishes as soon as amplitudes and gradients get stronger. Outside the area which is clasped by the zero-line, tilt is negative, whereas it is positive inside. At places which are crossed by the zero-line, during the build-up of the field, a change in sign of tilt response occurs, i. e. a reversal of tilt. It is obvious that at adjacent places a transient tilt reversal can also occur, but without a change in sign. Here, other isolines representing positive or negative tilt amplitudes fluctuate across.

The first zoom-out in Fig.4.9 from the point at $z = 22.5\text{ m}$, $r = 30\text{ m}$ shows from top to bottom tilt response $\Delta\gamma_r$, induced pore pressure p , and the matrix displacements in vertical direction with negative sign downwards, u_z , and radially with negative sign towards the well, u_r , each for one hour of pump activity, and with the grey hatched background for one hour after the pumping. The central contour plot only shows the data for pump activity, not for relaxation. A significant and comparatively strong and long lasting positive tilt reversal of type measured at site OE, see Fig.3.18, and as already modelled by Wang & Kümpel (2003) appears. Tilt first strikes to positive values, i. e. the observation position is inside the zero-line, takes the zero value after 12 min and thereafter takes negative amplitudes, i. e. the position is now outside the zero-line. After cessation of the pump the process seems to be reversed, but after one hour the tilt signal did not reach its initial value, i. e. zero position. An effective difference, for instance called Λ , remains. For an illustration of such an effective difference, a calculation with POEL can be done e. g. at the position $z = 4\text{ m}$, $r = 180\text{ m}$ where this difference is larger. Fig.4.10 shows the results. The straight curve (1) depicts the tilt response, if monotonous pumping would last for 2 h . The dashed line (2) shows relaxation, if the pump would be switched off after 1 h (as in the time series of Fig. 4.9). The difference between the value after one hour of pumping and the value after two hours equals the remaining offset Λ like depicted in Fig.4.10. However, besides other, unknown non-linear processes,

appearance of such a difference might explain a part of the offset in tilt $T1_{WD}$ after pumping at site WD. Furthermore, if pump cycles (pumping and free relaxation) are conducted in succession the differences at the end of each cycle sum up.

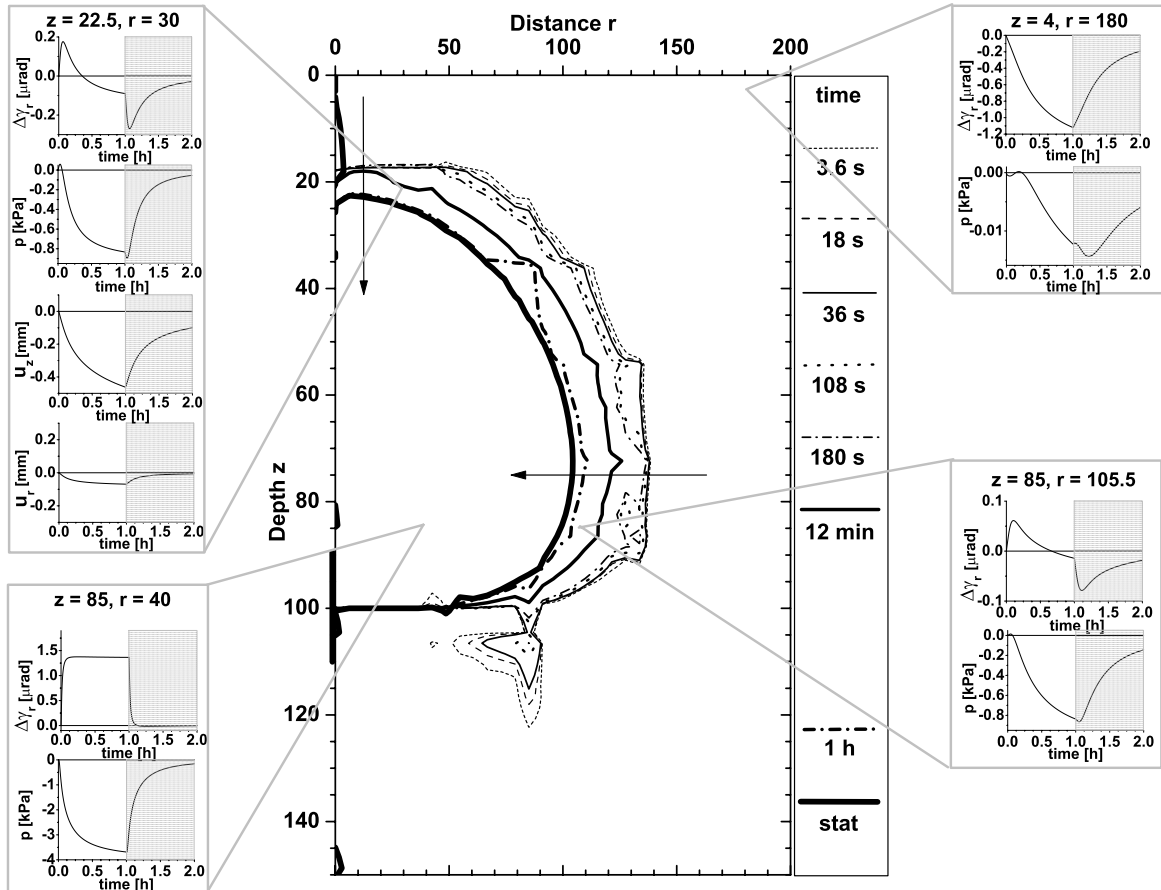


Figure 4.9: Evolution of zero-line of tilt in half-space model for selected time steps and zoom-outs of time series from selected points.

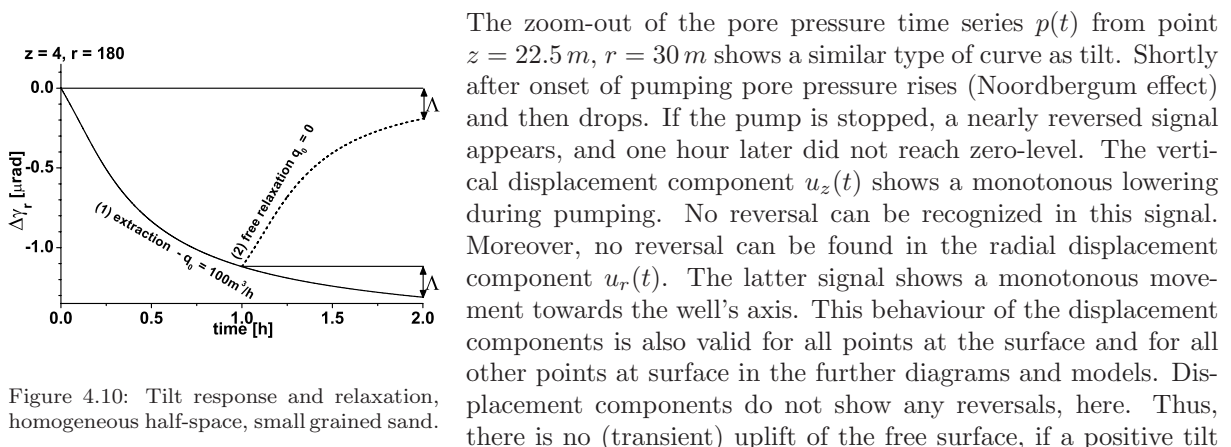


Figure 4.10: Tilt response and relaxation, homogeneous half-space, small grained sand.

reversal occurs close to surface, like speculated in section 3.2.2 for the signals observed at OE, Fig. 3.18. The positive reversal in tilt rather is consequence of a balancing process involving shearing and rotation as well as diffusion.

The tilt signal in the zoom-out at the upper right side in Fig.4.9 from position $z = 4\text{ m}$, $r = 180\text{ m}$ was already shown in Fig.4.10. No reversal is in the tilt response. The signal drops in the first hour of pumping, but did not achieve steady state. More surprisingly is the slight fluctuation in the pore pressure response here, at the beginning of the pump cycle. Fig.4.11 provides an enlarged view on this signal. First, pore pressure drops a bit, then rises above zero and thereafter drops monotonously until the pump stops. The physical process determining this behaviour of pore pressure is not yet clear. Again, it might be a balancing process due to strong poroelastic coupling. The amplitude of the signal after 0.05 h is about -0.5 Pa , which corresponds to a change in height of water column of -0.05 mm – hardly detectable.

At the bottom of Fig.4.9, left side, the zoom-out shows the tilt and pore pressure signals that are calculated at position $z = 85\text{ m}$, $r = 40\text{ m}$. A sharp rise in tilt can be seen. Steady state seems to be reached early. At later times, when pumping is stopped, the signal recovers completely (in the scaling of the diagram). Tilt response is positive since the calculation point is inside the zero-line. The rapid rise is due to the close position to the well screen (and the comparatively high value of hydraulic diffusivity, D). The pore pressure signal directly drops monotonously but did not achieve steady state.

The last inset at the right side, at the bottom in Fig.4.9, depicts the time series computed for position $z = 85\text{ m}$, $r = 105.5\text{ m}$. Around this point, the movement pattern of the zero-line is comparable to the motions of the line at position $z = 22.5\text{ m}$, $r = 30\text{ m}$. The complete line contracts monotonously. The Noordbergum effect, even smaller, also occurs. In the homogeneous half-space model a negative tilt reversal, like the signals observed at site OE, Fig.3.7 and site BV, Fig.3.26 could not be recognized at any of the calculation points. Even if this is only a numerical proof for one set of parameters, it is a clue to the assumption that negative tilt reversals only occur in heterogeneous half-spaces.

Fig.4.12 shows that in the homogeneous half-space of small grained sand the steady state in pore pressure at position $z = 22.5\text{ m}$, $r = 135\text{ m}$ is mostly reached after 24 h to 36 h . A corresponding experiment to achieve steady state has to run for that time-span without any interruption. If steady state needs not to be reached more exactly, a shorter duration of pumping is sufficient. In Fig.4.12 about 6 h seem to be appropriate. At positions closer to the well, steady state is achieved earlier and for farther positions later. The time, when steady state has established, mostly depends on the hydraulic diffusivity D . In a subsoil with less pervious layers of e.g. loam, the steady state would be generally reached much later. For such a situation Hsieh (1995) calculated times of up to two weeks with a comparable model configuration as here. This aspect will also be assessed in the further models, too.

4.3.2 3-Layer Model

The dynamic 3-layer model with parameters and geometry as in Tab.4.2 is discussed. The influence of a single layer that constrains the zero-line of tilt is proofed.

Fig.4.13 shows the contour plots of the zero-line for different time-steps during a one hour pump interval. Signature of the lines is as before, but an additional line, 30 min , thick dots, is added. The zoom-outs from selected positions of the model show the signals during pump time and during the first hour of relaxation. Again, the black arrows indicate the general movements of the tilt zero-line. At the top of the zero-line the movement is similar to the homogeneous half-space situation, but at its lateral flank motion turns back. The latter type of movement appears above and below the less pervious loam mix

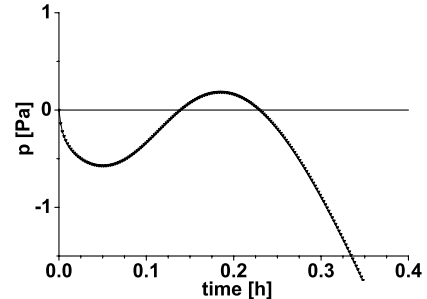


Figure 4.11: Double reversal of the pore pressure signal, $z = 4\text{ m}$, $r = 180\text{ m}$ in homogeneous half-space, small grained sand.

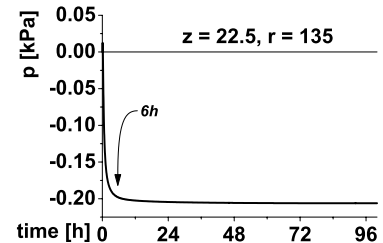


Figure 4.12: Long-term pore pressure signal in homogeneous half-space of small grained sand.

layer. The contour line for 30 min is more laterally extended than the earlier one for 12 min and the later ones for 1 h and the steady state. In the loam mix layer the motion pattern is not so obvious from Fig.4.13, but a contraction of the zero-line during the time between 12 min and steady state can be identified.

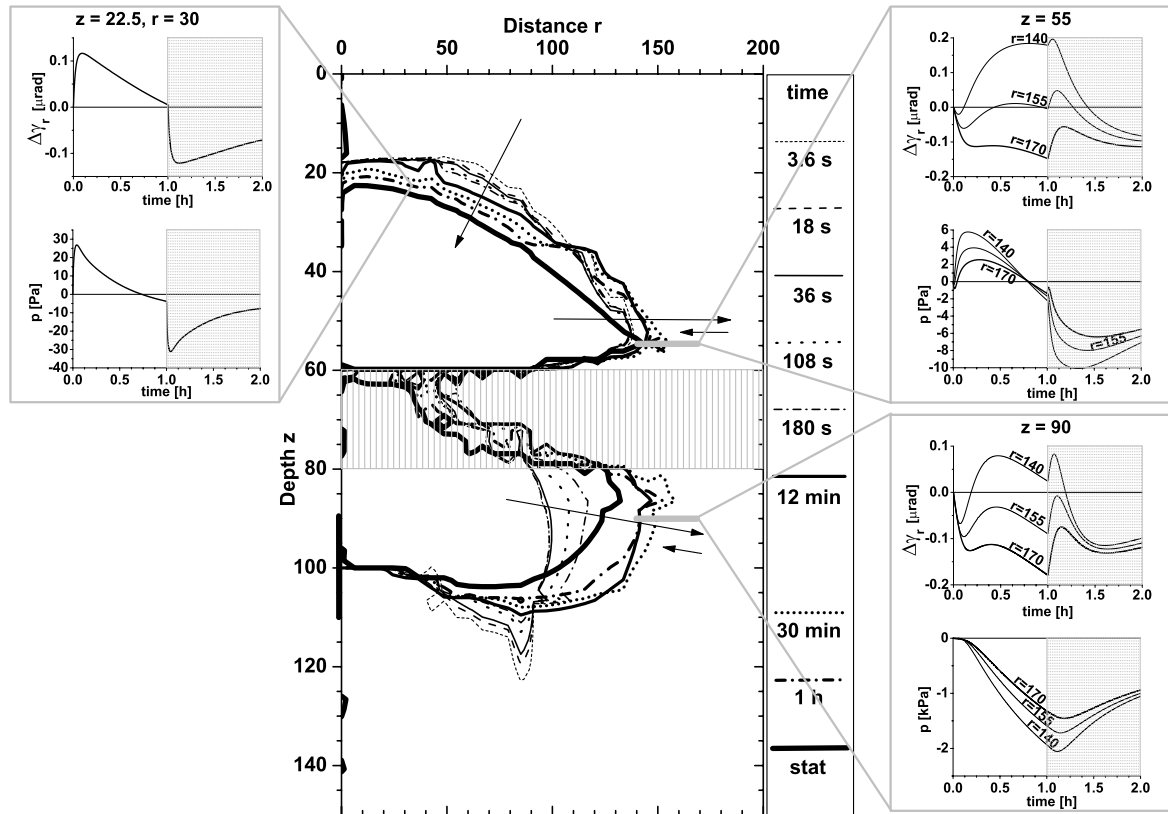


Figure 4.13: Evolution of zero-line of tilt in 3-layer model for selected time steps and zoom-outs of time series from selected points. Parameters and geometry as given in Tab.4.2.

The first zoom-out from position $z = 22.5\text{ m}$, $r = 30\text{ m}$ confirms the zero-lines movement at its top. A positive tilt reversal is computed, which is accompanied by the Noordbergum effect. With respect to the homogeneous half-space, strength of tilt response to positive direction is halved, whereas duration of the reversal is longer, about 1 h. Also, the pore pressure response is different. These signal alterations are most likely a consequence of the increased hydraulic diffusivity D in the top layer and a reduced value of that parameter in the less pervious loam mix layer. The increased D in the top layer leads to a smaller response in tilt, whereas diffusion to the well is delayed by the loam mix layer and leads to a longer lasting tilt reversal and Noordbergum effect.

More interesting are the signals drawn in the zoom-outs at the right side of Fig.4.13. Both show tilt and pore pressure. The upper zoom-out is from three different radial positions, $r = 140\text{ m}$, 155 m , 170 m , at a depth $z = 55\text{ m}$, close to the upper boundary of the loam mix layer. The lower one is from the same three radial distances, but at a depth of $z = 90\text{ m}$, near to the layer's lower boundary. Negative tilt reversals occur. At depth $z = 55\text{ m}$ the course of the tilt signals strongly varies with radial distance. Tilt response at distance $r = 170\text{ m}$ is somewhat similar to the negative tilt reversals observed at site OE, Fig.3.7. The signal curve from $r = 155\text{ m}$ is more similar to the reversals from site BV, Fig.3.26, even if the negative reversal in the calculated signal here is followed by a positive one. Amplitudes and rise times of signal flanks do not fit the observations. At $r = 140\text{ m}$ a negative reversal appears only in the first minutes after onset of pumping and is followed by a stronger response with positive tilt angles. Of similar style

as these three tilt signals from $z = 55\text{ m}$ are the ones from the deeper positions at $z = 90\text{ m}$, but in the latter, maxima and minima are more distinctive.

Pore pressure signals from the latter both depths are quite different. At the positions above the slab ($z = 55\text{ m}$) a double reversal, i.e. a slight drop followed by the Noordbergum effect that seems to end up in a monotonous lowering occurs at $r = 155\text{ m}$ and 170 m , whereas the Noordbergum effect without a preceding head drop emerges at $r = 140\text{ m}$. The amplitudes are rather small. At the deeper positions ($z = 90\text{ m}$) the response in pore pressure is somewhat delayed, without any signal fluctuation, and then shows a level drop. However, with the assumption of a pure diffusion process and despite the higher hydraulic diffusivity in the upper layer, pore pressure response should appear firstly at the larger depth, the closer position with respect to the well screen, i.e. at the position below the less pervious layer. The fact that a response first occurs at the more shallow, i.e. the farther position, demonstrates again the influence of fluid-matrix coupling.

4.3.3 4-Layer Model

The first more realistic subsoil model may be the 4-layer scenario. Geometry and parameters are as in Tab.4.5. Fig.4.14 shows the time dependent contour lines of the tilt zero-line together with selected zoom-outs plotted after the same concept as in the previous sections. The zero-line at 108 s is left out.

The time series of the pore pressure signal from $z = 15\text{ m}$, $r = 10\text{ m}$, shows the Noordbergum effect with a duration of nearly 40 min and a maximum amplitude of 25 Pa . This is about a rise in level of 2.5 mm , Eq.2.4, four times smaller than the effect recorded at site BV, Fig.3.26. The diagram here below, $z = 85\text{ m}$, $r = 10\text{ m}$ shows a pump induced draw down of about 43 kPa in well head. The range of the signal amplitude, it equals a lowering of about 4.3 m , is like observed in the active wells at site OE. However, extraction rate at OE is 2.5 times larger than in the calculation here. Tilt response from $z = 4\text{ m}$, $r = 120\text{ m}$, upper right side, also shows a signal with a strength similar to the tilt observations, e.g. at position T1_{OE} at site OE in response to pumping from B1_{OE}, see Fig.3.17 – even if the response in the observed data is more rapid. The latter fact could be due to a signal delay from the larger geometrical distances in the model than at site OE. The calculated tilt signal achieves only about half the amplitude of the steady state solution. The latter is denoted in the plot by the line beside ‘MAX’.

A more rapid tilt response with a subsequent negative reversal was calculated at points $z = 55\text{ m}$ and $r = 135\text{ m}$, 140 m , 155 m , drawn in the mid of the right side in Fig.4.14. The three tilt signals are similar to the ones already seen at the same depth in the previous 3-layer model. However, amplitudes are about two times stronger. The negative tilt reversals measured at site OE and BV can not be matched to these curves here. For this purpose, the calculated signals should appear much closer to the surface, i.e. the zero-line (and the whole field) should show its transient fluctuations at more shallow depths. This can be caused by an additional less pervious layer close to the surface. In the first 6-layer steady state model, Fig.4.5, the zero-line was ‘pulled-up’ by adding an additional loam mix layer at depths 10 m to 20 m with respect to the steady state 4-layer model, Fig.4.4. Moreover, the tiltmeters, which recorded negative tilt reversals at sites OE and BV, were installed below a less pervious layer, the topsoil. The next model will consider an adjusted 6-layer scenario to produce negative tilt reversals with amplitudes in the range of the measurements at site OE and at shallow depth below a less pervious layer.

However, an additional aspect of the 4-layer model is in the upper part of the clay layer at the bottom of the model section. A stronger and long lasting Noordbergum effect appears. This is shown in the zoom-out at the bottom of the left side in Fig.4.4. The pore pressure signal is calculated at position $z = 140\text{ m}$, $r = 30\text{ m}$ for a 10 h pump test with 10 h of regeneration. The Noordbergum effect has a maximum amplitude of about 0.3 kPa here, i.e. a corresponding rise in well head of about 3 cm , and lasts over 2.8 h . When withdrawal of ground water is stopped, the fluid level does not start rising immediately. Lowering goes on. This is due to the very low hydraulic diffusivity of the clay layer. Processes are drastically delayed. Compared with the steady state for infinite pumping in Fig.4.4, after 10 h of pumping, the amplitude has reached only about one tenth of its final value.

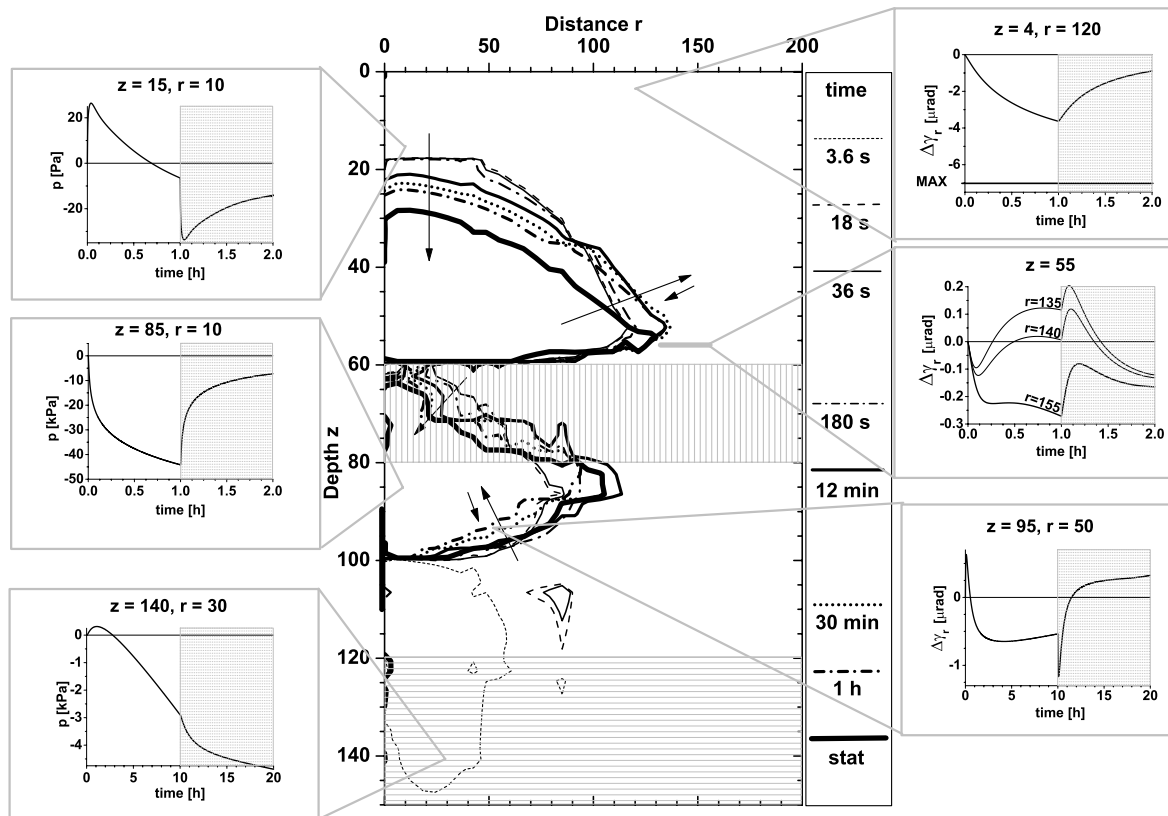


Figure 4.14: Evolution of zero-line of tilt in 4-layer model for selected time steps and zoom-outs of time series from selected points. Parameters and geometry as in Tab.4.5.

Another, new type of tilt response occurs around position $z = 95 \text{ m}$, $r = 50 \text{ m}$. The movement of the zero-line first shows a contraction followed by an expansion. The zero-line after 30 min is inside the steady state line, but outside the line that appears after 1 h . That motion is reflected in the tilt signal plotted in the zoom-out at the bottom of the right side of Fig.4.4. The signal is depicted for a 10 h pump cycle. On this time scale, a rapid positive tilt reversal is followed by a gradual negative one which ends up in a slow drift back towards positive tilt. A likewise calculation of a longer pump cycle of 50 h confirms that the tilt signal crosses zero from negative to positive response after about 25 h . The general behaviour of this tilt signal, despite its rise times of signal flanks and exact amplitudes, looks in principle like the horizontal mirror inverse of the signals drawn in the zoom-out above, from $z = 55 \text{ m}$. Such type of behaviour was not seen in the 3-layer model and thus appears to be a consequence of the bottom layer of clay here.

4.3.4 Adjusted 6-Layer Model

The adjusted 6-layer subsoil model was used to describe (qualitatively) the negative tilt reversals measured at T1_{OE} and also at T2_{BV} where at the same time the Noordbergum effect was observed. The geology of the experimental sites is in principle, but not true to scale, translated to the model here. The topsoil layer is taken into account by a less pervious layer at a depth between 10 m and 20 m . The model is more general than a model where the topsoil is placed immediately at surface. It respects a free upper aquifer, too. A subsoil of such a type is often reported from the Lower Rhine Embayment (GLA-NW, 1988, Hennigsen & Katzung, 1998, Verbandswasserwerk, 1998).

For a better comparison to the former calculations, the model geometry of the steady state 6-layer model in section 4.2.3 was used. The poroelastic properties of the 6-layer model were adjusted in iterative steps until the calculation grossly fits the general courses of tilt and pore pressure observations. This led to new parameter sets for the single layers. The parameters that were finally adapted are listed in Tab.4.9. Due to these new values other names for the layers were applied.

depth	stratum	G	ν	ν_u	B	D	α	K_f
0 ... 10	1.aquifer, GW 1	0.14	0.12	0.43	0.86	11.9	0.995	$5 \cdot 10^{-4}$
10 ... 20	1.aquiclude	0.39	0.16	0.36	0.65	0.0227	0.998	$5 \cdot 10^{-7}$
20 ... 60	2.aquifer, GW 2	0.08	0.08	0.45	0.95	20.2	0.959	$1.3 \cdot 10^{-3}$
60 ... 80	2.aquiclude	0.410	0.19	0.37	0.65	0.0445	0.978	$8.4 \cdot 10^{-7}$
80 ... 120	3.aquifer, GW 3	0.125	0.08	0.44	0.92	1.09	0.970	$4.8 \cdot 10^{-5}$
120 ... ∞	basement	0.50	0.25	0.40	0.75	0.0104	0.857	$1 \cdot 10^{-7}$

Table 4.9: Poroelastic parameters and geometry for a 6-layer model that is adjusted to match negative tilt reversals at shallow depth. [G] = GPa, [D] = m^2/s , [K_f] = m/s . All digits are significant. Geometry in m .

Adjustment of the model was achieved as follows: With respect to the first 6-layer model, Tab.4.6, hydraulic diffusivity D was increased in the second aquifer and in the second aquiclude. The D -value was decreased in the third aquifer GW3 that is tapped by the production well. In GW3, in principle, a large value of D causes tilt of minor strength with a rapid rise of the signal flank, whereas low values of D cause a delay in tilt response, but a larger amplitude. Wang & Kümpel (2003) already showed this influence of the hydraulic diffusivity. Additionally, the shear modulus G was decreased in all layers, so that the whole half-space is less rigid and allows larger, but slower deformation response to pumping. These modifications lead to (1) a larger tilt amplitude in the region of the third aquifer, (2) a faster propagation of that tilt response through the second aquifer (with a high D) and (3) a larger deformation in the second aquifer (as G is smaller there). In a homogeneous half-space, amplitude and rise time of the tilt signal behave opposite to each other if parameters D or G are varied. In a layered half-space the parameters can be adjusted for each stratum separately. With respect to the whole (layered) half-space, this allows to overcome the opposite influence of both these parameters.

Moreover, with respect to the values in Tab.4.6, the contrasts of the values of the shear modulus between layers was increased for the second and third aquifer and their adjacent aquicludes. It turned out that a (aquiclude) layer with a large value of G placed in the top region of an aquifer with a low value of G ‘pulls up’ and spatially extends the tilt zero-line, if previously the zero-line was in that aquifer; compare the steady state models in section 4.2. Furthermore (except in the basement of the model), the Poisson ratio ν was reduced, strongest in the aquifers. This leads in steady state to a somewhat contracted zero-line, compare Figs.4.8(a), (c). The latter adjustment works in opposition to the pull-up and extension caused by the high contrast in shear modulus. Both modifications, reduced ν and high contrast in G cause the flank of the zero-line to become steeper.

The other parameters, undrained Poisson ratio, ν_u and Skempton coefficient, B were adjusted only to take care for the different porosities of aquifers and aquicludes, to keep the condition for α , see Eqs.2.11, 2.14. B is increased in the aquifers and decreased in aquicludes, in both cases by about 0.1. α gets high values close to 1.00. The α -values for the aquifers are now (slightly) smaller than the values for the aquicludes (compare also the start values in Tab.4.6). Only the value in the first aquifer is somewhat larger, which is due to a smaller value of B with respect to the other aquifers here. This, and also the slightly larger values of G and ν in this upper stratum accounts for a possible compaction of GW1. The

basement has the lowest value of α that is caused by the smaller difference between ν and ν_u , and a higher value of B with respect to the aquicludes.

Fig.4.15 shows the zero-line of tilt for different time-steps during 1 h of pumping and for the steady state together with selected zoom-outs like in the previous sections.

In the second aquifer, GW 2, the zero-line clasps a wide area. Time variation of its course in that part of the model is largest at the flank, i.e. around a radial distance between $r = 120\text{ m}$ at its upper part and $r = 170\text{ m}$ at its lower part. The movement of the line is indicated by the arrows. Negative reversals of tilt occur in the upper part, whereas in the lower part movement of the zero-line is monotonously. Monotonously is also the movement of the line in the third aquifer, in contrast to the 4-layer and the 3-layer models. Some erroneous loops of the zero-line initially appear in the model region of the third aquifer.

The first zoom-out, upper left side of Fig.4.15, from position $z = 15\text{ m}$ and $r = 5\text{ m}$ in the upper aquiclude shows, from top to bottom, tilt response $\Delta\gamma_r$ and vertical and horizontal displacements, u_z and u_r . All signals are strictly monotonously indicating tilt towards the well, subsidence and displacement in direction to the well axis, respectively. At radial distance $r = 100\text{ m}$, the zoom-out at the upper right side of Fig.4.15, subsidence, indicated by u_z , is not so strong as at the previous position, but horizontal displacement seen in u_r has a larger amplitude.

Negative tilt reversals occur below the upper aquiclude, at point $z = 22.5\text{ m}$, $r = 135\text{ m}$ shown in the zoom-out in the middle part of the right side of Fig.4.15. This is the new type of signal measured at T1_{OE} in response to pumping from B2_{OE}, Fig.3.7, and observed at T2_{BV} when ground water was pumped through B2_{BV}, Fig.3.26. The drop of the modelled signal down to an amplitude of nearly $-0.4\ \mu\text{rad}$, until the negative reversal, takes around 12 min, longer than in the measurements. Also, the absolute maximum amplitude, when the signal reverses, is minor, especially with respect to site BV. At this site, the amplitude was about $-4\ \mu\text{rad}$, ten times stronger than here, and with an extraction rate of only $2.5\text{ m}^3/\text{h}$, 40 times smaller than in the model. With respect to the situation at site OE the amplitude matches somewhat better. In this experiment extraction rate was $250\text{ m}^3/\text{h}$, 2.5 times larger than in the model, and tilt response, when the signal reverses, was measured to be $-1.0\ \mu\text{rad}$ to $-1.2\ \mu\text{rad}$. Even if the model only grossly matches the overall subsoil structure at the sites, the modelled and observed signals show qualitatively the same behaviour. However, the fact that the accompanying positive tilt reversals, see Figs.3.19, T9R_{OE}, T7R_{OE}, did not appear in this model suggests the need of further refinements.

The zoom-out at the bottom of the left side of Fig.4.15 from point $z = 70\text{ m}$, $r = 5\text{ m}$ depicts tilt response $\Delta\gamma_r$ as well as displacement components u_z and u_r . The tilt signal shows a positive tilt reversal in the center depth of the second aquiclude. After onset of pumping the signal grows rapidly to positive values and then, more slowly, decreases to smaller amplitudes. The amplitudes of displacement u_z in the lower aquiclude at $z = 70\text{ m}$, $r = 5\text{ m}$ have a strength of -3.18 mm after one hour of pumping. Subsidence is stronger than at the shallow position $z = 15\text{ m}$ and $r = 5\text{ m}$, in the center depth of the upper aquiclude, where u_z has a strength of -2.39 mm after the same time span. The radial displacement u_r is stronger at the deeper position, too. With the assumption that these displacement components reflect the local motion of the whole aquicludes near the well axis, the deeper aquiclude shows a stronger subsidence than the upper one.

The displacement u_z from position $z = 15\text{ m}$, $r = 100\text{ m}$ has an amplitude of -1.52 mm , which is of nearly the same strength as u_z from the deep aquiclude at position $z = 70\text{ m}$, $r = 100\text{ m}$, where an amplitude of -1.49 mm is induced after one hour of withdrawal. Also, the difference in u_r between both the latter positions is small. At position $z = 15\text{ m}$, $r = 200\text{ m}$ (time series are not depicted), u_z has an amplitude of -0.64 mm and at $z = 70\text{ m}$, $r = 200\text{ m}$ of -0.56 mm . Here u_r is also smaller at the deeper position. A slight (transient) uplift of the clay layer at the bottom of the model is indicated by the displacement component u_z from point $z = 125\text{ m}$, $r = 15\text{ m}$ denoted by the grey dot in the contour plot and drawn in the zoom-out at the lower right corner of Fig.4.15.

Fig.4.16 qualitatively summarizes, like suggested by the calculated time series, the possible vertical motions of the model layers and tilt in sketches of three time steps. In Fig.4.16(a) the pump is not active, the

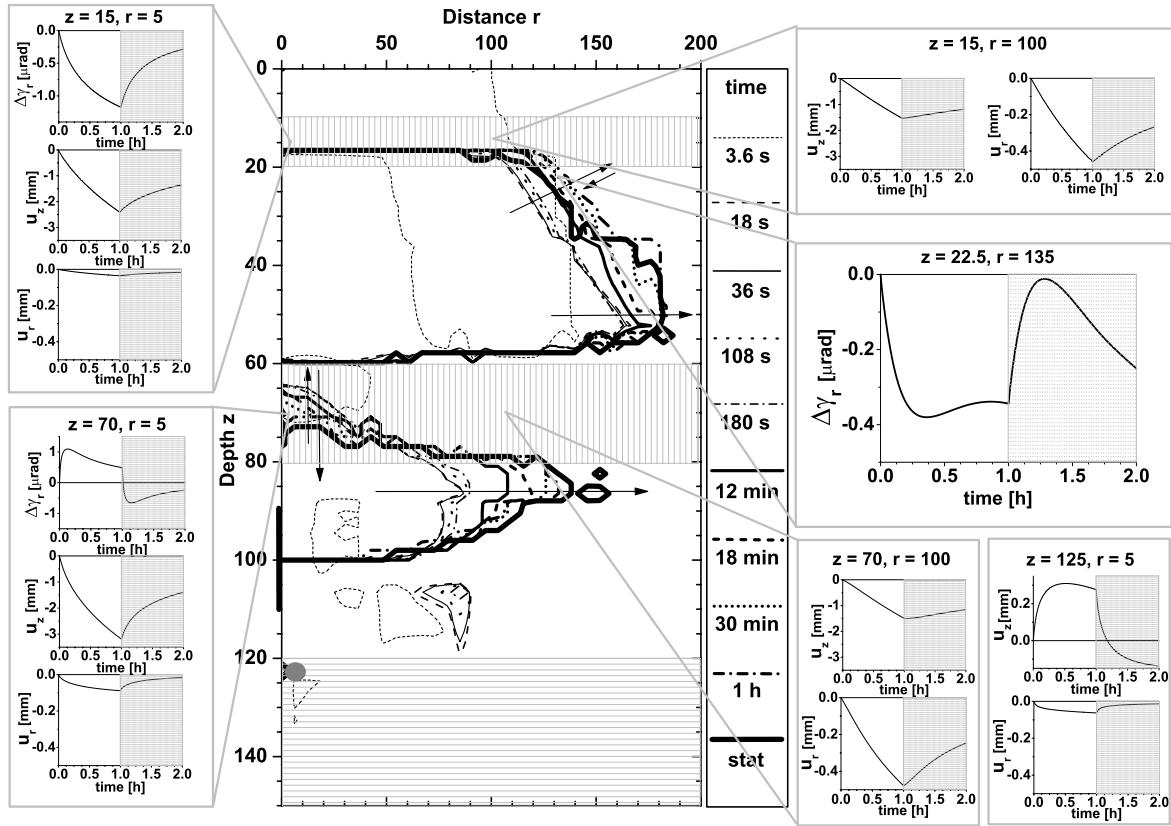


Figure 4.15: Evolution of zero-line of tilt in adjusted 6-layer model for selected time steps and zoom-outs of time series from selected points. Parameters and geometry as in Tab.4.9. Pore pressure data is plotted in Fig.4.17.

layers are horizontally and the tiltmeter vertically aligned. When the pump is switched on, Fig.4.16(b), an initial negative tilt response occurs, the layers above the well show a subsidence, the bottom layer, AC-3 an uplift. During ongoing pumping, Fig.4.16(c), subsidence of the lower aquiclude AC-2 is stronger than that of AC-1, uplift of AC-3 forms back.

The modelled pump induced pore pressure is presented in Fig.4.17. Unfortunately, the contour plot of the pore pressure zero-line, which clasps areas where the Noordbergum effect occurs is not very accurate. This is caused by the gridding process used for contour line plotting. To overcome that disadvantage several zoom-outs are drawn in Fig.4.17.

The first zoom-out is taken from point $z = 4\text{ m}$, $r = 40\text{ m}$, upper left side. A faint but long lasting Noordbergum effect appears. This is due to the two less pervious aquicludes that cause a long signal delay and therefore prevent pore pressure to drop stronger close to the surface. The zoom-out here below, from position $z = 40\text{ m}$, $r = 10\text{ m}$, shows that the Noordbergum effect also occurs in the section of GW 2 close to the well, even if it is not indicated by the course of the zero-line of pore pressure. Here, the effect has a maximum amplitude of 0.03 kPa corresponding to a rise in well head of 3 mm and a duration until 20 min after the onset of the pump. The amplitude of the Noordbergum effect measured at site BV is three times larger, Fig.3.26. Its duration was about 10 min to 15 min and initiated by a sharp rise in pore pressure. In the model, the effect is preceded by an initial drop in the signal, i.e. a double reversal occurs.

At a somewhat larger radial distance, $z = 40\text{ m}$, $r = 50\text{ m}$ the Noordbergum effect is smaller, the maximum amplitude is 0.01 kPa with a duration of nearly 10 min and is associated with a smaller preceding drop

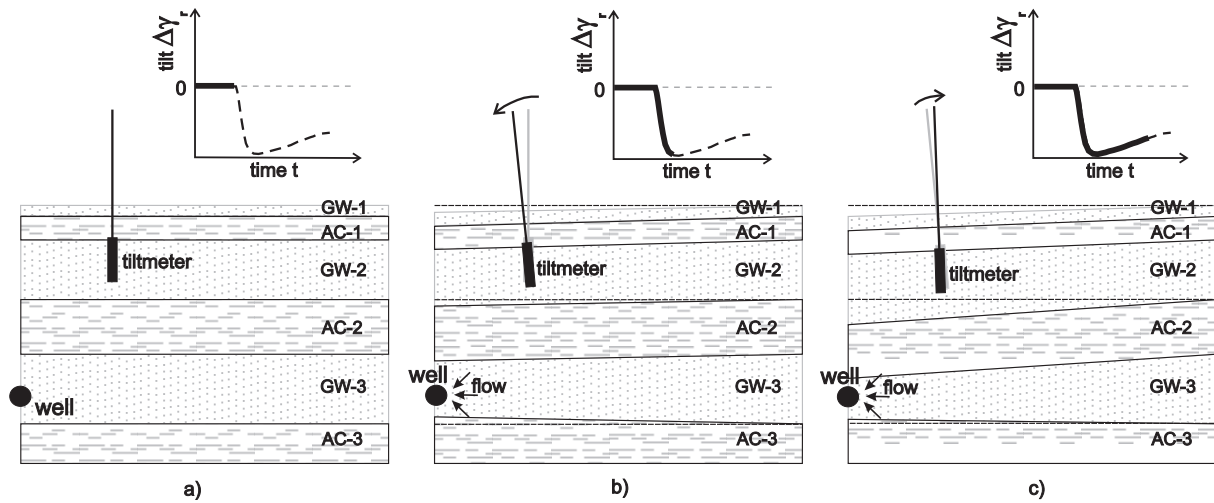


Figure 4.16: Sketch of possible vertical layer motions and tilt like suggested by the adjusted 6-layer model. Evolution of tilt $\Delta\gamma_r$ until the present time is sketched by the thick line in the diagrams, its further path by the thin dashed, curved line. The present strike of the tiltmeter is made clearly noticeable by the straight line attached at the tiltmeter's top, the foregoing position by the grey line. (a) pump is off, layers and tiltmeter are in rest. (b) pump has just been turned on, layers above the well show initial subsidence, the tiltmeter strikes towards the well. (c) Ongoing pumping, subsidence of AC-2 gets stronger and stronger with respect to subsidence of AC-1, tilt turns back. Not true to scale.

in pore pressure. The Noordbergum effect also appears in the second aquiclude. At position $z = 70\text{ m}$, $r = 10\text{ m}$, it has a strength of 1 kPa and a duration of 6 min . A double reversal is not observed here. Somewhat more horizontally apart, position $z = 70\text{ m}$, $r = 40\text{ m}$, pore pressure rise is 0.1 kPa . Some very faint double reversals in pore pressure are depicted in the zoom-outs placed at the right side of Fig.4.17. In the upper free aquifer, positions $z = 4\text{ m}$, $r = 135\text{ m}$ and $z = 4\text{ m}$, $r = 180\text{ m}$, somewhat strange examples of this type of pore pressure responses occur, see also Fig.4.11.

The position where the negative tilt reversals occur, $z = 22.5\text{ m}$, $r = 135\text{ m}$, is close to the boundary of the section in which the Noordbergum effect occurs. Here, the pore pressure effect is present, but extremely small with an amplitude of 0.005 kPa and a duration of 2.4 min . Somewhat deeper and horizontally apart, $z = 40\text{ m}$, $r = 170\text{ m}$, the pore pressure response is strictly monotonously and the signal drop continues in the selected time window, even if the pump is stopped. The next zoom-out below shows the pore pressure signal calculated at position $z = 55\text{ m}$, $r = 30\text{ m}$ close to the upper boundary of the deep aquiclude. The Noordbergum effect appears with an amplitude of 0.01 kPa , a duration until 15 min after onset of pumping and a preceding drop, i.e. again a double reversal. The last two zoom-outs at the bottom of the right side of Fig.4.17 show the pore pressure signal from position $z = 90\text{ m}$, $r = 170\text{ m}$ and from position $z = 110\text{ m}$, $r = 60\text{ m}$. The former diagram shows that also in the productive aquifer, the drop in pore pressure goes on after cessation of the pump. Again, this is mostly determined by the hydraulic diffusivity of that aquifer.

Another aspect of most of the modelled time dependent signals is that the steady state is not nearly achieved. In the adjusted 6-layer model, no signal seems to end in steady state. Except for the tilt signal with the negative reversals from position $z = 22.5\text{ m}$, $r = 135\text{ m}$, Fig.4.15, where indeed the signal temporarily rests at a plateau. If only such a signal is observed until the plateau is achieved, it could be deceptively assumed that the signal will no longer change. Many of the observed radial pump induced tilt responses, except at site WD, may suggest that the steady state is achieved after some hours, or at the latest, after a day of pumping. To obtain a gross theoretical estimation about the time when steady state is achieved, long-term time series for tilt, pore pressure and displacement response were calculated at selected points of the adjusted 6-layer model and are discussed in the next section.

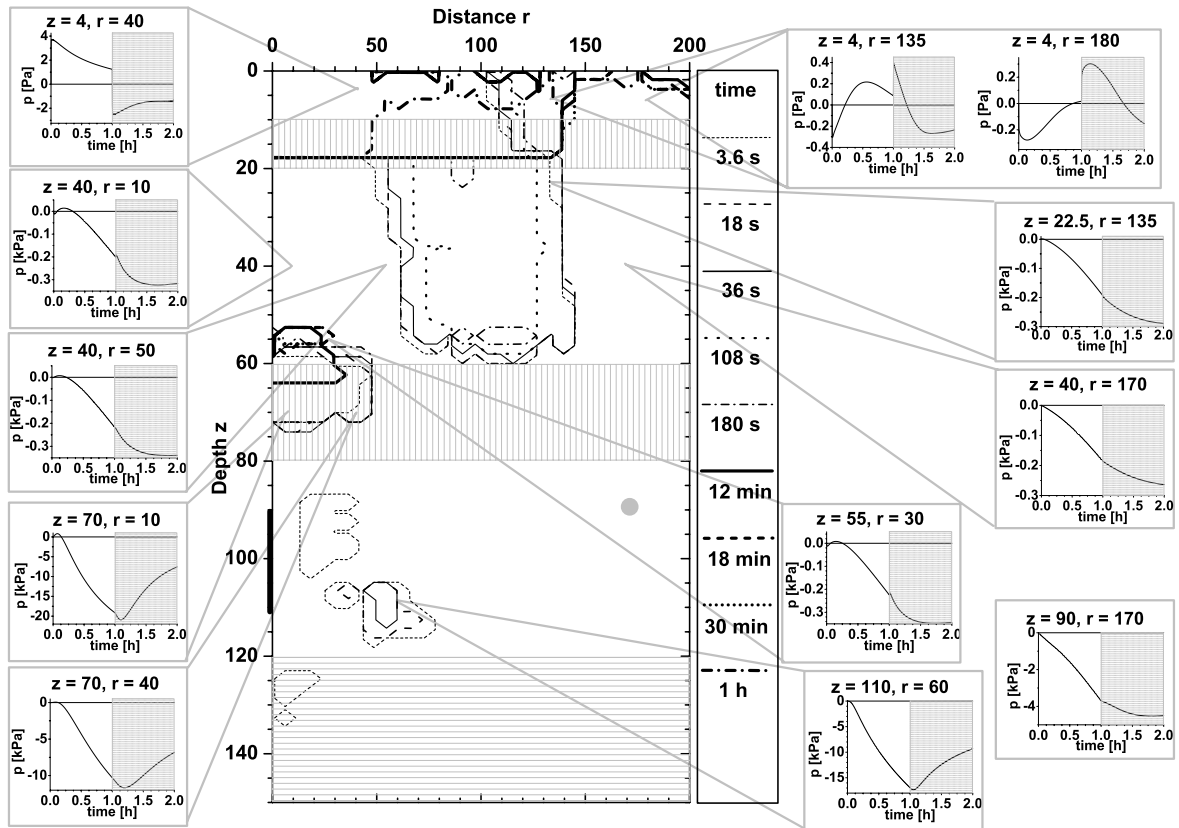


Figure 4.17: Evolution of zero-line of pore pressure in adjusted 6-layer model for selected time steps and zoom-outs of time series from selected points. Parameters and geometry as in Tab.4.9.

4.3.5 Long-Term Signal Evolution, Adjusted 6-Layer Model

Fig.4.18 shows the long-term calculation for tilt and displacement as zoom-outs from the steady state contour plot of the adjusted 6-layer model. The first two are from position $z = 4\text{ m}$, $r = 300\text{ m}$ at the top of the figure. Both insets show radial tilt response $\Delta\gamma_r$ (black line), vertical displacement u_z (dash-dotted line), and radial displacement u_r (dotted line). The left diagram illustrates the time series for pumping over 100 days with an extraction rate of $100\text{ m}^3/\text{h}$. The right one accounts for a duration of withdrawal of 600 days at a rate of $350\text{ m}^3/\text{h}$ (and therefore does not correspond to the amplitudes in the contour plot). Amplitude ratio between both diagrams (of all signals) is a factor of about 3.5. Tilt response in both insets achieves steady state after 80 days to 100 days with an amplitude of $-8.5\text{ }\mu\text{rad}$ in the left inset. Radial displacement u_r seems to reach steady state with a value of nearly -5.5 mm after a time span of about 500 days (right). Subsidence indicated by the ongoing drop in u_z did not stop, even after 600 days of pump activity in the right inset.

The zoom-outs at the left side of Fig.4.18 show the tilt response from three radial distances, $r = 120\text{ m}$, 135 m , 170 m at two depths. The first is from $z = 15\text{ m}$ in the center of the upper aquiclude, and the second from $z = 22.5\text{ m}$ around the position where the negative tilt reversals occur, see Fig.4.15. The

time series are now calculated for 12 h of withdrawal each. Tilt signals from $z = 15\text{ m}$ show a monotonous response that is stronger at the positions closer to the well. At the depicted time scaling the curves are not stationary at the end of pumping. Since the typical time span of pump tests in this study is of about 2 h (shaded in grey) steady state, as previously stated, may not have been achieved in the experiments.

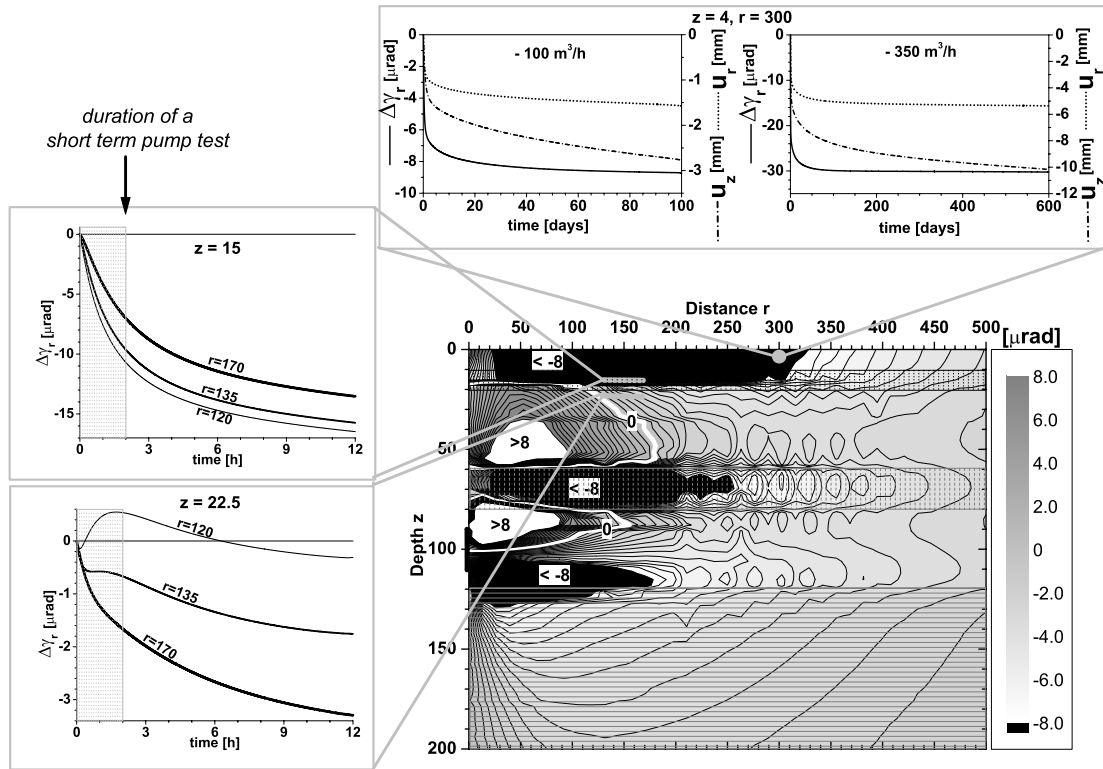


Figure 4.18: Steady state solution and long-term signal evolution of tilt for the adjusted 6-layer model, Tab.4.9. Zoom-outs show signal evolution at selected positions. Steady state tilt maximum at surface is in a radial distance of about 98 m with an amplitude of $-21\ \mu\text{rad}$. Geometry in m.

More different in their course and their radial dependence are the tilt signals from the deeper position at $z = 22.5\text{ m}$ in the upper part of the second aquifer. At $r = 120\text{ m}$, a negative tilt reversal followed by a positive excursion with an additional negative response hereafter. This is a double reversal. Due to contour plotting in differently sized cross sections of the model in Fig.4.18 and Fig.4.15, this tilt signal behaviour did not exactly correspond to the spatial fluctuation of the tilt zero-line in Fig.4.15. The time series at $r = 135\text{ m}$ corresponds better and shows the negative reversal as already seen from that position in Fig.4.15. Actually, after the tilt signal has passed its negative reversal, it lasts at a certain level for about 1 h before it gets unstable and a further ongoing response to negative values starts.

Long-term pore pressure signals of the adjusted 6-layer model together with the steady state contour plot are shown in Fig.4.19. The upper right zoom-out, from point $z = 4\text{ m}$, $r = 300\text{ m}$ in the first free aquifer shows a temporary plateau in the pore pressure signal. After about 70 min, pore pressure starts falling again. Pumping lasts over 3 h. Double reversals, like previously seen at smaller radial distances, Fig.4.17, do not occur here.

Pore pressure signals from depth $z = 22.5\text{ m}$ and radial distances $r = 120\text{ m}$, 170 m are drawn in the upper zoom-out at the left side of Fig.4.19. At both positions steady state is not achieved after 12 h of pump activity. The curves cross each other because at the position closer to the well, the Noordbergum effect and final drop in well head is stronger than at the more distant place.

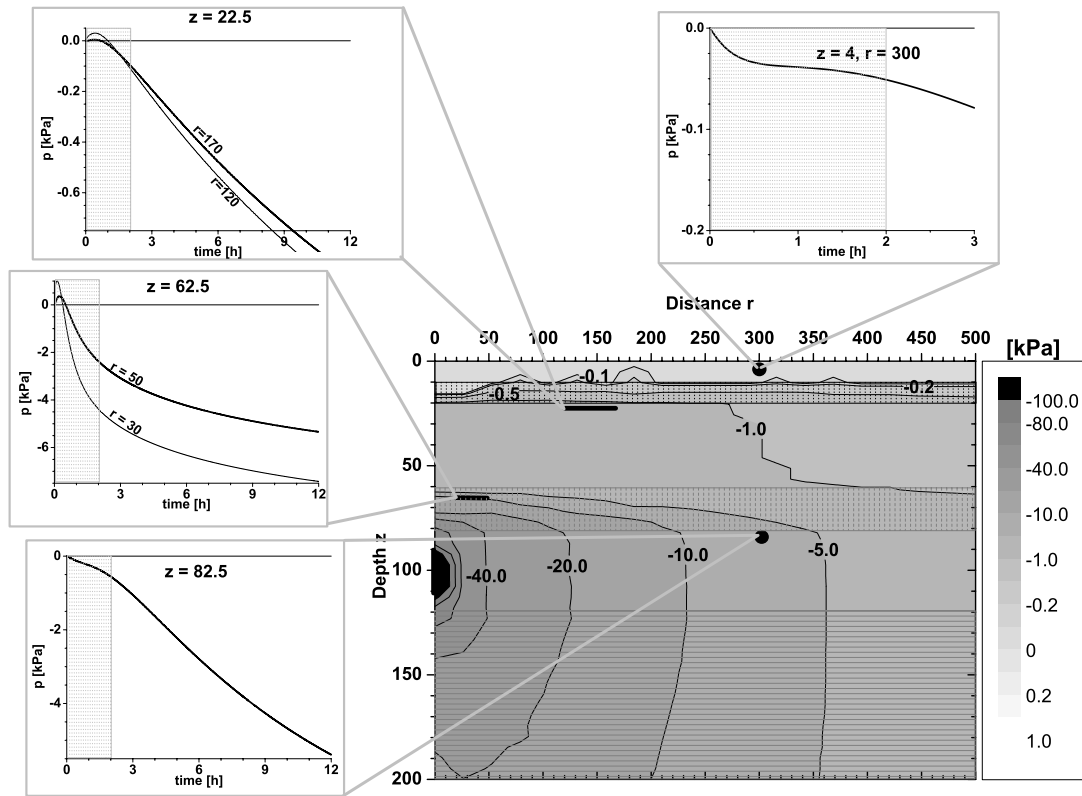


Figure 4.19: Steady state and long-term evolution of pore pressure data for the adjusted 6-layer model, Tab.4.9. Geometry in m . Close to the surface, the contour plot depicts wrong values due to the plotting routine.

At two deeper positions, $z = 62.5 m$, $r = 30 m$, $50 m$, in the upper part of the deep aquiclude, the signals show a stronger Noordbergum effect and final drop in pore pressure. Again, steady state is not achieved after $12 h$ of withdrawal. A stable pore pressure signal is also not reached after $12 h$ at position $z = 82.5 m$, $r = 300 m$ in the productive aquifer, as shown in the last zoom-out at the bottom of the left side in Fig.4.19. At this point, pore pressure was also computed for a longer time span. Fig.4.20 shows the result. Steady state is nearly reached after about $100 h$ of pumping.

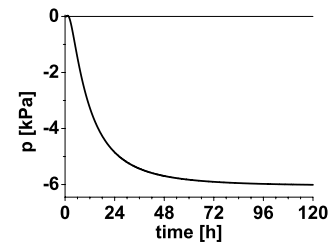


Figure 4.20: Long-term pore pressure signal calculated at position $z = 82.5 m$, $r = 300 m$ in the productive aquifer of the adjusted 6-layer model.

4.3.6 Sensitivity of Transient Signals to Variations of Parameters and Layering

During computation of the adjusted 6-layer model it turned out that especially the transient signal part showing reversals at more shallow depths, is sensitive to variations of poroelastic parameters even in deeper layers. To numerically test the general sensitivity, the parameters of the deeper, less pervious layer from $z = 60 m$ to $80 m$ of the first 6-layer model were altered. Original geometry and parameter values are in Tab.4.6. The response signals of tilt and pore pressure were recalculated. In every step of recalculation, each of the five poroelastic parameters was changed independently from the others, first to a lower and second to a higher value than in Tab.4.6.

Fig.4.21 shows the alterations of the pump induced tilt and pore pressure responses from position $z = 22.5 m$, $r = 90 m$. Fig.4.21(a) displays the transient tilt signals for a $1 h$ pump test with $1 h$ of relaxation and Fig.4.21(b) the corresponding pore pressure responses. From top to bottom the parameters G , ν , ν_u ,

B and D were tuned. The solid lines in (a), (b) show the signal response without a parameter variation. This signal is repeatedly shown in each panel, all five times. The dashed lines mark the response signal if the corresponding parameter is decreased, the dotted lines indicate an increased value.

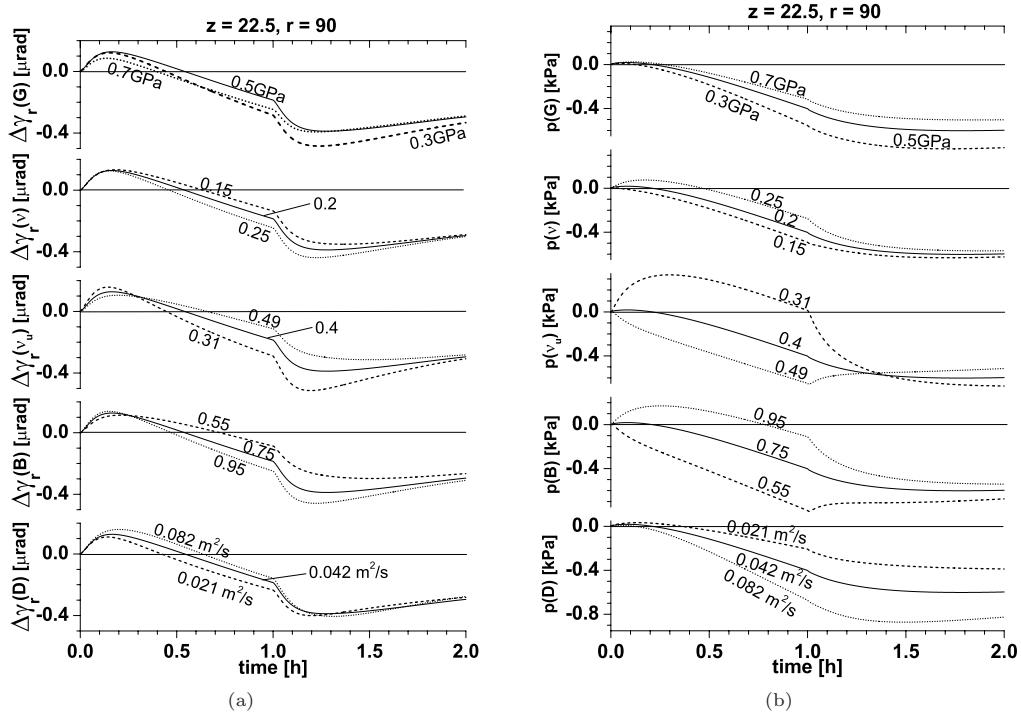


Figure 4.21: Parameter sensitivity of transient tilt, (a) and pore pressure signals, (b), calculated for position $z = 22.5\text{ m}$, $r = 90\text{ m}$ of the first 6-layer model as in Tab.4.6. Single parameter values of the layer at depth $z = 60$ to 80 m were changed as denoted in the corresponding plots. The adjusted parameters from top to bottom are G , ν , ν_u , B and D .

If the shear modulus G is increased, absolute tilt amplitudes become smaller and zero-crossing is earlier than in the unchanged case. The same behaviour, but less strong, occurs for a decreased shear modulus. The latter fact appears to be unexpected for a homogeneous half-space, but might be a consequence of layering. In pore pressure response, for an increased G , the Noordbergum effect is slightly enhanced, whereas the remaining signal gets smaller. If G is decreased, the Noordbergum effect is also decreased in its amplitude and the ongoing signal shows larger absolute values.

Changes of tilt and pore pressure response to variations of the other parameters can be inspected in Fig.4.21 in a similar manner. Variation of Poisson ratio ν , in the applied range, shifts almost the complete time series of tilt and pore pressure. Only the first absolute maximum in tilt is mostly unchanged. The curves depicting pore pressure response spread in the plot vertically from a variation of the Skempton coefficient B and hydraulic diffusivity D , whereas an alteration of the parameters also caused a different type of signal, e.g. ongoing rise or drop, after cessation of the pump. The remaining signals cross each other during pumping or relaxation, if parameters are changed. Many additional systematical investigations of these dependencies from parameter variations in single layers or more complex situations may be possible. The important fact is that altered parameters in a comparatively deep layer can cause a small, but detectable change in transient tilt and pore pressure response to pumping.

Precision measurements of these transient signals could open up a new technique for a comparatively accurate determination of poroelastic parameters. Compared with the range of natural parameter variations, see also Tab.2.3, the sensitivity of short term tilt observations like e.g. over one hour, seems to be best for changes in shear modulus G , undrained Poisson ratio ν_u , Skempton coefficient B , and hydraulic diffusivity D . For longer observation times tilt measurements also become more sensitive to changes in the Poisson ratio ν . For a short observation time, pore pressure measurements seem better suited to recognize changes in the parameters. However, in contrast to the tilt response, the overall amplitude of the pore pressure signal rapidly decreases at each additional, less pervious layer. The signal may become undetectable under certain subsoil conditions. That problem also occurs in the determination of layer

boundaries of aquifers from pore pressure observations during common pump tests. Singh (2001) investigated this problem. Even with enhanced analyses, the accuracy of boundary determination from level observations strongly depends on the duration of pumping, i. e. how strong the signal gets beyond a less pervious layer. Amplitudes of tilt signals seem to decrease not so strong at layer boundaries. Thus, tilt measurements seem better suited here. They may be able to support the type of hydrological analyses outlined in Singh (2001).

Here, only the parameter dependency of transient signals with reversals is estimated. The signals were calculated for positions in a depth range of some m and are not very close to surface. It seems also possible to use recordings from more shallow positions and without signal reversals for reservoir controlling. In that case determination of parameters may be not so accurate as here. No zero crossing of the signal appears and adaption of calculation to data becomes more difficult. This is a general disadvantage of observations at a larger distance, apart from the zero-line. The problem could possibly be reduced if more tiltmeters at shallow depth were used and all signals were fitted simultaneously. The reservoir parameters may be derived from the course of the signals, the change of parameters during exploitation from the change of the signals' course from pump-cycle to pump-cycle. A study of the determination of hydraulic parameters from the transient well level response to pumping, also from occurrence of the Noordbergum effect, is presented by Broska & Barnette (1999). Again, additional tilt observations could support the approach and may reduce the number of degrees of freedom in measurements and interpretations.

However, only the sensitivity of synthetic signals were tested. For an experimental test of the sensitivity of the transient signals to a variation of subsoil parameters, measurements have to be conducted at different sites with known geological settings, or at a site where the settings change in a known manner. An experimental test in controllable analogue models in the laboratory seems better suited.

Another aspect emerged during dynamic modelling was the type of movements of the tilt zero-line in dependency of the selected layering. Tab.4.10 has an overview of the layering in the used model subsoil and the corresponding types of calculated transient tilt signals. Even if the dependency listed in Tab.4.10 accounts only for the models here, the fact that there seems to be a connection between special types of zero-line movements and layering might be used for further interpretations. Again, the dependency may be investigated in small scale analogue models in the laboratory, where the layer structure can be arranged in a controlled manner.

Fig.	layering	type of transient tilt response
4.9	homogeneous half-space	<ul style="list-style-type: none"> • monotonously contracting zero-line, • positive reversals only
4.13	3-layers	<ul style="list-style-type: none"> • positive reversals in the upper part of the zero-line, • double reversal, first negative then positive at the flank of zero-line above and below the intermediate layer
4.14	4-layers	<ul style="list-style-type: none"> • positive reversals in the upper part of the zero-line, • double reversal, first negative then positive at the flank of zero-line above and below the intermediate layer, • double reversal, first positive then negative at the bottom of the zero-line below the intermediate layer
4.15	6-layers, adjusted	<ul style="list-style-type: none"> • no reversals in the upper part of the zero-line, • double reversal, first negative then positive at the flank below the first intermediate layer, • positive reversal in the second intermediate layer • monotonous movement at the flank and the bottom of the zero-line, above and below the second intermediate layer

Table 4.10: Overview of the transient tilt signal features and related layer structure of the used models.

Chapter 5

Discussion

Some aspects of surface deformation imaging, of tiltmeter operation and of the modelling approach will be discussed in the following.

5.1 Surface Deformation Imaging

Observations with tiltmeter clusters installed at shallow depth are one method among others to measure (pump induced) soil movements. Hence, the method applied here demonstrates only one way to obtain surface deformation images. Other techniques used for observations of e.g. tectonic processes or landslides can be applied, too. Such methods are, for instance, levelling, GPS (Global Positioning System) (Campbell et al., 2002, Mora et al., 2003), scattering techniques (e.g. laser scanning) (Colesanti et al., 2003, Haugerud et al., 2003, Rowlands et al., 2003) or satellite based altimetry techniques like InSAR (Interferometric Synthetic Aperture Radar) (Vasco et al., 2002b). Especially the latter both allow, in principle, a dense coverage of the experimental site with observation points. Still, a more extended array of tiltmeters and a longer observation time at single tiltmeter positions is advantageous. However, the advantage of tilt measurements is high precision in quasi continuous observation mode at moderate costs. Generally, the number of instruments that is finally required depends on the local variability of the geological structures in subsoil and on the strived spatial resolution. The here obtained surface deformation images confirm a comparatively good practicability of the new method using tiltmeters.

It would be useful to install a tiltmeter array at some site that has a known distinctive structure in subsoil, e.g. with a buried quaternary channel like at site WD. This will be a further and possibly better test for the method than the ‘flat’ situation at OE. The data from site OE confirms with a high significance the mostly horizontally layered stack of subsoil strata that has already been known from former geological interpretations. However, to assess a more heterogeneous situation by poroelastic modelling, additional investigations into 2-D and 3-D (interpretation) techniques need to be done.

The surface deformation images shown here were drawn from averaged tilt values. Moreover, due to the calculation of these mean values from a small number of selected tilt amplitudes in response to single pump cycles of variable length and with residual disturbances, errors were somewhat large. Accordingly, the surface deformation images neither account for the tilt field established after a certain time of pumping nor for the field in steady state. Surface deformation imaging should be carried out with time resolution and with a larger data basis. The images could be drawn from the data obtained exactly after certain times during pumping and relaxation. The pump cycles itself should preferably be of equal length.

The superposition principle was used for early interpretations of the surface deformation images drawn from the averaged total tilt amplitudes and the strike direction of tilt. This demonstrated possible analysis techniques for further investigations. The use of the superposition principle seems well suited for analysing the data from an area with two or more wells. Furthermore, adding and subtracting induced tilt fields can be useful, if pumping is applied with variable rates of fluid extraction from a single well. For instance, in a single well, the extraction rate could be enlarged in distinctive steps. If the superposition

principle is valid, i. e. the subsoil responds linearly, the values of the induced tilt field with a certain rate should be equal to two times the values of a tilt field that is induced with half that extraction rate.

5.2 Tiltmeter Operation

Tiltmeters were operated in three different installation schemes: Borehole tiltmeters installed in a casing, borehole tiltmeters installed without a casing and platform tiltmeters in hollows.

In the first scheme, borehole tiltmeters were installed in tampered sand in a sealed PVC-casing. The casing itself was cemented in a 3 m to 4 m deep borehole. This type of installation is mostly applicable for long term monitoring. It is recommended by the tiltmeter manufacturer and used in several studies (AGI, 1999a, Bonaccorso et al., 1999, Sleeman et al., 2000, Kümpel et al., 2001, Lehmann, 2001, Mentés & Fabian, 2001a, Mentés, 2002). The tiltmeter is protected against the strongest influences from surface. These are precipitation and short term temperature variations. Also, the borehole can not collapse. However, if a large number of instruments has to be installed that type of installation is lavish.

For the set-up of instruments in a shorter time the borehole tiltmeters were directly tampered in sand inside freshly drilled shallow boreholes without a casing. The borehole depth was between 1.5 m and 2.8 m. For this, a drilling car was used. This type of installation was at least twenty times faster than the previous one. The measurements obtained useful data. However, data was disturbed by near surface influences and settling of the instrument. A higher effort of data correction was necessary. Longer observation times to record a larger number of tilt signals would enhance the data basis and could minimize this problem.

The use of platform tiltmeters in hollows seemed to be the easiest way to observe tilt. However, due to stronger meteorological disturbances, the necessary data correction was more difficult. The observation interval with respect to the previous types of installation must be further extended to get useful tilt signals. Nevertheless, pump induced tilt could be observed with that set-up, too. The data did not look so well suited for a quantitative analysis. Platform tiltmeters seem to be applicable if overall pump induced tilt is strong, for instance, five to ten times the overall total tilt amplitudes recorded at site OE.

For a better comparison of the data from different observation points, the installation depth of the tiltmeters should be nearly equal. If shallow layers with high contrasts in the poroelastic parameters are present, tilt response, like reported from modelling, can vary strongly with installation depth. This might be most important for surface deformation imaging and for the determination of the radial distance of the tilt maximum at surface. Moreover, if a shallow layer is known at a site, one instruments can be installed directly below and another one above that layer. Possibly, transient tilt reversals can be observed.

The largest difference between the measurements with tiltmeters in a borehole with and without a casing should be in the coupling to the soil, and thus in the effective base length – disturbances not considered. The effective base length determines the resolution of the spatial signal wave length. Here, it is assumed that the effective base length of all types of installation is small with respect to the wave length of the observed signal. However, exact values can not be stated. The lower boundary of the base length, if a good coupling to the ground can be achieved, may be well defined as the body length of the borehole tiltmeter. The upper boundary is more speculative and could be the length of the more or less rigid casing, if used. The effective base length by using platform instruments installed on a concrete plate in hollows may also be well defined from the lengths of the concrete plates edges, if the plate has a good contact to the subsoil. The unknown value of the effective base length may also lead to some problems if tiltmeters are installed close to a layer boundary in subsoil. The signal can change significantly within a distance smaller than the base length. Moreover, since the base length and coupling to the ground is hard to define, a conversion of vertical tilt data, e. g. recorded by the borehole tiltmeters, to horizontal tilt, e. g. measured by platform instruments, is also problematic.

A faster installation of tiltmeters can be achieved by some refinements of the sensor system. To simplify the installation of the tiltmeters, the instrument should be able to adjust its sensors itself. Tampering of the sand should become completely unnecessary or easier. Time consuming adjustment should no longer be necessary. Some types of tiltmeters have build-in components to readjust the sensors (AGI, 2001), but these instruments are too expensive to be used in clusters of several instruments.

The set-up of the electronics used for the tiltmeter operation can be simplified, too. All necessary equipment, i. e. batteries, data logger, switches and read out interfaces, can be moved from the massive shelter box used here to a smaller, sealed casing that fits in the upper part of the borehole. A WLAN (Wireless Local Area Network) (Brandt, 2002, Clark et al., 2002, Leung et al., 2002) can simplify the data retrieval and the communication between the data logger and the readout computer. After the installation, operation could be controlled from a central position (Letz et al., 2003).

5.3 Modelling Approach

The study could provide convincing explanations for many of the observed signals. It may be surprisingly that the analyses are on the basis of comparatively very simple time dependent poroelastic half-space models. This fact supports the assumption that poroelasticity is a well suited rheology for a description of pump induced near surface tilt and pore pressure changes. Moreover, the program POEL is useful to assess the type of the observed physical processes. However, an accurate adaption of observation and calculation could not be achieved. A scaling between the here used models and the situations at the experimental sites seems hardly possible. In further approaches, the definite subsoil geometry with accurately adjusted parameters for the sites OE and BV should be taken into consideration. Generally, the models may contain ambiguities. The measurements may be described by the modelling, but the used model does not need to account for the subsoil structure.

The adjusted 6-layer model was assumed to qualitatively account for the general subsoil conditions at the sites OE and BV and, since it seemed to be a more realistical model, was used to calculate the tilt response signals for longer durations of withdrawal. These long term calculations support the assumption that in the experiments steady state in tilt and pore pressure response is most often not achieved. A stronger tilt response over a comparatively long time span of up to several days, month and even years can follow. Since in principle, for the observation of transient signals, a shorter recording time is sufficient, a pump test is recommended to be done with a sequence of several short-term pump cycles. This part of the pump test could be followed by a longer lasting withdrawal. Then, it could be seen whether the precise course of tilt and pore pressure signals changes stronger in later times of the pumping like suggested by the here used model.

The program POEL works fast and with a high reproducibility, even if large parameter contrasts at layer boundaries are introduced. At such boundaries common Finite-Element algorithms can produce erratical results. A deeper reason for such problems can be the digitalization error, which occurs in computational number processing (Bathe, 1990). Grid refinements can not remove this intrinsic error. They are also limited with respect to an appropriate computation time and memory usage. However, in its recent state, the modelling procedure for an accurate adaption to measurements is work intensive. The algorithm of POEL could be implemented in a graphical front end that directly allows parameter manipulation and modelling runs. Plotting of distinct time series from different points in the region could be automated, too. A direct comparison with the observations would become easier. An inversion algorithm (Vasco et al., 2001) seems to be a solution for the time consuming parameter manipulation in forward modelling. However, the problem of ambiguity seems to be more seriously as there is in tendency a minor control of the poroelastic parameters and subsoil geometry.

The models here mostly account for pump induced tilt and pore pressure. With POEL, investigations of other signals, i. e. volume strain, shear angle, rotation angle and Darcy velocity, for an easier and better interpretation of the physical point motions can be done. The motions during the here called balancing processes as well as the double reversals should be assessed. Depth dependent parameters may also be taken into account. The limitation of the models to one dimension seems not very strong with respect to the simplified local geology at sites OE and BV. Since the tangential signal part may bear additional valuable information, it should be strived for dynamic 3-D modelling. A 2-D-modelling could deal with a fault, a channel and with surface displacements and topography. If such scenarios can be modelled, a calculated surface deformation image can be subtracted from the one obtained from the measurements. This would allow investigations of the residual part between model and observation.

Chapter 6

Summary

Pump test experiments were successfully conducted at three different sites in Germany. The new method of surface deformation imaging was applied with the data from the site OE. Different transient pump induced signals in tilt and pore pressure were observed. Tilt reversals were discovered and the Noordbergum effect was recorded. With the program POEL, in a comprehensive modelling approach on the basis of poroelasticity, many of the observations could be explained qualitatively.

The new method of surface deformation imaging on the basis of pump induced tilt response was demonstrated and proofed to be useful for further investigations of the subsoil. The surface deformation images were drawn from pump induced near surface tilt signals that were caused by the production wells of the waterworks at the site OE. Therefore, useful tilt signals were recorded with 10 borehole tiltmeters at 16 different positions at shallow depth, and on the surface with two platform instruments at positions next to three places of borehole tiltmeters. An advantage of the method is the possibility of early interpretations with the use of symmetry rules (and superposition principle). If the symmetry rules are applied to surface deformation images, subsoil inhomogeneities may be identified directly as asymmetries in the images. For site OE, the images suggest that the subsoil can be seen as mostly horizontally layered. A large and distinctive heterogeneity is most likely not present. However, some minor and shallow disturbances could be identified. It is likely that these disturbances result from the loading of the waterworks fresh water tank, some of them could also reflect influence from a topsoil layer that partly covers the area and from the tapped main aquifer that might become thinner or gets a lower hydraulic diffusivity nearby one of the production wells.

Limitations of the method were discovered, too. The number of tiltmeters used is still too small for a more comprehensive investigation of the subsoil properties. The spatial resolution and data basis should be enhanced in further investigations. For the experiment at site OE, a number of about 25 tiltmeter positions was suggested for a significantly better spatial resolution. Due to the installation of some of the instruments in boreholes without a casing, the corresponding raw data was disturbed by meteorological influences. The data of the platform instruments was disturbed strongly and was not used for surface deformation imaging. Platform tiltmeters turned out to be useful when the signal to noise ratio is better than here. Settling of the instruments also disturbed the signals. Tiltmeters should not be installed immediately before the pump test. The recordings at every tiltmeter position should cover several tens of short-term pump cycles, each with a nearly equal duration of a few hours. Since modelling showed that pump induced response of tiltmeters at shallow depth and close to layer boundaries can generally change strongly with the depth of installation, it is recommendable to install the instruments at equal depths.

The installation of a single observation point and the data retrieval are the most time consuming parts of the field work. A solution for this problem are self adjusting tilt sensors and operation of the tiltmeters through a WLAN (Wireless Local Area Network). Furthermore, software tools for faster data imaging, also for the model generated data, should be developed.

The time dependency of the surface deformation images becomes obvious from the transient phase of single time series of the pump test data. Numerous highly significant and strongly changing signals

were observed. Elliptical signatures in the hodographs of tilt data from site BV also reflect the time dependency of the near surface tilt field. Surface deformation images should be drawn for different time steps.

The most prominent signals recorded at site OE were the newly discovered transient positive and negative reversals of tilt in response to pumping. Negative reversals were also observed in parallel to the Noordbergum effect at site BV. The occurrence of these signals of a non-monotonous response to monotonous pumping can only be explained by a strongly coupled transient interaction between pore fluid and soil matrix. The transient interaction was called a balancing process between diffusion and deformation.

Very strong tilt was recorded at site WD. Probably, the presence of a quaternary channel is the reason. It provides a restricted, effective reservoir volume. The induced pore pressure gradient per unit volume becomes strong and tilt response will be large.

Actually, steady state models showed that a reduction of the reservoir volume around a well by low pervious strata can lead to a larger tilt response at the surface. Also, the distance of the tilt maximum at the surface with respect to the well is influenced by the layering in subsoil, e. g. the distance can increase with respect to the homogeneous half-space.

Geological subsoil interpretations for the sites OE and BV were used to construct simplified 1-D multi-layered poroelastic half-space models. The models described a stack of vertically alternating aquifers and aquicludes. Steady state as well as time dependent models were calculated to get insights into the pump induced tilt and pore pressure distributions and to explain the kind of observed phenomena. With an adjusted 6-layer model, taking more realistic subsoil conditions into account, negative tilt reversals of the observed type could be computed. The computation of long term response to ongoing withdrawal over days, months and years with this model showed that the steady state in tilt and pore pressure change is not achieved even after a longer time of pumping. This is true for observation positions at shallow depth with respect to the well screen's depth, and also for deeper places somewhat more apart from the well screen inside the tapped aquifer.

Modelling of the transient signals, especially if signal reversals occur, revealed a high sensitivity of the pump induced tilt and pore pressure changes to comparatively small adjustments of poroelastic parameters even in deeper layers of the model. This may open up a useful and fast method for the derivation of subsoil parameters. With the use of transient signals for subsoil interpretations, the conclusions would be drawn from short term pump tests in which the steady state is not achieved. The tests have to last only until the build-up of the amplitudes at the different observation points is strong enough to be detectable. Moreover, modelling of tilt points to a link between the type of the transient reversal and the arrangement of the layers in the subsoil.

In conclusion, the study showed several new aspects of the method of surface deformation imaging. It presented various insights in the near surface tilt and pore pressure changes occurring during pump tests, and their interpretation by poroelasticity. It outlined some next steps to a new type of geophysical approach with the purpose of controlling and prospecting subsoil and reservoir quality during ongoing fluid withdrawal. With the techniques discussed here, the number of deep boreholes used in classical hydrological methods could be reduced. A denser coverage with observation points should be achieved in areas above reservoirs. Case studies that use the new technique are still rare. The number of tiltmeters is mostly restricted and the involved phenomena are still not completely understood. 2-D and 3-D effects like the influences of a buried channel or a fault, or the cause for the here observed elliptic hodographs require additional research. In any case, further investigations to develop this new technique are very promising.

Chapter A

Appendix

A.1 Assembling of an Observation Position

The tiltmeter positions (with pressure transducers for well head logging) in this study were installed and operated like outlined exemplary in the following.

A.1.1 Tiltmeters

After selecting the sites and tiltmeter positions, the boreholes for the borehole tiltmeters were drilled.

Boreholes:

Borehole drilling was done with three different tools. The first tool, [Eijkelkamp \(1998\)](#), was operated manually, the second, [Stihl \(2001\)](#), with a benzine motor. As a third tool, a drilling car was used. All tools turned out to be useful for boreholes with diameters between 0.2 m to 0.5 m and depths down to 4 m . The deeper the borehole, the larger the diameter was chosen. This enabled an easier installation of the casing in the borehole, and of the tiltmeter in the casing hereafter if the borehole was not exactly vertical. Drilling down a spiral drill like depicted in [Fig.A.1](#), was done with a benzine motor that could be plugged at the top of the drill. The most difficult part during drilling was pulling up the bore tool when it was filled with excavation. In some cases an excavator could be used for lifting up the tool, see [Fig.A.1](#). In the other cases the drill was lifted manually, or by the drilling car if this tool was used. Lifting the tool manually required at least four forceful persons.

Casing:

If a casing was used, prior to its installation, it was sealed against moisture by silicone glue. The glue was put in the screw threads of the different casing tubes. At its bottom end, the casing was closed by a screw top. [Fig.A.2\(left\)](#) shows the casing, length 4 m , used at position $T1_{OE}$, see [Fig.3.3](#). This casing



Figure A.1: Borehole drilling with a spiral drill ([Stihl, 2001](#)), tiltmeter position $T4_{OE}$, see [Fig.3.3](#). The borehole is at the right side of the photo in front of the excavator. The spiral drill can also be operated by a drilling car.

was build in the borehole with the use of cement. The vertical adjustment of the casing was checked with a plump line. It has been tried and tested that at least one person can push down the casing, another person controls the vertical adjustment and a third one slowly fills up the ring space between casing and borehole with cement. The casing was fixed against buoyancy in the liquid cement. Fig.A.2(right) shows the lowering of the casing into the borehole. After a day, the fixation of the casing was removed. Before the protective cap of steel was placed above the borehole a mark of the north direction was attached in the casing by the use of a compass. If the protective cap was installed first, the compass was influenced by the magnetization of the cap.

Borehole Tiltmeters:

The general installation of borehole tiltmeters is described in

AGI (1999a). However, some special tasks applied here will be named: Prior to the lowering of the tiltmeter (a photo of an instrument is in Fig.A.3), a 10 cm thick layer of small grained quartz sand was filled in the borehole and tamped. Thereafter, the tiltmeter was connected to the batteries and each of its output components to a digital voltmeter. At the connection terminal of the tiltmeter, the gain of the instrument was first set to the position 'low' and the low-pass filter turned 'off'. At its top, the borehole instruments have a frame that is oriented in the direction of the Y-axis of the tiltmeter. The frame was used to mark the positive Y-direction. The orientation of the tiltmeter in the borehole could be controlled by that frame and the use of a torch. After lowering of the tiltmeter, sand was filled in the ring space between the instrument body and the casing/borehole, layer by layer. Each layer, not thicker than 10 cm, was tamped, Fig.A.4. The vertical adjustment of the tiltmeter was controlled by the digital voltmeters. After the ring space was filled by two thirds the tiltmeter got a good contact to the casing/borehole. The gain of the tiltmeter and the resolution of the digital voltmeters was increased to resolve further adjustments. When the ring space was filled completely and adjustment was fine, the low-pass filter was turned 'on'.



Figure A.3: Borehole Tiltmeter, AGI 722a, with connector and connection terminal.

Platform Tiltmeters:

Fig.A.5 shows the installation of the platform tiltmeter PLT8_{OE} close to T8_{OE}. In a nearly 0.4 m deep hollow, a concrete plate was placed on a 10 cm thick layer of sand with grooves. The platform tiltmeter was installed on this plate and adjusted by turning its support screws. A cover protected the hollow. A similar type of installation was described by Tofani & Horath (1990).

Electrical Connections and Data Logger:

Rechargeable batteries and the connection terminal of the tiltmeter were placed inside a shelter box in an additional box that was protected against rising water. Furthermore, a third, completely water protected box was placed in this additional box. The third box kept the data logger and protected it from moisture. 200 g of drying grains were placed in this box, too. The cable



Figure A.2: Installation of the casing, T1_{OE}. In the front of the right photo the second, manually operated drilling tool (Eijkelkamp, 1998) is depicted.

guides in all boxes were water proofed. The data loggers used here are of type ‘Grant Squirrel’ with a resolution of 12 Bit or 16 Bit (Grant, 2003a,b). For the surface deformation imaging at site OE, also self made data loggers with 16 Bit resolution were brought in (Grüneberg, 2002).

Maintenance and Data Retrieval:

Fig.A.6 shows maintenance tools at T2_{OE}, the boxes with data logger and batteries, a laptop, toolbox, a folder for protocol sheets, digital voltmeter and a doormat to sit down or kneel in front of the shelter box. The first maintenance task was retrieval of data from the logger to a laptop. The recent run of measurements was stopped, the data downloaded and the clock in the logger readjusted. While the data was downloading, all components and signals were checked manually with a digital voltmeter. The components and signals were: voltages of all batteries (changed if voltage was below 12.0 V) and the output voltages of the tiltmeter from both tilt and the temperature sensor; if other sensors (pressure transducers, thermistors, rain gauge, ...) are installed, the corresponding output values were checked, too. The batteries were changed, only if necessary, because disconnecting the tiltmeter from the batteries caused erroneous signals for several hours after reconnection. This was most likely due to a temperature disturbance in the instrument. Before a new run of the data logger was started, the signal values at the loggers’ display were checked for each sensor and the drying grains in the innermost box were changed. If the memory of the data logger was filled, old and saved data in the logger were deleted, so that there was enough data space for the new run. Finally, the new run of the logger could be started and all boxes were closed.



Figure A.4: Installation of a bore-hole tiltmeter by tampering, T4_{OE}.



Figure A.5: Hollow for a platform tiltmeter at PLT8_{OE}, with B2_{OE} in background behind the bushes (left), and installed instrument, AGI 701-2 (right, arranged).

during maintenance. Inspection of the data was done with the laptop immediately at the station or somewhat later, after the data was saved.

A.1.2 Pressure Transducers

Fig.A.7 shows a common pressure transducer, here of type In-Situ Inc. TROLL-4000 (In-Situ, 1995). The depicted instrument has an integrated data logger. The data cable to connect the instrument to a laptop is shown, too. Such type of instrument was used at site OE. Another type of pressure transducers, In-Situ Inc. PXD-260/261 (In-Situ, 1989, Fabian, 1998), without a data logger, was used at site BV. All used pressure transducers had a sensor membrane with integrated silicon strain gauges. A constant current flows through the strain gauges which have a calibrated resistivity characteristic. If the membrane deforms, caused by a rise or fall of the fluid pressure acting on one side of the membrane, the resistivity of the strain gauges changes due to the Piezo effect described e.g. by Schrüfer (1994). This



Figure A.6: Data retrieval and maintenance tools, T2_{OE}.

change in resistivity leads to a change in current and can be measured electronically, converted by an analogue to digital converter and stored in a memory chip (Tränkler & Obermeier, 1998, Niebuhr & Lindner, 2001). Sensor membrane and electronics are enclosed in a steel body. At its front side, the membrane has contact to the fluid, whereas free space at its back side is connected to the outside air pressure at the top of the well's casing through a small pipe. With that construction, the air pressure acting on the water surface in the well and therefore leading to an increased pressure at the water side of the sensor membrane is mostly compensated. However, depending on the diameter and the length of the small pipe, this compensation mechanism depends on the frequency of air pressure changes. The pressure transducers used here, are compensated best for air pressure signal periods not shorter than 10 min to 20 min (Fabian, 1998).



Figure A.7: Pressure Transducer TROLL-4000, used in B1_{OE}, B2_{OE}, B3_{OE}.

A.2 Transformations of Tilt Angles

Total tilt $\Delta\gamma$, Eq.2.3, is independent of the spatial reference system, because the tilt measurements must supply the same value in every coordinates. The individual tilt values $\Delta\gamma_r$ and $\Delta\gamma_t$ with respect to the individual axes will change, if another coordinate system is chosen, Fig.A.8. For an arbitrary coordinate system with axes x and y in the horizontal plane corresponding with the subsoil's surface, the tilt angles will read as $\Delta\gamma_x$ and $\Delta\gamma_y$. Thus

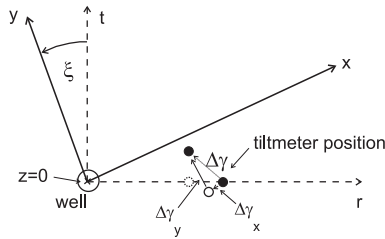


Figure A.8: Transformation between two coordinate representations of tilt in the horizontal x - y plane \subseteq t - r plane. The new x - y system is rotated right hand side around the z -axis (the well) by the angle ξ .

$$\Delta\gamma = \sqrt{\Delta\gamma_x^2 + \Delta\gamma_y^2}. \quad (\text{A.1})$$

The transformation of the tilt values $\Delta\gamma_r$ and $\Delta\gamma_t$ from a t - r in a x - y system, to the values of $\Delta\gamma_x$ and $\Delta\gamma_y$ as shown in Fig.A.8, can be calculated by:

$$\begin{pmatrix} \Delta\gamma_x \\ \Delta\gamma_y \end{pmatrix} = \underbrace{\begin{pmatrix} \cos(\xi) & \sin(\xi) \\ -\sin(\xi) & \cos(\xi) \end{pmatrix}}_{:=T_{\xi+}^{x,y \leftarrow t,r}} \begin{pmatrix} \Delta\gamma_t \\ -\Delta\gamma_r \end{pmatrix}. \quad (\text{A.2})$$

If the angle ξ is negative, i.e. a left handed revolution of the x - y system, the transformation will be:

$$\begin{pmatrix} \Delta\gamma_x \\ \Delta\gamma_y \end{pmatrix} = \underbrace{\begin{pmatrix} \cos(\xi) & -\sin(\xi) \\ \sin(\xi) & \cos(\xi) \end{pmatrix}}_{:=T_{\xi-}^{x,y \leftarrow t,r}} \begin{pmatrix} \Delta\gamma_t \\ -\Delta\gamma_r \end{pmatrix}. \quad (\text{A.3})$$

The reverse transformation from an arbitrary x - y system into a t - r system would be more useful for analysing tilt data. Generally, in an experiment, each tiltmeter is oriented with its sensor axes in a

selected direction of the compass. This orientation defines the reference system of the tiltmeter itself. It is the x-y coordinate system sketched for the borehole tiltmeter in Fig.2.2. In that case, the two tilt sensors of each instrument measure the tilt angles $\Delta\gamma_x$ and $\Delta\gamma_y$. In a pump test experiment, the lines between each tiltmeter position and the production well define the radial axes of individual t-r systems, one system for each of the single tiltmeters. To obtain the values $\Delta\gamma_t$ and $\Delta\gamma_r$ at each tiltmeter position, the data has to be transformed backwards with respect to the above transformations. An inversion of the matrices $T_{\xi+}^{x,y\leftarrow t,r}$ and $T_{\xi-}^{x,y\leftarrow t,r}$ in Eqs.A.2 and A.3 results in the transformation of $\Delta\gamma_x$ and $\Delta\gamma_y$ to $\Delta\gamma_t$ and $\Delta\gamma_r$. For each tiltmeter position, the transformation angle ξ has a special value.

With $T_{\xi+}^{x,y\leftarrow t,r} T_{\xi-}^{x,y\leftarrow t,r} = \mathbf{1}$, $T_{\xi+}^{x,y\leftarrow t,r^{-1}} = T_{\xi-}^{t,r\leftarrow x,y}$ and $T_{\xi-}^{x,y\leftarrow t,r^{-1}} = T_{\xi+}^{t,r\leftarrow x,y}$ the backward transformation of the situation in Fig.A.8 is

$$\begin{pmatrix} \Delta\gamma_t \\ -\Delta\gamma_r \end{pmatrix} = \underbrace{\begin{pmatrix} \cos(\xi) & -\sin(\xi) \\ \sin(\xi) & \cos(\xi) \end{pmatrix}}_{:=T_{\xi-}^{t,r\leftarrow x,y}} \begin{pmatrix} \Delta\gamma_x \\ \Delta\gamma_y \end{pmatrix} \quad (\text{A.4})$$

for left handed rotations of the angle ξ from the x-y system into the t-r system, and

$$\begin{pmatrix} \Delta\gamma_t \\ -\Delta\gamma_r \end{pmatrix} = \underbrace{\begin{pmatrix} \cos(\xi) & \sin(\xi) \\ -\sin(\xi) & \cos(\xi) \end{pmatrix}}_{:=T_{\xi+}^{t,r\leftarrow x,y}} \begin{pmatrix} \Delta\gamma_x \\ \Delta\gamma_y \end{pmatrix} \quad (\text{A.5})$$

for right handed rotations of the angle ξ from the x-y into the t-r coordinates. To rotate tilt data from the measurements, $\Delta\gamma_x$ and $\Delta\gamma_y$ in Eqs.A.4, A.5 could be identified with the calibrated output values of the tiltmeter's sensors.

The strike orientation or direction of the total tilt $\Delta\gamma$, Eq.A.1, in a horizontal plane with respect to a coordinate system, e. g. the x-y system, is called herein Γ , see Fig.A.9. The value of Γ can be obtained from

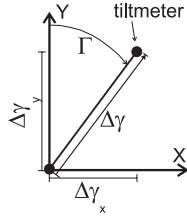


Figure A.9: Tilt $\Delta\gamma$ and its orientation Γ of strike in a x-y system.

$$\Delta\gamma_x = \Delta\gamma \cdot \sin(\Gamma), \quad \Delta\gamma_y = \Delta\gamma \cdot \cos(\Gamma),$$

and is derived by

$$\Gamma = \arcsin\left(\frac{\Delta\gamma_x}{\Delta\gamma}\right) \quad \text{or} \quad \Gamma = \arccos\left(\frac{\Delta\gamma_y}{\Delta\gamma}\right), \quad (\text{A.6})$$

from both components $\Delta\gamma_x$ or $\Delta\gamma_y$ and the total tilt $\Delta\gamma$. In Eqs.A.6 the values of Γ are not unique due to the definitions of the inverse functions \arcsin and \arccos . If Eqs.A.6 are used for the data transformation, the definition of the inverse function (Bronstein & Semendjajew, 1987) has to be respected to get the correct value and the sign.

A.3 Auxiliary Data to Site OE

A.3.1 Configuration Data of Wells and Tiltmeters

→next page

Wells:

well	aquifer	l [m]	q [m^3/h]	z_1 [m]	z_2 [m]	z_3 [m]	z_4 [m]	d [mm]
B1	GW2	17	250		42.5			800
B2	GW2	17	250		42.2			600
B3	GW4	21	85				156.2	400
P1	GW1	7.5		7.5				50
..	GW2	13			37.8			50
..	GW3	15				93.0		50
..	GW4	19					155.0	50
P2	GW1	6.5		7.0				50
..	GW2	15			34.0			50

Table A.1: Configuration and hydrological data of wells, site OE. $l \hat{=}$ mean hydraulic head below surface, $q \hat{=}$ yield, $z_i \hat{=}$ center depth of well screen tapping the i -th aquifer below surface, $d \hat{=}$ diameter of casing. Continuously active: B1 since 1981, B2 since 1989, B3 since 1997.

Tiltmeters:

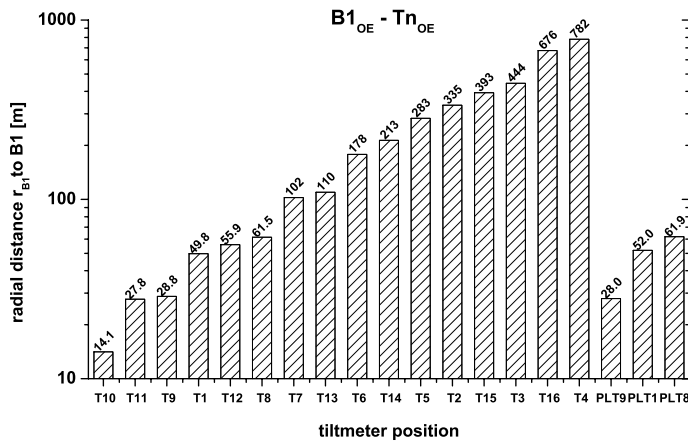


Figure A.10: Radial (horizontal) distances r_{B1} between production well $B1_{OE}$ and tiltmeter positions at site OE.

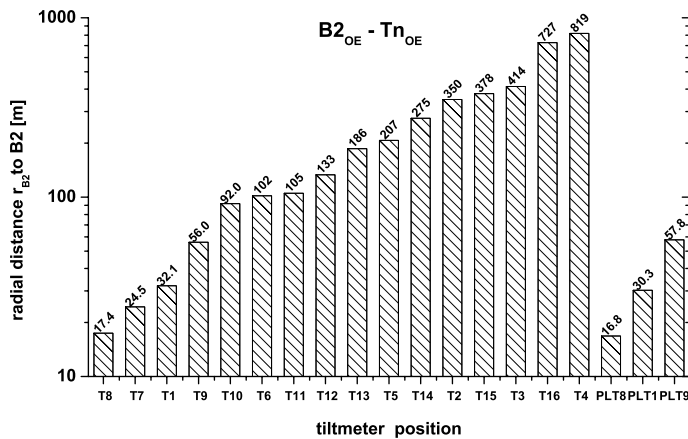


Figure A.11: Radial (horizontal) distances r_{B2} between production well $B2_{OE}$ and tiltmeter positions at site OE.

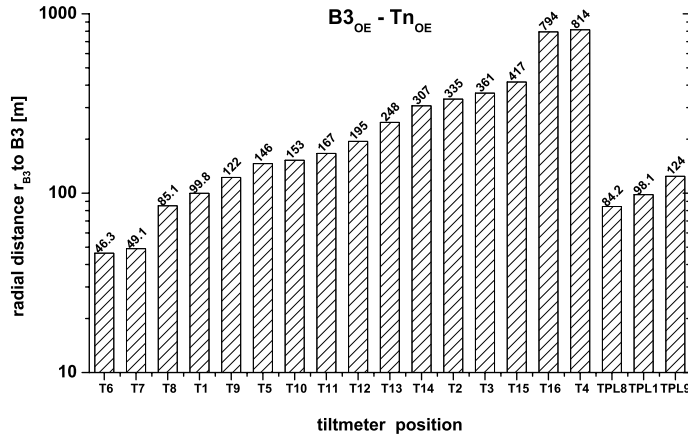


Figure A.12: Radial (horizontal) distances r_{B3} between production well $B3_{OE}$ and tiltmeter positions at site OE.

A.3.2 Second Regional Geological Cross Section, OE

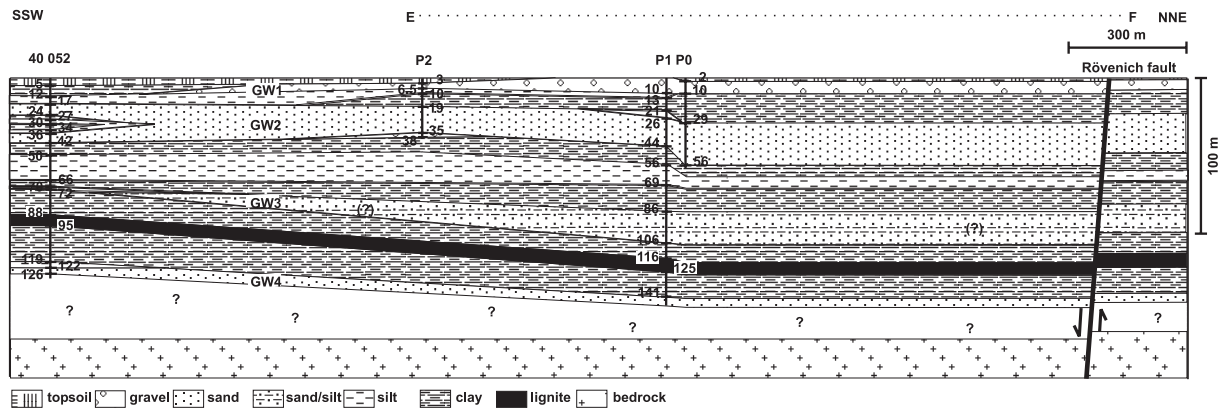


Figure A.13: Second regional simplified geological cross section, OE, E—F in Fig.3.3. 4 times vertically exaggerated. The cross section extends over the borders of Fig.3.3. An additional well, 40 052, is sketched. Numbers beside the wells indicate depth in *m* of the boundaries between adjacent layers. Aquifers $GW1_{OE}$ to $GW4_{OE}$ are marked. Geological interpretation was mostly done by [Martau \(2001\)](#) on the basis of [GLA-NW \(1988\)](#), [Wallbraun \(1992\)](#), [Erftverband \(1999\)](#), [Verbandswasserwerk \(1999\)](#), [Rheinbraun \(2000\)](#), [Hoffmann \(2002\)](#).

A.3.3 Correction of Tilt Data

A correction was necessary for the data obtained from borehole tiltmeters which were installed without a casing, and from platform instruments. The aim of correction was to remove (1) short period signals from background noise, e. g. caused by civilization, (2) long period trends caused, e. g. by settling after installation of the instruments, (3) single events, e. g. due to moistening after precipitation. The correction should reduce disturbance not caused by pump activity. Therefore, it was tried to find an arbitrary time dependent function fitting best the annoying signal parts, but not signals caused by pumping. This function was subtracted from the measurements. Modelling of the underlying physical processes of the disturbances was not made.

Fig.A.14 shows two examples of data correction procedure. The first is from the data of $T8_{OE}$, sub figures (a), (b), (c). In that case, correction works very well. It is the best correction of all data.

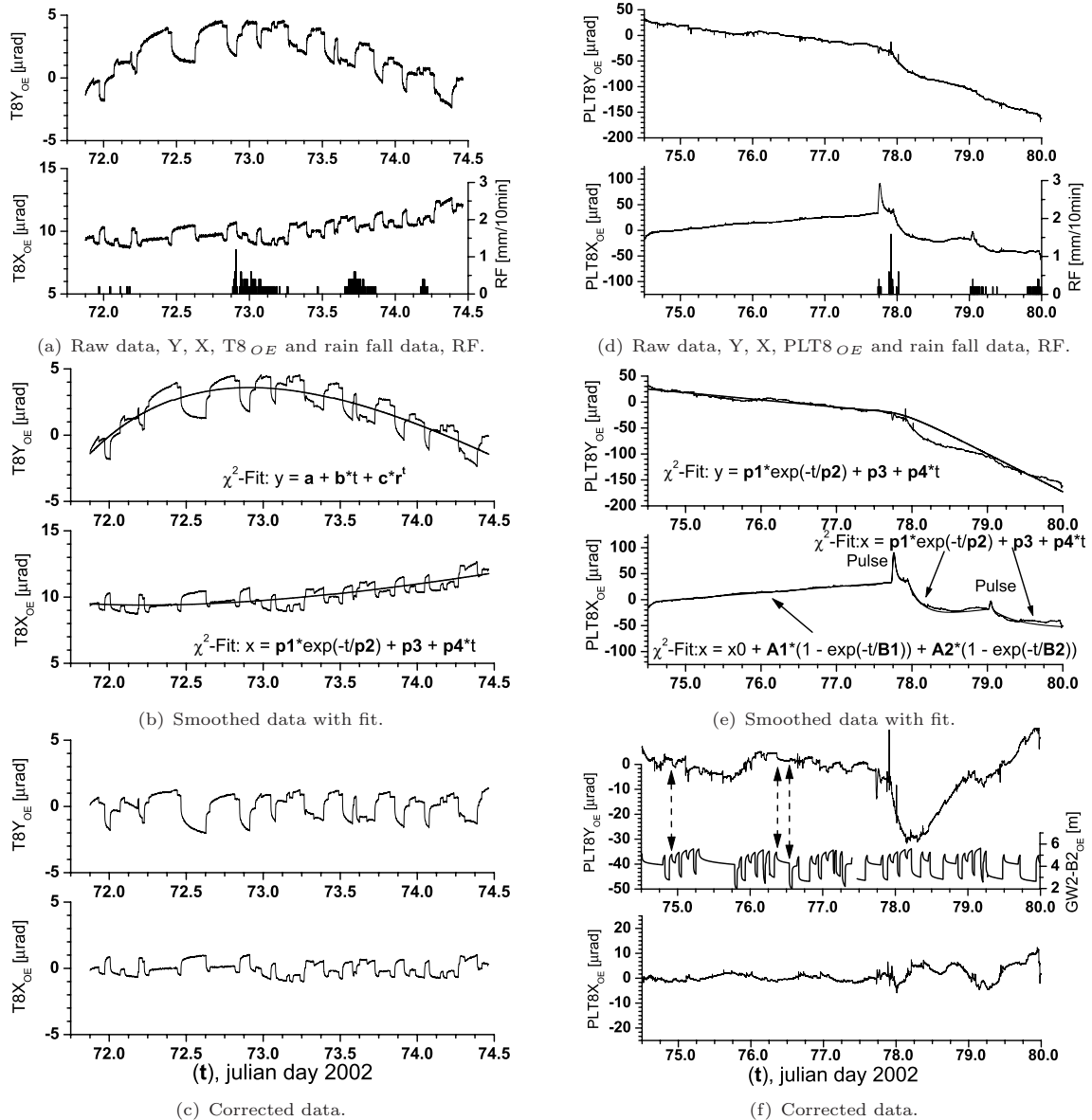


Figure A.14: Correction of data from a borehole tiltmeter installed without casing, (a), (b), (c), left, and a platform tiltmeter, (d), (e), (f), right. First, the data is smoothed. Then, a best fitting function is adapted to trends and events and subtracted from data. For PLT8X_{OE}, (e) the fit had to be done at individual parts of the time series with different types of functions. After correction the signal of PLT8Y_{OE} shows pump cycles, marked by the dashed arrows in (f).

One annoying signal part in both tilt components X, Y has a high frequency and is possibly caused by industrial noise. Such type of disturbance was often observed in the Lower Rhine Embayment (von Seht & Wohlenberg, 1996, Fabian, 1998, Kümpel et al., 2001). The other part of noise is a long period variation with a smoothly curved course. The latter may consist of two influencing factors: settling after installation of the instrument and a damped moistening effect after precipitation events. The rain fall is shown in Fig. A.14(a). Since T8_{OE} is installed at a somewhat larger depth of 2.45 m bottom end of instrument below surface, disturbance of the tilt signals caused by rain fall may occur not instantaneously but somewhat damped by the overlying subsoil.

Correction of the high frequency part, (1) was done by *Savatzki-Golay* filtering. The effect is a smoothing of the data. Here, in a moving window that covers 9 data points, a polynomial regression of degree 3 is

adapted to the data to determine the smoothed value of the center point of the window. This method has the advantage over e.g. adjacent averaging, that it better keeps edges in the course of the signal like they occur at start and cessation of pumping (Press et al., 1988, Vetterling et al., 1988, Microcal Software, Inc., 1999). The smoothed curves are plotted in Fig.A.14(b). The trace of the signal plots is thinner as before. The noise has been reduced. In the next step (2) a best adapting function was fitted to the smoothed curves, Fig.A.14(b). A χ^2 -fit (Leo, 1994) was carried out to minimize the difference between signal and fit function. The used fit function is printed in Fig.A.14(b). Other data sets, not shown here, were corrected mostly by other types of fit functions. The used functions were taken from the fit function selection provided in the χ^2 -fitting tool of Origin6.1 (Microcal Software, Inc., 1999). The parameters of the functions, named a , $A1$, $A2$, b , $B1$, $B2$, c , r , $p1$, $p2$, $p3$ and the value of χ^2 are not presented. They contain no relevant information here. The variable in the functions is the time denoted by t . Since the time series from T8_{OE} were not disturbed by single, outstanding events, the correction could be finished by subtracting the fit functions of the χ^2 -fit from the smoothed curves. The corrected tilt signals are in Fig.A.14(c).

The second example of tilt data correction is in Fig.A.14(d), (e), (f). This was the most complicated correction process. Fig.A.14(d) illustrates the raw data from a platform tiltmeter installed at position PLT8_{OE} next to T8_{OE}, Fig.A.5, and shows data of precipitation, RF. The original tilt signals do not show evidence of any pump cycle and are dominated by a strong trend and huge disturbances immediately after rain fall events (see the large tilt amplitudes with respect to the data of the borehole tiltmeter, T8_{OE}). Correction steps were like in the foregoing case. However, the annoying signal parts of longer signal periods changed their character with ongoing data sampling, see Fig.A.14(e). First, there is a somewhat linear trend at the beginning of the data from both tilt components. It is followed by a strong non-linear excursion, PLT8Y_{OE}. In this latter time span, the signal of the X-component, PLT8X_{OE}, shows two pulses. For a correction of these influences, the χ^2 -fit was carried out only at parts of the time series. The type of fit function had to be changed between the parts to get the best fit, Fig.A.14(e). The result is shown in Fig.A.14(f). There, the corresponding well level record of production well B2_{OE} is plotted, too. A comparison between the well level observation and PLT8Y_{OE} shows indeed some significant pump induced tilt signals, marked by arrows in (f). Due to the orientation of PLT8Y_{OE} in direction to B2_{OE} the pump induced signal in PLT8X_{OE} is small and hard to see. Even in the parts of the corrected tilt signal after the first rain fall event, julian days after 78.5, pump induced tilt can be recognized.

The correction of the tilt data with the here outlined procedure works fine. However, absence of annoying signals with wavelengths in the range of the periods of the pump-cycles is a major precondition for a correction that uncovers useful tilt signals for further quantitative conclusions. Another precondition is an overall not too noisy signal without huge and frequent disturbances of several times larger amplitudes than the utility signal. In the outlined examples, data from T8_{OE} can be used for quantitative interpretations, but that from PLT8_{OE} seems to be somewhat problematically, especially for analyses of the early transient signal flanks.

A.3.4 Error Plots of Deformation Image Data, OE

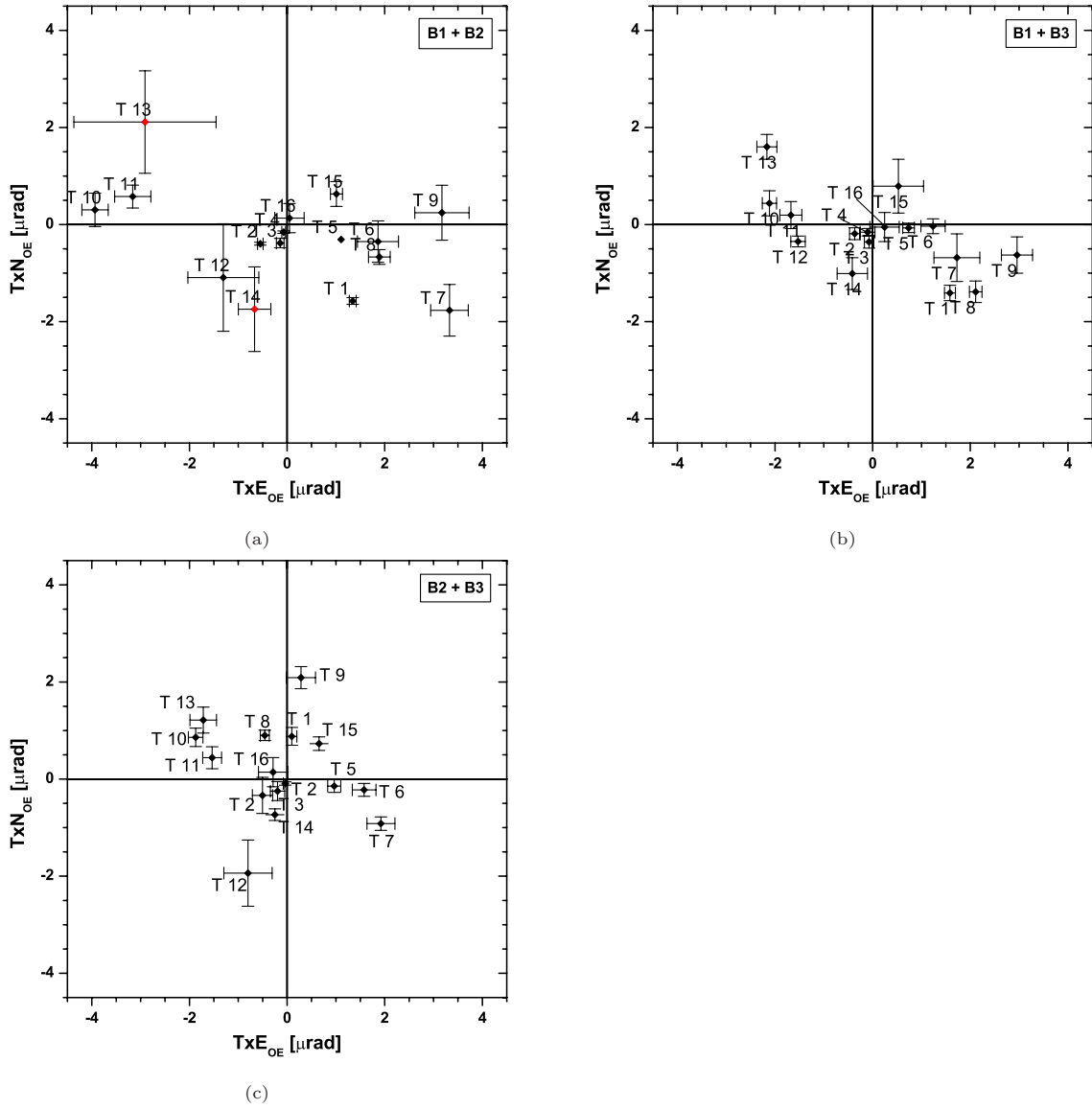


Figure A.15: Error plots of surface deformation image data, site OE. The diagrams show the arithmetic mean of the selected maximum tilt amplitudes that were induced by pumping at the particular positions at site OE, with their standard deviation, 1σ confidence level. In the plots, the vertical axis, TxN_{OE} scales the tilt angle $\Delta\gamma_N$ with positive sign in northern direction, and the horizontal axis, TxE_{OE} , the tilt angle $\Delta\gamma_E$ with positive sign in eastern direction. The 'x' indicates that axis scaling is the same for the data form all positions. Compare Sec.3.1.2.

A.4 Auxiliary Data to Site BV

Configuration data of tiltmeters and wells:

tilt pos./ well	aquifer	l [m]	q [m^3/h]	r [m]	ζ [m]	z [m]	d [mm]
T1	in GW1			13.1	2.23		200
T2	in GW1			6.1	2.68		200
B1	GW1	1.6	2.5			7.0	50
B2	GW2	2.1	2.5			25.5	50
B3	GW3	6.5	2.5			37.5	50

Table A.2: Configuration and hydrological data of wells and tiltmeters, site BV. $l \hat{=}$ mean hydraulic head below surface, $q \hat{=}$ yield, $r \hat{=}$ radial distance of tiltmeters to the wells, $\zeta \hat{=}$ center depth of the tiltmeter body below surface, $z \hat{=}$ center depth of well screen below surface, $d \hat{=}$ diameter of casing.

A.5 Auxiliary Data to Site WD

Configuration data of tiltmeters and wells:

tilt pos./ well	aquifer	l [m]	q [m^3/h]	r_1 [m]	r_2 [m]	ζ [m]	z [m]	d [mm]
T1	in GW1			70	470	1.58		200
T2	in GW1			140	525	1.58		200
B1	GW2		200				94.5	?
B2	GW2		150				99.5	?
P1D	GW2	1.3					36.5	50
P2D	GW2	1.3					49.6	50
P2S	GW1(?)	1.0					23.6	50

Table A.3: Configuration and hydrological data of wells and tiltmeters, site WD. $l \hat{=}$ mean hydraulic head below surface, $q \hat{=}$ yield, $r_1 \hat{=}$ radial distance of tiltmeters to the well B1_{WD}, $r_2 \hat{=}$ radial distance of tiltmeters to the well B2_{WD}, $\zeta \hat{=}$ center depth of the tiltmeter body below surface, $z \hat{=}$ center depth of well screen below surface, $d \hat{=}$ diameter of casing.

A.6 POEL

The program POEL was developed by R. Wang from GeoForschungsZentrum Potsdam. It was used here to calculate the poroelastic diffusion–deformation processes in multi-layered half-spaces. A more detailed description of the mathematical structure of POEL is given in Wang & Kümpel (2003). Recently, POEL has become available in its second version where it calculates wave number spectra and time series in mostly arbitrary time windows. The program is protected by a copyright/user agreement. The calculated data accounts for matrix displacement, strain tensor components, radial vertical tilt, pore pressure change and Darcy velocity. Calculated data, the spectra and the time series are stored by POEL in different files, one for each corresponding observable. The program is written in Fortran77. POEL is a single console program, `poel.exe` that is controlled by an input file `*.dat`. The input file describes the actual model scenario.

A.6.1 A Comparison with the Analytic Solution

A check of the functionality of POEL can be done with the analytic steady state solutions of the poroelastic equations in a homogeneous half-space, Eqs.2.19 printed in Fig.2.9. POEL should calculate nearly the same values for tilt and pore pressure like the analytic solution provides. Therefore, the values for tilt and pore pressure obtained by the analytic solution, with the parameters like in Fig.2.9, were computed on the calculation points of the grid in Fig.4.1. The corresponding POEL solution was subtracted from these values. Fig.A.16 shows the differences between the analytic steady state and the POEL steady state solution for tilt and pore pressure. The overall deviation between both solutions is less than 0.1 percent.

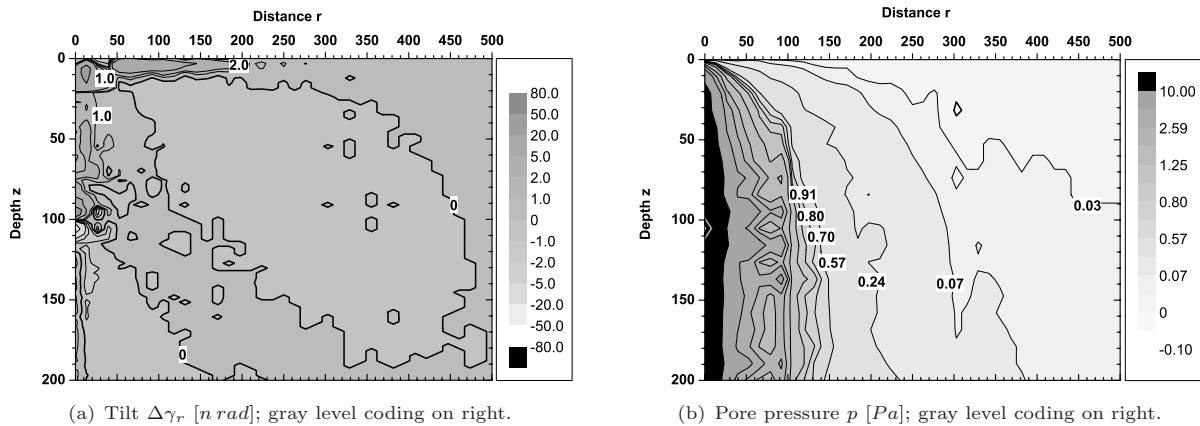


Figure A.16: Difference between the steady state analytic and the POEL solutions for a homogeneous half-space of smallgrained sand with a point source at depth $100\ m$. The amplitude scaling of the plots here is 10^3 times enhanced for tilt and 10^4 times for pore pressure with respect to the previous common scaling. With the same scaling, largest differences would be seen only in a radius of $20\ m$ around the source. They are less than $0.1\ \mu rad$ for tilt and $0.1\ kPa$ for pore pressure.

A.6.2 Difference between Point- and Line-Sink

The difference effect between the here used line sink for the production well that extends vertically between $90\ m$ and $110\ m$, and a point sink at a depth of $100\ m$ is shown in Fig.A.17. Both data was calculated with POEL on the grid in Fig.4.1. Except for the settings for the source, all parameters in the input files are the same. The values of the tilt and pore pressure fields caused by the line sink are subtracted from the values that result form the calculation with a point sink. Overall in the far field of the source, the line sink causes negligibly larger tilt and smaller pore pressure changes.

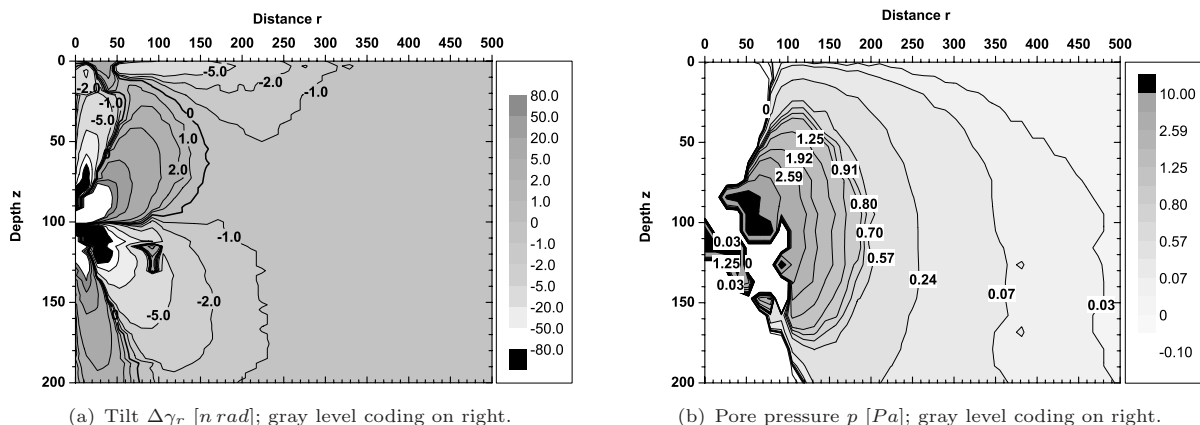


Figure A.17: Difference of the induced tilt and pore pressure distribution if pumping is done from a point and a line sink. Due to the enhanced scaling of the amplitudes in both diagrams, 10^3 times enhanced for tilt and 10^4 times for pore pressure with respect to the common scaling in the study, a difference distribution can be seen. The largest differences, even still small, occur within a distance of $20\ m$ around the line sink.

A.7 Time Slices – Half-Space, 3, 4, 6 Layers

The time slices printed in the following illustrate the tilt and pore pressure development in different half-spaces during the first hour after onset of pumping, except for the homogeneous half-space, where steady state is included. The data of the selected time steps is from the time dependent solutions calculated with POEL on the grid of calculation points of Fig.4.1. The models of section 4.3 were used.

The models are represented by different numbers of time slices. The mutation of the particular solution fields of some models is not so strong between some successive time steps – see for instance Fig.A.18(g) which time slice is kept out. Caused by the gridding of the contour plots, the field distributions are not completely accurate. This is in model regions where gradients and/or amplitudes are small with respect to the strongest amplitudes and gradients that occur in the whole diagram. The adjusted 6-layer model has nine different time steps. In the pore pressure contours of this model, Figs.A.25, the area where the Noordbergum effect occurs is not correctly depicted. Here, only the model sections where the effect has a larger amplitude are delineated. The gridding was not able to accurately handle the model parts between the two less pervious layers, depths $z = 20\text{ m}$ to 60 m . The Noordbergum effect also occurs in that part of the model, see Fig.4.17.

The figures on the further pages show:

- Fig.A.18, A.19: Homogeneous half space. Poroelastic parameters are in Tab.4.8. With steady state included.
- Fig.A.20, A.21: 3-layer model with a buried less pervious slab. Poroelastic parameters are in Tab.4.2.
- Fig.A.22, A.23: 4-layer model. Poroelastic parameters are in Tab.4.5.
- Fig.A.24, A.25: Adjusted 6-layer model. Poroelastic parameters are in Tab.4.9.

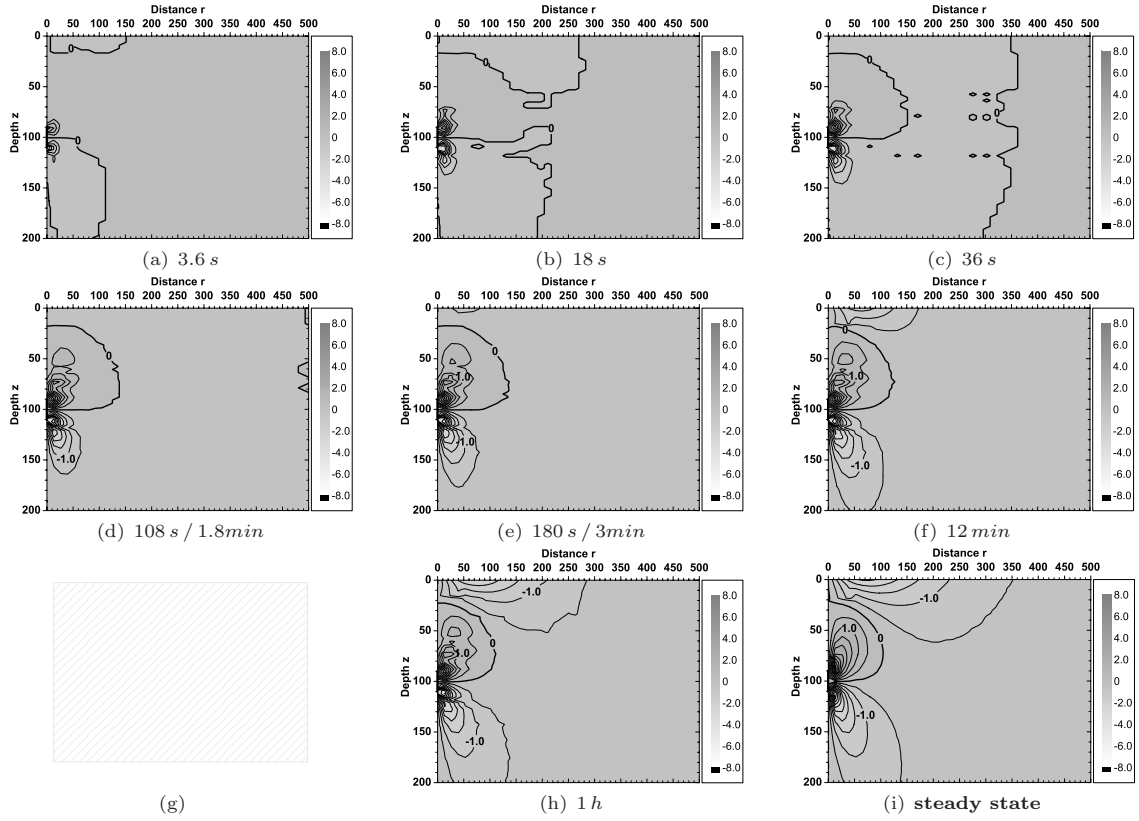


Figure A.18: Time slices, tilt $\Delta\gamma_r$ [μrad], homogeneous half-space, ‘small sand’.

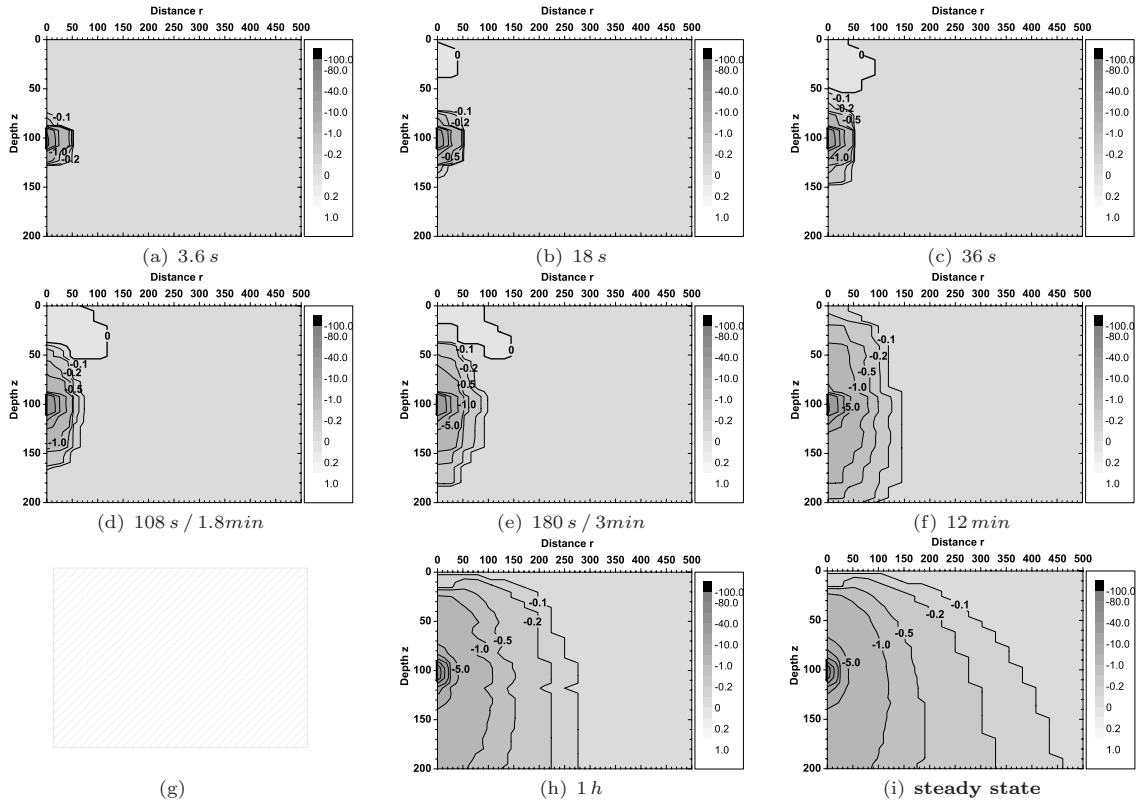


Figure A.19: Time slices, pore pressure p [kPa], homogeneous half-space, ‘small sand’.

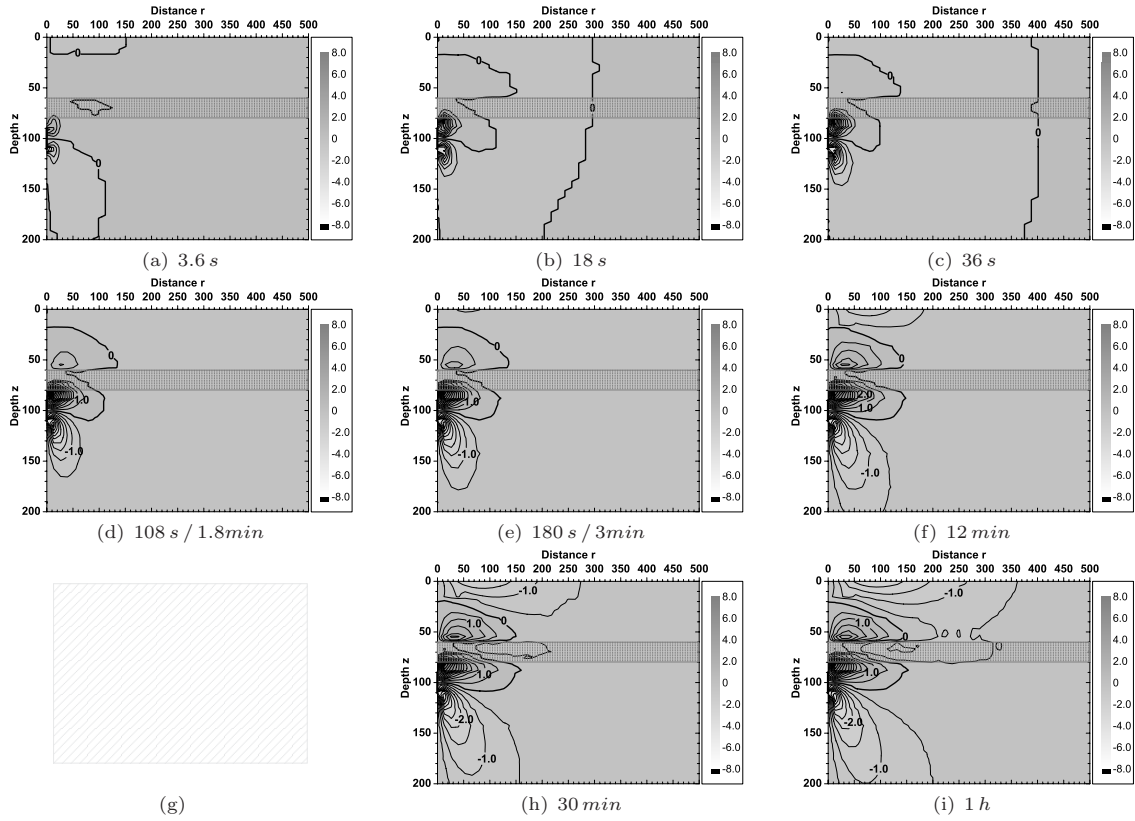


Figure A.20: Time slices, tilt $\Delta\gamma_r$ [μrad], 3-layer model, ‘mid sand–loam mix–small sand’.

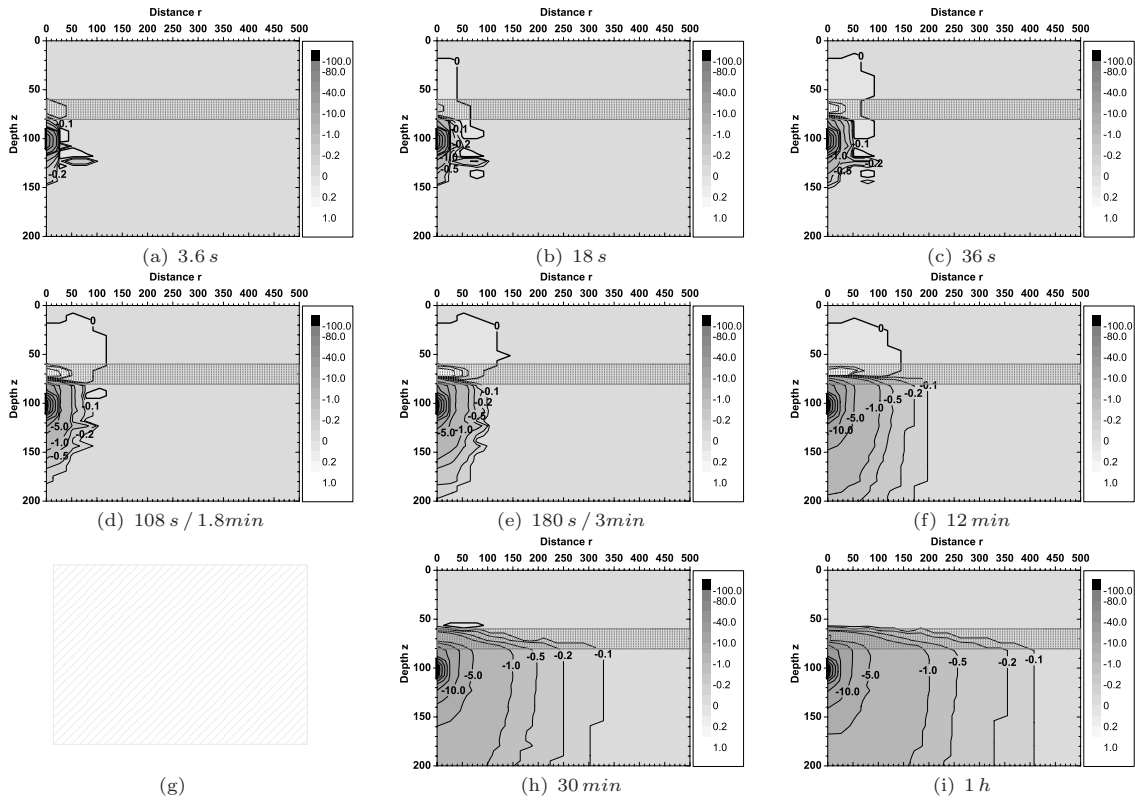


Figure A.21: Time slices, pore pressure p [kPa], 3-layer model, ‘mid sand–loam mix–small sand’.

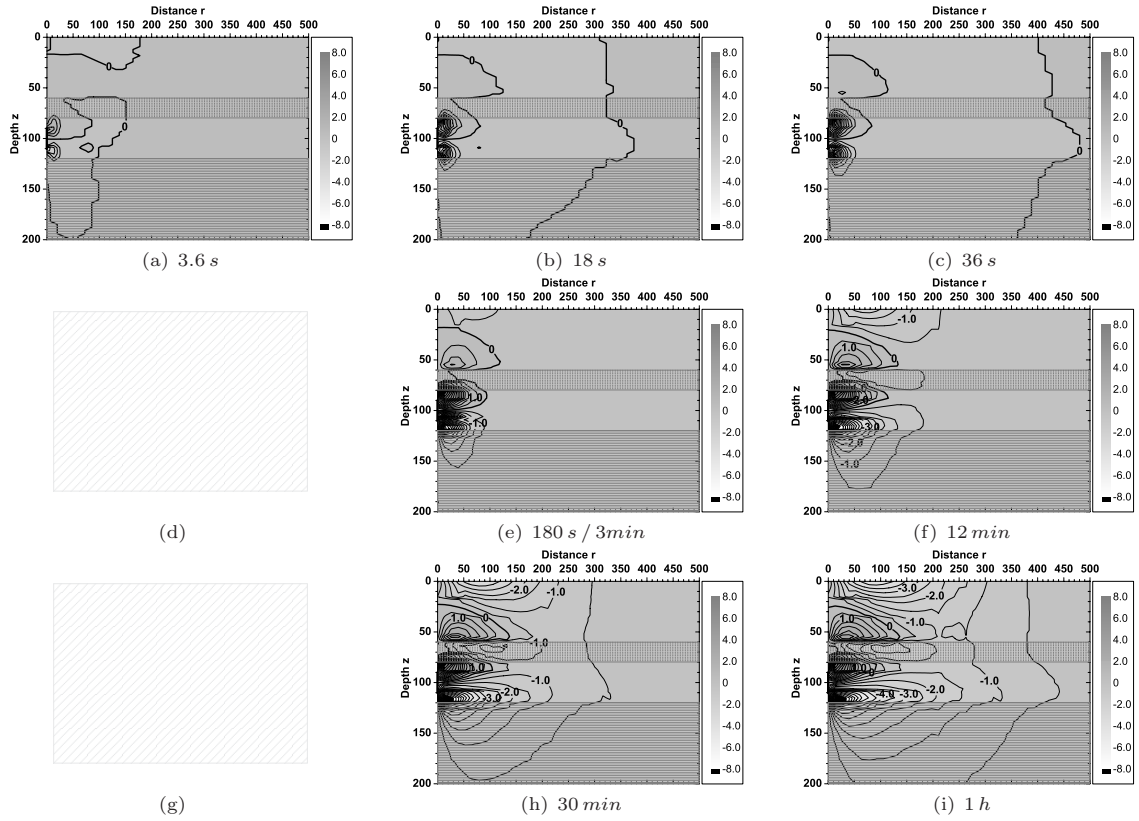


Figure A.22: Time slices, tilt $\Delta\gamma_r$ [μrad], 4-layer model, ‘mid sand–loam mix–small sand–clay’.

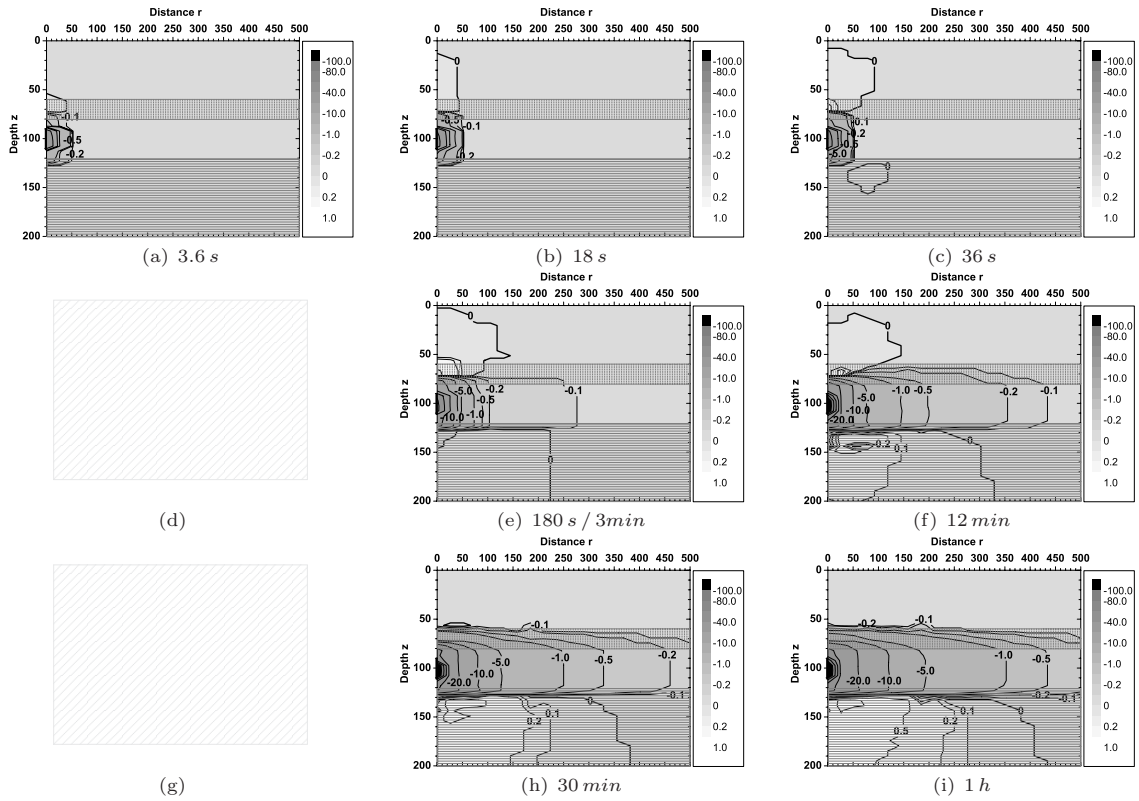


Figure A.23: Time slices, pore pressure p [kPa], 4-layer model, ‘mid sand–loam mix–small sand–clay’.

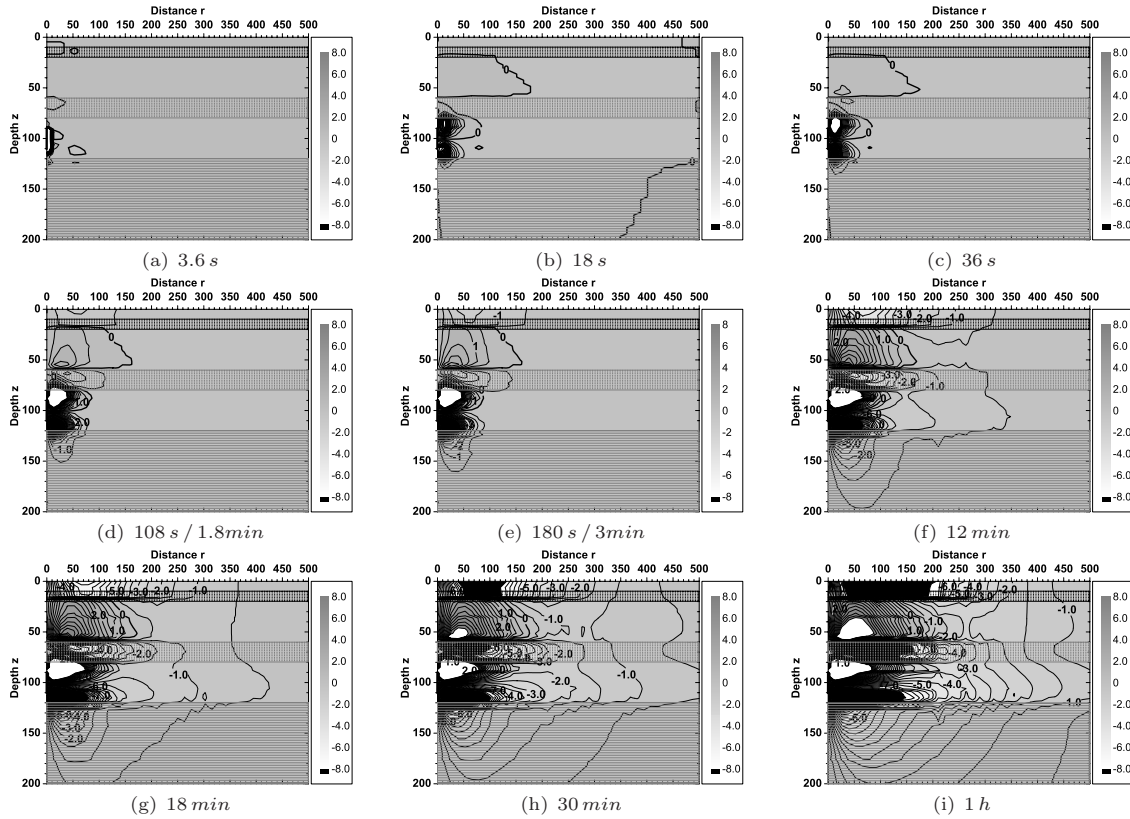


Figure A.24: Time slices, tilt $\Delta\gamma_r$ [μrad], adjusted 6-layer model.

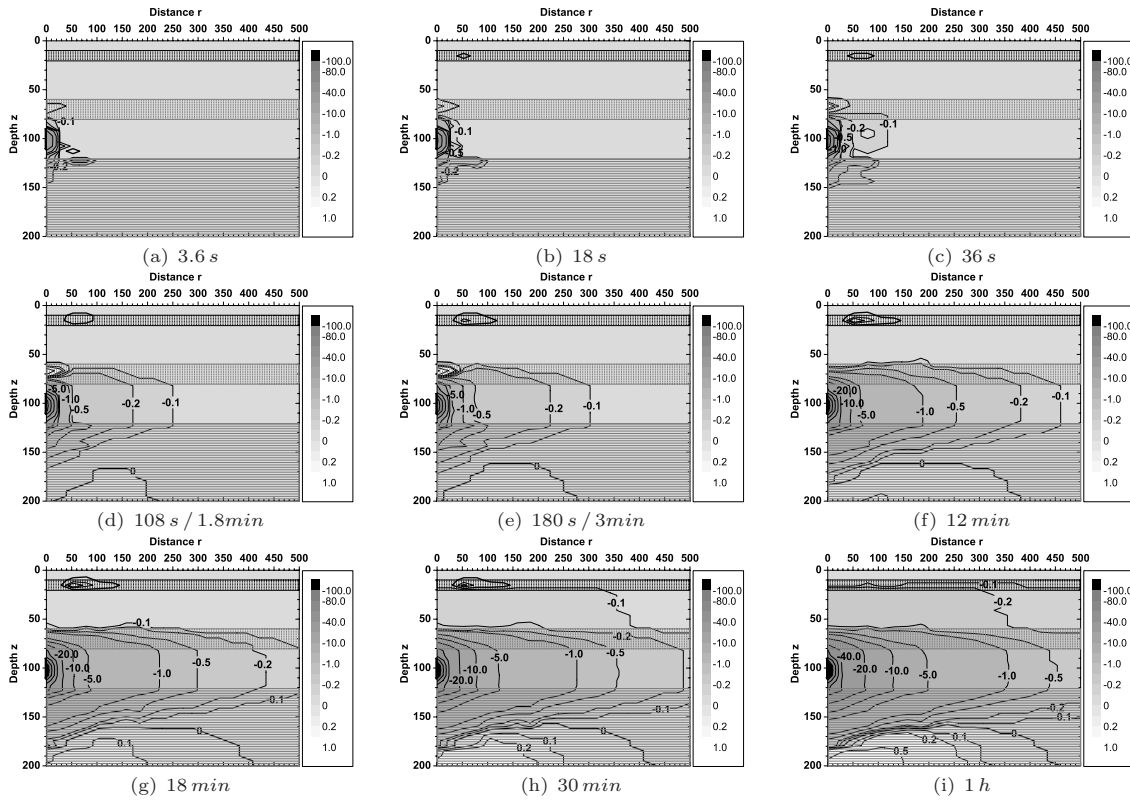


Figure A.25: Time slices, pore pressure p [kPa], adjusted 6-layer model.

Bibliography

- AGI (1991). User's manual no. B-91-1004, model 722 borehole tiltmeter. Applied Geomechanics Inc., Santa Cruz, CA 95062 (USA), <http://www.geomechanics.com/>.
- AGI (1997). User's manual no. B-88-1016, rev. D., 700-series platform and surface mount tiltmeters. Applied Geomechanics Inc., Santa Cruz, CA 95062 (USA), <http://www.geomechanics.com/>.
- AGI (1999a). User's manual no. B-91-1004, rev. B., model 722 borehole tiltmeter. Applied Geomechanics Inc., Santa Cruz, CA 95062 (USA), <http://www.geomechanics.com/>.
- AGI (1999b). User's manual no. B-94-1002, rev. C., model 84208 long board signal conditioner. Applied Geomechanics Inc., Santa Cruz, CA 95062 (USA), <http://www.geomechanics.com/>.
- AGI (2000). User's manual no. B-92-1003, rev. B., series 755, 756 and 757 miniature tilt sensors. Applied Geomechanics Inc., Santa Cruz, CA 95062 (USA), <http://www.geomechanics.com/>.
- AGI (2001). Data sheet, Geodetic borehole tiltmeter model 510. Applied Geomechanics Inc., Santa Cruz, CA 95062 (USA), <http://www.geomechanics.com/>.
- Agnew, D. C. (1986). Strainmeters and tiltmeters. *Review of Geophysics*, 24(3):579–624.
- Bathe, K.-J. (1990). *Finite-Elemente-Methoden*. Springer-Verlag Berlin Heidelberg New York, 2nd edn. ISBN 3-540-15602-X, 820 pp.
- Berger, J. (1975). A note on thermoelastic strains and tilts. *Journal of Geophysical Research*, 80(2):274–277.
- Bilham, R. (1993). Borehole inclinometer monument for millimeter horizontal geodetic control accuracy. *Geophysical Research Letters*, 20(20):2159–2162.
- Biot, M. A. (1941). General theory of three-dimensional consolidation. *Journal of Applied Physics*, 12:155–164.
- Biot, M. A. (1955). Theory of elasticity and consolidation for a porous anisotropic solid. *Journal of Applied Physics*, 26(2).
- Biot, M. A. (1956a). General solutions of the equations of elasticity and consolidation for a porous material. *Journal of Applied Mechanics*, 78:91–96.
- Biot, M. A. (1956b). Theory of propagation of elastic waves in a fluid-saturated porous solid: I. low frequency range. *Journal of the Acoustical Society of America*, 28:168–178.
- Biot, M. A. (1956c). Theory of propagation of elastic waves in a fluid-saturated porous solid: II. high frequency range. *Journal of the Acoustical Society of America*, 28:179–191.
- Biot, M. A. (1973). Nonlinear and semilinear rheology of porous solids. *Journal of Geophysical Research*, 78(23).
- Biot, M. A. & Willis, D. (1957). The elastic coefficients of the theory of consolidation. *Journal of Applied Mechanics*, 24:594–601.
- Bonaccorso, A., Falzone, G. & Gambino, S. (1999). An investigation into shallow borehole tiltmeters. *Geophysical Research Letters*, 26:1637–1640.
- Bonatz, M. (2000). A long-basis vertical tiltmeter for tectonic investigations (tectometer). Scientific report to CEE-Project, Etudes géophysiques complexes dans des zones tectoniques actives, pp. 1–10.

- Braitenberg, C. (1999). The hydrologic induced strain-tilt signal; a review. *Marées terrestres*, Bruxelles, 131:10171–10181.
- Brandt, D. (2002). Wireless LAN technology — The current state of wireless LAN technology, A Datanamics Labs Research white paper. Datanamics Non-Stop Networks, 4045 South Spencer Street, Suite B-38, Las Vegas, Nevada, <http://www.datanamics.com>.
- Bronstein, I. N. & Semendjajew, K. A. (1987). *Taschenbuch der Mathematik*. Verlag Harri Deutsch, Thun u. Frankfurt a.M., 23rd edn. ISBN 3-87144-492-8.
- Broska, J. C. & Barnette, H. J. (1999). Hydrogeology and analysis of aquifer characteristics in west-central Pinellas County, Florida. In: U.S. Geological Survey Open Field Report, Tallahassee, Florida, 99-185, p. 23.
- Burbey, T. J. & Helm, D. C. (1999). Modeling three-dimensional deformation in response to pumping of unconsolidated aquifers. *Environmental & Engineering Geoscience*, 5(2):199–212.
- Campbell, J., Kümpel, H.-J., Fabian, M., Fischer, D., Görres, B., Keyzers, C. J. & Lehmann, K. (2002). Recent movement patterns of the Lower Rhine Embayment from tilt, gravity and GPS data. *Netherlands Journal of Geosciences / Geologie en Mijnbouw*, 81(2):223–230.
- Clark, M. V., Leung, K. K., McNair, B. & Kostic, Z. (2002). Outdoor IEEE 802.11 cellular networks: radio link performance. *Proceedings of IEEE ICC 2002*, New York.
- Cleary, M. P. (1977). Fundamental solutions for a fluid-saturated porous solid. *International Journal of Solids and Structures*, 13(9):785–806.
- Colesanti, C., Ferretti, A., Prati, C. & Rocca, F. (2003). Monitoring landslides and tectonic motions with permanent scatterers technique. *Engineering Geology*, 68(1–2):3–14.
- Diallo, M. S. & Appel, E. (2000). Acoustic wave propagation in saturated porous media: reformulation of the Biot/Squirt flow theory. *Journal of Applied Geophysics*, 44:313–325.
- Domenico, S. N. (1977). Elastic properties of unconsolidated porous sand reservoirs. *Geophysics*, 42(7):1339–1368.
- d'Orey de Lantremange, N. (1998). Qualification test of the dual-axis bubble-type resistive tiltmeter (AGI-700 series): earth tides recorded and analyzed in the underground laboratory of Walferdange. *Marée Terrestres. Bulletin d'Informations*, 129:9953–9962.
- Dvorkin, J. & Nur, A. (1993). Dynamic poroelasticity: A unified model with the Squirt and the Biot mechanisms. *Geophysics*, 58(4):524–533.
- Eijkelkamp (1998). *Katalog und Teilleiste*. Eijkelkamp Agrisearch Equipment, Postfach 4, 6987 ZG Giesbeek, die Niederlande, <http://www.eijkelkamp.com>.
- Erftverband (1995). Pers. communication: Bohrprofil, Grundwassermessgruppen 99773.3. Erftverband Bergheim, Pfaffendorfer Weg 42, D-50126 Bergheim.
- Erftverband (1996). Grundwasser im südlichen Verbandsbereich. Erftverband Bergheim, Pfaffendorfer Weg 42, D-50126 Bergheim.
- Erftverband (1999). Pers. communication: Bohrprofile, Grundwassermessgruppen 39007.4, 39008.4, 39009.2, 39010.1, 99718/4 und Grundwassergleichenplan April 1997 Horizont 10 und 16. Erftverband Bergheim, Pfaffendorfer Weg 42, D-50126 Bergheim.
- Fabian, M. (1998). Untersuchungen zum Nachweis seismisch induzierter Drucksignale im gespannten Aquifer an einer ausgewählten Lokation in der Niederrheinischen Bucht. unpublished. Dipl. thesis in physics, Math.-Nat. Fak., Univ. Bonn.
- Fabian, M. & Kümpel, H.-J. (2003). Poroelasticity: observations of anomalous near surface tilt induced by ground water pumping. *Journal of Hydrology*, 281(3).
- Fabian, M., Rebscher, D. & Kümpel, H.-J. (2000). Bohrlochneigungsmessungen, Ergebnisse zum Pumpversuch Bremerhaven–Wulsdorf. *Schriftenreihe des SFB 350*, Univ. Bonn, 94.
- Feynman, R. P., Leighton, R. B. & Sands, M. (1991). Bd. 2. Hauptsächlich Elektrodynamik und Struktur der Materie. Oldenburg Verlag GmbH, München, 2nd edn.

- Fritz, J. (1998). Pers. communication: Lagepläne flach und tief verfilterter Grundwassermessstellen und Geologischer Schnitt, Wassererschließungsgebiet Wulsdorf. Niedersächsisches Landesamt für Bodenforschung (NLfB), Außenstelle Bremen.
- Fritz, J. (2001). Pers. communication: Holozänbasiskarte und Quartärbasiskarte, Bremerhaven Wulsdorf. Niedersächsisches Landesamt für Bodenforschung (NLfB), Außenstelle Bremen.
- Gambolati, G. (1974). Second-order theory of flow in three-dimensional deforming media. *Water Resources Research*, 10(6):1217–1228.
- Gambolati, G., Teatini, P., Baú, D. & Ferronato, M. (2000). Importance of poroelastic coupling in dynamically active aquifers of the Po River Basin, Italy. *Water Resources Research*, 36(9):2443–2459.
- Gambolati, G., Teatini, P. & Tomasi, L. (1999). Stress-strain analysis in productive gas/oil reservoirs. *International Journal for Numerical and Analytical Methods in Geomechanics*, 23(13):1495–1519.
- GLA-NW (1988). *Geologie am Niederrhein*. Geologisches Landesamt Nordrhein–Westfalen, Krefeld, 4th edn., 124 pp.
- Gouly, N. R. (1976). Strainmeters and tiltmeters in geophysics. *Tectonophysics*, 34:245–256.
- Gouly, N. R. (1998). Relationships between porosity and effective stress in shales. *First Break*, 16.
- Grant (2003a). Squirrel SQ1000 Data Logger. Grant Instruments (Cambridge) Ltd, Shepreth Cambridgeshire SG8 6GB, <http://www.grant.co.uk/>.
- Grant (2003b). Squirrel SQ1600 Data Logger. Grant Instruments (Cambridge) Ltd, Shepreth Cambridgeshire SG8 6GB, <http://www.grant.co.uk/>.
- Grecksch, G. (1999). Analyse und Interpretation von Brunnenspiegelschwankungen als Folge des Roermond-Erdbebens vom April 1992. *Berichte aus der Geowissenschaft*. Shaker Verlag, Aachen. ISBN 3–8265–6117–1. Diss. thesis, Math.-Nat. Fak., Univ. Bonn.
- Green, D. H. & Wang, H. F. (1986). Fluid pressure response to undrained compression in saturated sedimentary rock. *Geophysics*, 51(4):948–956.
- Greiner, W. (1991). *Klassische Elektrodynamik*. Theoretische Physik, Band 3. Verlag Harri Deutsch, Frankfurt a.M., Thun.
- Grundfos (2002). Grundfos – A wide range of quality pumps, catalogue. Grundfos Management A/S, Poul Due Jensens Vej 7, DK-8850 Bjerringbro, <http://www.grundfos.com/>.
- Grüneberg, S. (2002). Pers. communication. Institut für Geowissenschaftliche Gemeinschaftsaufgaben GGA, Stilleweg 2, D-30655 Hannover.
- Haugerud, R. A., Harding, D. J., Johnson, S. Y., Harless, J. L., Weaver, C. S. & Sherrod, B. L. (2003). High-resolution lidar topography of the Puget Lowland, Washington. *GSA Today*, 13(6):4–10.
- Hennigsen, D. & Katzung, G. (1998). *Einführung in die Geologie Deutschlands*. Enke-Verlag, Stuttgart, 5th edn., 244 pp.
- Hoffmann, M. (2002). Pers. communication. Erftverband Bergheim, Pfaffendorfer Weg 42, D-50126 Bergheim.
- Höltig, B. (1996). *Hydrogeologie*. Enke-Verlag, Stuttgart, 5th edn., 441 pp.
- Holzhausen, G. R. (1997). Tiltmeter temperature coefficients: Source, definition and use to improve accuracy. *Geotechnical News*, pp. 51–56.
- Hsieh, P. A. (1995). Poroelasticity simulation of ground-water flow and subsurface deformation. In: U.S. Geological survey open field report, subsidence interest group conference. Las Vegas, Nevada, February 14–16, 97–47, pp. 5–9.
- In-Situ (1989). Operators's manual, submersible pressure transducer model PXD–260. In-Situ Inc., 210 South 3rd Street P.O. Box I Laramie, WY 82070–0920 (USA), <http://www.in-situ.com/>.

- In-Situ (1995). Operators's manual, version 1.00: TROLL model SP4000-232. In-Situ Inc., 210 South 3rd Street P.O. Box I Laramie, WY 82070-0920 (USA), <http://www.in-situ.com/>.
- Jianfeng, Z. (1999). Quadrangle-grid velocity–stress finite difference method for poroelastic wave equations. *Geophysical Journal International*, 139:171–182.
- Karasaki, K., Freifeld, B., Cohen, C., Grossenbacher, K., Cook, P. & Vasco, D. (2000). A multidisciplinary fractured rock characterization study at Raymond field site, Raymond, CA. *Journal of Hydrology*, 236(1-2):17–34.
- Kau, P. (2000). Pers. communication. Verbandswasserwerk GmbH Euskirchen, Walramstr. 12, D-53879 Euskirchen.
- Kim, J.-M. & Parizek, R. R. (1997). Numerical simulation of the Noordbergum effect resulting from groundwater pumping in a layered aquifer system. *Journal of Hydrology*, 202:231–243.
- Kim, J.-M. & Parizek, R. R. (1999). Three-dimensional finite-element modelling for consolidation due to groundwater withdrawal in a desaturating anisotropic aquifer system. *International Journal for Numerical and Analytical Methods in Geomechanics*, 23(6):549–571.
- Klostermann, J., Kremers, J. & Röder, R. (1998). Rezente tektonische Bewegungen in der Niederrheinischen Bucht. *Fortschritte in der Geologie von Rheinland und Westfalen*, pp. 557–571.
- Krauss, I. (1974). Die Bestimmung der Transmissivität von Grundwasserleitern aus dem Einschwingverhalten des Brunnen–Grundwasserleitersystems. *Journal of Geophysics*, 40:381–400.
- Krauss-Kalweit, I. & Kalweit, H. (1984). Einschwingverfahren zur Grundwassererkundung; Eine Lösung für viele Anwendungen. Schwarzwaldweg 5a, 6094 Bischofsheim, Germany.
- Krusemann, G. P. & de Ridder, N. A. (1994). Analyses and evaluation of pumping test data. ILIR Publication 47. International Institut for Land Reclamation and Improvement, Wageningen, Netherlands, 377 pp.
- Kuchling, H. (1988). Taschenbuch der Physik. VEB Fachbuchverlag Leipzig, Lizenzausgabe für den Verlag Harri Deutsch, Thun, 10th edn., 676 pp.
- Kümpel, H.-J. (1982). Tilt Measurements. What do they tell us? *Terra Cognita*, 2:391–399.
- Kümpel, H.-J. (1989). Verformungen in der Umgebung von Brunnen. Habil. thesis, Math.-Nat. Fak., Univ. Kiel.
- Kümpel, H.-J. (1991). Poroelasticity: parameters reviewed. *Geophysical Journal International*, 105:783–799.
- Kümpel, H.-J. (1996). In-situ Deformationsmessungen zur Bestimmung hydraulischer Bodenkennwerte. In: Merkel, B., Dietrich, P. G., Struckmeier, W. & Löhnert, E. P. (eds.), *Grundwasser und Rohstoffgewinnung*, Reihe GeoCongress, chap. 2, pp. 291–296. Verlag Sven v. Loga, Köln.
- Kümpel, H.-J. (1997). In-situ deformation measurements for evaluation of hydraulic rock parameters. In: Wang, S. & Marinos, P. (eds.), *Proc. 39th Int. Geol. Congr. Beijing*, no. 23 in *Engineering Geology*, pp. 481–487. VSP, Utrecht.
- Kümpel, H.-J. (2003a). Scale aspects of geo-data sampling. In: Neugebauer, H. J. & Simmer, C. (eds.), *Dynamics of multiscale earth systems*, no. 97 in *Lecture Notes in Earth Sciences*, pp. 5–15. Springer, Heidelberg.
- Kümpel, H.-J. (2003b). Thermo-Hydro-Mechanical Coupling in Fractured Rock. In: Kümpel, H.-J. (ed.), *Pure and Applied Geophysics*, topical issue, 160, pp. 809–1161. Birkhäuser, Basel.
- Kümpel, H.-J. & Fabian, M. (2003). Tilt monitoring to assess the stability of geodetic reference points in permafrost environment. *Physics and Chemistry of the Earth*, 28:1249–1256.
- Kümpel, H.-J., Grecksch, G., Lehmann, K., Rebscher, D. & Schulze, K. C. (1999). Studies of in situ pore pressure fluctuations at various scales. *Oil & Gas Science and Technology – Rev. IFP*, 54(6):679–688.
- Kümpel, H.-J., Lehmann, K., Fabian, M. & Mentés, G. (2001). Point stability at shallow depth – experience from tilt measurements in the Lower Rhine Embayment, Germany, and implications for high resolution GPS and gravity recordings. *Geophysical Journal International*, 146:699–713.

- Kümpel, H.-J., Varga, P., Lehmann, K. & Mentés, G. (1996). Ground tilt induced by pumping – preliminary results from the Nagycenk test site, Hungary. *Acta Geodaetica et Geophysica Hungarica*, 31:67–78.
- Landes-Aufn. (1895). Topographische Karte 1:25000, Blatt 3094. Königlich Preussische Landes-Aufnahme, 1893.
- Langguth, H. R. & Treskatis, C. (1987). Umgekehrte Wasserspiegelreaktionen bei hydrologischen Pumpversuchen; der Nachweis von "Noordbergum-Effekt" und einer entsprechenden Druckabnahme ("Rhader-Effekt") beim Wiederanstieg in halbgespannten Aquiferen. *bbr. Brunnenbau, Bau von Wasserwerken, Rohrleitungsbau*, 38(10):369–376.
- Langguth, H. R. & Treskatis, C. (1989). Reverse water level fluctuations in semiconfined aquifer systems – "Rhade Effect". *Journal of Hydrology*, 109(1–2):79–93.
- Lehmann, K. (2001). Porendruckinduzierte Neigungssignale in geringen Tiefen und ihre Modellierung im homogenen Halbraum. *Berichte aus der Geowissenschaft*. Shaker Verlag, Aachen. ISBN 3-8265-8902-5. Diss. thesis, Math.-Nat. Fak., Univ. Bonn, download: <http://www.shaker-online.com/>.
- Leo, W. R. (1994). *Techniques for nuclear and particle physics experiments; A how-to approach*. Springer-Verlag New-York, 2nd edn. ISBN 0-387-57280-5.
- Letz, H., Jentzsch, G. & Jahr, T. (2003). Deformationsbeobachtungen in der Umgebung der KTB: Stationssuche, Vorerkundung und Installation der Neigungsmesser. In: 36. Herbsttagung des Arbeitskreises Geodäsie/Geophysik, 29.10. bis 01.11.2003, Außenstelle Grubenhagen des GGA-Instituts.
- Leung, K. K., McNair, B., Cimini, L. J. & Winters, J. H. (2002). Outdoor IEEE 802.11 cellular networks: MAC protocol design and performance. *Proceedings of IEEE ICC 2002, New York*.
- Lewis, R. W. (1991). Coupling versus uncoupling in soil consolidation. *International Journal for Numerical and Analytical Methods in Geomechanics*, 15(8):533–548.
- Lewis, R. W., Makurat, A. & Pao, W. K. S. (2003). Fully coupled modeling of seabed subsidence and reservoir compaction of North Sea oil fields. *Hydrogeology Journal*, 11(1):142–161.
- LVermA-NW (1995). Topographische Karte 1:25000, Blatt 5305. Landesvermessungsamt Nordrhein-Westfalen, Muffendorfer Strasse 19–21, D-53177 Bonn.
- Martau, R. (2001). Pers. communication. Geological Institut, Univ. Bonn.
- Maruyama, T. (1994). Fluid pressure responses of a water-saturated porous elastic multi-layered half-space to water pumping and atmospheric loading. *Journal of Physics of the Earth*, 42:331–375.
- McCarthy, J. M. & Yeh, W. W. G. (1990). Optimal pumping test design for parameter estimation and prediction in groundwater hydrology. *Water Resources Research*, 26(4):779–791.
- Mentés, G. (2002). Monitoring local geodynamical processes by borehole tiltmeters in the vicinity of the Mecsekajka-Fault in Hungary. In: Kahmen, H., Niemeier, W. & Retscher, G. (eds.), *Geodesy for geotechnical and structural engineering II*, pp. 278–287. Department of Applied and Engineering Geodesy, Institut of Geodesy and Geophysics, Vienna University of Technology, Vienna, Austria. ISBN 3-9501492-1-X.
- Mentés, G. & Fabian, M. (2001a). Investigation of ground and object motion at the TV tower in Sopron, Hungary. *Acta Geodaetica et Geophysica Hungarica*, 36(4):391–398.
- Mentés, G. & Fabian, M. (2001b). Investigation of motion due to mechanical coupling between ground and the TV tower at Sopron, Hungary. In: Zhenglu, Z., Retscher, G. & Guo, J. (eds.), *Proceedings of the IAG Workshop on Monitoring of Constructions and Local Geodynamic Processes*, Wuhan, China, pp. 56–62.
- Mentés, G., Lehmann, K., Varga, P. & Kümpel, H.-J. (1996). Some calibration of the Applied Geomechanics Inc. borehole tiltmeter model 722. *Acta Geodaetica et Geophysica Hungarica*, 31:79–89.
- Microcal Software, Inc. (1999). *Origin User's Manual Version 6*. Microcal Software, Inc., One Roundhouse Plaza, Northampton, MA 01060, USA.
- Mora, P., Baldi, P., Casula, G., Fabris, M., Ghirotti, M., Mazzini, E. & Pesci, A. (2003). Global Positioning System and digital photogrammetry for the monitoring of mass movements; application to the Ca'di Malta landslide (north Apennines, Italy). *Engineering Geology*, 31(1–2):103–121.

- Neuzil, C. E. (2003). Hydromechanical coupling in geologic process. *Hydrogeology Journal*, 11(1):41–83.
- Niebuhr, J. & Lindner, G. (2001). *Physikalische Meßtechnik mit Sensoren*. Oldenburg Verlag. ISBN 3486270079, 500 pp.
- Nur, A. & Byerlee, J. D. (1971). An exact effective stress law for elastic deformation of rock with fluids. *Journal of Geophysical Research*, 76(26):6414–6419.
- Pan, E. (1999). Green's functions in layered poroelastic half-spaces. *International Journal for Numerical and Analytical Methods in Geomechanics*, 23:1631–1653.
- Peters, J. & Beaumont, C. (1985). Borehole tilt measurements from Charlevoix, Quèbec. *Journal of Geophysical Research*, B14:12,791–12,806.
- Press, W. H., Flannery, B. P., Teukolsky, S. A. & Vetterling, W. T. (1988). *Numerical recipes in C – The art of scientific computing*. Cambridge University Press, Cambridge, 1st edn. ISBN 0-521-35465-X.
- Rajapakse, R. K. N. D. & Senjuntichai, T. (1993). Fundamental solutions for a poroelastic half-space with compressible constituents. *Journal of Applied Mechanics*, 60:847–856.
- Rebscher, D. (1996). Nachweis von in-situ Bodendeformationen gravitativen und vegetativen Ursprungs mittels Neigungsmessungen in Bonn-Ippendorf. Diss. thesis, Math.-Nat. Fak., Univ. Bonn.
- Rheinbraun (1997). Pers. communication: Schichtenfolge im rheinischen Braunkohlenrevier, GA 1/1 GZ-D7/0240 Red. BT 3 De 07/97. Rheinische Braunkohlenwerke AG Köln, HV, Abt. Wasserwirtschaft BT 3.
- Rheinbraun (2000). Pers. communication: Erftbecken – Schnitt 97b und Oberfläche Grundwassersohle 7B Bereich Rövenicher Sprung. Rheinische Braunkohlenwerke AG Köln.
- Rice, J. R. & Cleary, M. P. (1976). Some basic stress diffusion solutions for fluid-saturated elastic porous media with compressible constituents. *Reviews of Geophysics and Space Physics*, 14(2):227–241.
- Rodriguez, J. D. (1983). The Noordbergum effect and characterization of aquitards at the Rio Maior mining project. *Ground Water*, 21(2):200–207.
- Rogers, J. S., Jones, F. W. & Rouleau, P. (1986). Tiltmeters: A review and a new instrument. *AOSTRA Journal of Research*, 3(1):35–40.
- Rojstaczer, S. & Agnew, D. C. (1989). The influence of formation material properties on the response of water levels in wells to Earth tides and atmospheric loading. *Journal of Geophysical Research*, 94:12403–12411.
- Rowlands, K. A., Jones, L. D. & Whitworth, M. (2003). Landslide laser scanning: a new look at an old problem. *Quarterly Journal of Engineering Geology and Hydrogeology*, 36(2):155–157.
- Rudnicki, J. W. (1986). Fluid mass sources and point forces in linear elastic diffusive soils. *Mechanics of Materials*, 5:383–393.
- Sahay, P. N. (2001). Dynamic Green's function for homogeneous and isotropic porous media. *Geophysical Journal International*, 147(3):622–629.
- Schiffmann, R. L. (1970). The stress components of a porous medium. *Journal of Geophysical Research*, 75:4035–4038.
- Schrüfer, E. (1994). *Elektrische Meßtechnik*. Carl Hanser Verlag München.
- Schulze, K. C. (2002). Charakter von Fluidpegel- und Porendruckschwankungen in Tiefbohrungen, Ergebnisse von KTB und Kola. *Berichte aus der Geowissenschaft*. Shaker Verlag, Aachen. ISBN 3–8322-0876–3. Diss. thesis, Math.-Nat. Fak., Univ. Bonn, download: <http://www.shaker-online.com/>.
- Singh, S. K. (2001). Identifying impervious boundary and aquifer parameters from pump-test data. *Journal of Hydraulic Engineering*, 17(4):280–285.
- Skempton, A. W. (1954). The pore-pressure coefficients A and B. *Geotechnique*, 4:143–147.
- Skempton, A. W. (1960a). Effective stress in soils, concrete and rocks. In: *Proceedings of the Conference on Pore Pressure and Suction in Soils*, pp. 4–16. Butterworth, London.

- Skempton, A. W. (1960b). Terzaghi's discovery of effective stress. In: Bjerrum, L., Casagrande, A., Peck, R. B. & Skempton, A. W. (eds.), *From Theory to Practice in Soil Mechanics*, pp. 42–53. John Wiley, New York.
- Sleeman, R., Haak, H. W., Bos, M. S. & van Gend, J. J. A. (2000). Tidal tilt observations in the Netherlands using shallow borehole tiltmeters. *Physics and Chemistry of the Earth (A)*, 25:415–420.
- Sommerfeld, A. (1978). *Vorlesungen über Theoretische Physik*, Bd. 6, Partielle Differentialgleichungen in der Physik. Verlag Harri Deutsch, Frankfurt am Main, 6th edn. ISBN 3-87144-379-4, 298 pp.
- Sommerfeld, A. (1979). *Vorlesungen über Theoretische Physik*, Bd.2, Mechanik der deformierbaren Medien. Verlag Harri Deutsch, Frankfurt am Main, 6th edn. ISBN 3-87144-375-1, 446 pp.
- Stihl (2001). Datenblatt STIHL BT 360 - Das leistungsstarke Zweimann-Gerät. STIHL Vertriebszentrale AG & Co. KG, Robert-Bosch-Str. 13, 64807 Dieburg, Deutschland, <http://www.stihl.de>.
- Taguchi, I. & Kurashige, M. (2002). Fundamental solutions for a fluid-saturated, transversely isotropic, poroelastic solid. *International Journal for Numerical and Analytical Methods in Geomechanics*, 26(3):299–321.
- Terzaghi, K. (1925). *Erdbaumechanik*. Franz Deuticke, Vienna.
- Terzaghi, K. (1943). *Theoretical Soil Mechanics*. John Wiley and Sons, New York.
- Tofani, G. & Horath, F. (1990). Continuous tiltmeter monitoring to identify ground deformation mechanisms. *Geotechnical News*, 8(2).
- Tränkler, H.-R. & Obermeier, E. (1998). *Sensortechnik. Handbuch für Praxis und Wissenschaft*. Springer Verlag. ISBN 3540586407, 1584 pp.
- Valliant, H. D. & Burris, L. J. (1987). Evaluation of a miniature horizontal pendulum tilt transducer. In: Preprint of paper presented at Thirteenth Biennial Test Symposium Hollman Air Force Base, New Mexico, 6-8 October 1987.
- Vasco, D. W., Karasaki, K. & Doughty, C. (2000). Using surface deformation to image reservoir dynamics. *Geophysics*, 65(1):132–147.
- Vasco, D. W., Karasaki, K. & Kishida, K. (2001). A coupled inversion of pressure and surface displacement. *Water Resources Research*, 37(12):3071–3089.
- Vasco, D. W., Karasaki, K. & Myer, L. R. (1998). Monitoring of fluid injection and soil consolidation using surface tilt measurements. *Journal of Geotechnical and Geoenvironmental Engineering*, 124(1):29–37.
- Vasco, D. W., Karasaki, K. & Nakagome, O. (2002a). Monitoring reservoir production using surface deformation at the Hijiori test site and the Okuaizu geothermal field, Japan. *Geothermics*, 31(3):303–342.
- Vasco, D. W., Wicks, C., Karasaki, K. & Marques, O. (2002b). Geodetic imaging: High resolution reservoir monitoring using satellite interferometry. *Geophysical Journal International*, 149:555–571.
- Verbandswasserwerk (1998). 90 Jahre Verbandswasserwerk GmbH Euskirchen. Verbandswasserwerk GmbH Euskirchen, Walramstr. 12, D-53879 Euskirchen.
- Verbandswasserwerk (1999). Pers. communication: Grundwassergleichen 2. Grundwasserstockwerk Wasserwerk Oberelvenich, Geologischer Schnitt I + II, Schematischer Schnitt, Bohrprofile von Brunnen und Grundwassermessstellen 39017/0, 840090, 840079, 040049–040052. Verbandswasserwerk GmbH Euskirchen, Walramstr. 12, D-53879 Euskirchen.
- Verruijt, A. (1969). Elastic storage of aquifers. In: DeWiest, R. (ed.), *Flow through porous media*, pp. 331–376. Academic Press, New York.
- Vetterling, W. T., Teukolsky, S. A., Press, W. H. & Flannery, B. P. (1988). *Numerical recipes – Example book (C)*. Cambridge University Press, Cambridge, 1st edn. ISBN 0-521-35746-2, 0-521-35467-6 (diskette).
- von Seht, I. & Wohlenberg, J. (1996). Die seismische Bodenunruhe als Werkzeug zur Erkundung des Geologischen Untergrundes. In: *Mitteilungen der Deutschen Geophysikalischen Gesellschaft*, vol. 1, pp. 23–33. Deutsche Geophysikalische Gesellschaft.

- Wallbraun, A. (1992). Einfluß der Schollenrandstörungen in der Niederrheinischen Bucht auf den Grundwasserabfluß. Kartographie und Druck Peter List, Viktoriastrasse 18, D-5100 Aachen, 122 pp. Diss. thesis, Fak. f. Bergb. Hüttenwes. u. Geowiss., RWTH Aachen.
- Walters, D. A., Settari, A. & Kry, P. R. (2002). Coupled geomechanical and reservoir modeling investigating poroelastic effects of cyclic steam stimulation in the Cold Lake Reservoir. *SPE Reservoir Evaluation and Engineering*, 5(6):507–516.
- Wang, H. F. (1993). Quasi-static poroelastic parameters in rock and their geophysical application. *Pure and Applied Geophysics*, 141(2/3/4):269–286.
- Wang, H. F. (2000). *Theory of linear poroelasticity – with applications to geomechanics and hydrogeology*. Princeton University Press, Princeton, 287 pp.
- Wang, R. & Kümpel, H.-J. (2003). Poroelasticity: Efficient modelling of strongly coupled slow deformation processes in multi-layered half-space. *Geophysics*, 68(2):705–717.
- Weise, A., Jentzsch, G., Kiviniemi, A. & Kääriäinen, J. (1999). Comparison of long-period tilt measurements: results from the two clinometric stations Metsähovi and Lohja, Finland. *Geodynamics*, 27:237–257.
- Wyatt, F. & Berger, J. (1980). Investigations of tilt measurements using shallow borehole tiltmeters. *Journal of Geophysical Research*, 85(B8):4351–4362.
- Wyatt, F., Morrissey, S.-T. & Agnew, D. C. (1988). Shallow borehole tilt: A reprise. *Journal of Geophysical Research*, 93(B8):9197–9201.
- Zeng, D., Katsube, N. & Zhang, J. (1999). A hybrid finite element method for fluid-filled porous materials. *International Journal for Numerical and Analytical Methods in Geomechanics*, 23(13):1521–1534.
- Zimmerman, R. W. (2000). Coupling in poroelasticity and thermoelasticity. *International Journal of Rock Mechanics and Mining Sciences*, 37:79–87.
- Zimmerman, R. W., Somerton, W. H. & King, M. S. (1986). Compressibility of porous rocks. *Journal of Geophysical Research*, 91:12765–12777.

Acknowledgements – Danksagung

Herrn Professor Dr. H.-J. Kümpel gebührt mein besonderer Dank für die ausgezeichnete und intensive Betreuung sowie insbesondere für die konsequente Fortführung der Unterstützung und Förderung meiner Arbeit. Für weitere Unterstützung der Arbeit danke ich Herrn Professor Dr. H. J. Neugebauer und Herrn Professor Dr. E. Hilger sowie Herrn PD Dr. A. Hördt, dem auch mein Dank für die Übernahme des Korreferates gebührt. Herrn Professor Dr. J. Campbell danke ich für viel Beratung.

Ganz besonderer Dank gehört der Verbandswasserwerk GmbH Euskirchen und allen überaus freundlichen und hilfsbereiten Mitarbeitern, für die ich hier stellvertretend nennen möchte: Herrn A. Pütz für die Geschäftsführung, Herrn J. Goebels für den technischen Bereich und die Herren P. Kau, H. Hündgen und H. Wollersheim für den Außenbereich, Wasserwerk Oberelvenich. Sie unterstützten mich bei Arbeiten auf dem Wasserwerksgelände und bei der Anfertigung von Bohrungen, der Stationsbetreuung und den Messungen. Ohne diese zuvorkommenden Hilfeleistungen wären ganz wesentliche Teile dieser Arbeit nicht zustande gekommen. Weiterhin danke ich den Herren H.-J. Krahé, B. Weber, A. Bauer und der Betriebsgemeinschaft Orth sowie der Stadt Zülpich, die mir großzügig Messflächen zur Verfügung stellten.

Für zahllose Diskussionen über Messgeräte, Datenerfassungsmethoden und viele Ratschläge, als auch tatkräftige Unterstützung bei der Einrichtung von Neigungsmesserstationen danke ich Herrn Dr. Gy. Mentés vom Geodätischen und Geophysikalischen Forschungsinstitut der Ungarischen Akademie der Wissenschaften in Sopron, Ungarn. Etliche Ratschläge und Tipps zum Einsatz der Neigungsmesser gab mir zudem Herr Dr. G. R. Holzhausen, Applied Geomechanics Inc. .

Ebenso intensiven und umfangreichen Austausch, jedoch über Lösungen poroelastischer Probleme, mathematische Modellierung mit POEL und Interpretationen von Rechnungen und Experimenten hatte ich mit Herrn Dr. R. Wang vom GeoForschungsZentrum Potsdam. Ihm danke ich ganz besonders.

Meinen ‘HiWi’s, den Herrn Dipl.-Geol. R. Martau und Dipl.-Phys. M. Müller danke ich für ihre Ausdauer bei der Betreuung von Dauermessstationen sowie unzählige Hilfen, was bei weitem über das notwendige Maß hinausging. Bei den Oberflächendformationsmessungen halfen mir mit großem Einsatz Herr Dipl.-Ing. G. Druivenga und Herr Dipl.-Ing. S. Grüneberg vom Institut für Geowissenschaftliche Gemeinschaftsaufgaben, GGA, Hannover. Messgeräte stellten mir Frau Dipl.-Ing. H. Rifai, ebenfalls GGA-Institut, und Herr Dipl.-Ing. R. Harms von der Forschungszentrum Jülich GmbH zur Verfügung. Den Herren Dr. W. Kessels, Dr. C. Fulda und Dipl.-Ing. G. Zoth, GGA-Institut, sowie den Stadtwerken Bremerhaven danke ich für die Durchführung und Begleitung des Pumpversuchs bei Bremerhafen–Wulsdorf. Herr Dipl.-Geol. J. Fritz vom Niedersächsischen Landesamt für Bodenforschung (NLFb), Außenstelle Bremen, sei für die zahlreichen geologischen Informationen hierzu gedankt. Herr Dr. M. Hoffmann und Herr Dr. A. Wallbraun vom Erftverband Bergheim halfen mir bei der Auswahl von Messstationen in der Niederrheinischen Bucht, insbesondere der Lokation Oberelvenich. Herrn Dipl.-Ing. O. Bromorzki danke ich für geodätische Messarbeiten.

Herrn Dr. A. Dreist danke ich für die Rechneradministration im Institut. Für das freundschaftliche und produktive Arbeitsklima in der Gruppe Angewandte Geophysik bedanke ich bei meinen Kollegen Herrn Dipl.-Phys. C. Alteköster, Herrn Dr. G. Grecksch, Frau Dipl.-Phys. U. Herrmann, Herrn Dr. Ch. Keyzers, Herrn Dr. K. Lehmann, Frau Dr. S. Leonardi, Frau Dr. D. Rebscher und Frau Dr. K. C. Schulze. Für Korrekturen des Manuskripts danke ich insbesondere Frau Dr. S. Leonardi und Frau Dr. K. C. Schulze. Aus dem Sonderforschungsbereich 350 danke ich Herrn Dr. S. Hergarten und Herrn Dr. J. Schmidt für viele Hilfen und die ausgezeichnete Kooperation. Neben meinen Kollegen haben bei der Anfertigung von Bohrungen und der Einrichtung von Messstationen mitgeholfen die Herren E. Fabian, S. Ippendorf, W. Ippendorf, Dipl.-Ing. N. Kessler, Dr. W. Steinbeck, Dipl.-Ing. B. Tschöke und K. Jahnke.

Zum überwiegenden Teil wurde diese Arbeit finanziert und ermöglicht von der Deutschen Forschungsgemeinschaft (DFG) und dem Sonderforschungsbereich 350 (SFB 350), dem Institut für Geowissenschaftliche Gemeinschaftsaufgaben (GGA), Hannover, dem Geologischen Institut der Universität Bonn – Fachrichtung Angewandte Geophysik und dem Physikalischen Institut der Universität Bonn.

Publications of this series:

- No. 1** **Wefer, G., E. Suess and cruise participants**
Bericht über die POLARSTERN-Fahrt ANT IV/2, Rio de Janeiro - Punta Arenas, 6.11. - 1.12.1985.
60 pages, Bremen, 1986.
- No. 2** **Hoffmann, G.**
Holozänstratigraphie und Küstenlinienverlagerung an der andalusischen Mittelmeerküste.
173 pages, Bremen, 1988. (out of print)
- No. 3** **Wefer, G. and cruise participants**
Bericht über die METEOR-Fahrt M 6/6, Libreville - Las Palmas, 18.2. - 23.3.1988.
97 pages, Bremen, 1988.
- No. 4** **Wefer, G., G.F. Lutze, T.J. Müller, O. Pfannkuche, W. Schenke, G. Siedler, W. Zenk**
Kurzbericht über die METEOR-Expedition No. 6, Hamburg - Hamburg, 28.10.1987 - 19.5.1988.
29 pages, Bremen, 1988. (out of print)
- No. 5** **Fischer, G.**
Stabile Kohlenstoff-Isotope in partikulärer organischer Substanz aus dem Südpolarmeer
(Atlantischer Sektor). 161 pages, Bremen, 1989.
- No. 6** **Berger, W.H. and G. Wefer**
Partikelfluß und Kohlenstoffkreislauf im Ozean.
Bericht und Kurzfassungen über den Workshop vom 3.-4. Juli 1989 in Bremen.
57 pages, Bremen, 1989.
- No. 7** **Wefer, G. and cruise participants**
Bericht über die METEOR - Fahrt M 9/4, Dakar - Santa Cruz, 19.2. - 16.3.1989.
103 pages, Bremen, 1989.
- No. 8** **Kölling, M.**
Modellierung geochemischer Prozesse im Sickerwasser und Grundwasser.
135 pages, Bremen, 1990.
- No. 9** **Heinze, P.-M.**
Das Auftriebsgeschehen vor Peru im Spätquartär. 204 pages, Bremen, 1990. (out of print)
- No. 10** **Willems, H., G. Wefer, M. Rinski, B. Donner, H.-J. Bellmann, L. Eißmann, A. Müller,
B.W. Flemming, H.-C. Höfle, J. Merkt, H. Streif, G. Hertweck, H. Kuntze, J. Schwaar,
W. Schäfer, M.-G. Schulz, F. Grube, B. Menke**
Beiträge zur Geologie und Paläontologie Norddeutschlands: Exkursionsführer.
202 pages, Bremen, 1990.
- No. 11** **Wefer, G. and cruise participants**
Bericht über die METEOR-Fahrt M 12/1, Kapstadt - Funchal, 13.3.1990 - 14.4.1990.
66 pages, Bremen, 1990.
- No. 12** **Dahmke, A., H.D. Schulz, A. Kölling, F. Kracht, A. Lücke**
Schwermetallspuren und geochemische Gleichgewichte zwischen Porenlösung und Sediment
im Wesermündungsgebiet. BMFT-Projekt MFU 0562, Abschlußbericht. 121 pages, Bremen, 1991.
- No. 13** **Rostek, F.**
Physikalische Strukturen von Tiefseesedimenten des Südatlantiks und ihre Erfassung in
Echolotregistrierungen. 209 pages, Bremen, 1991.
- No. 14** **Baumann, M.**
Die Ablagerung von Tschernobyl-Radiocäsium in der Norwegischen See und in der Nordsee.
133 pages, Bremen, 1991. (out of print)
- No. 15** **Kölling, A.**
Frühdiagenetische Prozesse und Stoff-Flüsse in marinen und ästuarinen Sedimenten.
140 pages, Bremen, 1991.
- No. 16** **SFB 261 (ed.)**
1. Kolloquium des Sonderforschungsbereichs 261 der Universität Bremen (14.Juni 1991):
Der Südatlantik im Spätquartär: Rekonstruktion von Stoffhaushalt und Stromsystemen.
Kurzfassungen der Vorträge und Poster. 66 pages, Bremen, 1991.
- No. 17** **Pätzold, J. and cruise participants**
Bericht und erste Ergebnisse über die METEOR-Fahrt M 15/2, Rio de Janeiro - Vitoria,
18.1. - 7.2.1991. 46 pages, Bremen, 1993.
- No. 18** **Wefer, G. and cruise participants**
Bericht und erste Ergebnisse über die METEOR-Fahrt M 16/1, Pointe Noire - Recife,
27.3. - 25.4.1991. 120 pages, Bremen, 1991.
- No. 19** **Schulz, H.D. and cruise participants**
Bericht und erste Ergebnisse über die METEOR-Fahrt M 16/2, Recife - Belem, 28.4. - 20.5.1991.
149 pages, Bremen, 1991.

- No. 20 Berner, H.**
Mechanismen der Sedimentbildung in der Fram-Straße, im Arktischen Ozean und in der Norwegischen See. 167 pages, Bremen, 1991.
- No. 21 Schneider, R.**
Spätquartäre Produktivitätsänderungen im östlichen Angola-Becken: Reaktion auf Variationen im Passat-Monsun-Windsystem und in der Advektion des Benguela-Küstenstroms. 198 pages, Bremen, 1991. (out of print)
- No. 22 Hebbeln, D.**
Spätquartäre Stratigraphie und Paläozoozoographie in der Fram-Straße. 174 pages, Bremen, 1991.
- No. 23 Lücke, A.**
Umsetzungsprozesse organischer Substanz während der Frühdiagenese in ästuarinen Sedimenten. 137 pages, Bremen, 1991.
- No. 24 Wefer, G. and cruise participants**
Bericht und erste Ergebnisse der METEOR-Fahrt M 20/1, Bremen - Abidjan, 18.11.- 22.12.1991. 74 pages, Bremen, 1992.
- No. 25 Schulz, H.D. and cruise participants**
Bericht und erste Ergebnisse der METEOR-Fahrt M 20/2, Abidjan - Dakar, 27.12.1991 - 3.2.1992. 173 pages, Bremen, 1992.
- No. 26 Gingele, F.**
Zur klimaabhängigen Bildung biogener und terrigener Sedimente und ihrer Veränderung durch die Frühdiagenese im zentralen und östlichen Südatlantik. 202 pages, Bremen, 1992.
- No. 27 Bickert, T.**
Rekonstruktion der spätquartären Bodenwasserzirkulation im östlichen Südatlantik über stabile Isotope benthischer Foraminiferen. 205 pages, Bremen, 1992. (out of print)
- No. 28 Schmidt, H.**
Der Benguela-Strom im Bereich des Walfisch-Rückens im Spätquartär. 172 pages, Bremen, 1992.
- No. 29 Meinecke, G.**
Spätquartäre Oberflächenwassertemperaturen im östlichen äquatorialen Atlantik. 181 pages, Bremen, 1992.
- No. 30 Bathmann, U., U. Bleil, A. Dahmke, P. Müller, A. Nehr Korn, E.-M. Nöthig, M. Olesch, J. Pätzold, H.D. Schulz, V. Smetacek, V. Spieß, G. Wefer, H. Willems**
Bericht des Graduierten Kollegs. Stoff-Flüsse in marinen Geosystemen. Berichtszeitraum Oktober 1990 - Dezember 1992. 396 pages, Bremen, 1992.
- No. 31 Damm, E.**
Frühdiagenetische Verteilung von Schwermetallen in Schlicksedimenten der westlichen Ostsee. 115 pages, Bremen, 1992.
- No. 32 Antia, E.E.**
Sedimentology, Morphodynamics and Facies Association of a mesotidal Barrier Island Shoreface (Spiekeroog, Southern North Sea). 370 pages, Bremen, 1993.
- No. 33 Duinker, J. and G. Wefer (ed.)**
Bericht über den 1. JGOFS-Workshop. 1./2. Dezember 1992 in Bremen. 83 pages, Bremen, 1993.
- No. 34 Kasten, S.**
Die Verteilung von Schwermetallen in den Sedimenten eines stadtbremischen Hafenbeckens. 103 pages, Bremen, 1993.
- No. 35 Spieß, V.**
Digitale Sedimentographie. Neue Wege zu einer hochauflösenden Akustostratigraphie. 199 pages, Bremen, 1993.
- No. 36 Schinzel, U.**
Laborversuche zu frühdiagenetischen Reaktionen von Eisen (III) - Oxidhydraten in marinen Sedimenten. 189 pages, Bremen, 1993.
- No. 37 Sieger, R.**
CoTAM - ein Modell zur Modellierung des Schwermetalltransports in Grundwasserleitern. 56 pages, Bremen, 1993. (out of print)
- No. 38 Willems, H. (ed.)**
Geoscientific Investigations in the Tethyan Himalayas. 183 pages, Bremen, 1993.
- No. 39 Hamer, K.**
Entwicklung von Laborversuchen als Grundlage für die Modellierung des Transportverhaltens von Arsenat, Blei, Cadmium und Kupfer in wassergesättigten Säulen. 147 pages, Bremen, 1993.
- No. 40 Sieger, R.**
Modellierung des Stofftransports in porösen Medien unter Ankopplung kinetisch gesteuerter Sorptions- und Redoxprozesse sowie thermischer Gleichgewichte. 158 pages, Bremen, 1993.

- No. 41** **Thießen, W.**
Magnetische Eigenschaften von Sedimenten des östlichen Südatlantiks und ihre paläozeanographische Relevanz. 170 pages, Bremen, 1993.
- No. 42** **Spieß, V. and cruise participants**
Report and preliminary results of METEOR-Cruise M 23/1, Kapstadt - Rio de Janeiro, 4.-25.2.1993. 139 pages, Bremen, 1994.
- No. 43** **Bleil, U. and cruise participants**
Report and preliminary results of METEOR-Cruise M 23/2, Rio de Janeiro - Recife, 27.2.-19.3.1993. 133 pages, Bremen, 1994.
- No. 44** **Wefer, G. and cruise participants**
Report and preliminary results of METEOR-Cruise M 23/3, Recife - Las Palmas, 21.3. - 12.4.1993. 71 pages, Bremen, 1994.
- No. 45** **Giese, M. and G. Wefer (ed.)**
Bericht über den 2. JGOFS-Workshop. 18./19. November 1993 in Bremen. 93 pages, Bremen, 1994.
- No. 46** **Balzer, W. and cruise participants**
Report and preliminary results of METEOR-Cruise M 22/1, Hamburg - Recife, 22.9. - 21.10.1992. 24 pages, Bremen, 1994.
- No. 47** **Stax, R.**
Zyklische Sedimentation von organischem Kohlenstoff in der Japan See: Anzeiger für Änderungen von Paläozeanographie und Paläoklima im Spätkänozoikum. 150 pages, Bremen, 1994.
- No. 48** **Skowronek, F.**
Frühdiaagenetische Stoff-Flüsse gelöster Schwermetalle an der Oberfläche von Sedimenten des Weser Ästuares. 107 pages, Bremen, 1994.
- No. 49** **Dersch-Hansmann, M.**
Zur Klimaentwicklung in Ostasien während der letzten 5 Millionen Jahre: Terrigener Sedimenteintrag in die Japan See (ODP Ausfahrt 128). 149 pages, Bremen, 1994.
- No. 50** **Zabel, M.**
Frühdiaagenetische Stoff-Flüsse in Oberflächen-Sedimenten des äquatorialen und östlichen Südatlantik. 129 pages, Bremen, 1994.
- No. 51** **Bleil, U. and cruise participants**
Report and preliminary results of SONNE-Cruise SO 86, Buenos Aires - Capetown, 22.4. - 31.5.93. 116 pages, Bremen, 1994.
- No. 52** **Symposium: The South Atlantic: Present and Past Circulation.**
Bremen, Germany, 15 - 19 August 1994. Abstracts. 167 pages, Bremen, 1994.
- No. 53** **Kretzmann, U.B.**
⁵⁷Fe-Mössbauer-Spektroskopie an Sedimenten - Möglichkeiten und Grenzen. 183 pages, Bremen, 1994.
- No. 54** **Bachmann, M.**
Die Karbonatrampe von Organyà im oberen Oberapt und unteren Unteralt (NE-Spanien, Prov. Lerida): Fazies, Zyklus- und Sequenzstratigraphie. 147 pages, Bremen, 1994. (out of print)
- No. 55** **Kemle-von Mücke, S.**
Oberflächenwasserstruktur und -zirkulation des Südostatlantiks im Spätquartär. 151 pages, Bremen, 1994.
- No. 56** **Petermann, H.**
Magnetotaktische Bakterien und ihre Magnetosome in Oberflächensedimenten des Südatlantiks. 134 pages, Bremen, 1994.
- No. 57** **Mulitza, S.**
Spätquartäre Variationen der oberflächennahen Hydrographie im westlichen äquatorialen Atlantik. 97 pages, Bremen, 1994.
- No. 58** **Segl, M. and cruise participants**
Report and preliminary results of METEOR-Cruise M 29/1, Buenos-Aires - Montevideo, 17.6. - 13.7.1994. 94 pages, Bremen, 1994.
- No. 59** **Bleil, U. and cruise participants**
Report and preliminary results of METEOR-Cruise M 29/2, Montevideo - Rio de Janeiro, 15.7. - 8.8.1994. 153 pages, Bremen, 1994.
- No. 60** **Henrich, R. and cruise participants**
Report and preliminary results of METEOR-Cruise M 29/3, Rio de Janeiro - Las Palmas, 11.8. - 5.9.1994. Bremen, 1994. (out of print)

- No. 61** **Sagemann, J.**
Saisonale Variationen von Porenwasserprofilen, Nährstoff-Flüssen und Reaktionen in intertidalen Sedimenten des Weser-Ästuars. 110 pages, Bremen, 1994. (out of print)
- No. 62** **Giese, M. and G. Wefer**
Bericht über den 3. JGOFS-Workshop. 5./6. Dezember 1994 in Bremen.
84 pages, Bremen, 1995.
- No. 63** **Mann, U.**
Genese kretazischer Schwarzschiefer in Kolumbien: Globale vs. regionale/lokale Prozesse.
153 pages, Bremen, 1995. (out of print)
- No. 64** **Willems, H., Wan X., Yin J., Dongdui L., Liu G., S. Dürr, K.-U. Gräfe**
The Mesozoic development of the N-Indian passive margin and of the Xigaze Forearc Basin in southern Tibet, China. – Excursion Guide to IGCP 362 Working-Group Meeting "Integrated Stratigraphy". 113 pages, Bremen, 1995. (out of print)
- No. 65** **Hünken, U.**
Liefergebiets - Charakterisierung proterozoischer Goldseifen in Ghana anhand von Fluideinschluß - Untersuchungen. 270 pages, Bremen, 1995.
- No. 66** **Nyandwi, N.**
The Nature of the Sediment Distribution Patterns in the Spiekeroog Backbarrier Area, the East Frisian Islands. 162 pages, Bremen, 1995.
- No. 67** **Isenbeck-Schröter, M.**
Transportverhalten von Schwermetallkationen und Oxoanionen in wassergesättigten Sanden. - Laborversuche in Säulen und ihre Modellierung -. 182 pages, Bremen, 1995.
- No. 68** **Hebbeln, D. and cruise participants**
Report and preliminary results of SONNE-Cruise SO 102, Valparaiso - Valparaiso, 95.
134 pages, Bremen, 1995.
- No. 69** **Willems, H. (Sprecher), U. Bathmann, U. Bleil, T. v. Dobeneck, K. Herterich, B.B. Jorgensen, E.-M. Nöthig, M. Olesch, J. Pätzold, H.D. Schulz, V. Smetacek, V. Speiß, G. Wefer**
Bericht des Graduierten-Kollegs Stoff-Flüsse in marine Geosystemen.
Berichtszeitraum Januar 1993 - Dezember 1995.
45 & 468 pages, Bremen, 1995.
- No. 70** **Giese, M. and G. Wefer**
Bericht über den 4. JGOFS-Workshop. 20./21. November 1995 in Bremen. 60 pages, Bremen, 1996. (out of print)
- No. 71** **Meggers, H.**
Pliozän-quartäre Karbonatsedimentation und Paläozeanographie des Nordatlantiks und des Europäischen Nordmeeres - Hinweise aus planktischen Foraminiferengemeinschaften.
143 pages, Bremen, 1996. (out of print)
- No. 72** **Teske, A.**
Phylogenetische und ökologische Untersuchungen an Bakterien des oxidativen und reduktiven marinen Schwefelkreislaufs mittels ribosomaler RNA. 220 pages, Bremen, 1996. (out of print)
- No. 73** **Andersen, N.**
Biogeochemische Charakterisierung von Sinkstoffen und Sedimenten aus ostatlantischen Produktions-Systemen mit Hilfe von Biomarkern. 215 pages, Bremen, 1996.
- No. 74** **Treppke, U.**
Saisonalität im Diatomeen- und Silikoflagellatenfluß im östlichen tropischen und subtropischen Atlantik. 200 pages, Bremen, 1996.
- No. 75** **Schüring, J.**
Die Verwendung von Steinkohlebergematerialien im Deponiebau im Hinblick auf die Pyritverwitterung und die Eignung als geochemische Barriere. 110 pages, Bremen, 1996.
- No. 76** **Pätzold, J. and cruise participants**
Report and preliminary results of VICTOR HENSEN cruise JOPS II, Leg 6, Fortaleza - Recife, 10.3. - 26.3. 1995 and Leg 8, Vitória - Vitória, 10.4. - 23.4.1995.
87 pages, Bremen, 1996.
- No. 77** **Bleil, U. and cruise participants**
Report and preliminary results of METEOR-Cruise M 34/1, Cape Town - Walvis Bay, 3.-26.1.1996.
129 pages, Bremen, 1996.
- No. 78** **Schulz, H.D. and cruise participants**
Report and preliminary results of METEOR-Cruise M 34/2, Walvis Bay - Walvis Bay, 29.1.-18.2.96
133 pages, Bremen, 1996.
- No. 79** **Wefer, G. and cruise participants**
Report and preliminary results of METEOR-Cruise M 34/3, Walvis Bay - Recife, 21.2.-17.3.1996.
168 pages, Bremen, 1996.

- No. 80** **Fischer, G. and cruise participants**
Report and preliminary results of METEOR-Cruise M 34/4, Recife - Bridgetown, 19.3.-15.4.1996.
105 pages, Bremen, 1996.
- No. 81** **Kulbrok, F.**
Biostratigraphie, Fazies und Sequenzstratigraphie einer Karbonatrampe in den Schichten der Oberkreide und des Alttertiärs Nordost-Ägyptens (Eastern Desert, N'Golf von Suez, Sinai).
153 pages, Bremen, 1996.
- No. 82** **Kasten, S.**
Early Diagenetic Metal Enrichments in Marine Sediments as Documents of Nonsteady-State Depositional Conditions. Bremen, 1996.
- No. 83** **Holmes, M.E.**
Reconstruction of Surface Ocean Nitrate Utilization in the Southeast Atlantic Ocean Based on Stable Nitrogen Isotopes. 113 pages, Bremen, 1996.
- No. 84** **Rühlemann, C.**
Akkumulation von Carbonat und organischem Kohlenstoff im tropischen Atlantik: Spätquartäre Produktivitäts-Variationen und ihre Steuerungsmechanismen.
139 pages, Bremen, 1996.
- No. 85** **Ratmeyer, V.**
Untersuchungen zum Eintrag und Transport lithogener und organischer partikulärer Substanz im östlichen subtropischen Nordatlantik. 154 pages, Bremen, 1996.
- No. 86** **Cepek, M.**
Zeitliche und räumliche Variationen von Coccolithophoriden-Gemeinschaften im subtropischen Ost-Atlantik: Untersuchungen an Plankton, Sinkstoffen und Sedimenten.
156 pages, Bremen, 1996.
- No. 87** **Otto, S.**
Die Bedeutung von gelöstem organischen Kohlenstoff (DOC) für den Kohlenstofffluß im Ozean.
150 pages, Bremen, 1996.
- No. 88** **Hensen, C.**
Frühdiagenetische Prozesse und Quantifizierung benthischer Stoff-Flüsse in Oberflächensedimenten des Südatlantiks.
132 pages, Bremen, 1996.
- No. 89** **Giese, M. and G. Wefer**
Bericht über den 5. JGOFS-Workshop. 27./28. November 1996 in Bremen. 73 pages, Bremen, 1997.
- No. 90** **Wefer, G. and cruise participants**
Report and preliminary results of METEOR-Cruise M 37/1, Lisbon - Las Palmas, 4.-23.12.1996.
79 pages, Bremen, 1997.
- No. 91** **Isenbeck-Schröter, M., E. Bedbur, M. Kofod, B. König, T. Schramm & G. Mattheß**
Occurrence of Pesticide Residues in Water - Assessment of the Current Situation in Selected EU Countries. 65 pages, Bremen 1997.
- No. 92** **Kühn, M.**
Geochemische Folgereaktionen bei der hydrogeothermalen Energiegewinnung.
129 pages, Bremen 1997.
- No. 93** **Determann, S. & K. Herterich**
JGOFS-A6 "Daten und Modelle": Sammlung JGOFS-relevanter Modelle in Deutschland.
26 pages, Bremen, 1997.
- No. 94** **Fischer, G. and cruise participants**
Report and preliminary results of METEOR-Cruise M 38/1, Las Palmas - Recife, 25.1.-1.3.1997, with Appendix: Core Descriptions from METEOR Cruise M 37/1. Bremen, 1997.
- No. 95** **Bleil, U. and cruise participants**
Report and preliminary results of METEOR-Cruise M 38/2, Recife - Las Palmas, 4.3.-14.4.1997.
126 pages, Bremen, 1997.
- No. 96** **Neuer, S. and cruise participants**
Report and preliminary results of VICTOR HENSEN-Cruise 96/1. Bremen, 1997.
- No. 97** **Villinger, H. and cruise participants**
Fahrtbericht SO 111, 20.8. - 16.9.1996. 115 pages, Bremen, 1997.
- No. 98** **Lüning, S.**
Late Cretaceous - Early Tertiary sequence stratigraphy, paleoecology and geodynamics of Eastern Sinai, Egypt. 218 pages, Bremen, 1997.
- No. 99** **Haese, R.R.**
Beschreibung und Quantifizierung frühdiagenetischer Reaktionen des Eisens in Sedimenten des Südatlantiks. 118 pages, Bremen, 1997.

- No. 100** **Lührte, R. von**
Verwertung von Bremer Baggergut als Material zur Oberflächenabdichtung von Deponien - Geochemisches Langzeitverhalten und Schwermetall-Mobilität (Cd, Cu, Ni, Pb, Zn). Bremen, 1997.
- No. 101** **Ebert, M.**
Der Einfluß des Redoxmilieus auf die Mobilität von Chrom im durchströmten Aquifer. 135 pages, Bremen, 1997.
- No. 102** **Krögel, F.**
Einfluß von Viskosität und Dichte des Seewassers auf Transport und Ablagerung von Wattsedimenten (Langeooger Rückseitenwatt, südliche Nordsee). 168 pages, Bremen, 1997.
- No. 103** **Kerntopf, B.**
Dinoflagellate Distribution Patterns and Preservation in the Equatorial Atlantic and Offshore North-West Africa. 137 pages, Bremen, 1997.
- No. 104** **Breitzke, M.**
Elastische Wellenausbreitung in marinen Sedimenten - Neue Entwicklungen der Ultraschall Sedimentphysik und Sedimentechographie. 298 pages, Bremen, 1997.
- No. 105** **Marchant, M.**
Rezente und spätquartäre Sedimentation planktischer Foraminiferen im Peru-Chile Strom. 115 pages, Bremen, 1997.
- No. 106** **Habicht, K.S.**
Sulfur isotope fractionation in marine sediments and bacterial cultures. 125 pages, Bremen, 1997.
- No. 107** **Hamer, K., R.v. Lührte, G. Becker, T. Felis, S. Keffel, B. Strotmann, C. Waschkowitz, M. Kölling, M. Isenbeck-Schröter, H.D. Schulz**
Endbericht zum Forschungsvorhaben 060 des Landes Bremen: Baggergut der Hafengruppe Bremen-Stadt: Modelluntersuchungen zur Schwermetallmobilität und Möglichkeiten der Verwertung von Hafenschlick aus Bremischen Häfen. 98 pages, Bremen, 1997.
- No. 108** **Greeff, O.W.**
Entwicklung und Erprobung eines benthischen Landersystemes zur *in situ*-Bestimmung von Sulfatreduktionsraten mariner Sedimente. 121 pages, Bremen, 1997.
- No. 109** **Pätzold, M. und G. Wefer**
Bericht über den 6. JGOFS-Workshop am 4./5.12.1997 in Bremen. Im Anhang: Publikationen zum deutschen Beitrag zur Joint Global Ocean Flux Study (JGOFS), Stand 1/1998. 122 pages, Bremen, 1998.
- No. 110** **Landenberger, H.**
CoTReM, ein Multi-Komponenten Transport- und Reaktions-Modell. 142 pages, Bremen, 1998.
- No. 111** **Villinger, H. und Fahrtteilnehmer**
Fahrtbericht SO 124, 4.10. - 16.10.199. 90 pages, Bremen, 1997.
- No. 112** **Gietl, R.**
Biostratigraphie und Sedimentationsmuster einer nordostägyptischen Karbonatrampe unter Berücksichtigung der Alveolinen-Faunen. 142 pages, Bremen, 1998.
- No. 113** **Ziebis, W.**
The Impact of the Thalassinidean Shrimp *Callinassa truncata* on the Geochemistry of permeable, coastal Sediments. 158 pages, Bremen 1998.
- No. 114** **Schulz, H.D. and cruise participants**
Report and preliminary results of METEOR-Cruise M 41/1, Málaga - Libreville, 13.2.-15.3.1998. Bremen, 1998.
- No. 115** **Völker, D.J.**
Untersuchungen an strömungsbeeinflussten Sedimentationsmustern im Südozean. Interpretation sedimentechographischer Daten und numerische Modellierung. 152 pages, Bremen, 1998.
- No. 116** **Schlünz, B.**
Riverine Organic Carbon Input into the Ocean in Relation to Late Quaternary Climate Change. 136 pages, Bremen, 1998.
- No. 117** **Kuhnert, H.**
Aufzeichnung des Klimas vor Westaustralien in stabilen Isotopen in Korallenskeletten. 109 pages, Bremen, 1998.
- No. 118** **Kirst, G.**
Rekonstruktion von Oberflächenwassertemperaturen im östlichen Südatlantik anhand von Alkenonen. 130 pages, Bremen, 1998.
- No. 119** **Dürkoop, A.**
Der Brasil-Strom im Spätquartär: Rekonstruktion der oberflächennahen Hydrographie während der letzten 400 000 Jahre. 121 pages, Bremen, 1998.

- No. 120** **Lamy, F.**
Spätquartäre Variationen des terrigenen Sedimenteintrags entlang des chilenischen Kontinentalhangs als Abbild von Klimavariabilität im Milankovitch- und Sub-Milankovitch-Zeitbereich. 141 pages, Bremen, 1998.
- No. 121** **Neuer, S. and cruise participants**
Report and preliminary results of POSEIDON-Cruise Pos 237/2, Vigo – Las Palmas, 18.3.-31.3.1998. 39 pages, Bremen, 1998
- No. 122** **Romero, O.E.**
Marine planktonic diatoms from the tropical and equatorial Atlantic: temporal flux patterns and the sediment record. 205 pages, Bremen, 1998.
- No. 123** **Spieß, V. und Fahrtteilnehmer**
Report and preliminary results of RV SONNE Cruise 125, Cochin – Chittagong, 17.10.-17.11.1997. 128 pages, Bremen, 1998.
- No. 124** **Arz, H.W.**
Dokumentation von kurzfristigen Klimaschwankungen des Spätquartärs in Sedimenten des westlichen äquatorialen Atlantiks. 96 pages, Bremen, 1998.
- No. 125** **Wolff, T.**
Mixed layer characteristics in the equatorial Atlantic during the late Quaternary as deduced from planktonic foraminifera. 132 pages, Bremen, 1998.
- No. 126** **Dittert, N.**
Late Quaternary Planktic Foraminifera Assemblages in the South Atlantic Ocean: Quantitative Determination and Preservation Aspects. 165 pages, Bremen, 1998.
- No. 127** **Höll, C.**
Kalkige und organisch-wandige Dinoflagellaten-Zysten in Spätquartären Sedimenten des tropischen Atlantiks und ihre palökologische Auswertbarkeit. 121 pages, Bremen, 1998.
- No. 128** **Hencke, J.**
Redoxreaktionen im Grundwasser: Etablierung und Verlagerung von Reaktionsfronten und ihre Bedeutung für die Spurenelement-Mobilität. 122 pages, Bremen 1998.
- No. 129** **Pätzold, J. and cruise participants**
Report and preliminary results of METEOR-Cruise M 41/3, Vitória, Brasil – Salvador de Bahia, Brasil, 18.4. - 15.5.1998. Bremen, 1999.
- No. 130** **Fischer, G. and cruise participants**
Report and preliminary results of METEOR-Cruise M 41/4, Salvador de Bahia, Brasil – Las Palmas, Spain, 18.5. – 13.6.1998. Bremen, 1999.
- No. 131** **Schlünz, B. und G. Wefer**
Bericht über den 7. JGOFS-Workshop am 3. und 4.12.1998 in Bremen. Im Anhang: Publikationen zum deutschen Beitrag zur Joint Global Ocean Flux Study (JGOFS), Stand 1/ 1999. 100 pages, Bremen, 1999.
- No. 132** **Wefer, G. and cruise participants**
Report and preliminary results of METEOR-Cruise M 42/4, Las Palmas - Las Palmas - Viena do Castelo; 26.09.1998 - 26.10.1998. 104 pages, Bremen, 1999.
- No. 133** **Felis, T.**
Climate and ocean variability reconstructed from stable isotope records of modern subtropical corals (Northern Red Sea). 111 pages, Bremen, 1999.
- No. 134** **Draschba, S.**
North Atlantic climate variability recorded in reef corals from Bermuda. 108 pages, Bremen, 1999.
- No. 135** **Schmieder, F.**
Magnetic Cyclostratigraphy of South Atlantic Sediments. 82 pages, Bremen, 1999.
- No. 136** **Rieß, W.**
In situ measurements of respiration and mineralisation processes – Interaction between fauna and geochemical fluxes at active interfaces. 68 pages, Bremen, 1999.
- No. 137** **Devey, C.W. and cruise participants**
Report and shipboard results from METEOR-cruise M 41/2, Libreville – Vitoria, 18.3. – 15.4.98. 59 pages, Bremen, 1999.
- No. 138** **Wenzhöfer, F.**
Biogeochemical processes at the sediment water interface and quantification of metabolically driven calcite dissolution in deep sea sediments. 103 pages, Bremen, 1999.
- No. 139** **Klump, J.**
Biogenic barite as a proxy of paleoproductivity variations in the Southern Peru-Chile Current. 107 pages, Bremen, 1999.

- No. 140** **Huber, R.**
Carbonate sedimentation in the northern Northatlantic since the late pliocene. 103 pages, Bremen, 1999.
- No. 141** **Schulz, H.**
Nitrate-storing sulfur bacteria in sediments of coastal upwelling. 94 pages, Bremen, 1999.
- No. 142** **Mai, S.**
Die Sedimentverteilung im Wattenmeer: ein Simulationsmodell. 114 pages, Bremen, 1999.
- No. 143** **Neuer, S. and cruise participants**
Report and preliminary results of Poseidon Cruise 248, Las Palmas - Las Palmas, 15.2.-26.2.1999. 45 pages, Bremen, 1999.
- No. 144** **Weber, A.**
Schwefelkreislauf in marinen Sedimenten und Messung von *in situ* Sulfatreduktionsraten. 122 pages, Bremen, 1999.
- No. 145** **Hadeler, A.**
Sorptionreaktionen im Grundwasser: Unterschiedliche Aspekte bei der Modellierung des Transportverhaltens von Zink. 122 pages, 1999.
- No. 146** **Dierßen, H.**
Zum Kreislauf ausgewählter Spurenmetalle im Südatlantik: Vertikaltransport und Wechselwirkung zwischen Partikeln und Lösung. 167 pages, Bremen, 1999.
- No. 147** **Zühlsdorff, L.**
High resolution multi-frequency seismic surveys at the Eastern Juan de Fuca Ridge Flank and the Cascadia Margin – Evidence for thermally and tectonically driven fluid upflow in marine sediments. 118 pages, Bremen 1999.
- No. 148** **Kinkel, H.**
Living and late Quaternary Coccolithophores in the equatorial Atlantic Ocean: response of distribution and productivity patterns to changing surface water circulation. 183 pages, Bremen, 2000.
- No. 149** **Pätzold, J. and cruise participants**
Report and preliminary results of METEOR Cruise M 44/3, Aqaba (Jordan) - Safaga (Egypt) – Dubá (Saudi Arabia) – Suez (Egypt) - Haifa (Israel), 12.3.-26.3.-2.4.-4.4.1999. 135 pages, Bremen, 2000.
- No. 150** **Schlünz, B. and G. Wefer**
Bericht über den 8. JGOFS-Workshop am 2. und 3.12.1999 in Bremen. Im Anhang: Publikationen zum deutschen Beitrag zur Joint Global Ocean Flux Study (JGOFS), Stand 1/ 2000. 95 pages, Bremen, 2000.
- No. 151** **Schnack, K.**
Biostratigraphie und fazielle Entwicklung in der Oberkreide und im Alttertiär im Bereich der Kharga Schwelle, Westliche Wüste, SW-Ägypten. 142 pages, Bremen, 2000.
- No. 152** **Karwath, B.**
Ecological studies on living and fossil calcareous dinoflagellates of the equatorial and tropical Atlantic Ocean. 175 pages, Bremen, 2000.
- No. 153** **Moustafa, Y.**
Paleoclimatic reconstructions of the Northern Red Sea during the Holocene inferred from stable isotope records of modern and fossil corals and molluscs. 102 pages, Bremen, 2000.
- No. 154** **Villinger, H. and cruise participants**
Report and preliminary results of SONNE-cruise 145-1 Balboa – Talcahuana, 21.12.1999 – 28.01.2000. 147 pages, Bremen, 2000.
- No. 155** **Rusch, A.**
Dynamik der Feinfraktion im Oberflächenhorizont permeabler Schelfsedimente. 102 pages, Bremen, 2000.
- No. 156** **Moos, C.**
Reconstruction of upwelling intensity and paleo-nutrient gradients in the northwest Arabian Sea derived from stable carbon and oxygen isotopes of planktic foraminifera. 103 pages, Bremen, 2000.
- No. 157** **Xu, W.**
Mass physical sediment properties and trends in a Wadden Sea tidal basin. 127 pages, Bremen, 2000.
- No. 158** **Meinecke, G. and cruise participants**
Report and preliminary results of METEOR Cruise M 45/1, Malaga (Spain) - Lissabon (Portugal), 19.05. - 08.06.1999. 39 pages, Bremen, 2000.
- No. 159** **Vink, A.**
Reconstruction of recent and late Quaternary surface water masses of the western subtropical Atlantic Ocean based on calcareous and organic-walled dinoflagellate cysts. 160 pages, Bremen, 2000.
- No. 160** **Willems, H. (Sprecher), U. Bleil, R. Henrich, K. Herterich, B.B. Jørgensen, H.-J. Kuß, M. Olesch, H.D. Schulz, V. Spieß, G. Wefer**
Abschlußbericht des Graduierten-Kollegs Stoff-Flüsse in marine Geosystemen. Zusammenfassung und Berichtszeitraum Januar 1996 - Dezember 2000. 340 pages, Bremen, 2000.

- No. 161** **Sprengel, C.**
 Untersuchungen zur Sedimentation und Ökologie von Coccolithophoriden im Bereich der Kanarischen Inseln: Saisonale Flussmuster und Karbonatexport. 165 pages, Bremen, 2000.
- No. 162** **Donner, B. and G. Wefer**
 Bericht über den JGOFS-Workshop am 18.-21.9.2000 in Bremen:
 Biogeochemical Cycles: German Contributions to the International Joint Global Ocean Flux Study.
 87 pages, Bremen, 2000.
- No. 163** **Neuer, S. and cruise participants**
 Report and preliminary results of Meteor Cruise M 45/5, Bremen – Las Palmas, October 1 – November 3, 1999. 93 pages, Bremen, 2000.
- No. 164** **Devey, C. and cruise participants**
 Report and preliminary results of Sonne Cruise SO 145/2, Talcahuano (Chile) - Arica (Chile), February 4 – February 29, 2000. 63 pages, Bremen, 2000.
- No. 165** **Freudenthal, T.**
 Reconstruction of productivity gradients in the Canary Islands region off Morocco by means of sinking particles and sediments. 147 pages, Bremen, 2000.
- No. 166** **Adler, M.**
 Modeling of one-dimensional transport in porous media with respect to simultaneous geochemical reactions in CoTRem. 147 pages, Bremen, 2000.
- No. 167** **Santamarina Cuneo, P.**
 Fluxes of suspended particulate matter through a tidal inlet of the East Frisian Wadden Sea (southern North Sea). 91 pages, Bremen, 2000.
- No. 168** **Benthien, A.**
 Effects of CO₂ and nutrient concentration on the stable carbon isotope composition of C_{37:2} alkenones in sediments of the South Atlantic Ocean. 104 pages, Bremen, 2001.
- No. 169** **Lavik, G.**
 Nitrogen isotopes of sinking matter and sediments in the South Atlantic. 140 pages, Bremen, 2001.
- No. 170** **Budziak, D.**
 Late Quaternary monsoonal climate and related variations in paleoproductivity and alkenone-derived sea-surface temperatures in the western Arabian Sea. 114 pages, Bremen, 2001.
- No. 171** **Gerhardt, S.**
 Late Quaternary water mass variability derived from the pteropod preservation state in sediments of the western South Atlantic Ocean and the Caribbean Sea. 109 pages, Bremen, 2001.
- No. 172** **Bleil, U. and cruise participants**
 Report and preliminary results of Meteor Cruise M 46/3, Montevideo (Uruguay) – Mar del Plata (Argentina), January 4 – February 7, 2000. Bremen, 2001.
- No. 173** **Wefer, G. and cruise participants**
 Report and preliminary results of Meteor Cruise M 46/4, Mar del Plata (Argentina) – Salvador da Bahia (Brazil), February 10 – March 13, 2000. With partial results of METEOR cruise M 46/2. 136 pages, Bremen, 2001.
- No. 174** **Schulz, H.D. and cruise participants**
 Report and preliminary results of Meteor Cruise M 46/2, Recife (Brazil) – Montevideo (Uruguay), December 2 – December 29, 1999. 107 pages, Bremen, 2001.
- No. 175** **Schmidt, A.**
 Magnetic mineral fluxes in the Quaternary South Atlantic: Implications for the paleoenvironment. 97 pages, Bremen, 2001.
- No. 176** **Bruhns, P.**
 Crystal chemical characterization of heavy metal incorporation in brick burning processes. 93 pages, Bremen, 2001.
- No. 177** **Karius, V.**
 Baggergut der Hafengruppe Bremen-Stadt in der Ziegelherstellung. 131 pages, Bremen, 2001.
- No. 178** **Adegbie, A. T.**
 Reconstruction of paleoenvironmental conditions in Equatorial Atlantic and the Gulf of Guinea Basins for the last 245,000 years. 113 pages, Bremen, 2001.
- No. 179** **Spieß, V. and cruise participants**
 Report and preliminary results of R/V Sonne Cruise SO 149, Victoria - Victoria, 16.8. - 16.9.2000. 100 pages, Bremen, 2001.
- No. 180** **Kim, J.-H.**
 Reconstruction of past sea-surface temperatures in the eastern South Atlantic and the eastern South Pacific across Termination I based on the Alkenone Method. 114 pages, Bremen, 2001.

- No. 181** **von Lom-Keil, H.**
Sedimentary waves on the Namibian continental margin and in the Argentine Basin – Bottom flow reconstructions based on high resolution echosounder data. 126 pages, Bremen, 2001.
- No. 182** **Hebbeln, D. and cruise participants**
PUCK: Report and preliminary results of R/V Sonne Cruise SO 156, Valparaiso (Chile) - Talcahuano (Chile), March 29 - May 14, 2001. 195 pages, Bremen, 2001.
- No. 183** **Wendler, J.**
Reconstruction of astronomically-forced cyclic and abrupt paleoecological changes in the Upper Cretaceous Boreal Realm based on calcareous dinoflagellate cysts. 149 pages, Bremen, 2001.
- No. 184** **Volbers, A.**
Planktic foraminifera as paleoceanographic indicators: production, preservation, and reconstruction of upwelling intensity. Implications from late Quaternary South Atlantic sediments. 122 pages, Bremen, 2001.
- No. 185** **Bleil, U. and cruise participants**
Report and preliminary results of R/V METEOR Cruise M 49/3, Montevideo (Uruguay) - Salvador (Brasil), March 9 - April 1, 2001. 99 pages, Bremen, 2001.
- No. 186** **Scheibner, C.**
Architecture of a carbonate platform-to-basin transition on a structural high (Campanian-early Eocene, Eastern Desert, Egypt) – classical and modelling approaches combined. 173 pages, Bremen, 2001.
- No. 187** **Schneider, S.**
Quartäre Schwankungen in Strömungsintensität und Produktivität als Abbild der Wassermassen-Variabilität im äquatorialen Atlantik (ODP Sites 959 und 663): Ergebnisse aus Siltkorn-Analysen. 134 pages, Bremen, 2001.
- No. 188** **Uliana, E.**
Late Quaternary biogenic opal sedimentation in diatom assemblages in Kongo Fan sediments. 96 pages, Bremen, 2002.
- No. 189** **Esper, O.**
Reconstruction of Recent and Late Quaternary oceanographic conditions in the eastern South Atlantic Ocean based on calcareous- and organic-walled dinoflagellate cysts. 130 pages, Bremen, 2001.
- No. 190** **Wendler, I.**
Production and preservation of calcareous dinoflagellate cysts in the modern Arabian Sea. 117 pages, Bremen, 2002.
- No. 191** **Bauer, J.**
Late Cenomanian – Santonian carbonate platform evolution of Sinai (Egypt): stratigraphy, facies, and sequence architecture. 178 pages, Bremen, 2002.
- No. 192** **Hildebrand-Habel, T.**
Die Entwicklung kalkiger Dinoflagellaten im Südatlantik seit der höheren Oberkreide. 152 pages, Bremen, 2002.
- No. 193** **Hecht, H.**
Sauerstoff-Optopoden zur Quantifizierung von Pyritverwitterungsprozessen im Labor- und Langzeit-in-situ-Einsatz. Entwicklung - Anwendung – Modellierung. 130 pages, Bremen, 2002.
- No. 194** **Fischer, G. and cruise participants**
Report and Preliminary Results of RV METEOR-Cruise M49/4, Salvador da Bahia – Halifax, 4.4.-5.5.2001. 84 pages, Bremen, 2002.
- No. 195** **Gröger, M.**
Deep-water circulation in the western equatorial Atlantic: inferences from carbonate preservation studies and silt grain-size analysis. 95 pages, Bremen, 2002.
- No. 196** **Meinecke, G. and cruise participants**
Report of RV POSEIDON Cruise POS 271, Las Palmas - Las Palmas, 19.3.-29.3.2001. 19 pages, Bremen, 2002.
- No. 197** **Meggers, H. and cruise participants**
Report of RV POSEIDON Cruise POS 272, Las Palmas - Las Palmas, 1.4.-14.4.2001. 19 pages, Bremen, 2002.
- No. 198** **Gräfe, K.-U.**
Stratigraphische Korrelation und Steuerungsfaktoren Sedimentärer Zyklen in ausgewählten Borealen und Tethyalen Becken des Cenoman/Turon (Oberkreide) Europas und Nordwestafrikas. 197 pages, Bremen, 2002.
- No. 199** **Jahn, B.**
Mid to Late Pleistocene Variations of Marine Productivity in and Terrigenous Input to the Southeast Atlantic. 97 pages, Bremen, 2002.
- No. 200** **Al-Rousan, S.**
Ocean and climate history recorded in stable isotopes of coral and foraminifers from the northern Gulf of Aqaba. 116 pages, Bremen, 2002.

- No. 201** **Azouzi, B.**
Regionalisierung hydraulischer und hydrogeochemischer Daten mit geostatistischen Methoden. 108 pages, Bremen, 2002.
- No. 202** **Spieß, V. and cruise participants**
Report and preliminary results of METEOR Cruise M 47/3, Libreville (Gabun) - Walvis Bay (Namibia), 01.06 - 03.07.2000. 70 pages, Bremen 2002.
- No. 203** **Spieß, V. and cruise participants**
Report and preliminary results of METEOR Cruise M 49/2, Montevideo (Uruguay) - Montevideo, 13.02 - 07.03.2001. 84 pages, Bremen 2002.
- No. 204** **Mollenhauer, G.**
Organic carbon accumulation in the South Atlantic Ocean: Sedimentary processes and glacial/interglacial Budgets. 139 pages, Bremen 2002.
- No. 205** **Spieß, V. and cruise participants**
Report and preliminary results of METEOR Cruise M49/1, Cape Town (South Africa) - Montevideo (Uruguay), 04.01.2000 - 10.02.2000. 57 pages, Bremen, 2003.
- No. 206** **Meier, K.J.S.**
Calcareous dinoflagellates from the Mediterranean Sea: taxonomy, ecology and palaeoenvironmental application. 126 pages, Bremen, 2003.
- No. 207** **Rakic, S.**
Untersuchungen zur Polymorphie und Kristallchemie von Silikaten der Zusammensetzung $\text{Me}_2\text{Si}_2\text{O}_5$ (Me:Na, K). 139 pages, Bremen, 2003.
- No. 208** **Pfeifer, K.**
Auswirkungen frühdiagenetischer Prozesse auf Calcit- und Barytgehalte in marinen Oberflächen-sedimenten. 110 pages, Bremen, 2003.
- No. 209** **Heuer, V.**
Spurenelemente in Sedimenten des Südatlantik. Primärer Eintrag und frühdiagenetische Überprägung. 136 pages, Bremen, 2003.
- No. 210** **Streng, M.**
Phylogenetic Aspects and Taxonomy of Calcareous Dinoflagellates. 157 pages, Bremen 2003.
- No. 211** **Boeckel, B.**
Present and past coccolith assemblages in the South Atlantic: implications for species ecology, carbonate contribution and palaeoceanographic applicability. 157 pages, Bremen, 2003.
- No. 212** **Precht, E.**
Advective interfacial exchange in permeable sediments driven by surface gravity waves and its ecological consequences. 131 pages, Bremen, 2003.
- No. 213** **Frenz, M.**
Grain-size composition of Quaternary South Atlantic sediments and its paleoceanographic significance. 123 pages, Bremen, 2003.
- No. 214** **Meggers, H. and cruise participants**
Report and preliminary results of METEOR Cruise M 53/1, Limassol - Las Palmas - Mindelo, 30.03.2002 - 03.05.2002. 81 pages, Bremen, 2003.
- No. 215** **Schulz, H.D. and cruise participants**
Report and preliminary results of METEOR Cruise M 58/1, Dakar - Las Palmas, 15.04..2003 - 12.05.2003. Bremen, 2003.
- No. 216** **Schneider, R. and cruise participants**
Report and preliminary results of METEOR Cruise M 57/1, Cape Town - Walvis Bay, 20.01. - 08.02.2003. 123 pages, Bremen, 2003.
- No. 217** **Kallmeyer, J.**
Sulfate reduction in the deep Biosphere. 157 pages, Bremen, 2003.
- No. 218** **Røy, H.**
Dynamic Structure and Function of the Diffusive Boundary Layer at the Seafloor. 149 pages, Bremen, 2003.
- No. 219** **Pätzold, J., C. Hübscher and cruise participants**
Report and preliminary results of METEOR Cruise M 52/2&3, Istanbul - Limassol - Limassol, 04.02. - 27.03.2002. Bremen, 2003.
- No. 220** **Zabel, M. and cruise participants**
Report and preliminary results of METEOR Cruise M 57/2, Walvis Bay - Walvis Bay, 11.02. - 12.03.2003. 136 pages, Bremen 2003.
- No. 221** **Salem, M.**
Geophysical investigations of submarine prolongations of alluvial fans on the western side of the Gulf of Aqaba-Red Sea. 100 pages, Bremen, 2003.
- No. 222** **Tilch, E.**
Oszillation von Wattflächen und deren fossiles Erhaltungspotential (Spiekeroooger Rückseitenwatt, südliche Nordsee). 137 pages, Bremen, 2003.

- No. 223** **Frisch, U. and F. Kockel**
Der Bremen-Knoten im Strukturnetz Nordwest-Deutschlands. Stratigraphie, Paläogeographie, Strukturgeologie. 379 pages, Bremen, 2004.
- No. 224** **Kolonic, S.**
Mechanisms and biogeochemical implications of Cenomanian/Turonian black shale formation in North Africa: An integrated geochemical, millennial-scale study from the Tarfaya-LaAyoune Basin in SW Morocco. 174 pages, Bremen, 2004.
- No. 225** **Panteleit, B.**
Geochemische Prozesse in der Salz- Süßwasser Übergangszone. 106 pages, Bremen, 2004.
- No. 226** **Seiter, K.**
Regionalisierung und Quantifizierung benthischer Mineralisationsprozesse. 135 pages, Bremen, 2004.
- No. 227** **Bleil, U. and cruise participants**
Report and preliminary results of METEOR Cruise M 58/2, Las Palmas – Las Palmas (Canary Islands, Spain), 15.05. – 08.06.2003. 123 pages, Bremen, 2004.
- No. 228** **Kopf, A. and cruise participants**
Report and preliminary results of SONNE Cruise SO175, Miami - Bremerhaven, 12.11 - 30.12.2003. 218 pages, Bremen, 2004.
- No. 229** **Fabian, M.**
Near Surface Tilt and Pore Pressure Changes Induced by Pumping in Multi-Layered Poroelastic Half-Spaces. 121 pages, Bremen, 2004.